Development of an advanced multi-cellular and dynamic flow model of the human alveolar airway

Joana Leonor Amaral Duarte de Moura

Submitted to Swansea University in Fulfilment of the Requirements for the Degree of Doctor of Philosophy

Swansea University

March 2022

Abstract

This project aimed to construct a 3D dynamic model of the human air-blood barrier. The model was an assembly of the alveolar region of the human lung, and the associated vasculature on the basolateral side, all integrated into a bioreactor under fluid flow. The alveolar model aimed to include epithelial cells, such as alveolar type I (NCI-H441 or hAELVi) and type II (A549), together with macrophages (PMA differentiated THP-1 (dTHP-1)). The biomaterial selected to mimic the alveolar region extracellular matrix was derived from the decellularization of human lung fibroblast cells, cultured into a sheet. To create the vasculature model, endothelial cells (HULEC 5a) were co-cultured with human lung fibroblasts (HLF-1) within a hydrogel. Two biomaterials were tested to support the growth of the vasculature model; (i) a gelatin and alginate mesh or (ii) a fibrin gel. Regarding the bioreactor, besides ensuring the sterility of the cellular model, the goal was to enable the culture of the alveolar *in vitro* model at the air-liquid interface (ALI) and the vascular model under fluid-flow dynamics.

To achieve what was proposed above, the project was divided into three parts; the first focused on the alveolar model, where the development of the decellularized membrane, as well as the cell culture model are described in chapters 3 and 4. The decellularization procedure included several approaches to remove the DNA content. These consisted of freeze-thaw cycles and exposure to surfactants such as sodium dodecyl sulfate (SDS) and Triton. The decellularized extracellular matrix (dECM), was tested as a scaffold or cross-linked with riboflavin or fibrin to support the growth of NCI-H441, hAELVi, A549 and dTHP-1 cells. It was observed that only monocultures of A549 and dTHP-1 cells were able to grow and proliferate under both submerged and ALI conditions upon the dECM crosslink with fibrin (dECM/fibrin). The second part of the project addresses the vasculature model (chapter 5). The gelatin and alginate mesh was first investigated to support the endothelial cells (ECs) growth, but with a lack of success. Moving forward, the fibrin gel was investigated, where a range of concentrations of fibrinogen and thrombin were tested. After some final gel volume adjustment, the fibrin was able to support the ECs growth and proliferation. The fibrin gel was characterized regarding its rheology and porosity which, together with cell proliferation data, 2.5 mg/mL fibrinogen and 5 U/mL thrombin mix was selected to build the vasculature co-culture model within the bio-matrix. Once established, supplemented media was designed to induce angiogenesis, which was able to promote, in static conditions, cell organization into 3D geometries resembling tip cells and cord formation. Under dynamic conditions, the vasculature shows ECs with tip cell morphology, however, cord formation was lacking, as was fibroblast proliferation. Finally, the third part is comprised of the bioreactor design, fabrication and simulation. Multiple iterations were designed, created and tested (chapter 6). Initially, the first and second version of the bioreactor was constructed in acrylic or polycarbonate. Yet, this did not allow for the alveolar model positioning. Therefore, subsequent versions were manufactured in laser cut to ensure complete transparency of acrylic and included a silicone part where the cellular model was placed. Based on these findings, a complete model was created by integrating the alveolar and vasculature models into the bioreactor (chapter 7). Under fluid flow, the full model showed a complete A549 cell monolayer populated with dTHP-1 on the apical layer. Though, unfortunately, when combined with all parts together, the vasculature model showed a lack of cell viability and proliferation.

In conclusion, the proposed model demonstrated the possibility to combine a diverse cell population with a physiologically relevant mechanical environment. The integrated model requires further optimizations, such as in the dECM biomaterial and a different cell source in the vasculature. However, a foundation to create a dynamic air-blood barrier system has been shown in order to gain further insight towards building anatomically and physiologically relevant non-animal models for next generation risk assessment.

Declarations and Statements

DECLARATION

This work has not previously been accepted in substance for any degree and is not being concurrently submitted in candidature for any degree.

Signed:

Date: 31.03.2022

STATEMENT 1

This thesis is the result of my own investigations, except where otherwise stated. Where correction services have been used, the extent and nature of the correction is clearly marked in a footnote(s).

Other sources are acknowledged by footnotes giving explicit references. A bibliography is appended.

Signed:

Date: 31.03.2022

STATEMENT 2

I hereby give consent for my thesis, if accepted, to be available for photocopying and for inter-library loan, and for the title and summary to be made available to outside organizations.

Signed:

Date: 31.03.2022

Table of Contents

Acknowledgments

List of Tables

List of Figures

Chapter 1

Chapter 2

Chapter 3

Chapter 4

Chapter 5

Chapter 6

Chapter 7

Chapter 8

List of Equations

Chapter 1

Chapter 2

Chapter 6

Abbreviations

Cell	HLF-1	Human Lung Fibroblast
	EC	Human Lung Microvasculature Endothelial Cells (HULEC-5a)
	THP-1	Peripheral Blood Monocytes From Acute Monocytic Leukemia
	dTHP-1	PMA Differentiated THP-1
	hAELVi	Human Alveolar Epithelial Cells (CI-Haelvi)
	H441	Alveolar Type II Cell Line NCI-H441)
	A549	Alveolar Type II Cell Line
	EP1	Alveolar Type I
	EP2	Alveolar Type II
Cell culture	PBS	Phosphate Buffered Saline
	FBS	Foetal Bovine Serum
	Pen/Strep	Penicillin-Streptomycin
	DMSO	Dimethyl Sulfoxide
	BSA	Bovine Serum Albumin
	hEGF	Human Epidermal Growth Factor
	VEGF	Vascular Endothelial Growth Factor 165
	S1P	Sphingosine 1-Phosphate
	bFGF	Fibroblast Growth Factor Basic
	PMA	Phorbol 12-Myristate 13-Acetate
	LPS	Lipopolysaccharide
	DMEM	Dulbecco'S Modified Eagle'S Medium
	RMP1 1640	Roswell Park Memorial Institute 1650
	MCDB131	Media Developed By Knedler And Ham
	IL6	Interleukin 6
	IL8	Interleukin 8
	TNF-α	Tumour necrosis factor alfa
	TGF-β	Transforming growth factor beta
	IL-1β	Interleukin 1 beta
Assays	Picogreen	Quant-iT™ PicoGreen™ dsDNA Assay Kit:
	FACs	Fluorescence-activated cell sorting
	SDS PAGE	sodium dodecyl sulfate–polyacrylamide gel electrophoresis
	MTS	MTS CellTiter 96® AQueous One Solution Cell Proliferation Assay
	LDH	Lactate Dehydrogenase
	ELISA	Enzyme-Linked Immunosorbent Assay
	DC	Detergent Compatible Protein Assay
	Sircol	Sircol Insoluble Collagen Assay
	Blyscan	Glycosaminoglycan Blyscan Assay
Chemicals	DPX	Dibutylphthalate Polystyrene Xylene)
	Triton	Triton X-100
	SDS	Sodium Dodecyl Sulfate
	NH_4OH	Ammonium Hydroxide
	NaOH	Sodium Hydroxide
	$NaCl_2$	Sodium Chloride

	NaN$_3$	Sodium Azide
	H$_2$SO$_4$	Sulfuric Acid
	CaCl	Calcium Chloride
	HEPES	2-[4-(2-Hydroxyethyl)Piperazin-1-Yl]Ethane-1-Sulfonic Acid
	Tris	Tris(hidroximetil)aminometano
	HCl	Hydrochloric Acid
	DAPI	4',6-Diamidino-2-Phenylindole Dihydrochloride
	H&E	Haematoxylin and Eosin Y
	DTT	Dithiothreitol
	NaAc	Sodium Acetate
	EDTA	Ethylenediaminetetraacetic Acid
	TE buffer	Tris-EDTA Buffer Solution
	TAE buffer	Tris-Acetate-EDTA Buffer Solution
	RIPA	Radioimmunoprecipitation Assay Buffer
	CHAPS	3-[(3-Cholamidopropyl)Dimethylammonio]-1-Propanesulfonate
	TEMED	N,N,N',N'-Tetramethylethane-1,2-Diamine
	Li-Lactate	Lithium lactate
	APS	Ammonium Persulfate
	NAD	Nicotinamide Adenine Dinucleotide
	INT	Iodonitrotetrazolium Chloride
	PMS	Phenazine Methosulfate
	Tris	2-Amino-2-(Hydroxymethyl)Propane-1,3-Diol
	PI	Propidium Iodide
	PDMS	Polydimethylsiloxanes
	PFA	Paraformaldehyde
	DPX	Dibutylphthalate Polystyrene Xylene
	PLA	Polylactic acid
	TPU	Thermoplastic polyurethane
	Tween	Tween-20, Polysorbate 20
	GAGs	Glycosaminoglycans
Others	ECM	Extracellular Matrix
	dECM	Decellularized Extracellular Matrix
	ALI	Air Liquid Interface
	dECM/fibrin	Decellularized Extracellular Matrix Crosslink With Fibrin
	NADPH	Nicotinamide Adenine Dinucleotide Phosphate
	dsDNA	Double Strand DNA
Equipment	Confocal	Confocal Laser Scanning Microscopy (CLSM
	SEM	Scanning Electron Microscopy
	BF	Bright Field Microscopy
	CNC machine	Automatic Computerized Numerical Control Machine

Chapter 1
General Introduction

1.1 Overview

The following introduction aims to provide an overview of the necessary background knowledge to support the rationale of the proposed *in vitro* model that formulates this thesis. In this way, the literature review begins with an outline of the anatomy of the human lung, emphasizing the alveolar region, cellular and extracellular environment. Afterwards, the mechanical side of the lung including physiological breathing and ventilation are discussed, together with the importance of surfactant for this motion. The current state of the art, regarding *in vitro* lung model strategies are then discussed, detailing the advantages and limitations of each technology. Furthermore, the mechanisms regarding vasculature formation, such as vasculogenesis and angiogenesis are subsequently introduced, as well as current *in vitro* models that mimic it. After this, the rationale for the herein presented project, alongside its specific aims and objectives are described.

1.1.1 Overview of Lung Anatomy

The human respiratory main function is to support the gas exchange process[1]. To address the high energetic demands of aerobic metabolism, the extraction of oxygen from the air and the removal of carbon dioxide waste from the bloodstream evolved to be maximized. The efficiency of the air-blood barrier relies on the large surface area, nearly the size of a tennis court, on the order of 130 m^3. This is combined with a thin barrier, that can reach only 0.3 μm on the thinnest parts. Where gas transfer takes less than a second to occur into a capillary network, which has the size of a red blood cell and is only 10% smaller than the alveolar surface area[2]. Further important functions of this organ are related to barrier protection, fluid balance, particle clearing, as well as mucus and surfactant production. Whilst all these functions are ensured, the organ maintains its cyclic deformation to support the inhalation and exhalation of air, thus making the lung a complex and dynamic organ to mimic.

To achieve such a mimicking, the manner of how the lung works must be known. Thus, briefly, air enters the nasal cavity passes through the trachea, where it branches into two bronchi. This branching mechanism continues for 22 more generations, where the continuous branching generates smaller airways until the alveolar sacs are reached. The extensive alveolar surface, the small thickness barrier in addition to the extreme proximity of a dense capillary network supports gas diffusion. In addition to the tree-like complex architecture, the extracellular matrix and cell population differ depending on the area of the lung[3].

The human lungs are confined to the thoracic cavity and can reach a total lung capacity of 6.0L and 4.2L for men and women respectively[4]. At the end of a breath, 80% of the lung volume is air, 10% tissue and 10% blood. The lung is divided into two lobes, the right side of the lung has three lobes and the left two. The organ is enclosed by a membrane known as the pleura which has a fundamental role in providing a link between the lung and the chest, ensuring efficient mechanical transduction of the breathing motion. The pleura is a membrane that is folded between itself, one side contacts with the lung (visceral pleurae) and the other is connected to the chest (parietal pleurae). Both layers are composed of squamous epithelial cells with long microvilli. In the middle, a thin film of serous fluid lubricates the surfaces, housing 75% macrophages, 23% lymphocytes and 1% mesothelial cells. Figure 1.1 provides a visual overview of the above description[3].
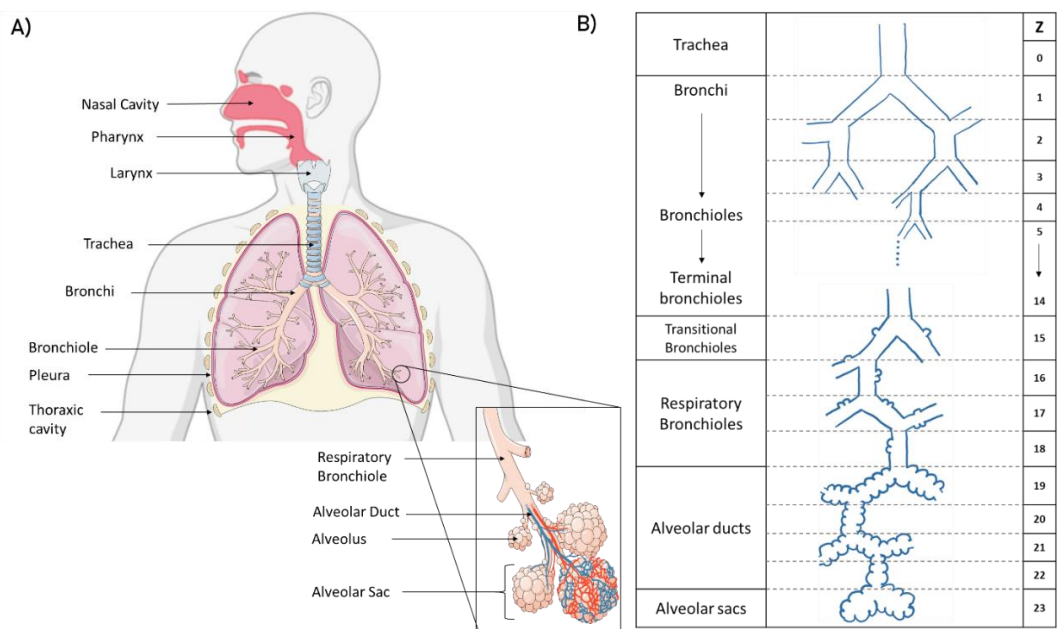
Figure 1.1: Lung anatomy illustration. A) Anatomy of the respiratory tract (images used from an image bank[5]). **B)** Illustration of the structure and dimensions along the 23 branching generations. Image adapted from Ochs, M and Weibel R. E, Fishman´s Pulmonary Disease and Disorder book, chapter2[3].

The lung's phenotype is created through 23 generations of successive branching, as illustrated in figure 1.1B. The air, when inhaled by the mouth or nose is directed to the trachea, forming branching generation zero. The trachea is a tube that is between 20-25 mm in width and 100 mm in length, and is maintained open during breathing due to the C-shaped bands of cartilage that provide structural integrity/rigidity (*i.e.* the incomplete cartilage rings allow the oesophagus to be accommodated behind the trachea). Then, the trachea branches into two main bronchi in

generation 1. The bronchi partitioning continues for more 2 generations and experiences a reduction in diameter from 12-16 mm to approximately 1-8 mm. Likewise, the trachea and the bronchi are kept open through a series of complete cartilaginous rings. Progressing in the generations, the latter are substituted by plates, which slowly diminish until null cartilage is present in the airways. At this point, the branching is at generation 4 and is composed of the bronchioles. This structure contains a range in diameters from 0.5-1 mm wall thickness. The ramification continues until terminal bronchioles are reached, where the internal diameter is expected to be lower than 0.5 mm. The end of terminal bronchioles defines the end of the conducting zone, which the main function is to support the passage of air during inhalation and exhalation. The latter holds a ventilatory dead space of about 150 ml, which has an important function, as air is inhaled and passes through the dead space the temperature is allowed to equilibrate with the human body and gain moisture. This phenomenon facilitates the diffusion of the gases in the alveolar region. Afterwards, belonging to generation 15, the transitional bronchioles are found, which as the name indicates, are characterized by a transitional area where the smooth walls of the conducting airways start to be interrupted by alveoli. Next, from generation 16 to 23, the alveolarization increases with branching. These generations include the respiratory bronchioles, alveolar ducts and finally the functional units of the lung, the alveolar sacs, with an average diameter in the order of 0.3 mm. This area from the transitional bronchioles until the alveolar sacs, generation 15-23, is also mentioned as the acinar airways[3].

The walls of the airways are composed of three main layers: an epithelial and connective tissue layer, a smooth muscle layer and a fibrous layer. There is a continuous change from the trachea to the alveoli sacs, however the lungs are normally separated into three anatomically distinct regions: trachea and bronchi, bronchioles and alveolar region. The following sections are going into detail about cell and matrix characterization of the three main sections of the lung. The final section of the lung, the alveolar region, is going to be described in higher detail since is the area of specific interest for this project.

1.1.1.1 Trachea and Bronchi

The first section of the lung, the trachea and bronchi, are characterized by a population of goblet cells, specialized in mucus secretion and ciliated cells, that continuously, and in synchrony, move their cilia. There are five ciliated cells to one goblet cell, figure 1.2 show their morphology and distribution. The mucus covers the surface until the bronchioles and is considered the first line of defence against particles or microbes inhaled, which due to the upward movement imposed by the ciliated cells is cleared from the airways and subsequently swallowed. Particles that

deposit the most in the area between the trachea and the bronchi have around 15 μm in diameter[6]. Another cell type to highlight is the clara cells (also known as club cells), which have diverse functions including secretion of club cell secretory protein (CCSP), and linkage to immune system regulation. These cells also contain high levels of cytochrome P450 activity, suggesting a role in detoxification and show progenitor activity during lung damage[7]. Other cell populations observed at this level of the proximal airways are basal cells, which form a monolayer along the basement membrane to provide the support for the other epithelium cells to attach, as well as pulmonary neuroendocrine cells, which can be found as individual cells or in clusters as pulmonary neuroendocrine bodies. Regarding the connective tissue present in the trachea and bronchi, its main component is hyaline cartilage as to referred before in section 1.1.1[3].
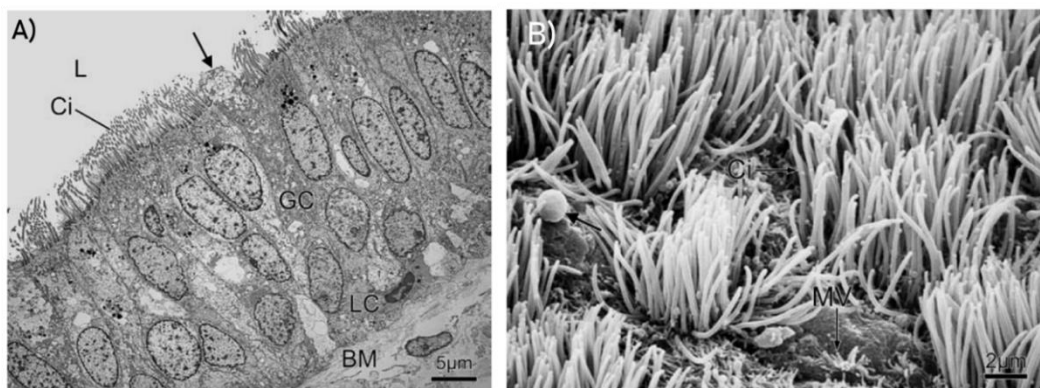
Figure 1.2: Morphology of trachea and bronchi area with scanning electron microscopy. A) cross section of the human bronchial epithelium highlighting ciliated cells (Ci), goblet cells (GC), basal membrane (BM), a leucocyte (LC), the lumen (L) where the air flows through and the arrow indicates segregated mucus. **B)** Represents the bronchial epithelium surface, with ciliated cells (Ci) and microvilli (MV). The arrow indicates the droplet segregated by the goblet cells. Image adapted from Ochs, M and Weibel R. E, Fishman´s Pulmonary Disease and Disorder book, chapter2[3].

1.1.1.2 Bronchioles

The cell population of the bronchioles differs only slightly from the trachea and bronchi. The ciliated and clara cells compose the epithelium in equal numbers. While the basal cells are absent, the goblet cells gradually reduce from bronchioles to respiratory bronchioles. The number of pulmonary neuroendocrine cells also falls and these cells are mostly found isolated in the bodies[3]. Figure 1.3 represents a scanning electron micrograph of the branching starting on the bronchioles until the alveolar sacs. The image shows the structure of the acinar airways, from the transitional bronchioles, identified with a T in the image, until the alveoli highlighted

with an A, where the airways start to be decorated with alveoli. Air rich in oxygen that reaches the acinus is directed to airways with a diameter in the order of 500 μm that falls until 270 μm in the alvoli[8]. The alveoli that share the same acini, share the same oxygen source. It is estimated that the lung has between 26 000 to 32 000 acini that have on average around 12 000 alveoli each[2,8].
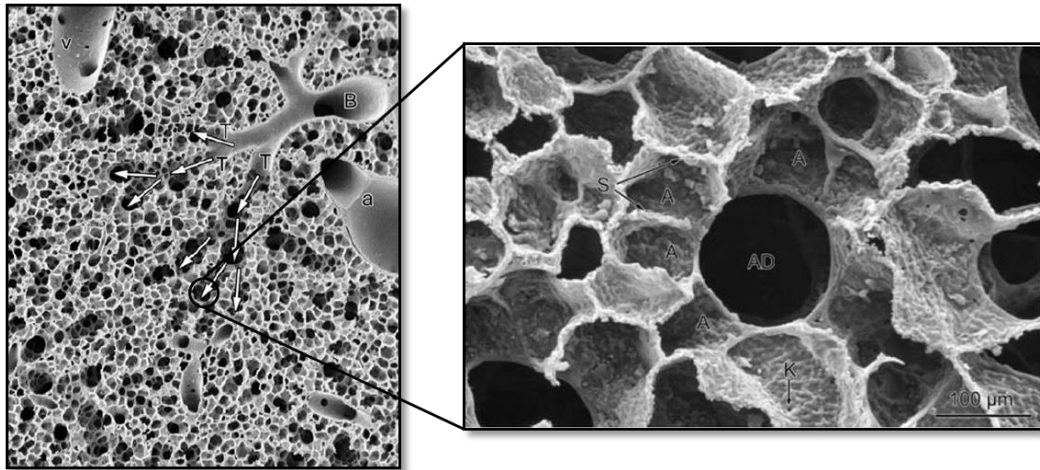
Figure 1.3: Cross section of the branching at the bronchioles level. The white arrows show the airways starting on the bronchioles (B), passing through transitional bronchioles (T), respiratory bronchioles and alveolar ducts. The picture also shows an artery (a) and a vein (v). The picture on the right shows a close up of the alveolar ducts (AD) surrounded by alveoli (A) which are separated by the septum (S). Image adapted from Ochs, M and Weibel R. E, Fishman´s Pulmonary Disease and Disorder book, chapter2[3].

1.1.1.3 Alveolar Region

In the 23rd generation of branching, the airways suddenly open into the alveolar sacs. An overall schematic is shown in figure 1.4. The alveolar surface area is characterized by having approximately 143 m^2, with 126 m^2 occupied by the capillaries that hold a total of 213 mL of blood[9]. This area contains a number of alveoli in the order of 480 million[10] with an average thickness of 2.2 μm[9]. But if instead of looking at the arithmetic mean of the alveoli thickness, is determined the harmonic mean, which gives more weight to smaller numbers, is calculated as a thickness for the air-blood barrier of 0.62 μm[9]. This is because half of the alveolar region actively participates in the gas exchange, where the epithelium and endothelium base membranes fuse reducing the air-blood barrier to a minimum of 0.3 μm [2]. The other half of the barrier contains a well-defined interstitial layer, where supportive cells and fibres are responsible for the 3D structure of the alveolar sacs. The air-blood barrier can be separated into three different layers: the epithelium layer lining the air space, the interstitial layer housing the

connective tissue and cells of support and the endothelium lining the capillaries. From section 1.1.1.3.1 to 1.1.1.3.3 is provided more detail on cell and matrix composition from these three layers.

Alveolar Epithelium		Alveolar type I Alveolar Type II
Interstitial Layer	Basal Membrane	Collagen I Collagen III Collagen IV Elastin Heparin Sulphate Chondroitin Sulphate
	Cell Composition	Fibroblasts Smooth Muscle Cells Macrophages
Endothelium Layer		Endothelial Cells Pericytes

Macrophage   Alveolar Type II
Fibroblats   Alveolar Type I
Endothelial Cells   Smooth Muscle Cell
Pericytes   Hypophase
Surfactant

Figure 1.4: Alveolar region basal membrane and cell composition. The table summarizes the cells and basal membrane characterizing the alveolar epithelium, interstitial layer and endothelium layer. The illustration represents a cross section of an alveolar sac, highlighting the thin alveoli, where the endothelial and alveolar type I cells contact for the gas transfer. On the other hand, the thick alveoli correspond to the septum (free edge) that separates adjacent alveoli. This area contains most of the fibres and supportive cells, such as alveolar type II, fibroblasts and smooth muscle cells. In addiction is also showed the alveolar macrophages, responsible for foreign bodies clearing and the pericytes that support the vasculature. The illustration also includes the surfactant lining layer and the hypophase – water-based layer rich in cytokines and growth factors for cell communication (images used from an image bank[5]).

1.1.1.3.1. Alveolar Epithelium

The alveolar epithelium is composed of type I and type II alveolar epithelial cells, EP1 and EP2 respectively (AECT1 and AECT2 are also commonly used abbreviations found in the literature to determine alveolar type I and II respectively). These two types of cells are represented in figure 1.5. Each alveolus has on average, an area in the order of 220 000 μm^2, where can be found 40 type I alveolar epithelial cells and 77 type II[11] (similar values are found on another reference[12] 47 type I and 92 type II per alveoli). Although being in the lower number, the EP1 covers 95% of the alveolar surface area, with each cell having approximately 5100 μm^2, while 180 μm^2 the EP2[11].

Type I cells have a squamous, flat and elongated shape with two membranes, the basal membrane that is attached to the epithelial basement membrane and the apical cell membrane that forms the surface of the alveolus. In between the two membranes lies a thin layer of cytoplasm with cytoskeletal fibril, microtubules and vesicles for cellular crosstalk[11,13]. The main function of these cells is to mediate the gas exchange, but some studies have advanced fluid homeostasis as one of the roles as well by the presence of aquaporin 5 ion channel and Cftr pores[14]. Other proteins also expressed by type I cells are: T1-α, caveolin-1, carboxypeptidase M and intercellular adhesion molecule 1 (ICAM-1) [13,15]. In this way, giving the thin and high surface area of alveolar type I, associated with the prime function in ensuring gas transfer, makes this cell type essential for the air-blood barrier integrity and subsequently important to be present in the alveolar *in vitro* models.
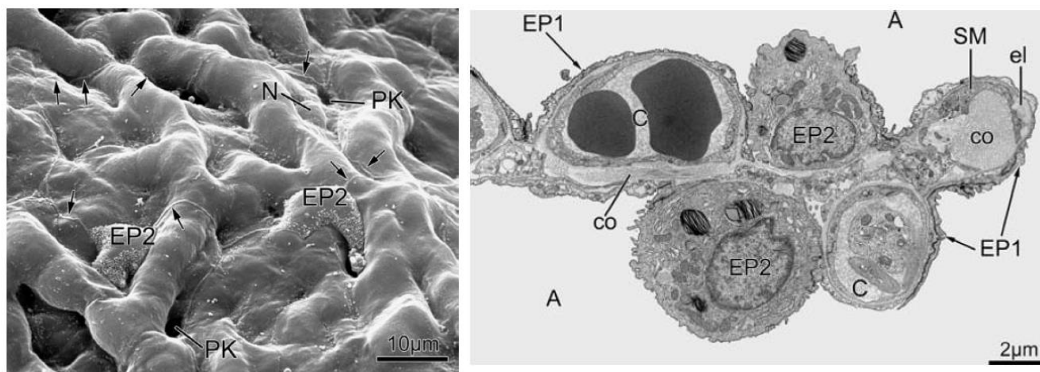
Figure 1.5: Alveolar epithelium scanning electron microscopy image. The left side image represents a scanning electron microscopy image of the alveoli wall. The picture contains two alveolar type II cells (EP2), the white dots represent microvilli. The arrow outlines an alveolar type I cell spreading over several capillaries with the nucleus represented by N. The image also contains two interalveolar pores of Kohn (PK). The right side image shows a scanning electron microscopy image of an alveolus septum. The image shows towards the right, closer to the free edge of the septum a smooth muscle cells (SM) and a cluster of fibres, such as elastic fibres (el) and collagen fibres (co). The picture contains two capillaries (C) where alveolar type I cells (EP1) are also found, with the thin cytoplasm leaflet surrounding the blood vessel and creating the air-blood barrier. The image also shows two alveolar type II cells (EP2), with the cytoplasm rich in organelles. The letter A represents the alveolus lumen. Image adapted from Ochs, M and Weibel R. E, Fishman´s Pulmonary Disease and Disorder book, chapter2[3].

In contrast, EP2 cells are cuboidal and are mostly found in the thicker parts of the alveoli, in the septal walls. These cells are responsible for the homeostasis of pulmonary surfactant: *i.e.* synthesis, storage, secretion and to some extent recycling. In this way, they have a high metabolism, with large a number of mitochondria, extensive endoplasmic reticulum with ribosomes, and a well-developed Golgi complex. These cells contain numerous laminar bodies,

that are directly responsible for the surfactant production and secretion, at *ca.* 200 to 500 per EP2 cell[3,11]. For more detail about the role of surfactants in facilitating breathing by lowering the lung surface tension and in the protection against pathogens refer to section 1.1.3.

In addition to the surfactant synthesis, secretion, and recycling, EP2 cells have other functions such as: fluid homeostasis, host defence, progenitor, epithelial repair and regeneration and Immunoregulatory functions[16,17]. The EP2 cells are considered the "defender of the alveolus" on account of the functions that undertake and the ability to communicate through membrane contact with resident cells or via cytokines and growth factors with mobile cells[16]. An important feature to ensure the alveolar function is the hypophase, which consists of a thin aqueous film found between the surfactant film and the alveolar wall. The hypophase is considered a reservoir for the factors secreted by the cells. The alveolar macrophages use the hypophase for moving[3]. Several interactions have been reported between macrophages and EP2. Some factors, such as hepatocyte growth factor and heparin-binding epidermal growth factor-like protein, when secreted by the macrophages make the EP2 cells enter cell division. Moreover, EP2 cells also secrete chemokines that can attract macrophages (RANTES and MCP-1) and foster their growth (GM-CSF)[16,17]. Regarding the interactions with the resident cells, alveolar type II epithelial cells have direct contact with EP1. The loss of EP1 cells triggers EP2 proliferation. Alveolar type I cells are unable to divide through mitosis, so the EP1 population is renewed due to mitotic division of type II alveolar epithelial cells, a process that lasts for 2-5 days. In addition, mechanical stimulation of EP1 generates a Ca^{2+} gradient that through gap junction reaches the EP2 and stimulates lamellar bodies secretion[16,17]. Another cell type that establishes contact with EP2 is the lung fibroblasts, during lung morphogenesis and lung repair (conditioning media from lung fibroblasts boost EP2 proliferation). The EP2-cell-derived insulin-like growth factor (IGF) type 1 stimulates fibroblasts to secrete collagen type I. However, the release of the surfactant may reduce collagen type I synthesis and provoke fibroblast apoptosis[16]. The secretion of interleukin (IL)-6 and IL-8 by the EP2 cells has been linked to inducing the differentiation of basophil, eosinophil, and neutrophil granulocytes. In addition, stimulation of EP2 with TNF-α leads to P-selectin expression by the endothelial cells, which is known to initiate leukocyte adherence[16,17].

1.1.1.3.2 Interstitial Layer

The interstitial layer physically separates the epithelial and the endothelial layers. It is composed with different cell types and an extracellular matrix (ECM). The interstitial layer is most abundant

in the septal area of the alveoli. The ECM present in this layer is essential for ensuring lung function. During inhale, it allows the alveolar sacs to expand without bursting and during exhale ensures the return to its original size without collapsing. The mechanical properties of the lung parenchyma are determined by the content of collagen, elastin and proteoglycans[18]. The structure of the alveolar sacs is maintained predominantly by collagen I and III. The collagen fibres are helical (300nm length and 1.5nm diameter) and recoiled at low lung volumes (at expiratory reserve volume) and become straight when lungs reach total volume capacity. In addition, collagen IV can be found in the interstitial layer which forms in contrast a sheet like structure, and despite an unknown role in lung mechanics it allows the epithelial cells to attach. Another important protein of the extracellular matrix is elastin. It is a small protein, with 72kDa protein, but has great resilience over a large range of strain, it responds linearly to stress up to 200% of strain. Elastin proteins organize themselves into cross-linked fibres that connect to the collagen fibres through proteoglycans. The most abundant proteoglycans in the alveolar ECM are heparin sulfate and chondroitin sulfate. Despite the contribution to the ECM network of fibres, proteoglycans are also able to influence intracellular signallings, such as promoting proteolytic protein secretion, cell migration and tissue remodelling[18,19].

With the same level of importance as the basement membrane composition is the cell composition and distribution. Alveolar interstitial cells represent about 36% of the total cell number in the human lungs, in the order of 210 cells per alvoli[12], and are composed of fibroblast and contractile cells, such as myofibroblasts, lipofibroblasts, smooth muscle cells and pericytes[3]. Alveolar fibroblasts have a spindle shape and are responsible for secreting extracellular matrix proteins that support alveolar structure[13]. The smooth muscle cells, often located at the end of the septum, contain high levels of α-actin, a cytoskeleton protein and marker of contractibility. This marker is also found in the other interstitial cells resident in the septal wall.

Despite the important contractile phenotype for maintaining the elasticity of the alveoli, interstitial cells also actively contribute to the remodelling and repair of the connective tissue. Fibroblasts are mechanosensitive cells programmed to support matrix synthesis and remodel, also help regulate inflammation, recruitment of immune cells and wound repair, contributing in this way to lung homeostasis. The Wnt/β-catenin signal induces fibroblast activation and collagen synthesis. During injury, fibroblasts differentiate into myofibroblasts, a cell type between fibroblast and smooth muscle cells characterized by expressing α-SMA–positive stress fibres (pericytes and bone MSC also contribute to enrich the myofibroblast population). Under mechanical stimulation, a TGF-β dependent pathway stimulates fibroblasts to differentiate into

myofibroblasts. Fluid flow further induces fibroblast-to-myofibroblast differentiation along with proliferation and collagen fibre alignment[3].

In addition, contributing to the second level of defence of the alveoli, are immune cells, namely interstitial macrophages, which are around 10% of the total alveolar cell population[3], around 57 cells per alveoli[12]. As well as histiocytes, which are cells that have phagocytic capacity. The interstitial macrophages are able to attach to the surface of the alveolar epithelium by pseudopodia and are able to amoeboid movement[3].   About the function of alveolar macrophages, an additional interesting element also found in the alveolar is the porous of Kohn, featured in figure 1.5. They connect two adjacent alveoli, are used for resident alveolar macrophages to move between alveoli[20] and assist during ventilation, allowing air to pass through[21].

1.1.1.3.3 Endothelium Layer

The endothelial layer contains the capillary network that supplies blood around each alveolus. The capillaries are of continuous and non-fenestrated type. They cover an area of around 126 m^2 as mentioned before, so just around 10% smaller than the alveolar area. It is estimated that endothelial cells contribute to around 30% of the total alveolar cell population[3], around 170 cells per alveoli[12]. In addiction, is also predicted that one alveolar epithelial type I cell spreads across 40 capillaries[11].

The pulmonary endothelium cells are subjected to two types of forces: shear and tension. Shear stress originates from the blood flow and tension is created by the cyclic movement of the human breathing pattern. The average diameter of the capillary network is between 2 and 5 μm, supporting a blood flow between 4.5 mL/min and 8.5 mL/min and a shear stress of 0.5 a 1 Pa[22]. To support the breathing movement the capillaries can double the size when stretching until total lung capacity. This is possible since the capillaries are interlaced in the meshwork of interstitial fibres, giving the mechanical support needed to withstand the stretching and relaxation of the alveolar sac[3].

The capillaries are formed with endothelial cells, which are four times more numerous than alveolar type I epithelial cells, though four times smaller. The thickness of the alveoli is variable, the thinner parts where both endothelial cells and EP1 membranes are fused to facilitate gas transfer have a thickness of 0.3 μm. Figure 1.6 illustrates this close cell-to-cell interaction. However, in the septum area, where the interstitial layer is more expressed such thickness can reach 2.5 μm. The occluding junctions between the endothelial cells allow water, solutes and

small molecules to be exchanged between the capillary's lumen and the interstitial space. The junctions are normally found in the transition between the thin and thick air-blood barrier and are coated with pericytes (contractile perivascular cells)[3].
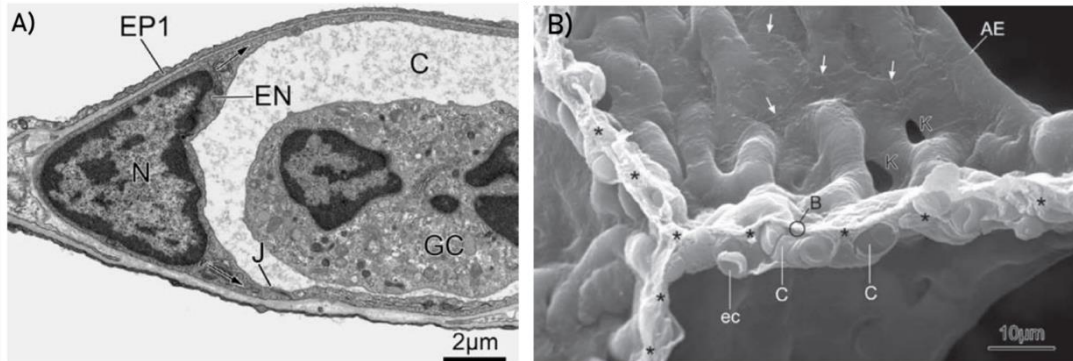
Figure 1.6: Scanning electron microscopy of Endothelium Layer. A) SEM image showing the close contact between the alveolar type I (EP1) and the endothelial cells (EC). The cytoplasm of the EP1 is extended to enwrap the endothelial cell. The letter J in the picture highlights the intercellular tight junctions and the GC a white blood cell. B) Human lung alveolar wall showing the blood capillaries (C), an erythrocyte (ec), the interalveolar pores of Kohn (K), tissue barrier (B), the asterisks mark the septum wall and the arrows the cellular junctions. Image adapted from Ochs, M and Weibel R. E, Fishman´s Pulmonary Disease and Disorder book, chapter2[3].

In summary, the alveoli are not independent structures, they are mechanically connected to the capillaries, upper airways, diaphragm, and pleura. In turn, the pleura links to the thoracic cavity. The movement imposed by breathing needs to be performed by all the previous structures in unison. In this way, there is a continuous network of fibres linking all structures to ensure efficient transduction of the movement. By examining figure 1.7, in the alveoli are found axial, septal and peripheral fibers. The axial fibres have origin in the upper airways, coating the walls as rings, when reaching the alveolus, they connect the individual alveoli by the septal wall. The peripheral fibres extend from the visceral pleurae into the septal wall. The septal fibres are the ones forming the interstitial layer basement membrane and are used by the axial and peripheral fibres as anchoring points. This network of fibres gives the structural support needed to maintain a 130 m^2 surface area with only 2.2 µm in thickness to participate in the gas-exchange process.

In addition, this structure also supports the different ventilation demands, when at rest or during exercise, where air flow velocity can increase up to ten times.[2] In the following section, 1.1.2, a brief description of the breathing patterns is given.
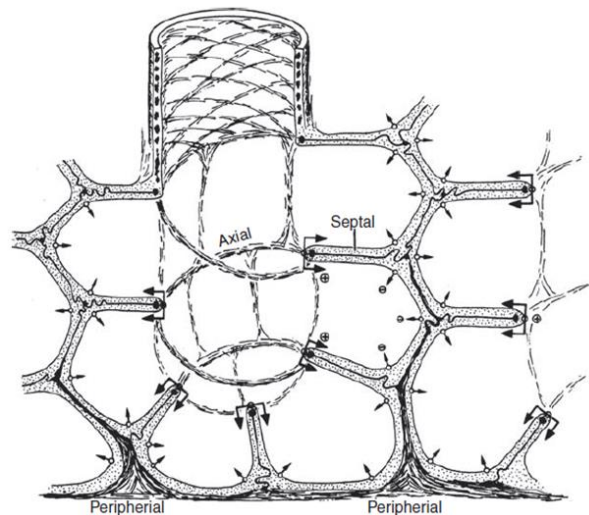
Figure 1.7: Schematic of alveolar ducts fibre organization. Illustration of the organization of the axial, septal and peripheral fibres in the alveolar ducts. The arrows indicate the direction of the tension created by the fibres. Image adapted from Ochs, M and Weibel R. E, Fishman´s Pulmonary Disease and Disorder book, chapter2[3].

1.1.2 Breathing Mechanism

The mechanism through which air enters and leaves the lung is driven by the pressure gradient established between the alveoli and the atmospheric pressure, around 1 mbar[2]. Furthermore, both the lungs and the chest exhibit elastic properties so that they may behave like a spring. When displaced from the original position, either due to stretching or compression, an opposing force is created propelling it to return to its original position. The fibre composition and contractile cells are supporters of the breathing movement, allowing the tissues to deform. Yet, this deformation is restricted since both the fibres and cells have a limit to their elasticity. Without such limits, the lung would collapse. In addition, an essential component of a functioning system is related to the fluid filling the pleura, as due to the high surface tension that is created in this section, the fluid prevents the parietal pleura and the visceral pleura from being pulling apart[23]. The intrinsic elasticity of the lung supports inhalation and exhalation movements. Lung compliance is used to assess the ability of the lung to expand. It is determined by the ratio between the change in volume over the change in pressure. The higher the compliance, the higher the volume change for the same applied value of pressure. Lung compliance during inhalation is different from during exhaling. It is also not linear. The lung compliance is higher at low lung volumes and decreases as the lung volume increases. In other words, as the lung starts to reach the total lung capacity it is more difficult to air to flow in (Figure 1.8)[3].
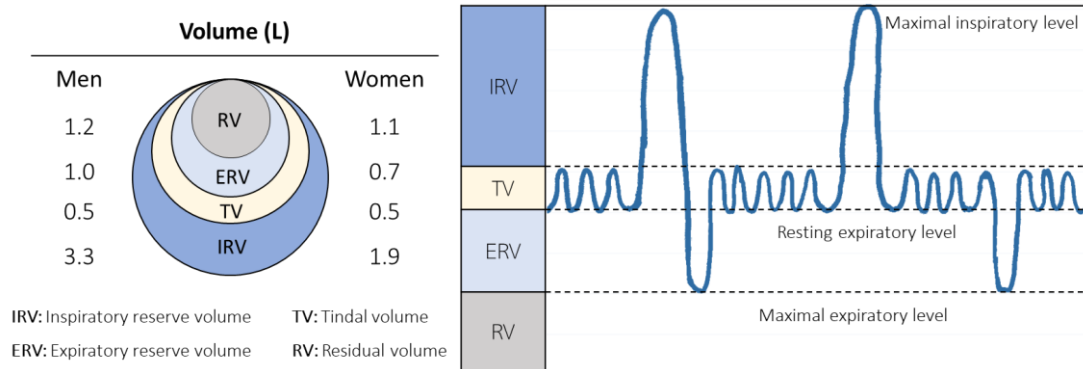
Figure 1.8: Schematics of lung volumes of men and women. RV corresponds to residual volume, ERV to expiratory reserve volume, TV to tidal volume and IRV to inspiratory reserve volume. Left Adapted from William F. Ganong. Review of Medical Physiology. Lange[4]. Right side image adapted from Ochs, M and Weibel R. E, Fishman´s Pulmonary Disease and Disorder book, chapter 33[3].

1.1.3 Surfactant Role and Composition

Pulmonary surfactant plays a major role in facilitating the expansion of the lung during breathing. The force exerted by the air in the walls of the lungs requires to have such magnitude to overcome the lung resistance and surface forces. The pulmonary surfactant lowers the surface tension increasing lung compliance. The surface tension is measured by the work required to be applied to increase the surface area by a specific amount. The lung surfactant lowers the work, facilitating the increase of the alveoli area during inspiration[23]. Measurements in the lung of rabbits determined the alveolar surface tension of around 30mN/m at total lung capacity (TLC) and 1 mN/m at 40% of TLC[24]. The early work of Clements also indicates a surface tension of lower than 1 mN/m at low lung volumes and 20–25 mN/m at TLC[25].

The Young-Laplace law, shown in equation 1.1 below, explains the relationship between the pressure required to prevent the collapse of a sphere (approximately the shape of the alveoli) – ΔP, with the surface tension -γ, and the radius[23].

$$\Delta P = \frac{2\gamma}{radius} \quad (Eq.\,1.1)$$

If was not for the lung surfactant, given the Laplace law, for the same value of surface tension, smaller alveoli (*i.e.* smaller radius) would have a greater tendency to collapse due to an increase of ΔP to keep the alveolus open. In addition, due to the interconnectivity of the alveoli ducts and the presence of the porous of Kohn the air would leave the smaller alveolus in favour of alveolus with larger diameters. Although, when considering the presence of surfactant, the value of

surface tension is variable from alveolus to alveolus. Smaller structures, to compensate have a thicker layer of surfactant that reduces even further the surface tension γ [23].

Pulmonary surfactant is a heterogeneous mixture of lipids and proteins that coats the inner side of the alveolar region, preventing direct contact between air and the alveolar surface[3]. A more thorough examination of the surfactant composition reveals that 90% are lipids and the remaining 10% are proteins. Within the lipids, roughly 40% is constituted by dipalmitoyl phosphatidylcholine (DPPC), which is tightly packed due to the presence of saturated acyl chains. Therefore, water is almost excluded from the interface lowering the surface tension and keeping the alveolar lumen dry. Other lipids incorporated in the surfactant barrier are unsaturated lipids such as, phosphatidylcholines (25%), anionic phosphatidylglycerol (8–10%), phosphatidylethanolamine (5%), phosphatidylinositol (3%), phosphatidylserine and sphingomyelin. Neutral lipids also compose the surfactant, cholesterol is the most abundant (8–10%)[3]. Regarding the protein composition of the surfactant, includes both hydrophobic and hydrophilic proteins. In the first group, are found the proteins SP-B and SP-C, involved in the formation and maintenance of the surfactant layer. Belonging to the second group, are the collectins SP-A and SP-D[3] (collectins are proteins that have collagen-like N-terminal regions, and C-terminal regions with calcium ion and carbohydrate-binding domains). These proteins can attach to the surface of different pathogens facilitating their clearance by the alveolar macrophages[16]. For further detail on surfactant lipid and protein constitution and function please refer to table 1.1.

The renewal of the air and the cyclic stretching of the alveolus stimulates surfactant secretions. EP1 may have a role in stimulating surfactant release by acting as a mechanotransducer. The mechanical stimulus of breathing is translated through an intracellular Ca^{2+} signalling pathway, which is transmitted *via* gap junctions to the EP2 cells. Other molecules also stimulate surfactant production, such as arachidonic acid, prostaglandins, histamine, and endothelin-1. The surfactant is secreted by the EP2 cells through exocytosis in lamellar bodies, with the participation of cytoskeletal proteins, such as microtubules and actin filaments. The fusion of the lamellar bodies with the plasma membrane is mediated by annexins and leads to the secretion of the lamellar bodies in the hypophase. Within the aqueous film of the hypophase, the surfactant is transformed into tubular myelin, with the help of phospholipids and SP-A, in high amounts of Ca^{2+}. Next, the surfactant is enriched in DPPC through the involvement of the surfactant proteins SP-B and SP-C. To finalize the process, the surfactant is transformed into an inactive vesicular form by the enzyme convertase[3]. About 85% of the surfactant is recycled, by proteins SP-A, SP-B and SP-C. The rest of the surfactant is degraded, which is ensured by alveolar

macrophages[16]. In short, the surfactant lowers the surface tension to facilitate the breathing movements, keeps the alveolar region dry, avoids the influx of fluid and participates actively in the innate immune system.

Table 1.1: Table summarizing the role of the several components of the lung surfactant[3].

Lipids	DPPC	▪ Surface tension–lowering[26]
	Phosphatidylcholines	▪ Suppress viral infection and inflammatory responses[27]
	Anionic phosphatidylglycerol	▪ Immunosuppressive role[26]
Proteins	SP-A	▪ Secreted by AEC2 and clara cells ▪ Host defence: binds to bacteria, fungi, and viruses to signal macrophage clearance. ▪ Regulates surfactant structure ▪ Mediates lipid aggregation and tubular myelin formation ▪ Involved in surfactant recycling ▪ Immunomodulator – inhibit dendritic cell maturation, allergen-induced-lymphocyte proliferation and eosinophil release of IL-8[26]
	SP-B and SP-C	▪ SP-C is exclusively secreted by AEC2. SP-B is secreted by AEC2 and clara cells ▪ Found anchor to DPPC ▪ Surface tension–lowering[26] ▪ Facilitate the delivery of phospholipids vesicles in DPPC ▪ Stabilize surfactant during the respiratory cycle ▪ Speed the formation and stability of surfactant ▪ Participate in surfactant recycling
	SP-D	▪ Secreted by AEC2 and clara cells ▪ Host defence ▪ Low affinity to the surfactant ▪ Participates in surfactant structure and homeostasis ▪ Influences surfactant particle size and its uptake by AEC2 ▪ Immunomodulator – inhibit allergen induced-lymphocyte proliferation[26]

The previous sections gave an overview of the lung's anatomy from the trachea until the alveolar sacs, specifying cells and extracellular matrix composition. But also gave detail on the breathing mechanism and the surfactant role in ventilation in keeping air-blood barrier integrity. After this overall picture of lung structure and function, the next sections focus on showing how the alveolar region is being mimicked *in vitro*

1.1.4 Overview of in vitro models

An *in vitro* model is a cell culture model that aims to represent an organ or part of it, recapitulating its function, cell organization or structure. The *in vitro* models are an alternative to animal testing, which have been extensively used to understand lung development, disease state and are considered a gold standard for toxicology risk assessment of new products[28,29,30].

But differences between murine and human lung exists, which prevents translating experiment results between species. These differences can be found at the level of anatomy, cell composition and physiology. At the cellular level, in the mouse, the junction between distal airways and alveolus airways live a population of bronchioalveolar stem cells (expressing bronchiolar club cell marker, Scgb1a, and alveolar type 2 cell marker, SP-C[31]). This cell population is important in the response to injury, however, is still under discussion the presence of this stem cell population in the human lung[14,28]. In addition, in human proximal airways, mucus producing goblet cells are abundant and secretory clara cells are limited, but in the mouse the number of club and goblet cells is inverse[14,32]. However, has been reported as well, that laboratory mice contain less number of goblet cells in the airways, which may be a result of living in a pathogen free environment[14]. In terms of the immune defence, the human alveolar macrophage population is more numerous, compared to rodents, translating into a higher capacity to clear particles[33]. Regarding the anatomical differences, the mouse has fewer branching generations, but more are dedicated to gas transfer compared to humans[34,35]. Also, the branching pattern differs between both species, in humans is regular until generation 6 and irregular onwards, in the mouse is always irregular. This makes the human branching pattern more susceptible to deposition at its bifurcation points[35]. The exposing methods used in the mouse have also its limitations. When using non-invasive methods, the mouse is conscient, in a confined space and under spontaneous breathing, which produces a nearly natural breathing pattern. However, the mouse is under stress which could interfere with the response obtained[30]. On the other hand, if the mouse is anaesthetized the dosage is controlled but the breathing frequency is decreased and is more difficult to maintain the mouse stable[30].

However, besides the advantages of animal models in providing whole-body response and had provided unquestionable advances in medicine, not just at the therapeutic level but also in understanding health and disease progression, it is questionable their utility in predicting the human response. The differences presented above limit the translation of animal data to human response. In addition, despite tight regulations to ensure animal wellbeing there are unquestionable ethical concerns about using animals as *in vivo* testing platforms. Furthermore, the US Food and Drug Administration (FDA) estimates the use of animal models as one of the

reasons for clinical trials failing. It is predicted by the FDA that only 10.4% of all drugs that enter a phase I clinical trial will reach the market[36]. In addition to the decline in drug approval, there has been an increase in the costs for drug development, rising to 2.6 billion per drug on average[37]. With this budget, the pharmaceutical industry's interest in *in vitro* models has increased[38]. The *in vitro* model field has also been stimulated by the introduction of tighter regulations in the cosmetic industry. In 2013, the European Commission prohibited animal testing of finished cosmetic products or their individual ingredients in the European Union (EU) as well as a marketing ban. This included prohibiting commercially available cosmetic products and ingredients in the EU which had been certified with animal testing[39]

In this way, the development of the *in vitro* model field is fostering the creation of holistic environments to better reproduce cell niches, which is essential to uncover unknown mechanisms of health or disease state of an organ or groups of organs. But also, to describe in better detail the impact of medicines or performing the risks assessment of new products. Models suitable to be integrated into exposure systems and at the same time prevent or mitigate animal use, will play a major role in the future of tissue engineering.

In the literature, nowadays there are several strategies to create an *in vitro* model. In this work, current *in vitro* strategies are separated into the next types: 2D monolayers, inserts, organ-on-a-chip, (bio)scaffold, 3D bioprinting and bioreactors. Table 1.2 focuses on demonstrating the potential and limitations of each strategy.

The analysis of table 1.2 shows the advantages of each technique isolated, but often advanced *in vitro* models combine several strategies that increase the level of complexity and capacity to design tissue/organ of interest. This holistic approach is well represented in the work of Taniguchi et al. (2018), where chondrocytes, endothelial cells, and mesenchymal stem cells isolated from a rat, were further combined to form spheroids that were used to print in a trachea analogue. The construct was matured in a bioreactor before final implantation in rat[40]. This example combined in one single model, spheroids, 3D bioprinting and a bioreactor, taking advantage of the different techniques to make a more physiological and anatomical relevant model. On section 1.1.4.1 and 1.1.4.2 examples of lung and vasculature *in vitro* models are given.

1.1.4.1 Overview of Lung in vitro models

An overview of the lung *in vitro* model field is present in table 1.3. The table shows the state of the art in the lung *in vitro* models, with special attention to the application, cells, matrix used

and the presence of air liquid interface, flow or dynamic air. However, the main objective of the table was to include as many applications as present in the literature for the same model type.

Starting the table 1.3 analysis on the inserts (also mentioned in the text as Transwells), this type of model is easily incorporated into the current laboratory practices, which makes them widely used. They allow cultures to be in contact with air, which early work has demonstrated to be important for lung cells to acquire the right morphology and fuction[41,42]. This type of model is able to reproduce the stratified organization of the lung from the trachea until the bronchus and simulate the physical barrier between the epithelial and endothelial epithelium in the alveolar sacs. Nowadays there are human airway models commercially available in inserts supplied by Epithelix and MatTek. The inserts also act as an excellent support material for (bio)scaffolds and when integrated into organ-on-a-chip and bioreactors can become dynamic. An example is the commercial availed bioreactor that takes an insert inside (patent number WO 2010/013068 A2, invented by Arti Ahluwalia, Daniele Mazzei and Bruna Vinci from the University of Pisa, Italy in 2009). The organoids are able to recapitulate lung embryonic development and contain a diverse cell population with near physiology and function, which makes them an essential tool to deliver cellular units for being integrated into any model type. The organ-on-a-chip major advantage is the ability to recreate in a small apparatus inter-organ crosstalk, with the association of several microdevices, each representing a tissue[43,44]. This is essential to evaluate all body responses. For lung on a chip models, the work of Wyss Institute was a game changer, the device allows media and air perfusion, a physical barrier between epithelial and endothelial cells, together with substrate stretching where cells are attached[45]. Regarding the 3D bioprinted model, despite being at its initial stage, has shown through the work of Jordan S. Miller group[46] the potential of the technique in recreating in the laboratory near-anatomy with vasculature integration constructs. But also, to recreate the stratified layer of the alveolar, bioprinted constructs show thinners layers and more evenly distributed cells. This shows the bioprinting technique's advantage in layering cells in a more accurate way than manually seeding[47]. Finally, the bioreactors are excellent providers of a barrier from the external world during de/recellularization protocols and in this way, give a second use to unsuited organs for transplantation. In conclusion, the organoids, scaffold and 3D bioprinting constructs can be used as biological building blocks of a model, further integrated into inserts, bioreactors or organ-on-a-chips for media or air perfusion.

Table 1.2: Review of the advantages and limitations of the current *in vitro* model strategies. ALI: air liquid interface, PET: Polyethylene terephthalate, Matrigel: commercially available hydrogel rich in protein and growth factors mixture secreted by Engelbreth-Holm-Swarm mouse sarcoma cells, which is liquid at low temperature and solidifies at 37ºC, PDMS: polydimethylsiloxane- biocompatible and transparent silicone-base material.

Model Type	Overview	Advantages	Limitations
2D monolayers	Cells seeded in Petri dishes or well plates under submerged conditions	- Simple to set up - Supports co-cultures - Allow surface coating for ECM-like mimic	- Static air/media - Absence of mechanical stimulation -Submerge experimentation -Lack of 3D environment
Inserts	Cells are seeded in a porous PET membrane in the upper or lower side, submerged or under ALI[48]	- Simple to set up - Supports co-cultures - Allow surface coating for ECM-like mimic - ALI -3D	- Static air/media - Absence of mechanical stimulation -Not study the effect of membrane material and porous dimension in culture outcome
Organoid	An organoid is defined as an *in vitro* 3D structure composed of an aggregate of multiple cell types. Stem/primary cells spontaneously assemble (under a highly supplemented media[49,50]) to recapitulate organogenesis[51]	-Near spatial organ organization - Recapitulate specific organ function to some extent - Generate a diverse cell population - Long term viability -Tolerant of freeze-thaw	- Static air/media - Inter- organoid high variability and immaturity[52] - Matrigel is the gold standard [52] [53]. - Absence of vascularization, immune and mesenchymal cells during organogenesis. These cell types need to be added[54] - Absence of mechanical stimulation[53]
(Bio)scaffolds	Cells are embedded in a porous soft-solid material. The materials can be synthetic, natural, a combination of both to ensure biological activity or obtained from decellularized tissues/organ/cell sheet[55]	- Cells can attach, proliferate, migrate, contact with active ingredients, or other cell types in a real 3D environment - Supports co-cultures	-Oxygen and nutrient diffusion limitations[56] -Absence of vascularization - Static air/media - Absence of mechanical stimulation -Scaffold heterogeneity - Standard post-processing techniques are more challenging [56]

Organ-on-a-chip	Micro-scale device in elastomeric material (PDMS). Soft lithography and replica moulding techniques are used to create layers of compartmentalized chambers and interfaces[57]	- Dynamic air/media - Supports mechanical stimulation - ALI - Supports co-cultures - Allow surface coating for ECM-like mimic	-Require special expertise and equipment[58] - The micro devices designs are very restricted to a porous membrane to recapitulate the air-blood barrier[59] - Cell seeding and surface coating can be challenging - Standard post-processing techniques are more challenging
3D bioprinting	Through additive manufacturing technology living and non-living materials are deposited layer-by-layer, to assemble in a pre-designed pattern[60].	- 3D environment - Supports co-cultures - Spatial control where cells and material are positioned	- Static air/media -Require special expertise and equipment - Materials need to be printable - Printing process can impair cell viability[61,62] - Standard post-processing techniques are more challenging -Oxygen and nutrient diffusion limitations
Bioreactor	Cylindrical vessels that support chemical/biological processes, are close and controlled systems. Operate in continuous, batch or fed batch. Allow compressive studies, agitation due to impellers or perfusion through pack bed or hollow-fibre and support decellularization and recellularization of lungs.[63]	- Dynamic air/media - Supports mechanical stimulation - ALI -3D environment - Supports co-cultures	-Require special expertise and equipment - Standard post-processing techniques are more challenging

Table 1.3: Review of the state-of-the-art lung *in vitro* model strategies.ES: external stimulation, ALI: air-liquid-interface, M: presence of dynamic media, A: presence of dynamic air, D: deformation of the cell substrate, A549: alveolar type II cell line, HMC-1: mast cell line, EA.hy 926: endothelial cell line, PMA: phorbol-12-myristate-13-acetate,THP-1: monocyte cell line, hESC human embryonic stem cell, AT2: alveolar type II, AL1: alveolar type I, PNECs: pulmonary neuroendocrine cells, PDGFRα+: primary lung stromal cells, hiPSCs: human induced pluripotent stem cells, HUVEC: human umbilical vein endothelial cells, NCI H441: alveolar type II cell line, HPMEC: human pulmonary microvascular endothelial cells, CCL-210: fibroblast cell line, pHPAEC: primary human pulmonary alveolar epithelial cells, IMR-90: fibroblast cell line, Matrigel: protein and growth factors mixture secreted by Engelbreth-Holm-Swarm mouse sarcoma cells, PLC: polycaprolactone, PEG: polyethylene glycol, NCO: isocyanate end groups, YIGSR: laminin derived peptide, RGD: aminoacid sequence Arg-Gly-Asp, PDMS: poly(dimethylsiloxane, PEGDA: PEG diacrylate, GelMA: Gelatin methacryloyl, IPF: Idiopathic pulmonary fibrosis, MMP: matrix metallopeptidase.

Model	Application	Cells	Matrix/Design	Outcome	ES	Ref
Inserts	toxicology	A549, HMC-1, EA.hy 926 PMA differentiated THP-1	Microporous membrane	ALI tetraculture showed less oxidative stress than submerged and monocultures. Exposure using a Vitrocell.	ALI	64
		EpiAirway commercially available *in vitro* organotypic model of human mucociliary airway epithelium (MatTek Corporation	Microporous membrane	Prevalidation of the model with 59 chemicals with submerged exposure.	ALI	65
Organoid	healthy model/ organ maturation	Precursor cells: hESC Present cells: AT2, AT1, after mice transplantation: mesenchymal, PNECs, vasculature, nerve fibres	Matrigel	lung organ-like structures *in vivo* with the vascular and neuronal network.	-	66
		Precursor cells: PDGFRAα+ stromal cells Present cells: AT1, AT2	Matrigel	Investigating the AT2 role in alveolar maintenance and repair.	ALI	67
	toxicology	Precursor cells: hESC, hiPSC, primary AT2 and FB / Present cells: AT2, AT1-like cells	Matrigel/submerged exposure with GNE7915 (5 µM) or amiodarone (10 µM)	Human AT2 model	-	68

(Bio)scaffolds	healthy model	HUVEC, NCI H441 and HPMEC	Electrospinning nano fibre mesh formation with PLC and NCO-sPEG. Functionalized with RGDs and YIGSR.	Suitable model for evaluating pathological conditions, drug efficacy, pollutants, and nanotoxicology.	-	69
		hMSC, mMSC, A549s, HpuVECs and HUVECs	Hydrogel from decellularized porcine lung + genipin crosslinker	Scaffold proof of concept with different cell types	-	70
	disease model	CCL-210, A549 and Primary AT2	Photodegradable PEG spheres containing the cells encapsulated in PEG	Higher MMP activity when fibroblasts are present	-	71
		A549	Dextran-chitosan hydrogel	low hydrophobicity and protein absorption, promote A549s to cluster	-	72
Organ-on-a-chip	healthy model	pHPAEC HUVEC	2 PDMS plates separated by a porous (8μm) and flexible PDMS membrane coated with fibronectin. Vacuum applied on lower plate deforms the membrane	cyclic stretch affects the permeability, metabolism, and cytokine secretion of epithelial cells	M/ D	73
	disease model	A549	PDMS channel bounded to glass with 3 inlets and outlets. The cells are cultured in the middle channel. Lateral channels used to gastric contents exposure	novel device to study gastric reflux effect as a trigger for IPF	M	74
	particle distribution	acellular	5 generations of branching until alveolar sacs with periodical expansion and contraction of the PDMS walls	physiological breathing motions on acinar airways to study inhaled aerosol transport	A/D	75,76,7 7
3D bioprinting	healthy model	A549 EA.hy926	4 layers bioprinted on a transwell: matrigel, EA.hy926 with media, matrigel and A549 with media	Printed co-cultured show more thin and uniform distributed cells compared to manually assembled co-culture	-	47
		IMR-90 A549	Near alveolar sac design with 600μm alveolus and 400μm channels in diameter in PEGDA and GelMA	Acellular models sustained oxygenation and flow of human red blood cells during tidal ventilation and distension.	A/ M/ D	46

				Coculture was kept submerged for one day.		
	disease model	A549	alginate, gelatin and matrigel mesh dispensed into a geometry lattice	The model supported influenza A virus infection patterns only observed before *in vivo*	-	65
Bioreactor	healthy model	iPSC-AT2 primary AT2	Collagen IV coated Millipore's Biopore Membrane on rotary reactor (0-100rpm) exposes half of the membrane to the media while the other half is at ALI	iPSC-AT2 and primary AT2 cultured in the reactor had higher levels of type I markers compared with the flask-grown treated with small molecules to induce differentiation.	M/ ALI	78
	Drug test	Primary pulmonary fibroblasts, A549 and HMEC-1	Silk collagen I on a customized Flexcell commercial system allowing media perfusion and ALI	The model supports myofibroblast differentiation and antifibrotic drug test	M/ ALI	79
	healthy model	normal/immortalized isolated AT2, EC, trachea-bronchus cells	decellularized human adult/paedriatic lung	Reactor implantation for de/recellularization shows vascular, alveolar–capillary junction formation, surfactant protein-C /D and collagen I	-	80

1.1.4.2 Overview of vasculature in vitro models

The success of the alveolar region as a gas exchange area is due to the network of capillaries that covers the respiratory airways. The endothelial cells are sparsely covered by mural cells (pericytes and SMS). In addition to the cellular components, capillaries are composed of collagen IV, laminin[81] and elastin[82]. Blood vessel formation is achieved by two processes: angiogenesis or vasculogenesis. The former, blood vessel development is regulated through the proliferation, migration, and remodelling of endothelial cells (ECs) from adjacent pre-existing blood vessels. In contrast, during vasculogenesis endothelial progenitor cells (EPCs) migrate to the area of interest and form *de novo* blood vessels. More details about these processes are given in the next two sections.

1.1.4.2.1 Vasculogenesis

The first evidence of vasculogenesis is found during embryo development when the cardiovascular system is being developed, by the structures termed blood islands. These structures are the equivalent of the bone marrow[83]. They are populated by hematopoietic stem cells (HSC) in the centre and endothelial precursor cells (or angioblasts) located at the periphery[81]. The capillaries are formed by the growth and fusion of several blood islands. Both HSC and endothelial precursor cells (EPCs) cells share several markers, such as vascular endothelial growth factor receptor-2 (VEGFR-2), angiopoietin-1 (Ang-1) receptor Tie-2, stem cell antigen-1 (Sca-1), and CD34, validating a common cell precursor, the hemangioblast[81]. VEGF secreted by the endoderm acts in a paracrine manner to support the differentiation of VEGFR-2-expressing mesodermal cells to angioblasts[81].

Vasculogenesis was thought to happen only during embryonic development, however, nowadays the concept of postnatal vasculogenesis is well accepted. EPCs persist after birth and can be found throughout adult life in bone marrow or circulation. EPC-mediated postnatal vasculogenesis also contributes to endogenous neovascularization of developing tumours, wound healing, and myocardial ischemia, as well as physiological neovascularization[81,83]. The mechanism is still not fully understood, but in the firsts instances, the EPCs migrate from the bone marrow into the peripheral blood. They migrate to the site of tissue ischemia or vascular injury. It is thought that a VEGF gradient may play a role in attracting the cells to the desired place. When migration is complete, EPCs adhere and transmigrate into the injured or hypoxic tissue to form a new endothelial monolayer and new blood vessels[84].

1.1.4.2.2 Angiogenesis

The early work of Ausprunk and Folkman[81] on tumour angiogenesis described for the first time the stages of sprouting angiogenesis. The process starts with the degradation of the basement membrane. Then endothelial cells (ECs) are allowed to migrate into the connective tissue to create a solid cord of ECs, marking the formation of the lumen. The progression of the ECs assembly in a cord disposition as well as the continuous synthesis of new basement membrane and the recruitment of mural cells (pericytes and SMC) give rise to new blood vessels[81].

The basement membrane degradation is mediated by matrix metalloproteinases (MMPs), as membrane type (MT)-MMP1 and plasminogen activators such as, urokinase plasminogen activator (uPA), heparanases, chymases, tryptases, and cathepsins. The breakdown of the membrane free's mural cells, endothelial cells as well as matrix-bound angiogenic growth factors like FGF (fibroblast growth factor), VEGF, transforming growth factor-β (TGF-β) and IL-1β, stimulates angiogenesis. The degradation of the membrane relies on a controlled balance, excessive destruction of the basement membrane removes the support to form novel blood vessels and inhibits angiogenesis. The tissue inhibitor metalloproteinases (TIMPs) and plasminogen activator inhibitor-1 (PAI-1) play a role in controlling the activity of the proteases. Then, the termination of angiogenesis is mediated by thrombospondin-1 (TSP-1), canstatin, tumstatin, endostatin, and platelet factor-4 (PF-4), and by inactivating of angiogenic cytokines such as stromal cell-derived factor 1[81].

During blood vessel formation tip and stalk cells, orchestrate the new vessel formation and branching. These cells originate from ECs differentiation. Tip cells lead angiogenesis through filopodia, the cytoplasmic projections extend beyond the cell edge guiding the new vessel formation. Mainly, tip cells do not divide only migrate to place themselves in the front of the nascent vessel. On the other hand, stalk cells with their proliferative profile follow the tip cells supporting the nascent vascular lumen formation. The regulation of tip and stalk cells depends on the balance between proangiogenic factors, such as VEGF and jagged1 (JAG1) and antiangiogenic factors, such as delta-like ligand 4 (DLL4) from Notch signalling. The VEGFA gradient guide the tip cells, whereas the VEGFA concentration determines the proliferation of stalk cells[81].

Upon stablishing of the lumen by the tip cells, they migrate via adhesion to the extracellular matrix, to drive forward the vessel formation. The stalk cells lay just behind, proliferating and elongating to give continuity to lumen formation and consequently vessel formation. Afterwards, maturation and stabilization of the vessels, require mural cells recruitment and

deposition of basement membrane. Then, after fusion of neighbouring branches, endothelial tip cells adopt a phalanx phenotype, marking the transition from active sprouting to quiescence. During this last state, cell–cell junctions are re-established, as well as deposition of basement membrane, maturation with pericytes and production of vascular maintenance signals[81,85].

Studies regarding lung embryonic development have identified Vegf-A gene as key factor in the alveolar capillary formation. Upon inactivation of the gene during alveologenesis, it was observed a decreased in pulmonary capillary and alveolar development and altered lung elastin and retinoic acid expression. The retinoic acid is produced by pulmonary endothelial cells and regulates pulmonary angiogenesis and elastin synthesis by induction of VEGF-A and fibroblast growth factor (FGF)-18, respectively. In an attempt to restore normal alveolar vasculature, the cells were treated with retinoid acid and vitamin A, which partially reversed the impaired vascular and alveolar development induced by VEGF inhibition[86].

1.1.4.2.3 Vasculature in vitro models

After showing above the two processes by which vasculature is formed *in vivo*, the next section presents several strategies for how this phenomenon is being recreated *in vitro*. The inability to conjugate vasculature network within the laboratory tissue analogues restricts their thickness. With no vasculature or network of channels, the nutrient and oxygen reach the cells only through diffusion. In high metabolic tissues, cells are no more than 100 µm from a high oxygen source[56]. Alveolar *in vitro* models should attempt to conjugate the vasculature network not only for a continuous source of nutrients and oxygen but also to model the epithelial-endothelial interaction, that is the functional aspect of the lung. From the toxicological point of view, this barrier modeling is also very important, since could show if the chemical or particle being tested enters the systemic circulation or if it is cleared in the alveoli. Table 1.4 shows examples of how vasculature is being modeled in vitro using the different model types.

Table 1.4: Review of current available strategies to form vasculature *in vitro*. ES: external stimulation, M: media perfusion, hMSC: human mesenchymal stem cells, HUVECs: human umbilical vein endothelial cells, EC: endothelial cells, fibrin: blood clot mimicking when adding fibrinogen and thrombin, PCL: Polycaprolactone, PLGA: poly(lactic-co-glycolic acid.

Model Type	Overview	Cells	Matrix/Design	ES	Ref.
Inserts	Test of topographical and biochemical cues in endothelial barrier	HUVECs	collagen coated PET-transwell membrane electrospinned with PLC nanofibres	-	87
Organoid	Organoid formation for tumour cell Invasion studies	primary EC and A549 lung cancer cells in a 3:1 ratio in methylcellulose	Dispersed fibroblasts in fibrin	-	88
(Bio)scaffolds	Test diffusion limits in a thick vascularized model	Fibrin gel populated with dispersed fibroblasts and beads coated with HUVECs		-	89
	Test MSC role in angiogenesis	Fibrin gel populated with dispersed MSC and beads coated with HUVECs		-	90
	Normal and tumour vasculature formation	HUVECs, smooth muscle cells and fibroblasts, MSC, HepG2 cell line	starPEG-heparin hydrogels	-	91
Organ-on-a-chip	PDMS device for vasculature formation studies	Primary EC and fibroblasts	PDMS device coated with fibrin	M	92
	Study of angiogenesis and thrombosis in a microvessel	HUVECs pericytes	PDMS reservoir filled with collagen with dispersed pericytes.	M	93
3D bioprinting	3D lattice structure resembling vasculature network	hMSC HUVECs	Vasculature ink: Pluronic F-127 and thrombin Cell ink: gelatin, fibrinogen and	M	94

1.1.4 Why to develop a new advanced alveolar *in vitro* model

The project aimed to find the gap in knowledge in the current *in vitro* models and try to address them with a new model. Table 1.3 indicates the different models and strategies used, depending on the model type and application. The inserts and organoids apply a more cellular approach to recreate the alveolar region while the others contain a more engineering approach. The idea of the project was to have in one model, both approaches and include features such as a diverse cell population with epithelial, endothelial, stromal and immune cell representation. In addition, include a vasculature representation that would be more complex than a monolayer of endothelial cells. The model would also give high priority to deriving biomaterials that would mimic the complexity of the extracellular matrix, in contrast to seeding cells in Transwells or collagen-based biomaterials. On the engineering side, the objective was to create a bioreactor that would give flexibility in testing the developed model, but also previous models created in Transwells. In addition, the bioreactor would need to allow a flow of media to mimic blood circulation and dynamic air to mimic the breathing mechanism and create a displacement. Finally, was necessary for the model to be compatible with exposure systems present in the lab, such as the ones from Vitrocell where a Transwell is inserted. But also, suitable to nebulizers, for exposures in the bioreactor itself.

These were the gaps identified and the reason for creating a new alveolar *in vitro* model. The model would be a step closer to representing the area of interest, which would allow better informed decisions, based upon cell-level toxicological assessments, to be taken regarding the safety of products and their constituents.

1.1.5 Proposed advanced alveolar in vitro model

To build the advanced, multi-cellular and dynamic model proposed in the title, the project was divided into three parts. This section focuses on showing the rationale behind the choices made for each part. As a brief outline, the first part of the project is dedicated to modelling the alveolar region. The second part shows the strategy to create the *in vitro* vasculature network associated with the alveolus. The third part is responsible to select technology that could house both the alveolar and vasculature model and at the same time deliver the media and air in dynamic mode. In figure 1.9 can be found an illustration of the cells and matrix composition selected for each part of the project. For the rest of this section, can be found more detail on the rationale for the decisions made in each chapter.
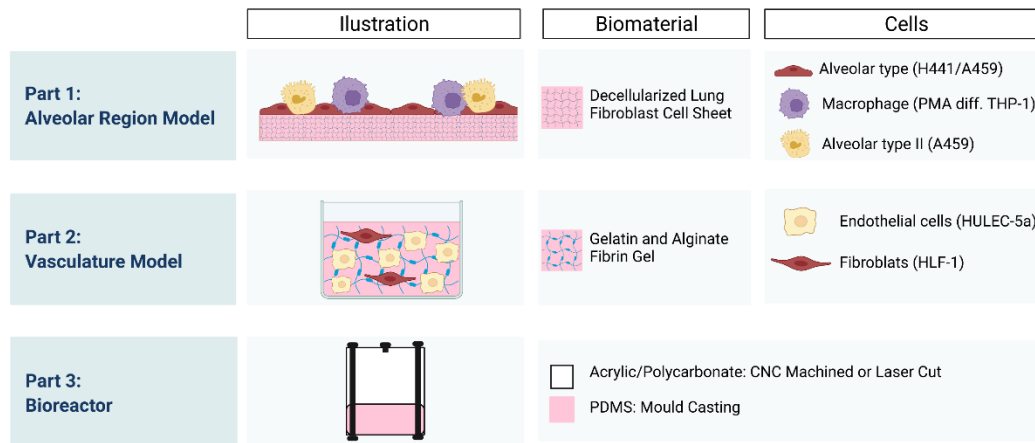
Figure 1.9: Overview of the project parts. To each part is given an illustration where is represented the biomaterial and the cells included.

After going through the alveolus cell and extracellular matrix composition in section 1.1.1.3, it was selected as essential cells to model the alveolar epithelium the hAELVi cell line to mimic the alveolar type I. For the alveolar type II, was selected the NCI-H441 cell line (or A549). Then, considering the final application of the model is for toxicological applications, a representation of the immune system is important, PMA differentiated THP-1 cells were chosen for that role. Regarding the matrix composition, after analysing the matrix composition of the current *in vitro* strategies in table 1.3, it was chosen to use a decellularized cell sheet strategy. The fibroblasts, HLF-1 cell line, were cultured for 21 days, after which the cells were lysed, and the nuclear content removed with a series of mechanical and chemical methods. Then, the decellularized extracellular matrix (dECM) was processed to be able to receive the alveolar epithelium on top.

For the vasculature formation is going to be used endothelial cells, HULEC cell line and fibroblasts, HLF-1 cell line, as supporting cells. The endothelial cells were seeded as individual cells or as spheroids. To address the matrix composition, two materials were tested, a mesh of gelatin and alginate or fibrin gels.

In the end, both tissues were incorporated into a bioreactor, with the alveolar on top of the vasculature model. The media contacts with the vasculature part only (to keep the alveolar part dry) and the air directly contacts with the alveolar side of the model. In this way, the alveolar model was stimulated with a continuous flow and air liquid interface.

The thesis aims to show the development of each part of the *in vitro* model and includes a pilot chapter in the end where the three parts were combined. On figure 1.10, to facilitate the reading, is shown the chapter's organization.
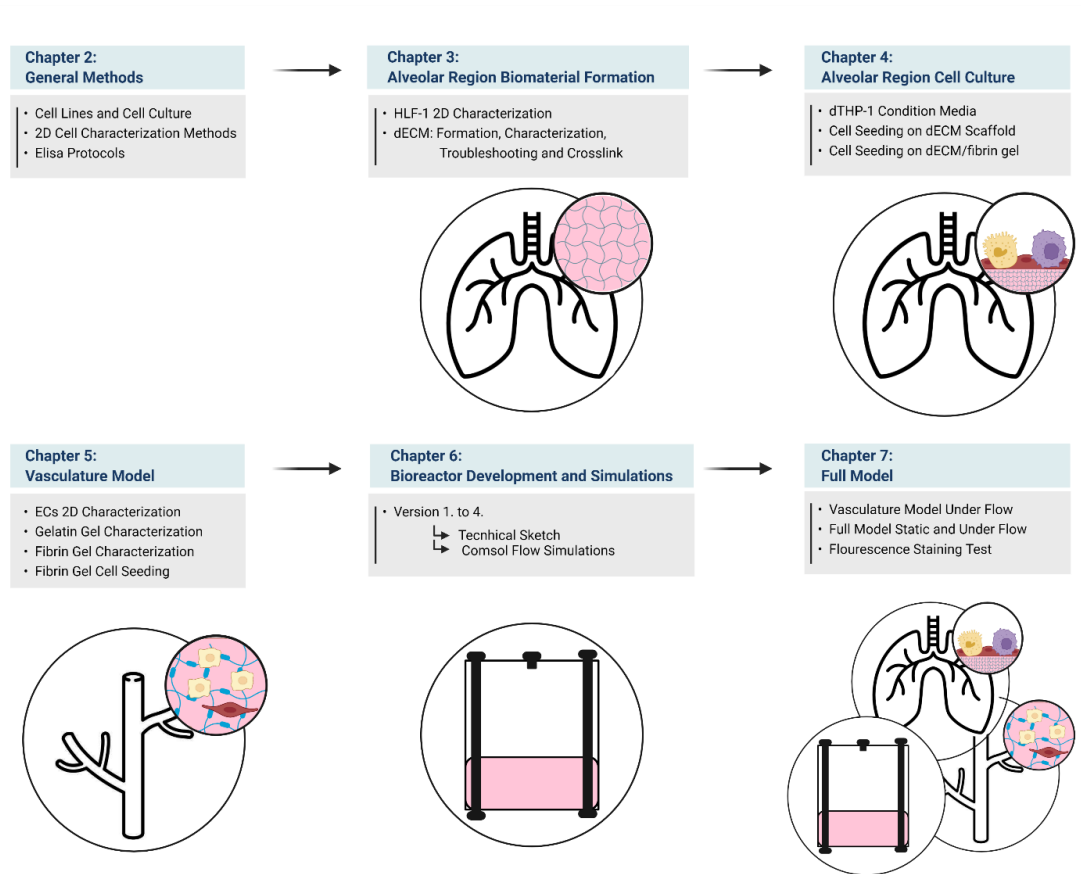
Figure 1.10: Overview of the thesis chapters

Chapter 2

General Materials and Methods

2.1 Chemical and Reagents

Table 2.1: List of chemical and reagents used in the thesis.

	Consumable	Company	Catalogue Number
Cell lines	HLF-1	ATCC	CCL-153
	EC	ATCC	HULEC-5a CRL 3244
	THP-1	ATCC	Tib-202
	H441	ATCC	HTB-174
	A549	ATCC	CRM-CCL-185
	hAELVi	inscreenex	INS-CI-1015
Cell culture	RMPI 1640 (1X) for THP-1	gibco	A1049-01
	RMP1640 (1X) for H441	gibco	31870-025
	DMEM, powder, low glucose, pyruvate	gibco	3160008
	MCDB 131 Medium, no glutamine	gibco	10372019
	hAELVi Medium	inscreenex	INS-ME-1013
	hAELVi Coating solution	inscreenex	INS-SU-1018
	hAELVi Freezing medium	inscreenex	INS-SU-1004
	Dimethyl Sulfoxide	Merk	D8418
	Phosphate Buffered Saline, Ph 7.4	gibco	10010015
	Foetal Bovine Serum, Heat-Inactivated	gibco	16140071
	Penicillin/Streptomycin	gibco	15140-122
	Epidermal Growth Factor	Merk	E9644
	Hydrocortisone	Merk	H4001-1MG
	L-Glutamine (200 Mm)	gibco	25030-024
	Trypsin-Edta (0.05%), Phenol Red	gibco	25300062
	Accutase® Solution	Merk	A6964
	Bovine Serum Albumin	Merk	A2153
	L-Ascorbic Acid	Merk	A5960
	Vascular Endothelial Growth Factor 165 Human	Merk	V5765
	Recombinant Murine Vegf165 (Vefg)	Peprotech	450-32
	Sphingosine 1-Phosphate	Merk	73914
	Human FGF-Basic	ThermoFisher Scientific	PHG0024
	Phorbol Myristate Acetate	Merk	P8139
	Lipopolysaccharides	Merk	L4391
	Fibrinogen (Human)	Enzyme Research Laboratory	FIB 1
	Thrombin (Human)	Enzyme Research Laboratory	HT1002a
	Fibrinogen (Bovine)	Merk	F8630
	Thrombin (Bovine)	Merk	T4648
Kits	Celltiter 96® Aqueous One Solution Cell Proliferation Assay	Promega	G3582

	Quant-It™ Picogreen™ Dsdna Assay Kit:	ThermoFisher Scientific	P7589
	Sircol Insoluble Collagen Assay	Biocolor	S200
	Glycosaminoglycan Blyscan Assay	Biocolor	B1000
	Dc Protein Assay Kit	Bio-Rad	5000111
	Qiaamp Dna Blood Mini Kit	QIAGEN	51104
	Methylene Blue (From Kiwk-Diff Kit, Solution 3)	Fisher Scientific	9990700
	Interleukin 1 beta ELISA	R&D Systems	DY201
	Interleukin 8 ELISA	R&D Systems	DY208
	Transforming Growth Factor beta 1 ELISA	R&D Systems	DY240
	Tumour Necrosis Factor alfa ELISA	R&D Systems	DY210
	Interleukin 6 ELISA	R&D Systems	DY206
Antibodies	Alexa Fluor 633 Phalloidin	Invitrogen	A22284
	CD31 Monoclonal Antibody Jc/70a	Invitrogen	MA5-13188
	Anti-CD31 Antibody [Jc/70a]	abcam	ab9498
	Recombinant Anti-Cd11b Antibody [Epr1344]	abcam	ab133357
	VE-Cadherin (D87f2) Xp® Rabbit Mab	Cell Signalling Technology	2500T
	Z0-1 Monoclonal Antibody (Zo1-1a12)	Invitrogen	33-9100
	Occludin Monoclonal Antibody (Oc-3f10)	Invitrogen	33-1500
	Goat Anti-Mouse Alexa Flour Plus 488	Invitrogen	A32723
	Alexa Flour 555 Donkey Anti-Rabbit	Invitrogen	A31572
	FITC Anti-Human Cd31 Antibody	Biolegend	303103
	Pe/Cyanine7 Anti-Human Cd34 Antibody	Biolegend	343515
	FITC Anti-Human Cd14 Antibody	Biolegend	325603
	FITC Anti-Human Cd11b Antibody	Biolegend	301330
	DAPI	Merk	D9542
	488 Conjugated Fibrinogen	ThermoFisher	F13191
Chemicals	Triton X-100	Merk	23,472-9
	DPX	Thermo Fisher Scientific	D/5330/05
	Paraformaldehyde	Merk	158127
	Glycine	Merk	G7126-5KG
	Haematoxylin	Merk	HX99311375
	Eosin Y	Merk	E4009
	Propidium Iodide	Merk	P4864
	Hoechst 33342 Trihydrate	Life technologies	H3570
	Alcian Blue 8gx	Merk	A3157
	Sybr Safe	Invitrogen	S33102
	Gel Loading Dye, Blue (6x)	New England Biolabs	B7021S
	Quick-Load® Purple 1 Kb Dna Ladder	New England BioLabs	N0552S
	Quick-Load® Purple 100 Bp Dna Ladder	New England BioLabs	N0551S

	Tris Base	Melford Biolaborties,	T60040
	Ethylenediaminetetraacetic Acid	Merk	E9884
	Sodium Dodecyl Sulfate	Thermo scientific	28365
	Ammonium Hydroxide	Merk	09859
	Hepes	Merk	H3375
	Tween-20	Fisher Bioreagents	BP337-100
	Sodium Chloride	Fisher Chemical	S/3120/63
	Ethanol	Fisher Chemical	E/650DF/17
	Methanol	Fisher Chemical	M/4056/17
	Acetic Acid	Fisher Chemical	A/0360/PB17
	Sodium Hydroxide	Acros Organics	206060010
	Hydrochloric Acid	VWR	E484
	Chloroform	Merk	472476
	Stacking Buffer 4x Solution	Melford	S28200
	Separating Or Resolving Buffer 4x Solution	Melford	S28100
	Acrylamide/Bis-Acrylamide, 30% Solution	Merk	A3449
	Ammonium Persulfate	ThermoFisher	17874
	N,N,N',N'-Tetramethylethylenediamine	Merk	T9281
	Trizma Base (Tris)	Merk	T4661
	Lithium lactate	Merk	L2250
	Nicotinamide Adenine Dinucleotide	Merk	N0632
	Iodonitrotetrazolium Chloride	Merk	I8377
	Phenazine Methosulfate	Merk	P9625
	Sodium Acetate	Merk	S2889
	Precision Plus Protein Dual Color Standard	Bio-Rad	161-0374
	Sample Buffer, Laemmli 2× Concentrate	Merk	S3401
	Coomassie Brilliant Blue R-250 Dye	ThermoFisher Scientific	20278
	Riboflavin 5'-Monophosphate Sodium Salt Hydrate	Merk	F6750
	PBS Tablets	VWR	E404-100TABS
	PDMS	Intertronics	Elastosil RT 601
	Gelatin	Merk	G2500
	Alginate	Merk	C3306
	Calcium Chloride	Merk	A9539
	Trypan Blue Solution (0.4%)	gibco	11538886
	Sodium Azide	Merk	S2002
	Novocyte Qc Particles	Agilent	8000004
	Novoflow	ACEA Biosciences	71B607

2.2 General Materials and Equipments

Table 2.2: List of general materials and equipment.

		Brand
Material	T175 Cell Culture Flasks	660175, Greiner bio-one
	T75 Cell Culture Flasks	658175, Greiner bio-one
	T25 Cell Culture Flasks	690175, Greiner bio-one
	6 well Plates	353046, Falcon, Corning
	12 well Plates	655180, Greiner bio-one
	24 well Plates	662160, Greiner bio-one
	48 well Plates	3548, costar
	96 well Plates	442404, Nuc, ThermoScientific
	96 well Half Area Plate	675061, Greiner bio-one
	1000 µL - Tips	S1111-6701, TipOne, Starlab
	200 µL - Tips	S1111-1706, TipOne, Starlab
	20 µL - Tips	S1120-1810, TipOne, Starlab
	25 mL Serological Pipettes	760180, Greiner bio-one
	10 mL Serological Pipettes	607180, Greiner bio-one
	5 mL Serological Pipettes	606180, Greiner bio-one
	2 mL eppendorf	Safe-Lock Tube 0030 123.344, Eppendorf
	1.5 mL eppendorf	616 201, Greiner bio-one
	500 µL eppendorf	14230200, Fisher Scientific
	200 µL eppendorf	14230225, Fisher Scientific
	Cell scraper	08-100-241, Fisher Scientific
	50 mL Falcon tubes	227261, Greiner bio-one
	15 mL Falcon tubes	188271, Greiner bio-one
	FACS Tubes	391-0000, VWR
	Slides	BPB019, RS France
	Covers lips	11961988, Fisher Scientific
	Pasteur Pipette	612-4497, VWR
	Blue role	7225, WypAll
	Virkon	Rely+On Virkon, Lanxess
Equipment	Centrifuge (cell culture)	Himac CT6E, VWR
	Centrifuge (for epis)	Centrifuge 5810 R, Eppendorf
	Centrifuge (for epis)	Centrifuge 5415 D, Eppendorf
	Microcentrifuge	Microcentrifuge Star Lab, Smart Instruments
	Heat Block	888700005, ThermoScientific
	Hotplate stirrer	CB302, Stuart
	Sonicator	Branson 102C (sonicator), Branson 550 (box)
	Scale (for milligrams)	R180 D, Sartorius Research
	Scale (for grams)	TE3102s Sartorius
	Incubator	NuairTM DHD AUTOFLOW CO2 Air-Jacketed Incubator
	Class II Cabinet	Mars, SCANLAF
	Haemocytometer	Marienfeld Counting Chamber Neubauer-improved bright line
	Plate Reader	FLOUstar Omega, BMG Labtech
	Water Bath	JB Nova, Grant Instruments
	Cell Culture Microscope (+Camera)	Zeiss Axiovert 40C (Zeiss AxioCamERC55)
	3D Printer	Creality CP-01 (P202J08D01172)

<u>2.3 Cell Culture</u>

2.3.1 Human Lung Fibroblasts

The human lung fibroblast (HLF-1) is a cell line derived from healthy human lungs acquired from the ATCC. The cells were cultured in Dulbecco's Modified Eagle's Medium (DMEM), supplemented with 10% Fetal Bovine Serum (FBS), and 1% Penicillin-Streptomycin (Pen/Strep) with 10,000 U/mL. The DMEM medium was in powder format, so the supplier instructions were followed (ThermoFisher Scientific, Gibco). To make a total of 1L of the medium was added to 1L of Millipore water 10g of DMEM powder and 3.7g of sodium bicarbonate. After complete solubilization of the powders, was added 1.4 mL of a 3M hydrochloric acid to adjust the pH to 7 and 10ml of the Pen/Strep. Then the medium was moved to the tissue culture hood to proceed to sterile filtration with a 0.22μm porous size filter. In this way, 45 mL of DMEM medium was filtered into a 50mL falcon tube and top up with 5 ml of FBS to make a complete DMEM medium. The freezing media for this cell line was composed of complete media with 5% (v/v) Dimethyl Sulfoxide (DMSO) as recommended by the ATCC.

For cell handling, the seeding density was 5000 cells/cm^2 and cells were passaged or frozen when 80% confluency was attained. Fresh media was added every two days. To subculture the cells, first, wasted media was removed and flasks washed once with Phosphate-buffered saline (PBS). Then, to promote cell detachment, flasks were placed in the incubator (humidified 37°C, 18% oxygen and 5% CO$_2$) with EDTA-Trypsin solutions for 5-10 minutes. The reaction was stopped by placing the flasks in the hood and by adding 5 times the volume of DMEM media to EDTA-Trypsin. The content of the flask was added to a vial that was centrifuged at 300xg for 5 minutes. After the centrifugation, the cells were counted to reseed for experiments or passage into a new flask at 5000 cells/cm^2. If frozen, cells were frozen down at 1 to 3 million cells/mL using freezing media. The HLF-1 cells were used in the experiments until passage 8. The cell counts were performed as described in section 2.4.1

2.3.2 Endothelial Cells

The endothelial cell line (ECs) was isolated from healthy human lung microvasculature and acquired from the ATCC. The ECs were cultured in MCDB131 media supplemented with 10% FBS, 10 ng/mL of human epidermal growth factor (hEGF), 1 μg/mL of hydrocortisone, 10 mM of glutamine and 1% Pen/Strep with 10,000 U/mL. The hydrocortisone was always added fresh to the media. The freezing media for this cell line was complete media with 7.5% (v/v) DMSO as recommended by the supplier (ATCC). The ECs were used in the experiments until passage 8. Regarding cell handling, the same protocol was followed as described in 2.3.1.

2.3.3 Monocyte: THP-1

The THP-1 cell line is a monocyte cell type isolated from peripheral human blood with acute monocytic leukemia. The cells were cultured in RPMI-1640 [-] Glutamine supplemented with 2mM glutamine and 1% Pen/Strep with 10,000 U/mL. The freezing media for this cell line was complete growth media supplemented with 5% (v/v) DMSO as recommended by the supplier.

The THP-1 cells are a non-adherent cell line. In this way, for passage, the cells were pipetted out of the flask, then centrifuged at 300 g for 5min. The cells were counted (as detailed in section 2.4.1) and subsequently seeded at 20000 cells/cm^2 (1x10^5 cells/ml in T75 flasks containing 15 mL). The cells were frozen at concentration of 1 million cells/mL using freezing media (complete media with 5% DMSO).

2.3.3.1 THP-1 PMA differentiation

To differentiate the monocyte cell line THP-1 into macrophages (dTHP-1) was used phorbol 12-myristate 13-acetate (PMA). The cells were seeded at 20000 cells/cm^2 supplemented with 20 nM of PMA dissolved in RPMI-1640 complete media (1x10^5 cells/ml in T75 flasks containing 15 mL supplemented with 30 μL of a 10 μM PMA stock solution). After 48h, cells had become adherent to the plastic so wasted media was pipetted out and fresh media added. Then, it was allowed a 24 hour recovery period before cell detachment. To retrieve the cells, flasks were washed once with PBS before treatment with accutase. Cell detachment occurred in the incubator (humidified 37°C, 18% oxygen and 5% CO$_2$) over a 5-15 minutes period. After cell detachment, accutase reaction was stopped by adding 5 times the volume of accutase of RPMI 1640 media. The cells were centrifuged at 300 g for 5 minutes and counted (as described in section 2.4.1). The cells were then reseeded at different seeding densities depending on the experiment that can be found in chapter 4 and 7.

2.3.4 Alveolar Type I: hAELVi

The CI-hAELVi Human Alveolar Epithelial cell line (hAELVI) is an alveolar type I cell isolated from healthy lungs, of patients undergoing lung tumour resection surgery, and immortalized using CI-SCREEN technology. Further information on the immortalization technology is described by Lipps et al (2018)[95], and details on the hAELVi immortalization approach are reported by Kuehn et al (2015)[96]. The hAELVi cell line is supplied by InScreenEX company from where can be found a detail manual instruction of how to handle these cells as well as purchase all the cell culture media and reagents[97]. The hAELVi cells are culture in huAEC Medium supplemented with

1%Pen/Strep, with media change every two days and coating of the surface is necessary to ensure cells adherence. To coat the flasks, a huAEC Coating Solution was added from 2 to 24 hours at 37 ° in the incubator (humidified air with 18% oxygen and 5% CO_2). The specified volumes can be found on hALEVi cells instruction manual, but for a T75 was used 2 mL of the coating solution. After the incubation period, the flasks were washed once with PBS before being used to remove excess coating. Coated flasks were stored at 4 °C for up to one month. To passage the cells, the same protocol was followed as in 2.3.1. To freeze the hAELVI cells, after cell trypsinization the cells were suspended in 2% FBS in PBS, centrifuged at 300 g for 5 minutes and resuspended in freezing media at 1 million cells/mL.

2.3.5 Alveolar Type II: H441

The NCI-H441 cell line (H441) are epithelial cells isolated from papillary adenocarcinoma of human lungs and acquired from ATCC. The cells were cultured in RMP1 1640 [+] 4.5g/L D-Glucose, [+] L-Glutamine, [+] 1.5 g/L Sodium Bicarbonate, [+]110 mg/L Sodium Pyruvate, supplemented with 1%Pen/Strep and 10%FBS. The same protocol as detailed in section 2.3.1 was used to handle the cells.

2.3.6 Alveolar Type II: A549

The A549s cell line, is an epithelial type II isolated from lung carcinoma. The cells were cultured in RPMI-1640 [-] Glutamine supplemented with 2mM glutamine and 1% Pen/Strep with 10,000 U/mL. For cell passaging and handling was followed the same protocol as in section 2.3.1.

2.4 2D Cell Characterization:

2.4.1. Trypan blue exclusion assay

Trypan blue is an exclusion dye used to access cell viability. If a cell is viable the cell membrane is intact and the dye is excluded. Alternatively, in a non-viable cell, the cell membrane becomes compromised and the trypan blue dye is able to penetrate making the cytoplasm blue[98].

The assay was conducted by initially adding 10 µl of the suspension of the specific cell type of interest (*e.g.* fibroblasts, endothelial cells) and mixed with 10 µl of trypan blue solution in an Eppendorf. The cell suspension is obtained using the method in section 2.3.1 for trypsinization. A total of 10 uL was then loaded into a haemocytometer. The cells having a blue cytoplasm were counted as dead and the rest counted as live. The number of live and dead cells was determined by equation 2.1. The dilution factor was 2, the plate area is in cm^2 and V corresponds to the

volume in mL of the cell suspension (from where the 10 µl were sampled). To determine the total cell number, and the live and dead ratio the equations 2-4 were followed.

$$\frac{Live/Dead\ cell\ number}{cm^2}$$
$$= \frac{\left(\frac{Number\ of\ cells\ counted}{Number\ of\ squares} \times 1000 \times Dilution\ Factor \times V\right)}{plate\ area} \quad (Eq.\ 2.1)$$

$$\frac{Total\ cell\ number}{cm^2} = Live\ cell\ number/cm^2 + Dead\ cell\ number/cm^2 \quad (Eq.\ 2.2)$$

$$Live\ Ratio = \frac{Live\ cell\ number}{Total\ cell\ number} \quad (Eq.\ 2.3)$$

$$Dead\ Ratio = \frac{Dead\ cell\ number}{Total\ cell\ number} \quad (Eq.\ 2.4)$$

Cell growth is characterized by an exponential tendency that follows equation 2.5. The y corresponds to cell number and x to time. The y_0 represents wherein the curve crosses the y axis (approximately the number of cells seeded on day 0) and K to the rate constant. Equation 2.6 determines the time constant, τ, and doubling time is determined by equation 2.7.

$$y = y_0 \times e^{Kx} \quad (Eq.\ 2.5)$$

$$\tau = \frac{1}{k} \quad (Eq.\ 2.6)$$

$$Doubling\ Time = \frac{ln\ (2)}{k} \quad (Eq.\ 2.7)$$

2.4.2. CellTiter 96® AQueous One Solution Cell Proliferation Assay

he MTS assay determines the metabolic activity of the cells. The tetrazolium compound is reduced by the NADPH in the cell. The compound that is formed, is formazan, which is coloured and soluble in culture media. To perform the assay the cells were seeded on a 96 well plate at 5000 cells/cm^2. The assay was performed with the HLF-1 and endothelial cells, for more detail refer to sections 3.2.1.3 and 5.2.2.2 respectively.

On the day of the experiment, the media was removed from the wells and fresh media with MTS, but without FBS was added. The albumin in the FBS interferes with the assay reducing up to 50% the absorbance value[99]. The MTS to media ratio was 1:5, which means, 20 µL of MTS was dissolved in 90 µL of media. Then the cells were placed in the incubator (humidified 37°C with 18% oxygen and 5% CO_2) for 1 hour for the reaction to take place. After the incubation period,

the media was removed and added to a new 96 well plate. The absorbance was measured by a plate reader (POLARstar Omega, BMG LABTECH) at 490nm. The negative control equated to a well where no cells were seeded. Subsequently, test sample absorbance values were subtracted from those of the negative control and divided by the plate area. The MTS value was further divided by the number of live cells per cm^2 determined by the trypan blue assay from section 2.4.1.

2.4.3. Quant-iT™ PicoGreen™ dsDNA Assay Kit

The Picogreen Kit is a fluorescence-based assay that determines double stranded DNA (dsDNA) content in an impure biological sample. To conduct this method, the diagnostic kit was used relevant to the manufacturer's guidelines. In the kit was supplied the: Quant-iT™ PicoGreen®dsDNA reagent (Picogreen dye), 20 times concentrated TE buffer (200 mM Tris-HCl, 20 mM EDTA, pH 7.5) and Lambda DNA standard (at 100µg/mL). The cells of interest (*e.g.* fibroblasts, endothelial cells) were seeded in a 24 well plate at 5000 cells/cm^2. On the day of the experiment, the cells were harvested as specified in section 2.3.1 for trypsinization. The pellet was resuspended in 200 µL of TE buffer (one time diluted in Millipore water) to lyse the cells. Next, 100 µL of the cell lysate and standards were loaded into a black 96 well plate (greiner, flat bottom). A total of 100 µL of the Picogreen dye solution diluted in PBS was then added to each well. The picogreen dye is supplied 200x concentrated, so for a full 96 well plate 10mL of the picogreen solution was made that contained 50µL of the picogreen dye into 10mL of PBS. Immediately, the plate was placed in a plate reader (POLARstar Omega, BMG LABTECH) where it was first shaken for 5 minutes at room temperature before exiting at 485 nm. The fluorescence emission was captured using a filter from capture from 510-520. The ng of DNA in the samples was determined *via* a calibration curve (as described below), y=mx+b, where *y* corresponds to the ng of DNA and *x* to the fluorescence.

The calibration curve was done by pipetting 4.8 uL of Lambda DNA standard (100 µg/mL) into 235.2µL of TE buffer, making a 2 µg/mL solution. From this solution 100 µL was added to the same 96 well plate used in the assay, creating the first standard of DNA of 100 ng (2 µg/mL x 0.1 mL= 0.2 µg, with the dilution factor of 2 of adding equal volumes of picogreen dye and sample, 0.2 µg /2 = 0.1 µg = 100 ng). The remaining standards were made *via* a series of 10x dilutions (Table 2.3). An example of a calibration curve is present in figure 2.1.

Table 2.3: Picogreen calibration curve volumes. Volume of TE buffer and DNA stock used to generate the DNA calibration curve used to determine the ng of DNA in unknown samples when using the Picogreen kit.

DNA solution (µl)	TE Buffer (µl)	Concentration (ng/ml)	Lambda DNA standard (ng)
4.8 µl of 100 µg/ml Lambda DNA standard	235.2	2000	100
20 µl of 2000 ng/ml DNA solution	180	200	10
20 µl of 200 ng/ml DNA solution	180	20	1
20 µl of 20 ng/ml DNA solution	180	2	0.1
0	100	0	0
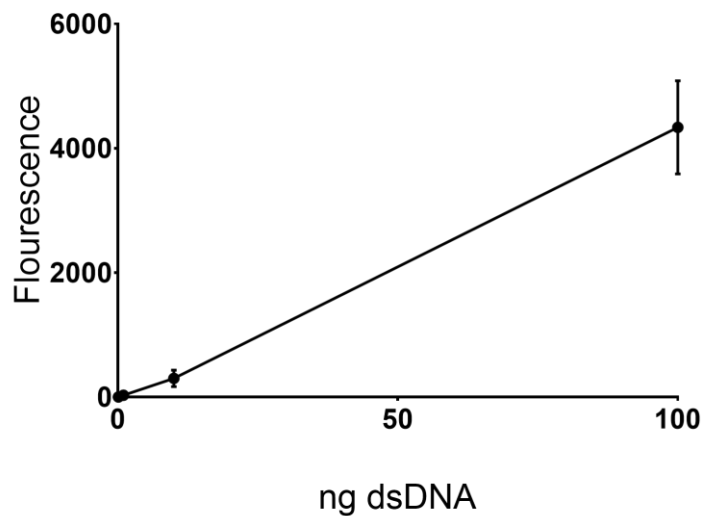
Figure 2.1: Picogreen representative calibration curve. Example of a picogreen calibration curve in TE buffer. The linear regression that fits the data is y= 0.023x – 0.0834. (n=3)

2.4.4. Dextran Blue

The dextran blue assay assesses the barrier integrity of the cell layer, specifically barrier cells (*e.g.* epithelial cells). The dextran blue compound is a high molecular weight dye with 2000k Da that is not able to penetrate the cell membrane. It is only able to diffuse through the space between cells, if available.

Cells, such as fibroblast and endothelial cells, were seeded at a density of 5000 cells/cm^2 on a 12 well Transwell. After removing the media from the top and bottom, 1 mL of media was freshly added to the bottom well. Then, 250 µL of the dextran blue dye was added to the top well. After incubating the cells for 2 hours (humidified 37°C with 18% oxygen and 5% CO$_2$), the media from the bottom reservoir was removed and the absorbance was measured at 600 nm using a plate reader (FLOUstar Omega, BMG LABTECH). The negative control for the dextran blue was an

insert where no cells were seeded. For data analysis, the absorbance of the samples was divided by the absorbance of the negative control. Then, was plotted together with that ratio the value of fresh media and a line at absorbance value 1.

2.4.5 Flow cytometry

Flow cytometry is a technique where a cell suspension passes through a nozzle where it is irradiated with a light beam. The forward and side scattering of the light in a single cell indicates cell size and organelle complexity respectively. In addition, it can detect fluorescently labelled antibodies attached to the cells[100].

On the day of the experiment, the cells were harvested as specified in section 2.3.1. After centrifugation, 1×10^5 viable cells (determined by the trypan blue assay from section 2.3.1) were stained with the antibody. The antibody was diluted in 1 mL of PBS. After pipetting up and down gently, the cells were placed on the ice for 45 min protected from the light. Then, the cells were centrifuged for 5 min at 300 g, the supernatant was discharged and 500 µL of FACs buffer (PBS with 1% BSA and 0.1% sodium azide) was added. The cells were then run in a NovoCyte Flow Cytometer. The negative control was a vial where no antibody was added. The data analyse was performed using FlowJo 10.7.1 software (license number 59222). Firstly, was gated the singlets by plotting the side and forward scattering of the negative control. This gate was applied to all samples. Then, was determined the number of events with and without fluorescence. For a detailed protocol on antibodies and volumes used for HLF-1 and ECs stain for flow cytometry consider sections 3.2.1.5 and 5.2.2.5 respectively.

2.4.6 Light microscopy

Bright field images were taken using a ZEISS Axiovert 40 C light microscopy with an attached AxioCam ERc5s camera (Carl Zeiss Microscopy GmbH, Germany). A total of 3 biological repeats, with 3 technical repeats each were imaged. The cells imaged using this microscope were the human lung fibroblast and the endothelial cells.

2.4.7. Confocal laser scanning microscopy

Confocal laser scanning microscopy (CLSM) enables the visualization of biological samples by capturing the fluorescence signals selectively bound to the features of interest. The differences between this microscopy and fluorescence microscopy are related to the introduction of lasers

that excites the samples, instead of total specimen illumination, and a combination of a pinhole before the detector that eliminates out-of-plane fluorescence. This produces higher resolution images that when assembled can generate a three-dimension image[101]. The CLSM equipment used throughout the thesis was a ZEISS LSM 710.

For the 2D cell characterization, the cells were seeded on a 12 well plate with a coverslip at the bottom of the well. The coverslips were autoclaved for sterility. On the day of the experiment, the cells were fixed with a 4% paraformaldehyde (PFA) solution for 15 minutes (500 µL) at room temperature. Then, washed two times with PBS, five minutes each wash. For long term storage, 0.1 M of glycine was added to each well and plates were placed at 4°C. To commence the stain, the coverslip was added to a new plate, washed three times with ice cold PBS to remove the glycine, five minutes each wash. The 2D cell characterization used the fluorescence stains detailed in table 2.4. A more detailed protocol for HLF-1 staining can be found in method section 3.2.1.7 and for ECs in section 5.2.2.7.1 to 5.2.2.7.3. To mount the coverslip, a drop of DPX (avoid adding bubbles in the process) was added to a microscope slide and the coverslip containing the cells was carefully flipped on top of the DPX. With the coverslip in position, slowly press it to remove excess DPX. When the DPX was dried, the coverslip was sealed with nail polish and stored in the dark at 4°C until imaging. A total of 3 biological, with 3 technical repeats each were imaged. Four images per technical repeat were taken: centre, upper, lower, left and right side of the slide.

Table 2.4: Fluorophores used in CLSM with the corresponded targets and dilutions. Legend: P: primary antibody, S: secondary to the secondary antibody.

Target	Stain Type		Fluorescence dye/Antibody	Concentration/ Dilution
Nucleus	Direct		DAPI (D9542, Merk)	1 µg/mL
F-actin	Direct		Phalloidin (A22284, Invitrogen)	1:200
CD31	Indirect	P	CD31 Monoclonal Antibody JC/70A (MA5-13188, Invitrogen)	1:100
		S	Goat anti-Mouse Alexa Flour Plus 488 (A32723, Invitrogen)	1:1000
VE-Cadherin	Indirect	P	VE-Cadherin (D87F2) XP® Rabbit mAb (2500T, Cell Signalling Technology)	1:400
		S	Alexa Flour 555 donkey anti-rabbit (A31572, Invitrogen)	1:1000

2.5 ELISA

2.5.1 Interleukin 6 Quantification

The Interleukin 6 (IL6) ELISA was performed in a 96-half area plate, so all the volumes indicated in the IL6 ELISA manual were half. First was added to each well, 50 µL of the capture antibody solution with 2 µg/mL in PBS, which was allowed to incubate overnight at room temperature. On the following day, the plates were washed three times with washing buffer (0.05% Tween in PBS) and blocked with reagent diluent (150 µL per well of 1% BSA in PBS) for one hour at room temperature. After washing the plate three times again with washing buffer it was added the samples and the standards to the wells diluted in reagent diluent. After 2 hours incubation period, the same washing step was applied before adding 50 µL of the detection antibody solution (50 ng/mL in reagent diluent for 2 hours). The plates were washed again before adding the streptavidin solution (50 µL of a 40-fold dilution in reagent diluent) for 20 minutes protected from light at room temperature. The plates were washed again one last time with washing buffer before adding the substrate solution, composed of a 1:1 solution of color reagent A and color reagent B. The substrate solution was let to react for 20 minutes protected from light at room temperature. To stop the reaction, 25 µL of 2N H_2SO_4 was added to each well. The plates were placed on a shaker for 5 minutes before reading the absorbance at 450 nm with 540 nm set for the correction wavelength using a plate reader (POLARstar Omega, BMG LABTECH). For the data analysis, first was subtracted the absorbance at 450 nm from 540 nm. Then, it was generated a calibration curve using a four-parameter logistic (4-PL) fitting using open-source software (MyCurveFit). The equation can be found in equation 2.8.

$$y = d + \frac{a - d}{1 + \left(\frac{x}{c}\right)^b} \quad (Eq\ 2.8)$$

Where y is the absorbance, x is the concentration, a corresponds to the absorbance value when concentration is 0, d corresponds to the absorbance value when concentration is maximal, c corresponds to the concentration value where the curve has an inflection point (halfway between a and d) and b corresponds to the slope of the curve. The rearranged equation to solve x is presented in equation 2.9. In this way, for the data analysis, the concentration value (x) at a determined absorbance (y) is determined by solving equation 2.9.

$$x = c + \left(\frac{a - d}{y - d} - 1\right)^{1/b} \quad (Eq.\ 2.9)$$

From the concentration of the samples was subtracted the concentration of the negative control. This corresponded to a well where the exact same experimental protocol was followed but no cells were seeded in the first place. The calibration table and plot for the IL6 ELISA can be seen in figure 2.2.

Standard (pg/mL)	IL6 Standard (180 ng/mL) Volume (µL)	Final Volume (mL)
600	3.3 into 1 ml reagent diluent	0.5
300	-	0.5
150	-	0.5
75	-	0.5
37.5	-	0.5
18.8	-	0.5
9.4	-	0.5
4.7	-	0.5
2.3	-	1
0	-	-

Figure 2.2: IL6 calibration curve. Left: IL6 standard calibration curve volumes with 10-points using 2-fold serial dilutions in reagent diluent. Right: The optical density (O.D.) at 450 nm in function of IL6 concentration The four-parameter logistic fitting determined the value of a 0.0291, b 0.6805, c 1×10^9 and d 59921. (n=1)

2.5.2. Tumour Necrosis Factor alpha Quantification

The Tumour Necrosis Factor alpha (TNF-α) followed the manual instruction, which is the same as for IL6 in section 2.5.1. However, one difference is in the capture antibody concentration, which had a concentration of 4 µg/mL in PBS. The calibration table and plot for the TNF-α ELISA can be seen in figure 2.3.

Standard (pg/mL)	TNF-α Standard (130 ng/mL) Volume (µL)	Final Volume (mL)
1000	7.7 into 1 mL reagent diluent	0.5
500	-	0.5
250	-	0.5
125	-	0.5
62.5	-	0.5
31.3	-	0.5
15.6	-	0.5
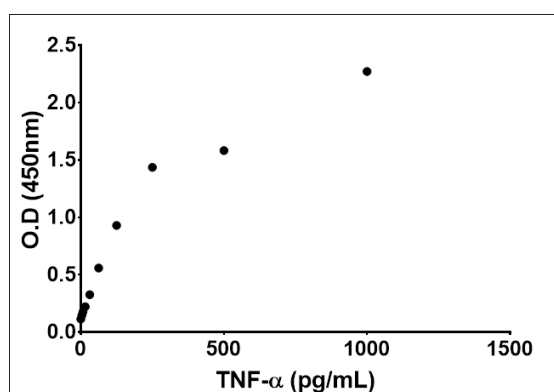
7.8	-	0.5
3.9	-	1
0	-	-

Figure 2.3: TNF-α calibration curve. Left: TNF-α standard calibration curve, with 10-points using 2-fold serial dilutions in reagent diluent. Right: Optical density (O.D.) at 450 nm in function of TNF-α concentration. The four-parameter logistic fitting determined the value of a 0.08349, b 0.87991, c 404.239 and d 3.15968. (n=1)

2.5.3 Transforming Growth Factor beta 1 Quantification

The Transforming Growth Factor beta 1 (TGF-β1) ELISA followed the manual instruction, which is the same as for IL6 in section 2.5.1, with a difference in the blocking buffer that contains 5% Tween in PBS. The washing buffer is 0.05% Tween in PBS. The reagent diluent is 1.4 mL of Reagent Diluent Concentrate 1 (#DY997, R&D systems) to 98.6 mL washing buffer. The TGF-β1 ELISA also required samples activation, first was added to 50 µL of the sample, 10 µL of 1 N HCl, after mixing well, the reaction was allowed for 10 minutes. To stop the activation, 10 µL of 1.2N NaOH/0.5M HEPES was used. (12mL of 10N NaOH, 11.9g HEPES in 88 mL of water). The samples were assayed immediately. For data analysis, the concentration must be multiplied by a factor of 1.4. The calibration table and plot for the TGF-β1 ELISA can be seen in figure 2.4.

Standard (pg/mL)	TGF-β1 Standard (160 ng/mL) Volume (µl)	Final Volume (mL)
2000	12.5 into 1 ml reagent diluent	0.5
1000	-	0.5
500	-	0.5
250	-	0.5
125	-	0.5
62.5	-	0.5
31.25	-	1
0	-	-

Figure 2.4: TGF-β calibration curve. Left: TGF-β1 standard calibration curve with 8-points using 2-fold serial dilutions in reagent diluent. Right: Optical density (O.D.) at 450 nm in function of TGF-β1 concentration. The four-parameter logistic fitting determined the value of a 0.0648, b 1.3814, c 424.959 and d 4.0520. (n=1)

2.5.4 Interleukin-8 Quantification

The interleukin-8 (IL8) ELISA followed the manual instruction, which is the same as for IL6 in section 2.5.1, with a difference in the reagent diluent, capture and detection antibody concentration. The reagent diluent contained 0.1% BSA, 0.05% Tween 20 in Tris-buffered Saline (20 mM Trizma base and 150 mM NaCl). The capture antibody concentration was 4 µg/mL in PBS and detection 10 ng/mL in reagent diluent. The calibration table and plot for the IL8 ELISA can be seen in figure 2.5.

Standard (pg/mL)	IL8 Standard (100 ng/mL) Volume (µL)	Final Volume (mL)
2000	20 µL into 1 mL reagent diluent	0.5
1000		0.5
500	-	0.5
250	-	0.5
125	-	0.5
62.5	-	0.5
31.3	-	1
0	-	-
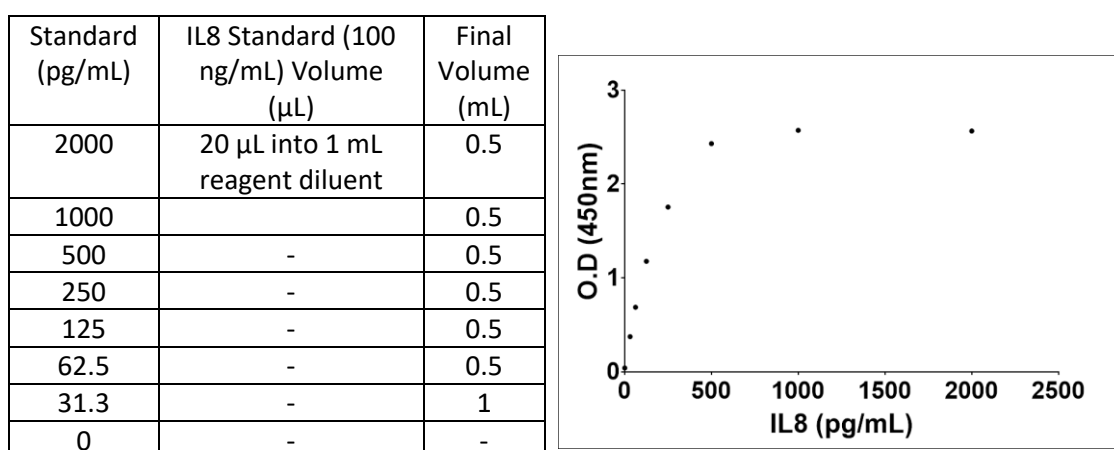
Figure 2.5: IL8 calibration curve. Left: IL8 standard calibration curve with 8-points using 2-fold serial dilutions in reagent diluent. Right: Optical density (O.D.) at 450 nm in function of IL8 concentration. The four-parameter logistic fitting determined the value of a 0.081, b 1.424, c 153.058 and d 2.707. (n=1)

2.5.5 Interleukin 1 beta Quantification

The Interleukin 1 beta (IL-1β) ELISA followed the manual instruction, which is the same as for IL6 in section 2.5.1, with a difference in the capture and detection antibody concentration. The capture antibody concentration was 4 µg/mL in PBS and detection 200 ng/mL in reagent diluent. The calibration table and plot for the IL-1β ELISA can be seen in figure 2.6.

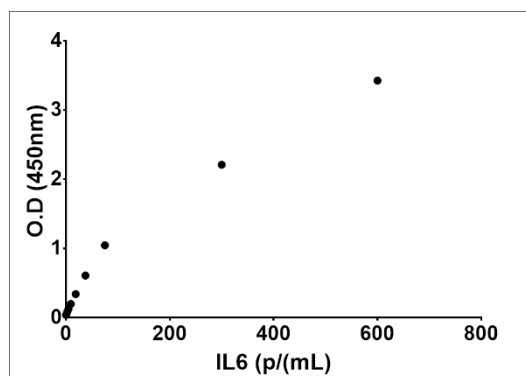| Standard (pg/mL)	IL8 Standard (95 ng/mL) Volume (μL)	Final Volume (mL)
250	2.6 μL into 1 mL reagent diluent	0.5
125		0.5
62.5	-	0.5
31.3	-	0.5
15.6	-	0.5
7.8	-	0.5
3.9	-	1
0	-	-
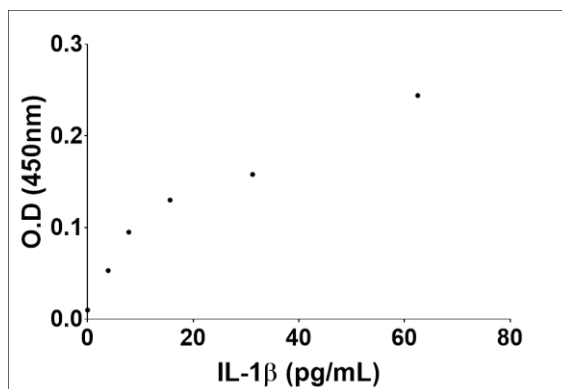
Figure 2.6: IL-1β calibration curve. Left: IL-1β standard calibration curve with 8-points using 2-fold serial dilutions in reagent diluent. Optical density (O.D.) at 450 nm in function of IL-1β concentration. The four-parameter logistic fitting determined the value of a 0.00921, b 0.527, c 2.5×10^8 and d 703.0. (n=1)

2.6 Lactate dehydrogenase Quantification

The LDH assay measures the amount of Lactate dehydrogenase (LDH). The LDH is an enzyme that catalyses the conversion of lactate into pyruvate in the presence of NAD^+. If the cell membrane becomes damaged as a result of stress, cytotoxicity or cell death, the LDH leaks and can be measured in the media[102].

The protocol followed is described in Busch M, *et al* (2021)[103]. In brief, first is added 50 μL of the sample to a 96 well plate and then added 150 μL of reaction mixture containing: 50 μL of Tris buffer (200 mM pH = 8), 50 μL Li-Lactate (50 mM), 46 μL NAD^+ (5 mM), 2 μL INT (65mM) and 2 μL PMS (29 mM). The reaction was allowed for 10 minutes protected from light, at room temperature and in a shaker before being stopped with 50 μL 1M H_2SO_4. The absorbance was read at 490 nm using a reference wavelength of 680 nm. For data analysis the absorbance at 490 was subtracted from the absorbance at 680 nm. Then the value of media was removed followed by divided by the cell number. Finally, the values were multiplied by the volume. In this way, it was possible to compare samples with different cell numbers and total volumes.

2.7 Cell count using ImageJ

To determine the cell number from DAPI stain images, the imageJ software was used. The script used can be found below together with a presentative input and output image obtained by the program (figure 2.7). Afterwards, the number of particles identified corresponded to the number of cells counted per image. The cell number determined per area of the image was

extrapolated for the area where the cells were cultured. A total of at least 10 images were analysed, to determine the average cell number. The script also determines the area of the particle identified.

```
run("Set Scale...", "distance=90,8 known=20 unit=mm");
run("8-bit");
setAutoThreshold("Default dark");
//run("Threshold...");
setAutoThreshold("Intermodes dark");
//setThreshold(21, 255);
setOption("BlackBackground", false);
run("Convert to Mask");
run("Convert to Mask");
run("Analyze Particles...", "size=0-infinity show=Outlines display exclude clear include summarize overlay");
close();
```
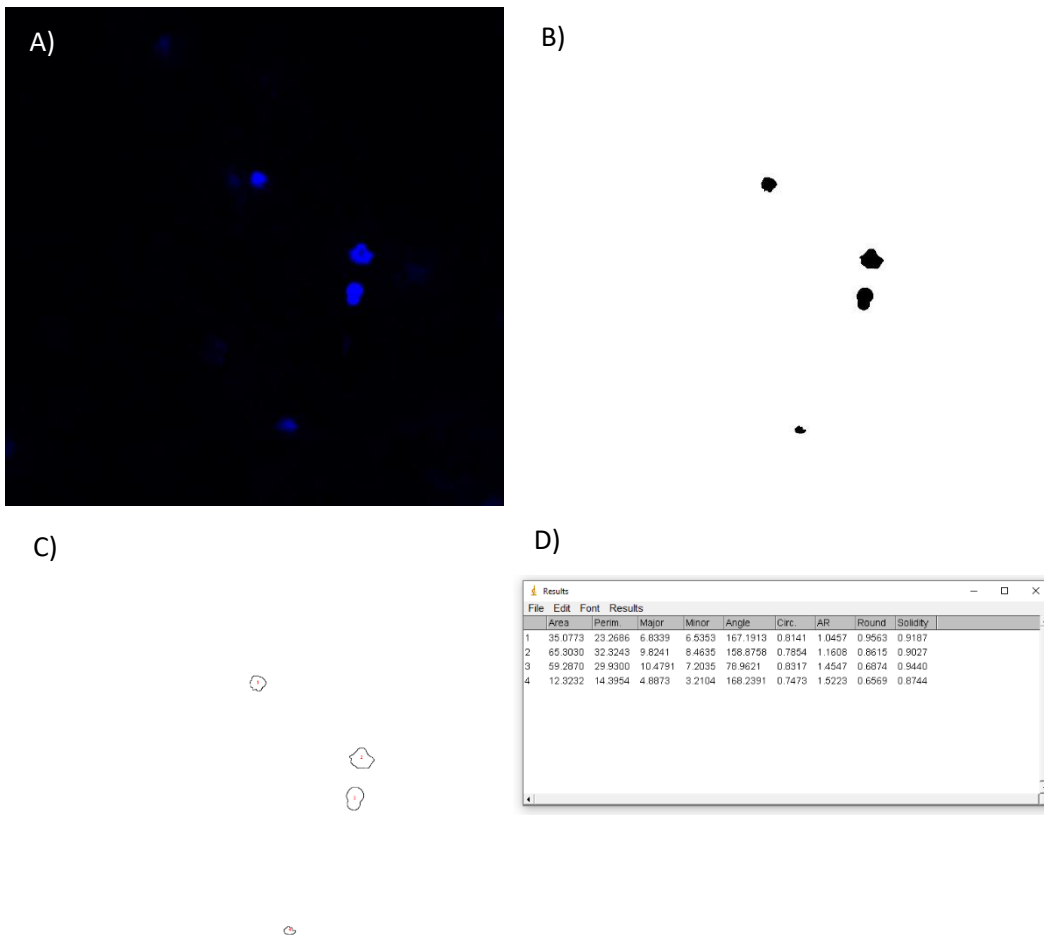

Figure 2.7 Cell count using ImageJ. A) Representative image of DAPI stain to quantify the cell number (dTHP-1 on dECM/fibrin membrane). B) Image output after threshold. C) Image output outlining the particles identified. D) Table output where can be seen the details of each particle found in the image, such as area

2.8 Statistical and data analysis

Raw data was handled using Microsoft Office Excel 365. The arranged data was then exported to GraphPad Prism version 8.4.3 (686) to generate graphs and statistical analyses (serial number: GP8-1621658-R).   The data was analyzed if at least $n = 3$ from independent biological replicates/cell passages was ensured. The data is presented as the mean ± standard error of the mean (SEM). The data was analyzed with ANOVA. Ordinary two-way ANOVA used Turkey´s multiple component test or Sidak's multiple component test. One-way ANOVA used Friedman Test and Dunn's multiple comparison test. The significance values were taken when $p < 0.05$, graphically denoted as *$p < 0.05$**, $p < 0.01$, ***$p < 0.001$. If the data in the graph does not contain an asterisk is because is not significant.

Chapter 3

Alveolar Region Biomaterial Formation
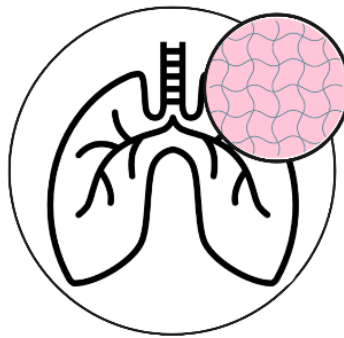
<u>3.1 Introduction</u>

The first data chapter of this PhD project presents the development of the biomaterial for the alveolar model. The rationale to create the scaffold started by looking at the *in vivo* extracellular matrix composition (ECM) where the alveolar epithelial cells can be found. The alveolar region is rich in collagen I, III and IV, as well as elastin, heparin sulfate and chondroitin sulfate, as detailed before in section 1.1.1.3.2 from the general introduction.

Then, it was considered the examples present already in the literature to find the knowledge gap. As already mentioned in the introduction, the most common animal used in toxicology is the mouse. But its limitation in translating human exposures, the serious ethical concerns, and the restriction of its use in a cosmetic application, promoted the development of the *in vitro* model field. In the development of *in vitro* lung models, the Transwells brought in a simple setup the possibility to introduce an air-liquid interface, which is a major promoter of fully differentiated epithelium and surfactant secretion[104]. However, cells culture in Transwells are attached to a PET porous membrane, if an extra surface coating step is not present. In this way, one of the aims of this project was to proportionate ALI to the alveolar model, but also a surface for cell attachment that was rich in molecules that were physiological relevant to the alveolar environment.

Taking into consideration the multi-component composition of the alveolar region ECM, as well as the currently published solutions, it would be difficult to find one biomaterial that could act as support and at the same time give a complete range of biochemical cues. On the other hand, it would be expensive to add each component and build the biomaterial from scratch. In this way, the strategy was to promote their secretion from the fibroblasts, the cells responsible for *in vivo* ECM deposition[105]. The biomaterial was created by first cultivating the human lung fibroblast and then recover the extracellular matrix that the cells secreted during the time in culture. A growing number of examples in the literature use this method to create biomaterials with an intrinsic rich composition, however, organs of animal origin are normally used. These strategies can be found to produce bioscaffolds[106,107,108] that later can be further reinforced with a crosslinker[109,110] or transformed into fibres by electrospinning[111,112]. This technology also allows to derive bioinks formulated for 3D bioprinting applications[113,114]. In addition, whole organ decellularization has been seen as a solution for bioengineering organ replacements, hence the growing field[115,116].

However, the aim of creating an *in vitro* model is to reduce animal use, which also includes animal derived products. In this way, this project explored the idea of deriving its own ECM but

from a cell sheet. The cell derived ECM (CDE) technology has gained high attention in recent years for being a pathogen free and less variable source of ECM when compared to human and animal tissue [117,118]. In this way, a biomaterial derived from the cells ECM can include a diverse range of biomolecules - collagens, GAGs and other proteins - similar to *in vivo* ECM composition. This, without relying on organ/tissues, which facilitates its implementation between labs. This technology has even the potential to be completely animal-free if efforts to remove FBS and other animal derived supplements are applied during cell handling and culture. In addition, a reduced number of resources are needed to implement CDE technology in the lab. However, this technology has also drawbacks, such as the long cell culture times needed for ECM secretion. In addition to the extensive characterization required to validate the decellularization and characterization of the remaining ECM. The removal of cell presence, especially its nucleic content, uses chemicals (acids or basis, detergents or enzymes) or physical methods (agitation, sonication or freeze-thaw cycles) that have the potential to disrupt the ECM architecture, composition and induce surface damage. In this way, a balance between DNA clearance with preservation of ECM integrity and its bioactivity needs to be met. This balance will dictate which decellularization methodology to select. To guide the process of decellularization Peter M. Crapo advances three requisites focusing on evaluating the extent of nucleic acid removal[119]:

- <50 ng dsDNA per mg dECM dry weight.

- <200 bp DNA fragment length.

- lack of visible nuclear material in tissue sections stained with DAPI or H&E.

The high attention to ensure nucleic acid removal is related to reducing adverse host reactions to the ECM derived biomaterials, especially when considering human applications[119]. However, these requirements were not reviewed for cell derived ECM technology or for non-clinical applications. But given the lack of guidelines in the literature, the ones above were considered.

After giving an overview of the CDE technology advantages and main obstacles, a series of how this technology has been reported in the literature is given. The most used strategy when using CDE technology is to grow the cells with the interested secretome in a substrate, which after decellularization is further reseeded with cells or implanted for regenerative medicine applications[117,118]. This substrate can be normal cell culture wear or scaffolds. Some examples where this technology was used in the literature can be found in the work of Xing, Q *et al* (2015). Human dermal fibroblast grown for 6 weeks under ascorbic acid on collagen coated PDMS, which after were decellularized with a range of SDS and seeded with PMA differentiated THP-1 to access inflammatory response[105]. Another example seeded L929 fibroblast in

polycaprolactone (PLC) electrospun scaffolds for 7 days, which after decellularization with 0.01% Triton were seeded with rat primary glomerulus endothelial cells to test cell expansion on PCL-ECM membrane[120]. One last example applied this technology to functionalize the porous membrane (cut from a Transwell) on an organ on a chip application. Fibroblasts grown for 6 days in the porous membrane were decellularized (0.1% SDS 0.1%) before HUVECs were seeded[121].

The CDE technology uses the substrate where the cells were initially cultured as a scaffold, but in this project, the decellularized cell sheet was further processed with pepsin to subsequently crosslink the collagen on the ECM. This approach is commonly used in tissue derived scaffolds or for bioinks as mentioned above. This is where it lays the novelty of the alveolar biomaterial presented in this chapter, which is to use the rationale from the cell derived ECM, but further process it to form a hydrogel.

To design the strategy to create a biomaterial from cell ECM that would be relevant to the alveolar niche, first was identified the cell type responsible to produce the extracellular matrix. Two cell types were identified with ECM secretion roles such as the endothelial cells and the fibroblast. The latter were the ones selected to experiment with to create the scaffold from decellularized cell sheet. Bear in mind that the decellularized derived scaffolds required extensive characterization, as mentioned above, to determine the level of cell removal and also to identify and quantify the diversity of molecules. This characterization can be found in this chapter.

In conclusion, this chapter includes the alveolar biomaterial derivation from a decellularized fibroblast cell sheet. A total of ten decellularization protocols were followed and the ECM product was characterized following the requirements presented above by Peter M. Crapo. In addition, the decellularized ECM was also characterized on collagen, protein and glycosaminoglycans content to complement the DNA characterization. In the literature, there are an extensive number of review papers on decellularization protocols[107,108,114,115,122–125], used throughout the work in this chapter to inform about decellularization chemical and physical methods used (and expected negative effects), available assays to characterize the ECM and methods on to crosslink the collagen present in the ECM.

3.2 Methods

To facilitate the reading, an overview of the chapter is illustrated on figure 3.1. The chapter is break into 5 different stages. Note that the of stage number and title associated is used throughout the chapter. The cell line selected to create the biomaterial was the human lung fibroblasts (HLF-1) that were cultured for 21 days, under ascorbic acid supplementation to promote extracellular matrix formation (stage 1). After the culture time, the cell sheet is decellularized, meaning the DNA content and other cellular constituents are removed using a combination of a physical method and chemical agents (stage 2). The decellularized extracellular matrix (dECM) was extensively characterized following the criteria mention before in the introduction by Peter M. Crapo article[119]: (1) <50 ng dsDNA per mg dECM dry weight, (2) <200 bp DNA fragment length and (3) lack of visible nuclear material in tissue sections stained with DAPI or H&E. To evaluate the extent of decellularization and damage to the ECM, DNA, collagen, glycosaminoglycans (GAGs) and protein content were quantified using qualitative and quantitative methods (stage 3). This gave rise to a troubleshooting section to understand the impact that the decellularization solutions have on the assays (stage 4). To finalize, the chapter contains the strategies undertaken to crosslink the dECM (stage 5).
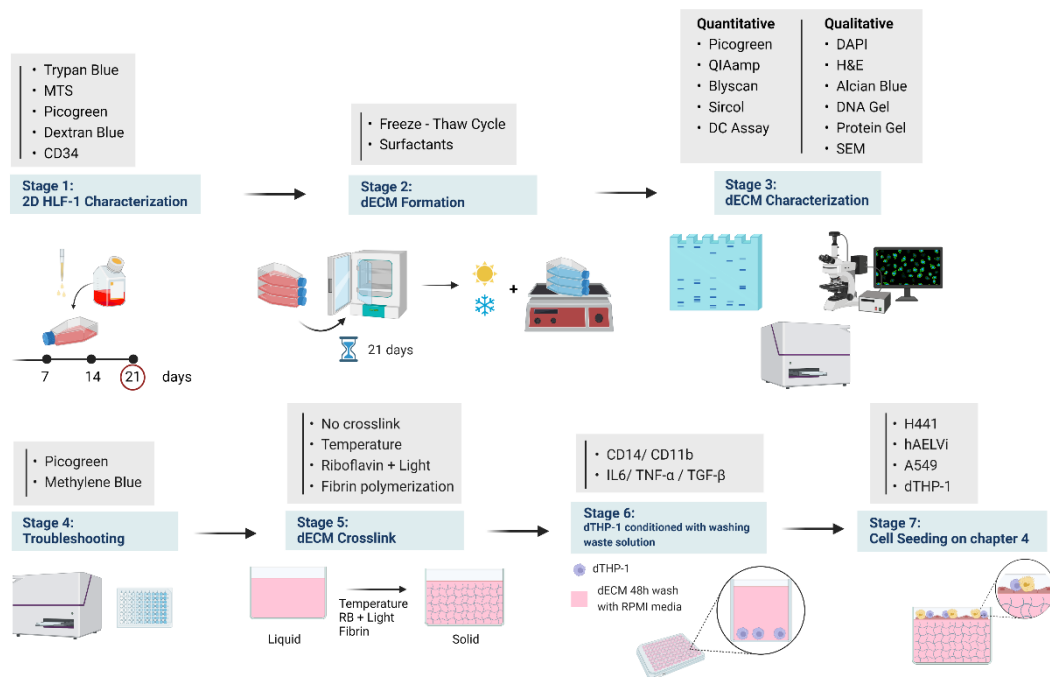
Figure 3.1: Overall chapter organization from stages 1 to 6. Stage 1 is characterized by the HLF-1 during 21 days for cell viability (trypan blue), metabolic activity (MTS), proliferation (Picogreen) and CD34 surface marker. In stage 2 are tested a range of mechanical and chemical treatments to decellularize the HLF-1 cell sheet grown for 21 days. In stage 3 the dECM is characterized with a list of quantitative and qualitative methods to determine DNA (Picogreen, QIAamp, DAPI, H&E and DNA gel), collagen (H&E and Sircol), protein (DC and protein gel) and glycosaminoglycans (Alcian blue and Blyscan) content. In stage 4 is determined the residual surfactant concentration and the impact of it on the picogreen assay. In stage 5 is experimented with different strategies

for dECM crosslink: temperature, riboflavin and light, fibrin polymerization or no crosslink. On stage 6 differentiated monocytes were exposed to the wasting solutions of the dECM to evaluate the potential negative impact that surfactant residues could have on this cells line. The last stage illustrated, number 7, represents the cell seeding, which is present in the scheme, but the results are in chapter 4. RB: riboflavin, dTPH-1: differentiated THP-1 (monocyte cell line), dECM: decellularized extracellular matrix. Created with BioRender.com.

3.2.1 Stage 1: 2D HLF-1 Characterization

The human lung fibroblasts were seeded at 5000 cells/cm^2 for the 2D characterization. The characterization lasted for 21 days. The time points analysed were from day 1 to 7 and then on days 14 and 21. The cells were cultured as detailed in section 2.3.1 The 2D HLF-1 characterization followed the protocols presented in the general methods section 2.4.

3.2.1.1. Trypan blue exclusion assay

The protocol followed is previously described in section 2.4.1.

3.2.1.2. CellTiter 96® AQueous One Solution Cell Proliferation Assay

The protocol followed is previously described in section 2.4.2.

3.2.1.3. Quant-iT™ PicoGreen™ dsDNA Assay Kit

The protocol followed is previously described in section 2.4.3.

3.2.1.4. Dextran Blue

The protocol followed is previously described in section 2.4.4.

3.2.1.5. Flow cytometry

The protocol followed is previously described in section 2.4.5. The HLF-1 were screen in the flow cytometry machine against surface marker CD34 (PE/Cyanine7 anti-human CD34). The total of 1x10^5 viable cells were diluted in 1 mL of PBS with 5 µL of the CD34.

3.2.1.6 Bright field microscopy

The protocol followed is previously described in section 2.4.6.

3.2.1.7. Confocal laser scanning microscopy

The protocol followed is previously described in section 2.4.7. The HLF-1 cells were stained with DAPI and Phalloidin. To commence the stain, the cells were permeabilized with a 0.2% Triton solution in PBS for 15min at room temperature. After washing 3x with PBS, cells were blocked with blocking buffer, 1% BSA in PBS, during 1 hour at room temperature. After the blocking period, the cells were washed 3x with PBS followed by the addiction of the Phalloidin solution (1:200 dilution in blocking buffer). The Phalloidin was added for 1 hour at room temperature, protected from light. After washing 5x with PBS to remove the phalloidin residues a DAPI solution with 1 µg/mL was added. The DAPI incubation lasted for 15min at room temperature in the dark. After washing 5x with PBS the coverslip was mounted. The coverslip was mounted to the glass slice as detailed in protocol 2.4.7 from general methods. The DAPI was excited with a 405nm laser and detected from 410-481 nm range. The Phalloidin was excited with a 633nm laser and the emission signal was captured from 638-759 nm range.

3.2.2 Stage 2: dECM formation

The HLF-1 were seeded at 5000 cells/cm^2 and cultured as detailed in section 2.3.1 during 21 days, with media change every two days. On the 9th day of culture, cells were supplemented with ascorbic acid at 500 µM (0.088 mg/mL). The ascorbic acid stock solution was prepared by dissolving 44 mg of ascorbic acid powder into 20 mL of deionized water. The solution was then syringe filter with a 0.22 µm porous size before being added to the fresh media. During media change, cells were PBS washed once before adding fresh media with ascorbic acid if applicable. On the 21st day of culture, the HLF-1 cells were decellularized. For this step, ten different conditions were applied, which were a combination of freeze and thaw (F-T), as physical method, an osmotic solution, with high content of sodium chloride (NaCl), a sodium dodecyl sulfate solution (SDS), that is an anionic surfactant and Triton X-100 (Triton) which is a non-ionic surfactant. These methods have the objective to disrupt cell membranes and consequently remove DNA. In table 3.1 can be found the composition of the four different solutions applied and in table 3.2 an outline of conditions 1 to 10.

To initiate the decellularization the flask was removed from the incubator (humidified 37°C, 18% oxygen and 5% CO$_2$) and placed in the hood. The wasted media was removed and was added PBS to wash. Afterwards, the specific protocol for each condition was followed. In addition, for all the conditions, between treatments, one PBS wash (1 minute no shaking) was applied and at

the end of all the treatments three PBS washes (1 minute no shaking). At this point, the content of the flask, the decellularized extracellular matrix (dECM), was scraped into eppendorfs and kept at -80°C until further use.

One last methodology aspect to consider is the volumes used throughout the process. The volume of media in the flask during HLF-1 culture, the decellularization solution volume and the amount of PBS used in the washes were always the same. For the T25 this volume was 5 mL, for the T75 was 12 mL and for the T175 was 25 mL.

Table 3.1: Decellularization solutions recipe. EDTA: Ethylenediamine tetraacetic acid, Tis: tris(hydroxymethyl)aminomethane, NH_4OH: Ammonium hydroxide.

Solution	Composition	Solvent
Osmotic solution	1 M NaCl 10 mM Tris 5 mM EDTA	Water
0.5% SDS solution	0.5 % SDS 10 mM Tris 25 mM EDTA	Water
0.05% SDS solution	0.05 % SDS 10 mM Tris 25 mM EDTA	Water
Triton 0.05%	0.05 % triton 20 mM of NH_4OH	Water
Triton 0.5%	0.5% triton 20 mM of NH_4OH	Water

Table 3.2: Overview of decellularization conditions from 1 to 10.

Decellularization Conditions	Protocol
Condition 1: Fresh	No decellularization procedure was applied. Cells were washed 3 times with PBS, scraped and stored at -80°C.
Condition 2 Freeze + Thaw	3 cycles freeze and thaw: - 30 minutes at -80°C freezer - 30 minutes at 37°C oven
Condition 3 Freeze + Thaw + 0.05%SDS	1. 3 cycles freeze and thaw 2. Osmotic solution for 1 hour at 50 rpm 3. 0.05% SDS solution for 30 min at 50 rpm
Condition 4 Freeze + Thaw + 0.5%SDS	1. 3 cycles freeze and thaw 2. Osmotic solution for 1 hour at 50 rpm 3. 0.5% SDS solution for 30 min at 50 rpm
Condition 5 Triton 0.05% (1X)	0.05% Triton solution for 3 minutes at 0 rpm
Condition 6 Triton 0.5% (1X)	0.5% Triton solution for 3 minutes at 0 rpm
Condition 7 Triton 0.05% (3X)	3 times of 0.05% Triton solution for 3 minutes at 0 rpm
Condition 8 Triton 0.5% (3X)	3 times of 0.5% Triton solution for 3 minutes at 0 rpm
Condition 9 Freeze +Thaw + 0.05%SDS + Triton 0.05%	1. 3 cycles freeze and thaw 2. Osmotic solution for 1 hour at 50 rpm 3. 0.05% SDS solution for 30 min at 50 rpm 4. 0.05% Triton solution for 3min at 0 rpm
Condition 10 Freeze +Thaw + 0.05%SDS + Triton 0.5% (3X)	1. 3 cycles freeze and thaw 2. Osmotic solution for 1 hour at 50 rpm 3. 0.05% SDS solution for 30 min at 50 rpm 4. 3 times of 0.5% Triton solution for 3 min at 0 rpm

3.2.3 Stage 3: dECM Characterization

The decellularized extracellular matrix was extensively characterized to determine the content of DNA, collagen, protein and glycosaminoglycans. A combination of quantitative and qualitative methods was performed for that end. To generate the dECM was followed the protocol detailed above, in section 3.2.2. The cells were grown in a T25 and ascorbic acid supplementation included 200 µL of the ascorbic acid stock solution (500µM) in 5 mL of DMEM complete media. Prior to characterization, the dECM required some processing such as freeze-drying, weight and digestion with papain solution. Figure 3.2 illustrates the steps from cell seeding until characterization.

Figure 3.2: Sequence of the tasks from HLF-1 seeding until characterization. Created with BioRender.com

3.2.3.1 dECM processing

3.2.3.1.1. Freeze-dry

The eppendorfs were removed from the -80°C freezer and allowed to be defrosted before centrifuging at 581 *g* for three minutes. The supernatant was removed without disturbing the dECM pellet. Then, was inserted in the eppendorf aperture a cotton bud. The lid was left open, and the vial wrapped in paraffin. Then, eppendorfs were transferred to the freeze-dyer machine (Scanvac CoolSafe Freeze-dryer). The instrument operates at -110°C and is connected to a vacuum pump, drying the dECM at low temperature and under vacuum. The paraffin was removed, and the machine started. The drying process lasted until no liquid was visible, normally from 3 to 6 hours. Afterwards, the dry dECM was weight or stored at -80°C until further use.

3.2.3.1.2 Weight

The dried dECM was allowed to equilibrate to room temperature before being weight using a scale (Sartorius Research R180 D). For that, new eppendorfs were labelled and weight. Then, in the tissue culture hood, the dried dECM were transferred to the new eppendorfs for being weight. Afterwards, the weight of the dECM was determined by minus the weight of the empty eppendorf from the full one. The dECM weight was recorded for data analysis normalization. The dECM was stored at -80°C until further use.

3.2.3.1.3 Papain digestion

The papain digestion is a cysteine protease with an optimal temperature activity at 65°C[126]. Alternative buffers were used to lyse the dECM, such as TE, RIPA and CHAPS detergent, however none of the buffers listed were able to digest the dECM. To commence the dECM papain digestion, the eppendorfs were brought to room temperature to thaw. Then, to each vial was added 450 µL of papain digestion solution (0.3 mg/mL papain digestion, 2 mM DTT, 20 mM NaAc and 1mM EDTA). The eppendorfs were placed in a heat block at 60°C for 15 minutes. A total of 3-5 cycles was done to completely dissolve the dried dECM, with a vortex between cycles.

3.2.3.2 dECM Characterization: Quantitative Methods

The qualitative characterization of dECM started after ensuring complete dECM digestion. The qualitative methods can be separated into two types, depending on the digestion method. The dsDNA, collagen, GAGs and protein quantification methods present from sections 3.2.3.2.1 to 3.2.3.2.4 required papain digestion. For these methods, the dECM was freeze-dried, weight and digested with papain as described in section 3.2.3.1. The total volume of 450 µL of papain digestion dECM was directed to each assay: 100 µL for dsDNA, 100 µL for collagen, 200 µL for GAGs and 5 µL for the protein quantification. On the other hand, the total nucleotide quantification from section 3.2.3.2.5 used proteinase K supplied by the kit for dECM digestion. For this method, the dECM was freeze-dried and weight but then was digested and assayed as manual instructions.

3.2.3.2.1 dsDNA Quantification

The dsDNA was quantified using the Quant-iT™ PicoGreen™ dsDNA Assay Kit. The protocol followed was the same as in section 2.4.3, however, instead of TE buffer to lyse the cells and dilute the DNA standard, the samples were processed with papain digestion as mentioned above in section 3.2.3.1.3 and DNA standards were diluted in papain digestion as well. For data analysis the ng of DNA was multiplied by a dilution factor to consider the dilution performed when a sample of 100 µL of digested dECM was removed from 450 µL, that is 4.5. Plus, the dilution of the assay, which is 2. In addition, the ng of DNA was further divided per dry dECM weight to accurately compare within and between decellularization conditions.

3.2.3.2.2 Collagen Quantification

The collagen content from the dECM was determined using the Sircol Insoluble collagen assay. The Sircol assay is a colorimetry collagen quantification assay. The Sircol Dye binds to the tripeptide sequence Glycine -X-Y present in collagen I,II,III,V and XI. After papain digestion, the dECM lysates were processed as manufacture guidelines. Very briefly, 1 mL of Sircol dye reagent was added to 100 µL of papain digested decellularized ECM. The reaction was left to occur for 30 minutes in a shaker, followed by a centrifugation step at 8050 *g* for 10 minutes. Next, the tubes were inverted over paper and 300 µL of acid-salt wash was added to remove unbonded dye from the pellet surface and walls. Afterwards, tubes were again centrifuged at 8050 *g* for 10 minutes. Then, the supernatant was carefully drained, to avoid pellet loss, and the tube walls and lid were clean with a cotton bud. Finally, was added 500 µL of Alkali Reagent, the tubes were vortexed until the entire pellet was dissolved, and absorbance was measured at 550 nm using a plate reader (POLARstar, BMG LABTECH).

For data analysis, first the absorbance was multiplied by 2.2 factor as manufacture instruction. Then, the data was analysed through a calibration curve, y=mx+b, where x corresponds to the µg of collagen and y to the absorbance. Representation of the calibration curve can be seen in figure 3.3 and table 3.3 contains the volumes used to make the standards. The µg of collagen was multiplied by a dilution factor to consider the dilution performed when a sample of 100 µL of papain digested dECM was removed from 450 µL, which is 4.5. In addition, the µg of collagen value was further divided by the dried dECM weight to accurately compare within and between decellularization conditions.

Table 3.3: Collagen standard curve.

Standard Mass (µg)	Collagen Standard (1mg/ml) Volume (µL)	Papain Digestion Volume (µL)
0	0	100
5	5	95
10	10	90
15	15	85
20	20	80
30	30	70
40	40	60

Figure 3.3: Collagen calibration curve plot. The plot represents the optical density at 555 nm (O.D.) in function of µg of collagen. The linear regression that fits the data is y= 0.0079x – 0.1063. (n=1)

3.2.3.2.3 Glycosaminoglycan Quantification

The glycosaminoglycans (GAGs) content was determined using the Blyscan™ Glycosaminoglycan Assay. The kit is a colorimetric GAGs quantification assay. After papain digestion, the dECM lysates were processed as instructed in the manual. Very briefly, 1 mL of Blyscan dye reagent was added to 100 µL of papain digested decellularized ECM. The reaction was left to occur for 30 minutes in a shaker, followed by a centrifugation step at 8050 *g* for 10 minutes. Next, the tubes were inverted over paper, 500 µL of dissociation agent was added, followed by vortex to dissolve the pellet. Next, tubes were centrifuged again at 8050 *g* for 5 minutes and absorbance was read at 656 nm using a plate reader (POLARstar Omega, BMG LABTECH).

The previous protocol determines the total number of GAGs in a sample, however, to determine the amount of N-sulfated and O-sulfated GAGs, the samples are exposed to Nitrous acid treatment. Regarding the GAGs present in the alveolar, an example of N-sulfated is heparin and O-sulfated is chondroitin sulfate. The nitrous acid reacts with N-sulfated GAGs converting them into O-sulfated. The total GAGs content minus the acid treatment, O-sulfated, corresponds to the N-sulfated GAGs.

To measure the N-sulfated glycosaminoglycans the manual instructs a series of reactions before starting the protocol detailed before. To 100 µL of papain digested dECM or GAGs standards was added 100 µL of sodium nitrite followed by 100 µL of acetic acid. The mixture was vortex and incubated for 60 minutes with occasional mixing. Then, was added to each vial 100 µL of

ammonium sulphamate and mixed for 10 minutes. From the final volume of 400 μL was sampled 100 μL to follow the protocol detail above.

The data was analysed through a calibration curve, y=mx+b, where x corresponds to the μg of GAGs and y to the absorbance. Representation of the calibration curve can be seen in figure 3.4 and table 3.4 contains the volumes used to make the standards. For data analysis the μg of GAGs was multiplied by a dilution factor to consider the dilution performed when a sample of 100 μL of papain digested decellularized ECM was removed from 450 μL, which is 4.5. The N-sulfated glycosaminoglycans were 4 times diluted compared to the total GAGs, so the final concentration was multiplied by a dilution factor of 4. In addition, the μg of GAGs value was further divided per dried dECM weight to accurately compare within and between decellularization conditions.

Table 3.4: GAGs standard curve.

Standard Mass (μg)	GAGs Standard (100μg/mL) Volume (μL)	Papain Digestion Volume (μL)
0	0	100
1	10	90
2	20	8'
3	30	70
4	40	60
5	50	50
6	60	40

Figure 3.4: GAGs calibration curve plot. Graph on the left hand side represents the optical density at 656 nm (O.D.) in function of μg of O-sulfated GAGs. The linear regression that fits the data is y= 0.1743x − 0.018. Graph on the right hand side represents the optical density at 656 nm (O.D.) in function of μg of GAGs. The linear regression that fits the data is y= 0.1762x − 0.0167. (n=1).

3.2.3.2.4 Protein Quantification

The protein was quantified using the DC assay, which is a colorimetry-based method to quantify the protein content. After papain digestion, the dECM lysates were processed as in the instruction manual. But very briefly, 5 μL of the papain digested decellularized ECM was pipetted into a 96 well plate, followed by 25 μL of reagent A' (20 μL of reagent S into 1 mL of reagent A) and 200 μL of reagent B. The plate was then incubated for 15 minutes on a shaker for the reaction to occur. Finally, the plate absorbance was read at 750 nm on a plate reader (POLARstar Omega, BMG LABTECH).

The data was analysed through a calibration curve, $y=mx+b$, where x corresponds to the ug of protein and y to the absorbance. Representation of the calibration curve can be seen in figure 3.5 and table 3.5 contains the volumes used to make the standards. For data analysis, the μg of protein was multiplied by a dilution factor to consider the dilution performed when a sample of 5 μL of papain digested decellularized ECM was removed from 450 μL, which is 90. In addition, the μg of protein was further divided per dried dECM weight to accurately compare within and between decellularization conditions.

Table 3.5: Protein standard curve.

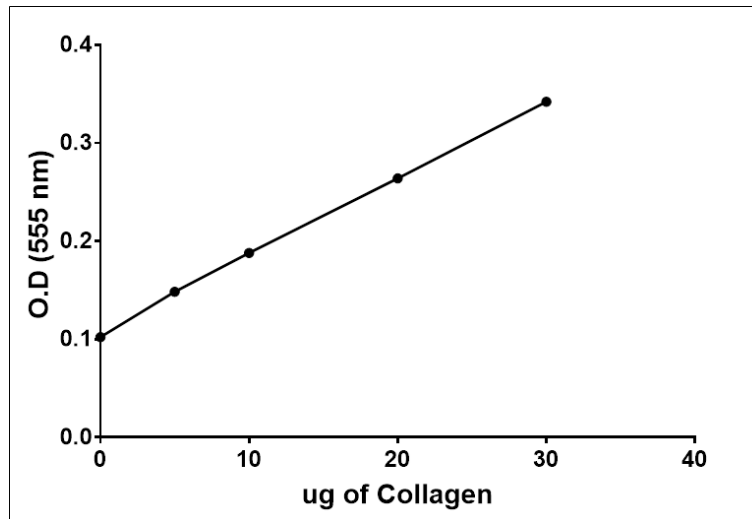| Standard Mass (μg)	Protein Standard (2.5 mg/mL) Volume (μL)	Papain Digestion Volume (μL)
0	0	5
2.5	1	4
5	2	3
7.5	3	2
10	4	1
12.5	5	0

Figure 3.5: Protein calibration curve plot. The plot represents optical density at 750 nm (O.D.) in function of µg of Protein. The linear regression that fits the data is y= 0.0147x + 0.0657. (n=1).

3.2.3.2.5 Total Nucleotide Quantification

The total nucleotide content of the decellularized ECM was determined using a nanodrop (Nanodrop ND-1000) after DNA extraction and purification using the DNA Blood Mini Kit. The protocol followed from the manual was the DNA Purification from Tissues and started with digesting the dried dECM with proteinase K (180 µL of ATL buffer and 20 µL of proteinase K) and incubating overnight at 56°C in a heat block. After complete digestion, the tubes were short centrifuged, before 200 µL of AL buffer was added to each tube. The reaction was allowed to develop for 10 minutes at 70°C in a heat block. After a short centrifugation step was added 200 µL of ethanol to each vial. The solution was homogenized through pulse-vortex for 15 seconds. Then, all the content of the vial was added to the QIAamp Mini spin column followed by centrifugation at 8050 *g* for 1 minute. It was discarded the tube containing the filtrate and added 500 µL of Buffer AW1. After centrifugation at 8050g for 1 minute, the filtrate was discarded again and added 500 µL of Buffer AW2. Next, it was added to the column 200 µL of the Buffer AE. The last centrifugation was performed at 8050g for 1 minute. Afterwards, the purified DNA content from QIAamp DNA Blood Mini Kit was quantified using the NanoDrop ND-1000. The nuclei acid protocol was selected in NanoDrop and samples were blanked with Buffer AE.

3.2.3.3 dECM Characterization: Qualitative Methods

3.2.3.3.1 Agarose DNA Gels

The purified DNA content from QIAamp DNA Blood Mini Kit (section 3.2.3.2.5) was run in a 1% agarose gel to visually assess the length of the DNA fragments. The protocol used was the following, first was reinforced the tray with autoclave tape (4 layers of autoclave tap otherwise gel will spill) and added the comb. Then, was prepared the agarose solution by dissolving 1% of agarose in TAE Buffer (1 mM EDTA, 40 mM Tris, 20 mM acetic acid). It was used a microwave to melt the solution, three cycles of 1.5 minutes at 450 W were applied. With the agarose still hot was added 1:10000 dilution of sybr safe and the liquid agarose solution was poured into the tray to solidify (protect it from light). In the meantime, the samples were prepared, 5 µL of loading dye (Loading Dye, Blue (6X)) was added per 20 µL of sample and kept on ice until loaded into the gel. When the agarose gel was solidified, the autoclave tape and comb were removed and the gel was placed in the horizontal electrophoresis system from Bio-Rad. Before adding the samples, it was added TAE buffer until the wells were fully covered. Two DNA ladders were used 10 µL per well: Quick-Load® Purple 1 kb DNA Ladder and Quick-Load® Purple 100 bp DNA Ladder. The lid of the system was closed and ensured that the gel was oriented from the negative pole to the positive. The gel was run at 120 V until the ladder reached the end of the gel. The gel was visualized in a ChemiDoc MP Imaging System from Bio-Rad using the sybr safe protocol (excitation peak at 280 nm and 502 nm, and emission at 530 nm).

3.2.3.3.2 DAPI Stain

The presence of DNA content was also evaluated by staining the decellularized ECM with DAPI. The cells were cultured in the same conditions as explained in 3.2.2. The cells were plated in 12 well plates and for ascorbic acid supplementation, 40 µL were added to 1 mL of media. At the end of the decellularization protocols, the dECM was fixed with 4% paraformaldehyde solution for 15 minutes at room temperature. Then, washed three times with PBS before storing at 4°C in 0.1 M of glycine until further use. On the day of the stain, plates were removed from the cold room, washed once with PBS to remove the glycine and stained with 1 µg/mL DAPI solution for 30 minutes at room temperature in the dark. The images were obtained on a Zeiss LSM 710 using a 405 nm excitation laser. A total of at least 3 biological replicas were imaged, with 4 technical repeats each. The technical repeats were images in 5 different fields of view.

3.2.3.3.3 H&E Stain

The presence of DNA and extracellular matrix was assessed by Hematoxylin and Eosin Y respectively. Hematoxylin coupled with aluminum ions is a cationic dye with the capacity to link to negative charges, such as from the nucleus. On the other hand, Eosin Y is a negative charge dye with affinity to positive charges present in the cytoplasm and extracellular matrix proteins with arginine, lysine and histidine amino acids. The protocol used for the H&E stain was the same followed for DAPI of section 3.2.3.3.2 until the storage at 4°C. To start the H&E stain, the plates were placed at room temperature and the glycine was removed with one PBS wash. Then, the hematoxylin solution was added for 6 minutes. After incubation time the wells were rinsed with water until all unspecific binding was washed away and the water was clear. Then, 1% Eosin Y solution in ethanol, was added for 2 minutes to each well of the plate. When incubation time was finished, the wells were washed until all unspecific binding is washed away and the water was clear. Afterwards, the wells were rinsed three times with 100% ethanol before being imaged on an Olympus BX51 microscope (software used was cellsens). A total of at least 3 biological replicas were imaged, with 4 technical repeats each. The technical repeats were images in 5 different fields of view.

3.2.3.3.4 Alcian Blue

Alcian blue is a cationic dye, that forms an insoluble complex with acidic glycosaminoglycans[127]. The presence of the GAGs is then visualized by bright field microscopy. Until the storage at 4°C, the same protocol was followed as described in section 3.2.3.3.2 for DAPI stain. Then, to start the alcian stain, the plates were placed at room temperature and wash once with PBS to remove the glycine. Then, the plates were incubated for 3 minutes with 3% acetic acid. Afterwards, a 1% alcian blue solution in 3% acetic acid was added for 30 minutes to each well. After incubation time, the wells were rinsed with water until all unspecific binding was washed and the water was clear. The wells were left in water until imaging to avoid drying. The wells were imaged on an Olympus BX51 microscope (software used was cellsens). A total of 4 biological replicas were imaged, with 4 technical repeats each. The technical repeats were images in 5 different fields of view.

3.2.3.3.5 SDS PAGE Protein Gel

The SDS PAGE gel is an electrophoresis technique that uses a polyacrylamide gel to separate denatured proteins by their molecular weight under an applied voltage. This technique was used to visually access the protein content of the dECM.

Sample preparation: Prior to running the dECM samples in the gel, they were digested and denatured. The protocol started with drying and weighting the dECM as described in sections 3.2.3.1.1 and 3.2.3.1.2 respectively. Then, the samples were digested with pepsin using the following recipe: 330 mg dried dECM, 10 mL of 0.5M acetic acid and 33 mg pepsin making a solution with 33 mg/mL of dECM. Note that if different mg of dECM was weight, the acetic acid volume and pepsin amount were adjusted. The dECM on pepsin solution was placed in an ultrasound water bath for 15 minutes. Then, a short centrifugation step was done to bring all the content of the tube to the bottom, before stirring for 23 hours. On the following day, the pepsin digested dECM was again placed in an ultrasound water bath for 15 minutes, centrifuged and stirred for another hour. At this moment, the pH of the pepsin digested dECM was adjusted to 7 with NaOH and the solution diluted from 33 mg/mL to 20 mg/mL with PBS. After sample digestion, the proteins were denatured with Laemmli buffer, 5 µL of digested dECM (corresponding to 100 µg of dECM) was added to 5 µL of 2x Laemmli buffer. The samples were boiled for 5 minutes using the T100 Thermal Cycler from Bio-Rad. The samples were short centrifuged and left to cool before being loaded into the gel. At this point, the samples can be stored at -20 °C.

Gel cast and recipe: Prior to gel formulation all the plastic and glass were clean with ethanol. Then, the gel cassette was assembled on the casting frames and vertically positioned on the casting stands. After ensuring that the apparatus is not leaking it was added the 7.5% resolving gel prepared as detailed in table 3.6. To seal the gel, it was added isopropanol on top. The polymerization was allowed for 40 minutes. Afterwards, the isopropanol was extensively washed away with water, before adding the staking gel, which recipe is described in table 3.6. The comb was added, and the gel was allowed to polymerize for 30 minutes. With complete polymerization, the frame was removed from the casting stand and the gel cassette disassembled from the frame. At this moment, the gel was either used or stored at 4°C in a humidified environment.

Table 3.6: Resolving and staking gel recipe to make a total of one gel.

	Resolving Gel (7.5%)	Staking Gel
Water	5 mL	1.75 mL
Separating or Resolving Buffer 4X Solution	2.5 mL	
Stacking Buffer 4X Solution	-	750 µL
30% Acrylamide	2.5 mL	500 µL
10% APS	100 µL	50 µL
TEMED	100 µL	3 µL

Electrophoresis: First, if stored, the gels were removed from the cold room. The comb was carefully removed to avoid damaging the wells and the gels were placed in the electrophoresis cell. It was always run 2 gels per electrophoresis cell. Then, the electrode reservoir was filled with running buffer Tris/glycine/SDS (10x recipe consisting of 250mM Tris, 1.92 M glycine, 1% SDS ph=8.3), before loading the samples, 5 µL of the ladder and 10 µL of dECM. The electrophoresis cell was connected to the power supply and gels were run at 120V for 60 minutes. The run lasted until the ladder reach the end of the gel.

Gel stain: After the gel run had finished, the gels were removed from the cassettes by popping the glasses. The area of the gels with the wells was removed, and the gel was placed in water. The gels were extensively washed in water, three cycles of 15 minutes in a shaker were done to remove SDS content. Then a solution of 1x Coomassie Brilliant Blue R-250 dye dissolved in destain solution was added for 2 hours under agitation. The 10xCoomassie solution contains 3 g/L of Coomassie dye in 45% methanol, 10% glacial acetic acid and 45% water. The destain solution is made of 10% methanol and 7% acetic acid in water.

Gel destain: After 2 hours with staining solution, the gels were washed with water and the Coomassie dye was removed with the destain solution described above. The destain took 24 hours under shaking conditions. To improve the Coomassie clearance from the gel, it was added absorbent paper (Kimwipes) in the tray where destain was taking place.

Gel imaging: The gels were imaged using the Molecular Imager ChemiDic XRS+ from Bio-Rad using the Trans White option.

3.2.3.3.6 Scanning electron microscopy

The dried dECM from section 3.2.3.1.1 was coated with a 2 nm chromium layer (Quorum Technologies Q150TE Coater) before being imaged on the Hitachi S-4800 Scanning Electron Microscope.

3.2.4 Stage 4: Troubleshooting

3.2.4.1 Digestion vs Quantification Method

To address the effect of the digestion process, papain digestion or protease K, on picogreen and nanodrop DNA quantification, it was digested a set of dECM samples with papain digestion and others with protease K. The ones digested with papain were analyzed in three different ways, 100 μL with the picogreen kit straight after papain digestion as recommends the protocol (referred as Papain + Picogreen). The rest of the 200 μL were clean with the QIAamp kit to obtain a pure nucleotide sample. The latter was analyzed with picogreen (referred as Papain + QIAamp + Picogreen) or nanodrop (mention as Papain + QIAamp + Nanodrop). The dECM digested with protease K were as the kit instructed, clean with QIAamp kit and then the DNA was quantified using nanodrop (mentioned as Protease K + QIAamp + Nanodrop) or picogreen (referred to as Protease K + QIAamp + Picogreen). After dECM digestion, the picogreen and the QIAamp assays follow the same protocol as in 3.2.3.2.1 and 3.2.3.2.5 respectively.

3.2.4.2 SDS and Triton effect on Picogreen dsDNA Measurements

To evaluate the effect of SDS and Triton residues on the dsDNA quantification using picogreen kit, it was diluted 100, 10, 1 and 0.1 ng of dsDNA standard in the SDS and triton solutions use during the decellularization protocol. The protocol followed was the same as in 3.2.3.2.1. For data analysis, for each condition, the zero was subtracted and divided by the calibration curve in papain digestion. The same experimental design was done but using the last PBS wash of the decellularization process to dilute 100, 10, 1 and 0.1 ng of dsDNA.

3.2.4.3 DMEM wash of dECM

The dried dECM was placed in a shaker for 48h with 500 μL of DMEM. After 24 hours the content of the vial was short centrifuged, the media was removed and was added fresh 500 μL of DMEM media for 24 hours. Then, dECM were short centrifuged again and added 300 μL of papain digestion overnight (>15 hours) at 50 °C. Afterwards, DNA and protein were quantified as described in 3.2.3.2.1 and 3.2.3.2.4 respectively.

3.2.4.4 SDS Quantification using Methylene Blue Assay

To quantify the presence of sodium dodecyl sulfate (SDS) in the dECM, it was used the methylene blue assay. The assay is a colorimetric method to detect the presence of anionic detergents, such as SDS, which binds to the methylene blue. This complex is then extracted using chloroform[128]. The concentration of SDS is then quantified by measuring the absorbance of the methylene blue complex in the chloroform phase (figure 3.6).

The protocol to determine the SDS content started by diluting the methylene blue solution (From Kiwk-Diff Kit, Solution 3) four times in water. Then, 1 µL of the sample was added to 99 µL of the diluted methylene blue solution. The vials were vortex three times for five seconds before adding 200 µL of chloroform (the chloroform step was done in a fume hood). The vials were vortex again three times for five seconds to mix both phases. Next, short centrifugation was applied to bring all the liquid droplets to the bottom. The vials were then incubated at room temperature for 30 minutes for complete phase separation. Then, was removed 100 µL from the bottom phase (chloroform phase) into a half area 96 well plate. The absorbance was measured at 650 nm using a plate reader[129] (POLARstar, BMG LABTECH). The data was analysed through a calibration curve, y=mx+b, where y corresponds to the absorbance and x to the %SDS.
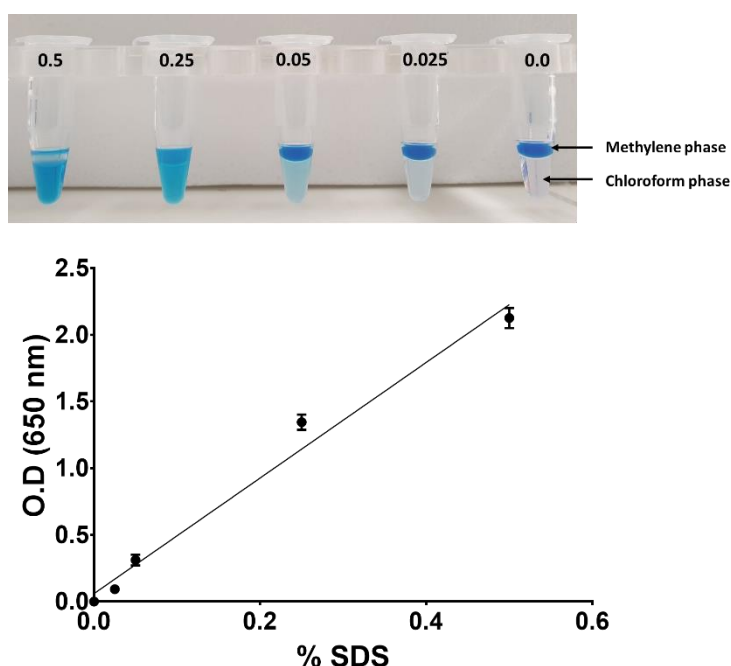
Figure 3.6: Methylene blue phase separation images and calibration curve. The top image represents the phase separation between methylene blue and chloroform between 0.5% to 0% of SDS. The methylene phase is the one on top and the chloroform is the bottom one. The plot at the bottom, represents optical density at 650 nm (O.D.) in function of the SDS percentage. The calibration curve is linear in the range of SDS presented, from zero to 0.5% SDS. The linear regression that fits the data is y=4.3326 + 0.0566 (n=10).

3.2.5 Stage 5: dECM Crosslink

The HLF-1 were seeded at 5000 cell/cm^3 in a T175 for the dECM formation. The same protocol as in section 3.2.2 was followed, but only condition number 10 was applied for the decellularization of the cell sheet. For ascorbic acid supplementation, 1 mL was added of the ascorbic acid stock solution into 25 mL of DMEM complete media during media changes. To create a flat dECM scaffold it was introduced in a 24 well plate a PDMS ring with 10 mm in diameter. This created a mould which the dECM was pipetted into. The mould was then topped up with two PDMS disks to seal the well. This setup is depicted in figure 3.7 and prevents the dECM to move upward in the well during freeze-drying. At the same time, creates a dry and flat dECM scaffold with 10 mm in diameter.

| * | PDMS ring | ** | PDMS ring + dECM |
| *** | PDMS disk | **** | PDMS disk 2 |
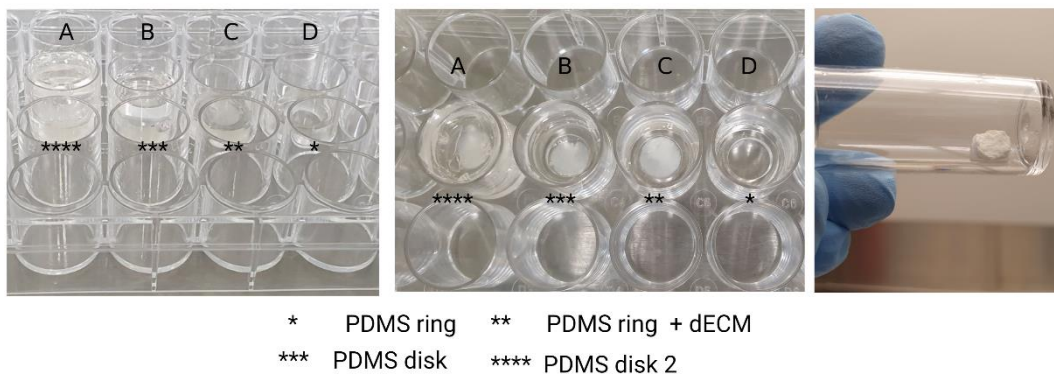
Figure 3.7: Freeze-dry setup. The left and middle images represent the freeze-dry setup in the 24 well plate side a top view respectively. The image on the right hand side represents the dry dECM scaffold. Created with BioRender.com

After assembling the 24 well plate, it was moved to the -80°C freezer before placing it in the freeze-dry machine. The plate was in the freeze-dry for one hour, before moving it again in the -80°C freezer for 30 minutes. Then, the plate was placed one last time in the freeze-dry between 1.5 to 2 hours. Once the freeze-dry cycle was finished the plate was stored at -80°C until further use. The image on the far right in figure 3.7 represents a flat dECM scaffold dried in the 24 well plate apparatus.

At this point, different crosslink strategies were undertaken, with the objective to make the scaffold suitable to support cell growth.

1. No Crosslink - Cells seeded on the dECM scaffold

2. Temperature Crosslink

3. Riboflavin Crosslink

4. Fibrin Polymerization

For point one, where no crosslink was applied, after the freeze-drying step in the 24 well plate, the scaffold was weight, as a control procedure, and then washed. This washing step involved the submerging of the scaffold in PBS or specific cell media during 48 hours, with media renewal after 24 hours. After the washing step, the scaffold was ready to be seeded with cells. This strategy is referred to no crosslink throughout the thesis and for results with cells refer to chapter 4.

The crosslink strategies that come after, from points 2 to 4, involve digestion of the dECM with the protease pepsin under an acidic environment. The action of this enzyme cleaves the telopeptide regions of collagen making it soluble [130,114]. Then, the adjustment of pH and temperature makes the collagen crosslink again. The mixing of riboflavin, a crosslink reagent, increases the number of new collagen bonds. These two strategies described, are points 2 and 3. The last approach, point 4, used fibrinogen and thrombin mixed with the neutralized pepsin digested dECM (neutralized dECM). In this approach, the polymerization of fibrin incorporates in its network the dECM (refer to chapter 5 for extensive fibrin characterization and use during vasculature model formation). The fibrin polymerization strategy also received cells, which data can be found in chapter 4. This overview is structured in figure 3.8 below and more detailed protocols can be found in sections 3.2.5.1 to 3.2.5.7, where the same nomenclature as in the figure is used.
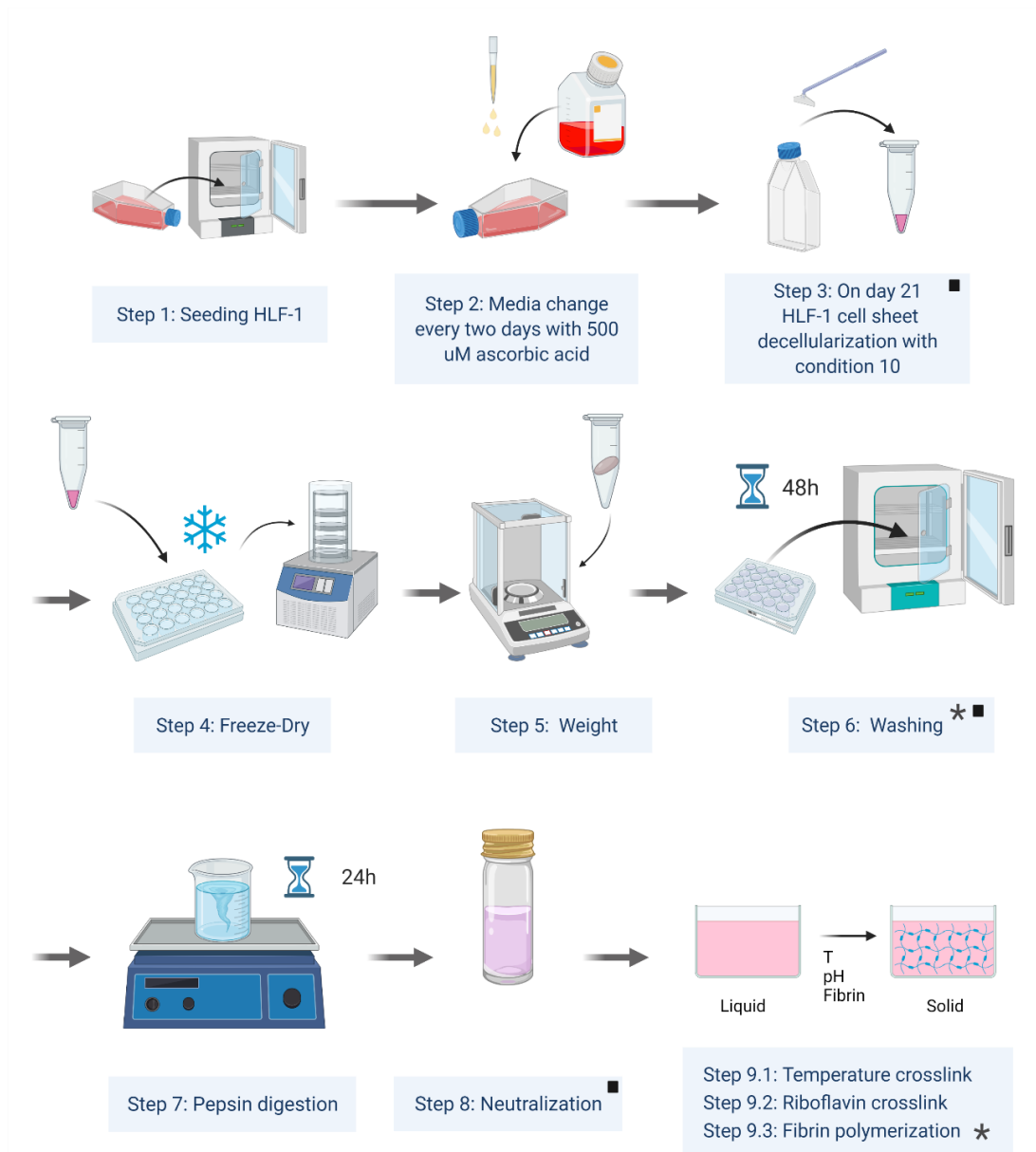
Figure 3.8: Overview of the methods undertaken for dECM crosslink. From steps one to three is illustrated the dECM formation with HLF-1 seeding, media change and ascorbic acid supplementation and decellularization step on day 21 following condition 10. Step 4 demonstrates the point in the methodology of the freeze-dry using a 24 well plate. Step 5 shows the weighing and step 6 the washing procedure. The step 7 and 8 refer to the pepsin digestion and neutralization respectively. In step 9 is illustrated the different crosslink strategies. The asterisk highlights points in the methodology where cells were seeded, after the washing step and fibrin polymerization. The black square notes where it was performed the methylene blue assay, on the last PBS washing after decellularization, on the washing from step 6 and after neutralization of the pepsin digested dECM from step 8. The T letter on step 9, stands for temperature. Created with BioRender.com

3.2.5.1 Step 1 to 5: HLF-1 seeding until weighing

The same protocol as in 3.2.2 was followed for dECM formation, but only condition 10 was used for decellularization. Then, for freeze-dry the procedure followed was detailed above in section 3.2.5 using the 24 well plate and the PDMS ring and disks apparatus. Finally, weighing followed the same protocol as in the processing stage in section 3.2.2.1.2.

3.2.5.2 Step 6: Washing

The washing step as illustrated in figure 3.8 is implemented after weighing the dry dECM, with the objective to further remove surfactant residues and to condition the scaffold with media to promote cell attachment. The washing procedure took 48 hours, with media change on the following day, with PBS or cell line specific media.

3.2.5.3 Step 7: Pepsin digestion

The dECM was digested with pepsin in a 0.5M acetic acid solution as described in section 3.2.3.3.5 for SDS PAGE sample preparation. But briefly, to 330 mg of dECM (dried weight) was added 10 mL of acetic acid with 33 mg of pepsin[114]. Note that the volume of acetic acid and weight of pepsin were adjusted to the weight of dECM. The mixture is placed in an ultrasound water bath for 15 minutes before being placed in the magnetic stirred (Stuart hotplate stirred CB302) for 24 hours. After 23 hours of digestion, the mixture was again placed in an ultrasound water bath for 15 minutes. Afterwards, was one more hour in the magnetic stir before finishing the digestion step[130,114].

3.2.5.4 Step 8: Neutralization

The neutralization step follows the complete 24 hours pepsin digestion. For that, the digested dECM was centrifuged at 581g for 3 minutes and at 4°C to remove undigested particles. To finish the protocol, the pH of the supernatant was adjusted to 7 with 3 M NaOH while keeping the samples on ice. Then, the neutralized dECM was diluted to 20 mg/mL, also on ice. Several solutions were used to dilute the dECM, such as 10XPBS, 1XPBS or cell specific media. At this point, the 20 mg/mL of neutralized dECM was stored at -80°C until further use[130,114].

3.2.5.5 Step 9.1: Temperature Crosslink

The polymerization of the neutralized dECM was promoted by raising the temperature to 37° C [130,114].

3.2.5.6 Step 9.2: Riboflavin Crosslink

The structure of riboflavin (also known as vitamin B2), more specifically the three-rings, provides the capacity to participate in redox reactions as well as absorption across the UV and visible spectrum (at 222 nm, 266 nm, 373 nm and 445 nm)[131]. The molecule has extensively been used in ophthalmic applications to promote new collagen links with the proteoglycans in the extracellular matrix in patients with keratoconus[132]. *In vitro*, has been used as a biocompatible photo-initiator to improve the stability of the biomaterials by crosslinking collagen in dECM[109,133], collagen[134] and gelatin[135].

This thesis used riboflavin as a photo-initiator and ascorbic acid as an electron donor to promote the photo-crosslink of collagen in the neutralized dECM. The light sources experimented with are presented in figure 3.9 and were a torch with 365 nm (ALONEFIRE SV10 5W), the laser head from Creality CP-01 3D Printer with 0.5W and wavelength from 450 – 500 nm and the UV germicidal lamps from tissue culture hood with 265 nm. For more detail on the reaction steps please consider the paper from Zaborniak, I *et al* (2021)[131], but in brief, in the presence of oxygen, the photoreduced riboflavin is re-oxidized, generating a mixture of lumiflavin, lumichrome, ribose fragments and reactive oxygen species (ROS), such as hydroxyl radical, superoxide radical anion and hydrogen peroxide. The main contributor to the polymerization is the hydroxyl radical. The presence of ascorbic acid accentuates the photoreduction of riboflavin as a result of its ability to transfer electrons[131]
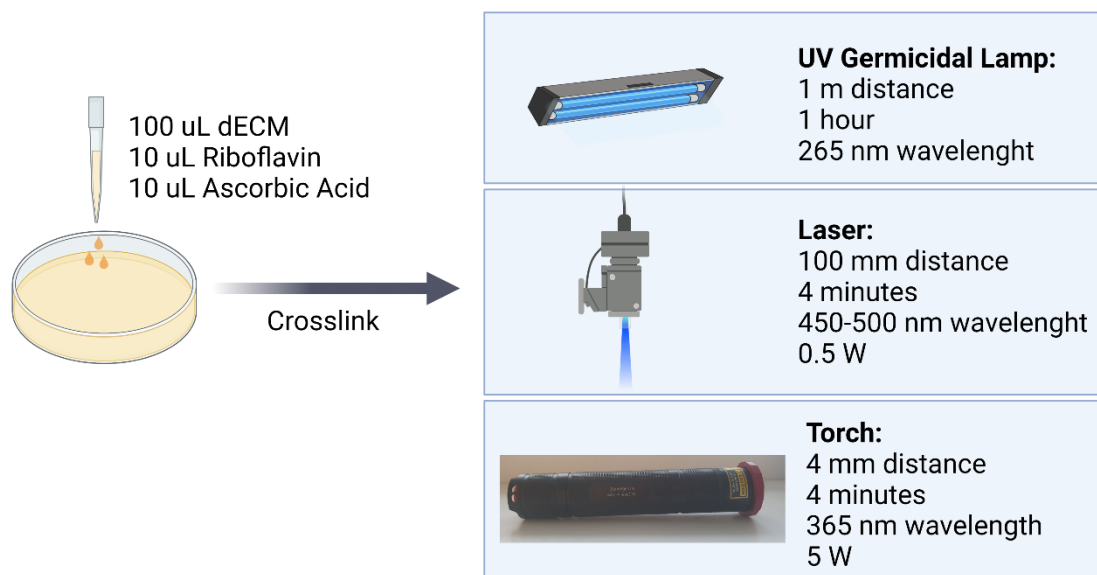
Figure 3.9: Schematic of the riboflavin crosslink. Created with BioRender.com

To initiate the dECM crosslink with riboflavin and ascorbic acid, it was followed protocol until step 8 from figure 3.8 and followed the protocols until 3.2.5.4. The solution used to dilute the dECM was 10xPBS. Regarding the riboflavin, the stock solution was prepared by dissolving 10 mg of powder in 10 mL of water and correcting the pH to 7 with 3M NaOH. The photosensitivity of the solution required protection from the light during solution preparation and handling. The stock solution was made fresh and discarded if changing in colour from bright yellow to brown occurred. The ascorbic acid stock solution was made fresh as well, by dissolving 10 mg of powder in 10 mL of water and correcting the pH to 5 with 3M NaOH. Both solutions were sterile filtered with a 0.22 µm porous size before use.

For the crosslink, 100 µL of 20% gelatin (dissolved on PBS), 10% gelatin and 20 mg/mL neutralized dECM were pipetted into 8 mm PDMS rings. Then, was added 10 µL of ascorbic acid (1 mg/mL stock solution) and riboflavin (1mg/mL stock solution) before crosslinking with the different light sources as shown in figure 3.9. The crosslink using the germicidal lamp from the tissue culture hood took 1 hour at approximately 1 meter distance between the lamp and the PDMS ring. The crosslink using the torch lasted for 4 minutes at a 4 mm distance. When using the laser head from the 3D print the crosslink lasted 4 minutes at a 100 mm distance. To test the success of the crosslink, it was tried to pipette the solution after light exposure. The solution that was able to be pipetted up and down before and after light exposure was considered not crosslinked. On the other hand, if when pipetting was found a viscous soft material, it was considered crosslink.

3.2.5.6.1 Riboflavin light spectrum

To investigate the activity of riboflavin, a light spectrum absorption was done. On a 96 well plate it was added 100 µL of 0.1 mg/mL riboflavin solution and using a plate reader (POLARstar Omega, BMG LABTECH) was obtained the spectrum from 220 nm to 600 nm. It was done a spectrum before and after light expousure.

3.2.5.6.2 Collagen quantification

To determine the collagen content was followed the protocol in section 3.2.3.2.2. The samples analysed were 20% gelatin, digested dECM for 24, 48 and 72 hours. For all samples, 4 mg (dry weight) were assayed.

3.2.5.7 Step 9.2: Fibrin Polymerization

For the fibrin polymerization, it was followed the protocol until 3.2.5.5, step 8 from figure 3.8. The dilution of the dECM was performed in cell specific media. The dECM was added to fibrinogen and thrombin to achieve a final concentration of 1.25 mg/mL and 5 U/mL respectively. Each dECM/fibrin gel was composed of 9.4 μL fibrinogen (10 mg/mL stock), 9.4 μL thrombin (40 U/mL stock) and 56.2 μL dECM (20 mg/mL stock). To promote polymerization first was added the dECM and fibrinogen to a 500 μL tube, then was added the thrombin. The total volume of 75 μL was quickly pipetted to a geometry with 0.3 cm^2. More detail on the geometry is given in chapter 4, section 4.2.5. The gels were left in the hood undisturbed for 15 minutes before being placed in the incubator (humidified 37°C, 21% oxygen and 5% CO$_2$) for 2 hours to complete polymerization. Any cell seeding was done after the 2 hours in the incubator.

Note that, if polymerization occurred in different surface areas, an adjustment of the dECM, fibrinogen and thrombin volumes were performed. During submerged conditions and full model assembly, the total polymerization area was 0.5 cm^2. In this condition, the volume of dECM, fibrinogen and thrombin was 93.6, 15.7 and 15.7 μL respectively. Making a total of 125 μL dECM/fibrin gel.

3.2.6 Stage 6.1: dTHP-1 Conditioned with Washing Waste Solution

The THP-1 were handled as detailed in section 2.3.3 and differentiated as mentioned in section 2.3.3.1. Then, the cells were seeded on 12 well plates at 1900 cells/cm^3 with coverslips on the bottom of the slide. The coverslips were previously autoclaved to ensure sterility. After the 24 hours recovery period, required from the THP-1 PMA differentiation protocol, it was added to the cells: fresh RPMI media, media supplemented with 1000 ng/mL LPS or conditioning media. The conditioning media consisted of the wasted RPMI used to wash the dECM scaffold for 48 hours, collected from step 6 from figure 3.8.

The plate was moved to the incubator (humidified 37°C, 18% oxygen and 5% CO$_2$) and after 3 hours the media was collected and stored at -20°C for cytokine media quantification. The cytokines analysed were: IL6, TNF-α and TGF-β. The protocol followed for the ELISAs can be found in sections 2.5.1 to 2.5.3. In addition to the data analysis present in the method, the values were also divided by the cell number. The cell number was determined by following the protocol in section 2.7

In addition to cytokine quantification, the cells were processed to be imaged on confocal microscopy. The cells were fixed with a 4% PFA solution for 15 minutes at room temperature.

The fixed cells were then washed with PBS once and stored in 0.1M glycine at 4°C until further use. A total of 3 biological repeats were done with 4 technical repeats each. To commence the staining protocol, the glycine was removed and the wells were rinsed once with PBS. Then, 150 µL of a PBS solution containing: 1 µg/mL of DAPI, 1:200 of Phalloidin and 10 µL of FITC anti-human CD11b Antibody or FITC anti-human CD14 Antibody (#301330 and #325603 from Biolegend respectively), were added to each coverslip. The slides were incubated for 1 hour at room temperature and protected from light. After the incubation period, the coverslips were washed three times before being mounted with DPX on a glass slide. The cells were imaged using the Zeiss LSM 710 with 405 nm laser to excite DAPI, 488 nm laser for the CD11b and CD14 and 633 nm laser for Phalloidin visualization.

In this result chapter can be found the protocol created to derive a biomaterial from the fibroblast extracellular matrix. The section was broken into 6 stages, presented already in figure 3.1. To derive this biomaterial was first investigated a long-term culture of the HLF-1 presented, in stage 1. After ensuring the fibroblast's viability for 21 days, several decellularizations conditions were used to remove the DNA content. This was evaluated after extensive characterization found in section 3.3.2 (stage 3 from figure 3.1), to determine the condition(s) that ensured a balance between DNA removal and ECM conservation. This section led to the next, stage 4 named troubleshooting, where it was investigated the reason behind odd values recorded during dECM characterization. After that, the decellularization condition to create the biomaterial was selected and investigated ways to crosslink the dECM (stage 5). The chapter also includes a final section evaluating the pro-inflammatory response that the dECM could initiate on dTHP-1.

3.3.1 Stage 1: 2D HLF-1 Characterization

 The 2D characterisation of the human lung fibroblast is shown in figure 3.10. The trypan blue data, graph 3.10A) shows the live cells over a period of 21 days, from days 0 to 7 the cells are in the exponential phase. The curve fitted is the following: $y=6091e^{0.3189x}$ with an initial value of 6091 and a rate constant of 0.3189 day^{-1}. With this data, it was also determined a time constant of 3.2 days (equation 2.6) and a doubling time of 2.2 days (equation 2.7) during the exponential phase. The trypan blue data was also used to generate the live and dead cell ratio plotted in figure 3.10B), following equations 2.3 and 2.4. The percentage of cell death is under 10% until day 6, yet on day 7 the percentage of cell death increases to 13%, maintained constant until day 14. The highest cell death is seen on day 21, reaching 25%. With an opposite tendency, the dsDNA content shows a steady increase along the 21 days, graph 3.10D). The increase is statistically significant between days 1 and 7 and days 1 and 21. Regarding the metabolic activity, plot 3.10E), the MTS content per number of live cells increase until day 3, then shows a decreasing tendency until day 21, except for day 14. However, the error bar of day 14 is high showing a big variance. Finally, the dextran blue assay, represented on plot 3.10F), shows a plateau until day 7, though, on days 14 and 21 the absorbance decrease reaching the value observed for fresh media.
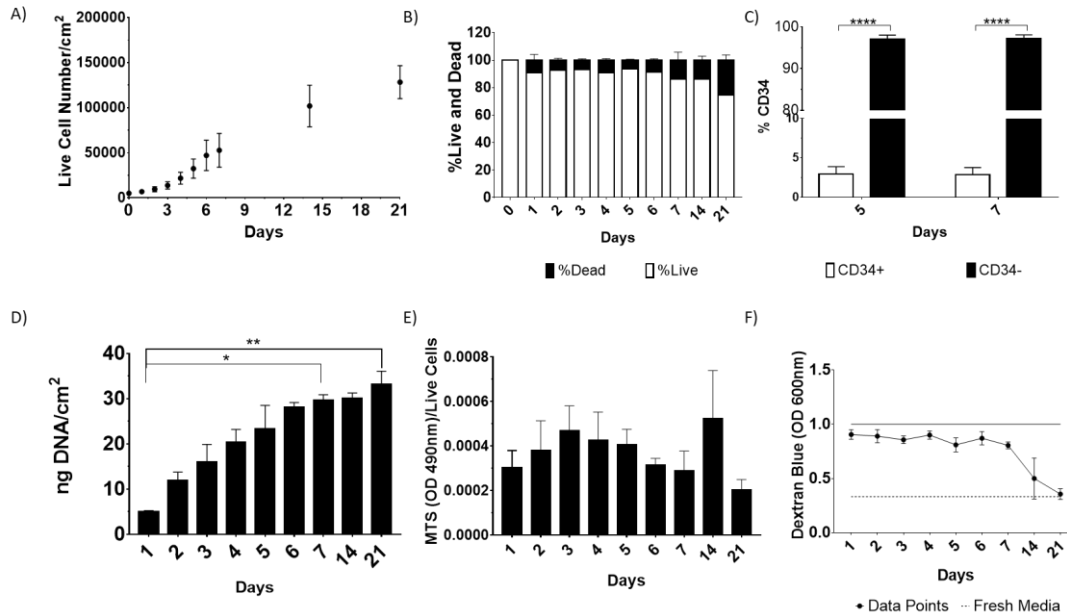
Figure 3.10: HLF-1 2D characterization. A) Live cells quantification with trypan blue over 21 days (n=3). From day 0 to day 7 the cell growth fits the following exponential curve: $y=6091e0.3189x$. B) Live and dead cells ratio using trypan blue assay (n=3). C) Expression of the CD34 marker on day 5 and 7 (n=3 and **** represents p<0.0001). D) Quantification dsDNA over 21 days using Picogreen Kit (n=3 and * represents p=0.0370 and ** p=0.0083). E) Metabolic activity quantification per live cell during 21 days using MTS assay (n=3). F) Dextran blue absorbance for 21 days to measure monolayer formation. The error bars represent SEM (n=3).

To complement the 2D HLF-1 characterization, inverted and fluorescence microscope images were taken to inspect the cell morphology (figure 3.11). From day 1 to day 21, cell confluency increases, showing spindle-shaped cells that with the course of time became even more elongated and condensed. Until day 7 there are still gaps between the cells that disappear at later culture time points. The fluorescence images show clearer the high confluency observed on days 14 and 21, where cells grow on top of each other, given the overlapping nucleus stained with DAPI in white. The F-actin fibres highlighted in yellow by the Phalloidin stain, are on days 1 and 5 of two types, a thick fibre delineating the cell and several thinner ones in the cytoplasm. But as the time in culture increases, only the thick fibres are observed.
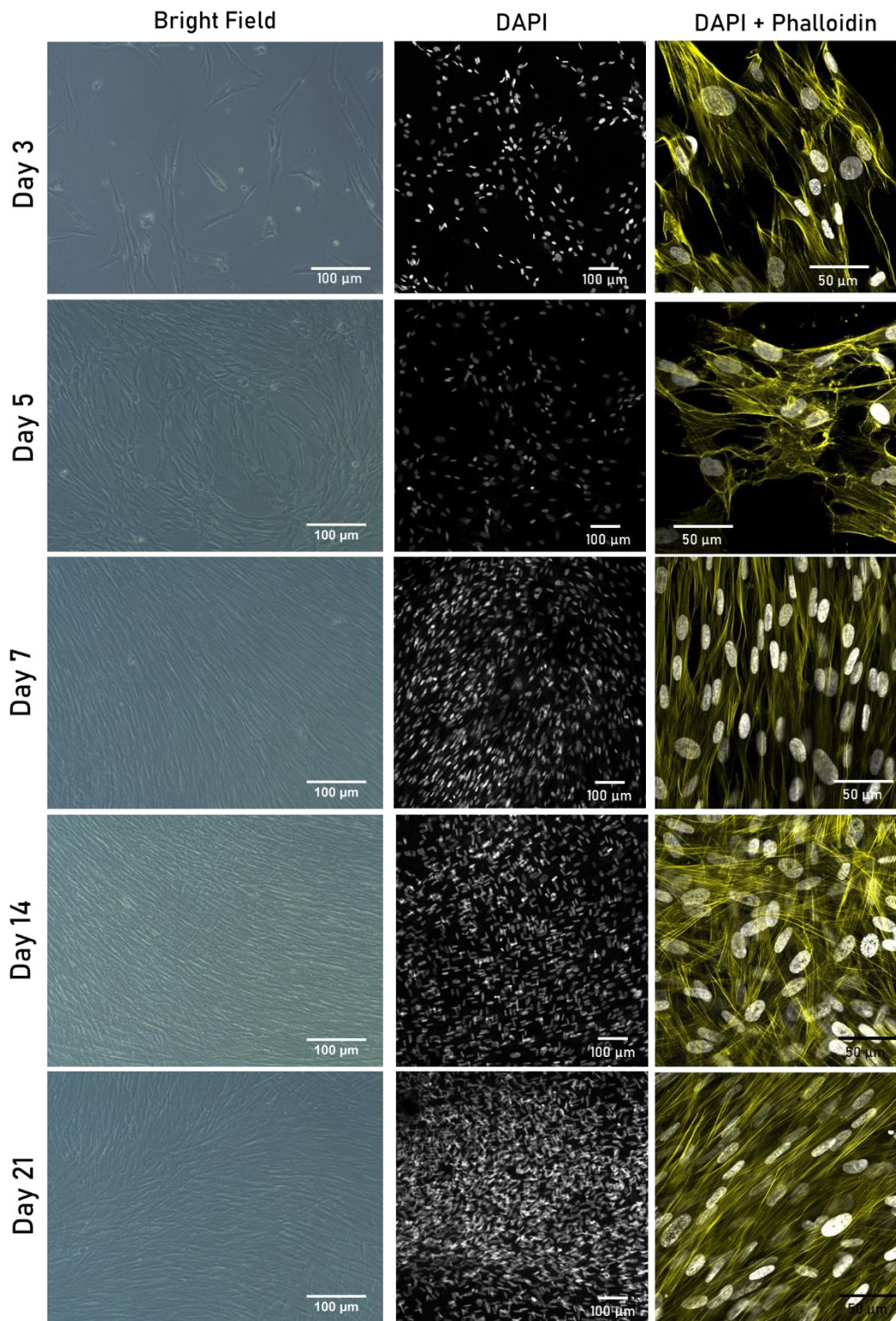
Figure 3.11: HLF-1 bright field and fluorescence images from 2D characterization. Images of the lung fibroblasts on days 3,5,7,14 and 21 of culture. The first column from the left shows bright field images of the HLF-1 cells (n= 3 scale bar represents 100 µm). The middle column illustrates the HLF-1 cell nucleus stained with DAPI, in white (n= 3 scale bar represents 100 µm). The right-side column depicts the nucleus stained with DAPI in white and F-actin stained with Phalloidin in yellow. (n= 3 and scale bar represents 50 µm)

3.3.2. Stage 3: dECM Characterization

The qualitative characterization of the decellularized HLF-1 cell sheet from conditions 1 to 10, is found in figures 3.12 and 3.13. The DAPI stain is found in the left side column in grey, used to visualize DNA. Haematoxylin and Eosin Y stain (H&E) are presented in the middle column. The Haematoxylin stains the nucleus, as DAPI, in a dark purple and Eosin Y stains the extracellular in pink. The dECM was also stained with alcian blue to visualize the GAGs residues, shown in light blue on the far right column.
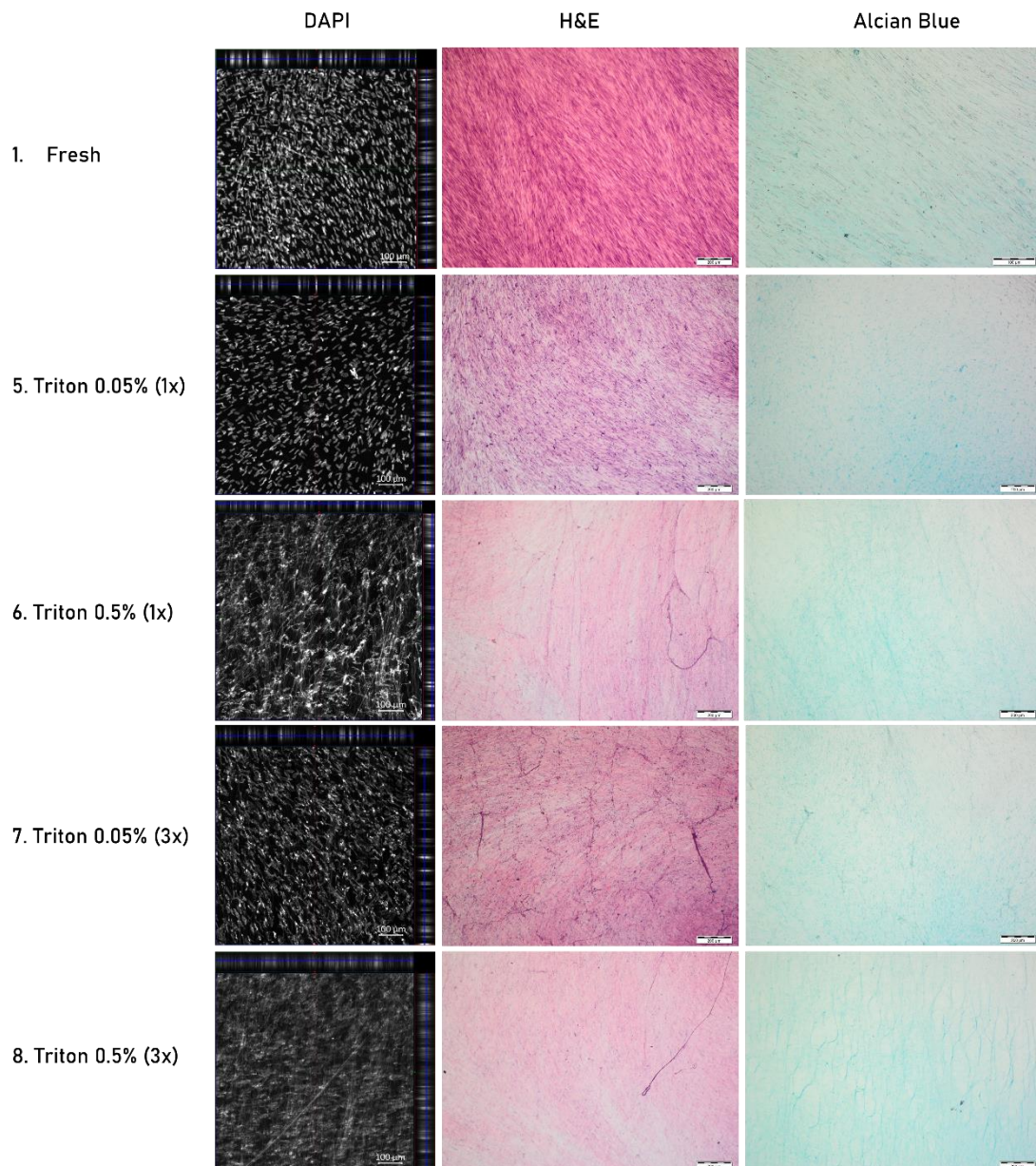
Figure 3.12: Fluorescence and bright filed images from dECM characterization. The decellularized conditions depicted are: fresh (1), triton 0.05% (1x) (5), triton 0.5% (1x) (6), triton 0.05% (3x) (7) and triton 0.5% (3x) (8). The column from the left shows in white the nucleus or nucleic acid residues stained with DAPI (scale bar represents 100 μm). The middle column shows the decellularized cell sheet stained with H&E (scale bar represents 200 μm). The right-side column depicts the decellularized cell sheet GAGs in blue stained with alcian blue (scale bar represents 200 μm). (n=3)

	DAPI	H&E	Alcian Blue
2. Freeze- Thaw			
3. Freeze- Thaw + 0.05%SDS			
4. Freeze- Thaw + 0.5%SDS			
9. Freeze- Thaw + 0.05%SDS + 0.05% Triton (1x)			
10. Freeze- Thaw + 0.05%SDS + 0.5% Triton (3x)			
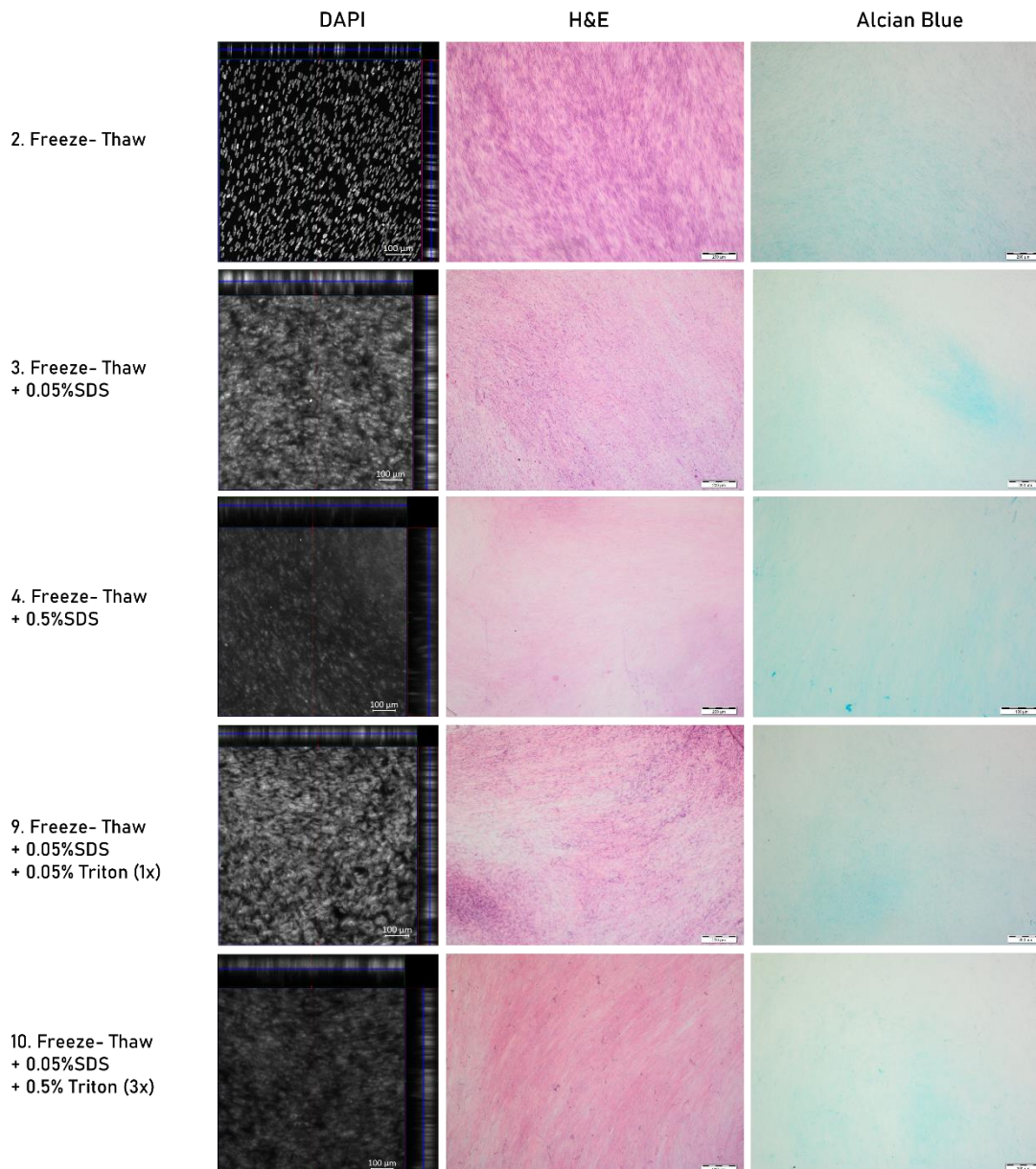
Figure 3.13: Fluorescence and bright filed images from dECM characterization. The decellularized conditions showed are: freeze – thaw (2), freeze - thaw + 0.05% SDS (3), freeze - thaw + 0.5% SDS (4), freeze – thaw + 0.05% SDS + 0.05% triton (1x) (9), freeze – thaw + 0.05% SDS + 0.5% triton (3x) (10). The column from the left shows in white an ortho view of the nucleus or nucleic acid residues stained with DAPI (scale bar represents 100µm). The middle column shows the decellularized cell sheet stained with H&E (scale bar represents 200 µm). The right-side column depicts the decellularized cell sheet GAGs in blue stained with alcian blue (scale bar represents 200 µm). (n=3)

The analysis of figures 3.12 and 3.13 show that conditions 1 and 2, corresponding to fresh and freeze-thaw respectively, retain an intact nucleus and show the presence of extracellular matrix with the intense pink stain of the eosin y. The mildest treatment with Triton, corresponding to

condition number 5, also shows an undamaged nucleus and rich ECM content like the fresh and freeze-thaw conditions. However, by increasing the concentration of Triton and the number of incubations times, from 1x to 3x, the H&E stain shows the DNA gradually being removed as the treatments get harsher. The DAPI continues to show a high amount of DNA, however, is no longer shown as an intact nucleus as seen in the fresh condition, but in structures like strings. These structures are also seen in the H&E stain. On the contrary, the SDS treatments cause the nucleus to appear as a diffused smear. On the H&E is observed some purple on condition 3 that is not presented on condition 4. The H&E stain of condition 4 is also accompanied by the reduction of the ECM by the decrease of pink colour from the eosin y. The dual approach of SDS and triton from conditions 9 and 10 still shows DAPI stain, however dimmer and diffused in condition 10. Looking at the H&E stain, condition 10 has less purple colour from DNA presence and at the same time conserves the pink colour linked to ECM presence. The alcian blue stain, is in general, more visible seen in conditions 1,2 and 3, leaving in the other conditions a slight distributed blue colour. However, the treatment with triton alone appears to conserve more the GAGs than with SDS, with visible round structures.

Moving on to the quantitative methods, the dECM was analysed for DNA, collagen, proteins and GAGs content. Figure 3.14A) and 3.14B) correspond to DNA quantification using picogreen kit and QIAamp kit respectively. Two features that stand out when comparing both graphs, the tendency between conditions, does not match and QIAamp y-axis graph is ten times higher. The quantification of the DNA through the picogreen kit shows a general increase of DNA content from conditions 1-10, except for condition 4. The milder decellularization treatments applied on conditions such as 1, 2 and 5 should present higher DNA content. On the other hand, harsher SDS and Triton treatments should lead to a decrease in DNA content, but the quantitative data are contrary to the results from the images presented in figures 3.12 and 3.13. When the DNA is quantified with the QIAamp kit, also does not follow the expected tendency, often harsher conditions such as 2 relative to 1, 4 to 3 and 10 to 9, show an increase of DNA content.

Regarding the collagen quantification present in plot 3.14C), the graph is aligned with what was expected. The control condition, the fresh, and condition 2 presents the higher values of collagen. Then, the SDS treatment showed from conditions 3 to 4 a complete loss in collagen, with the increase of SDS concentration ten times. On condition 4, the collagen was below the limit detected so was attributed 0 on the graph.
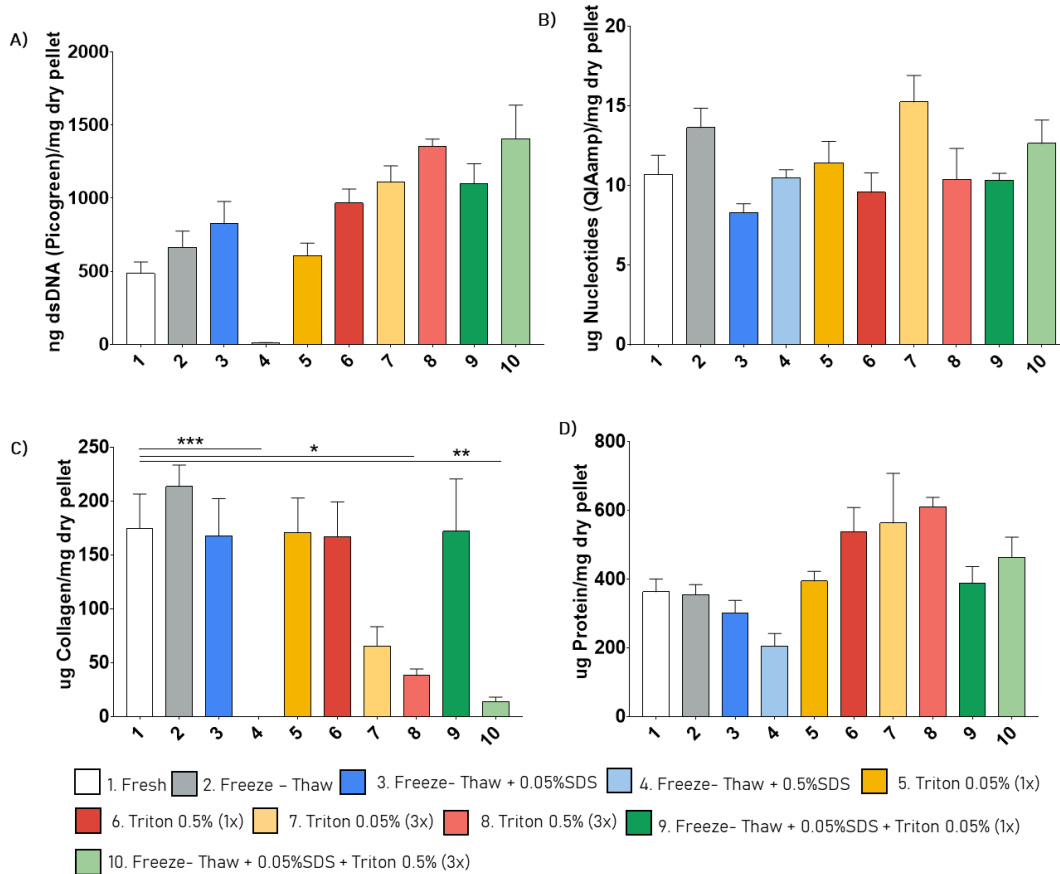
Figure 3.14: Qualitative characterization of the dECM. Each protocol is linked to a number and colour. A) Quantification of the DNA content using Picogreen Kit (n=4 to 7). B) Quantification of the DNA content with QIAamp Kit (n=3 to 6). C) Quantification of protein content (n=4 to 7 with *** representing p=0.006, * p=0.0274 and **p=0.0031). D) Quantification of collagen content (n=4 to 7). The error bars represent SEM.
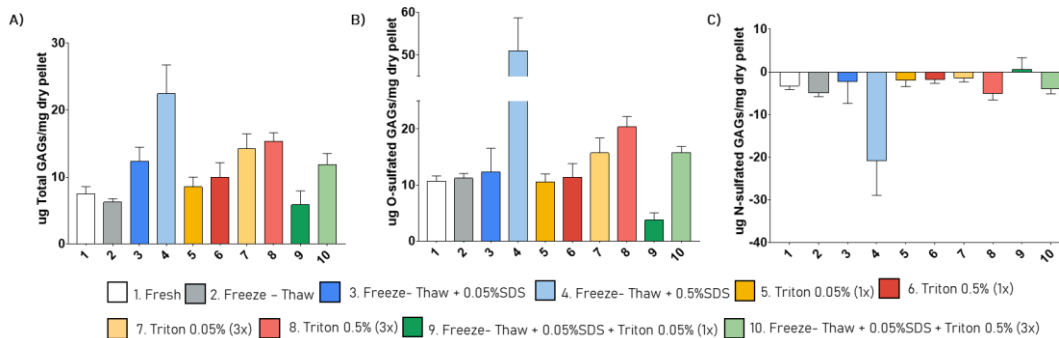
Figure 3.15: GAGs quantification of the dECM. A) Quantification of the total glycosaminoglycan content (n=4 to 9). B) Quantification of the O-sulfated glycosaminoglycan (n=4 to 10). C) Quantification of the N-sulfated glycosaminoglycan (n=4 to 9). The error bars represent SEM.

The Triton treatments are also aligned with what was anticipated. From condition 5 to 6 there is a slight decrease when triton concentration increase 10-fold. Then, when triton treatments are repeated 3 times (conditions 7 and 8) the collagen value is lower compared to conditions 5 and 6, which is expected. In addition to condition 8 suffers a more accentuated decrease compared to condition 7 since is subjected to 10x higher triton concentration. This loss in collagen is statistically significant when compared with condition 1. Condition 9 is a sum of conditions 3 and 5, as a result, applying the treatments separated or accumulate treatments does not have a negative effect on collagen amount. However, when triton concentration increases, as well as the number of repeats, such as in condition 10, the collagen drops significantly, similarly to what happened to condition 8. But condition 10 reaches a lower value than 8 since has an additional SDS treatment.

About the protein content, found in plot 4.14D), from conditions 1 to 5, the graph shows the tendency expected, as harsher treatments are in place protein concentration decreases. Condition 5 shows similar values to conditions 1 and 2, as it is the mildest Triton treatment, is expected to not cause a significant decrease in protein content. However, condition 6-10 tendency goes against expected, 6-8 have similar but higher values than the fresh condition. The condition 9-10 has a slightly lower value than 6-8 but is still higher than fresh.

The glycosaminoglycans (GAGs) quantification (figure 3.15) includes the total GAGs quantification, the N-sulfated and O-sulfated GAGs from 3.15A) to 3.15C) respectively. The tendency observed on 3.15A) and 3.15B) does not follow what is expected similar to what is observed on the DNA and protein quantification. From conditions 4 to 3, 6 to 5, 8 to 7 and 10 to 9 the ug of GAGs increase as the SDS and triton treatments get harsher. In addition, the N-sulfated GAGs, which are determined by the subtraction of the O-GAGs from the total-GAGs, show negative results.

The next feature assessed was the length of the DNA fragments quantified above. The QIAamp DNA samples were run in 1% agarose gel and a total of 1 µg of DNA was loaded from conditions 1-10 (figure 3.16). From the analysis of the image, is observed that the DNA fragments present from conditions 1-10 have a size around 10kb. Is also observed a smear along the channels but not so intense as the first band. Note that all samples were diluted in AE buffer (from the QIAamp kit), which band can be observed on the channel at most right.
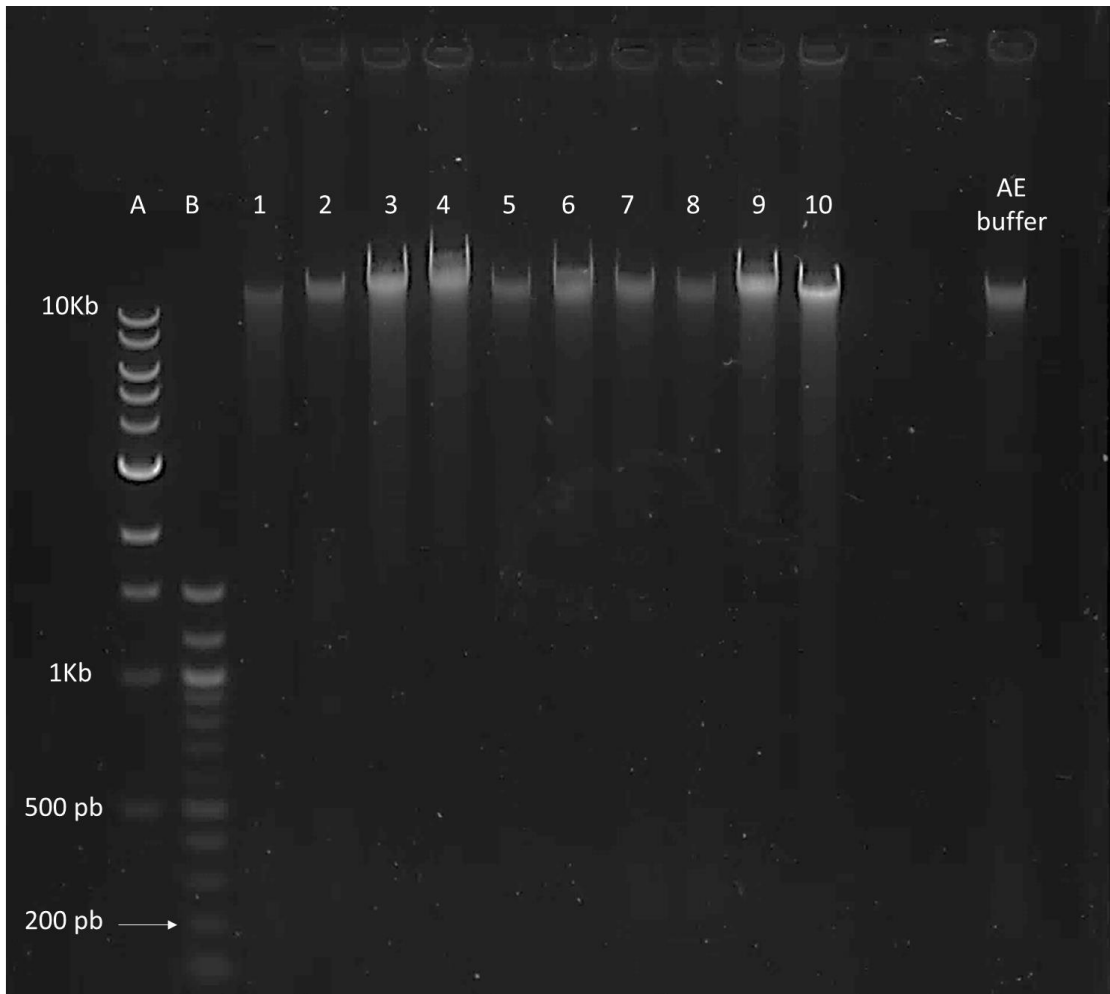
Figure 3.16: DNA gel. From left to right the conditions highlighted in white correspond to: A) 1kb DNA ladder, B) 100bp DNA ladder, 1) Fresh, 2) Freeze – Thaw, 3) Freeze – Thaw + 0.05%SDS, 4) Freeze – Thaw + 0.5%SDS, 5) Triton 0.05% (1x), 6) Triton 0.5% (1x), 7) Triton 0.05% (3x), 8) Triton 0.5% (3x), 9) Freeze – Thaw + 0.05%SDS + Triton 0.05% (1x) and 10) Freeze – Thaw + 0.05%SDS + Triton 0.5% (3x) and AE buffer. (n=3)

The next characterization of the decellularization product corresponds to the protein visualization with an SDS PAGE gel. Figure 3.17 represents an image with conditions 1, 9 and two biological repeats of condition 10. The only condition where several bands are present, apart from the ladder, is on the second repeat of condition 10. The rest shows a high content of small protein fragments at the end of the gel.
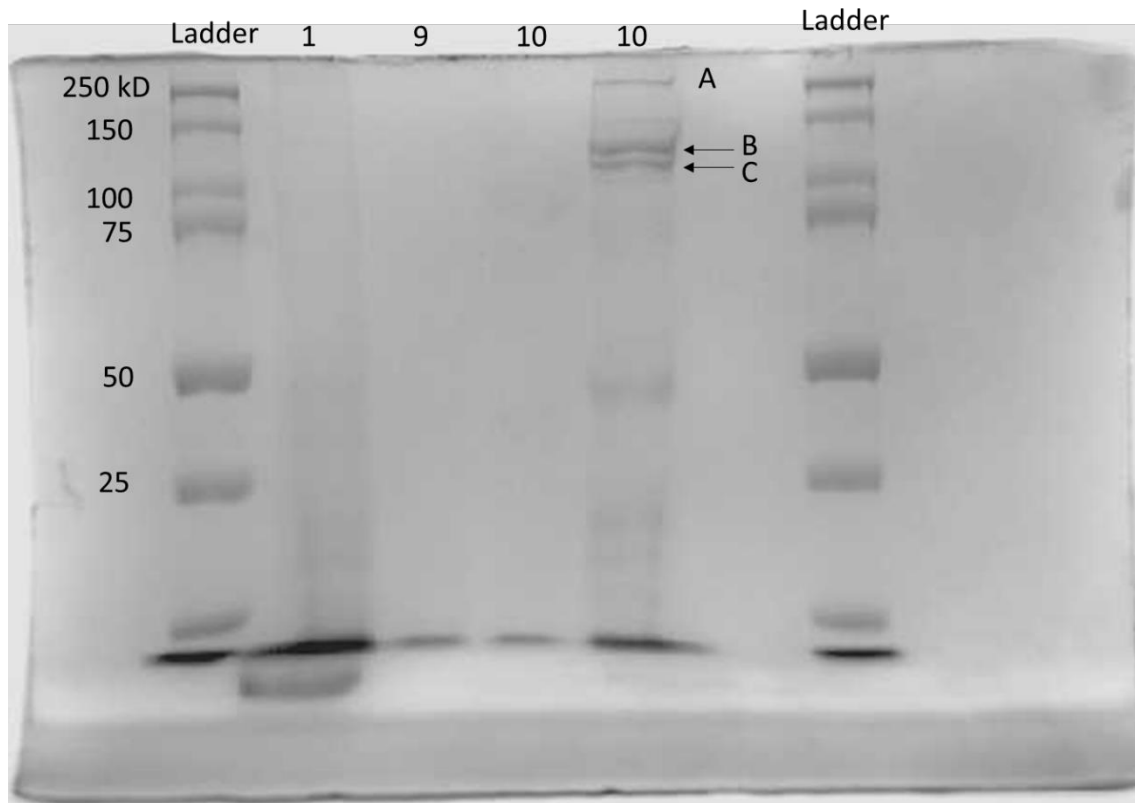
Figure 3.17: SDS PAGE gel. SDS PAGE gel of pepsin digested condition 1 (Fresh), 9 (Freeze – Thaw + 0.05% SDS + Triton 0.05%) and 10 (Freeze – Thaw + 0.05% SDS + Triton 0.5% 3x) (n=3).

The impact of the decellularization was also assessed by scanning electron microscopy (SEM) where it was compared the fresh condition with condition number 10 (figure 3.18). The difference between both conditions is the presence of porous in the fresh conditions, which are absent in condition 10

The characterization of the decellularized ECM giving the 10 different protocols was to identify a condition that showed a balance between removal of the nuclear content and at the same time promoting ECM preservation. Bearing in mind the requirements listed above in the introduction: <50 ng dsDNA per mg ECM dry weight, <200 bp DNA fragment length and lack of visible nuclear material in tissue sections stained with DAPI or H&E. The first two requirements were not met, with dECM showing much higher value of dsDNA and much bigger fragment length independent of decellularization condition applied. To build on the excess of DNA to consider the membrane decellularized, DNA, protein and GAGs plots show a tendency different from the expected. Considering the results before, the next section of this data chapter focuses on identifying the reason for such discrepancies (section 3.3.3: Troubleshooting).
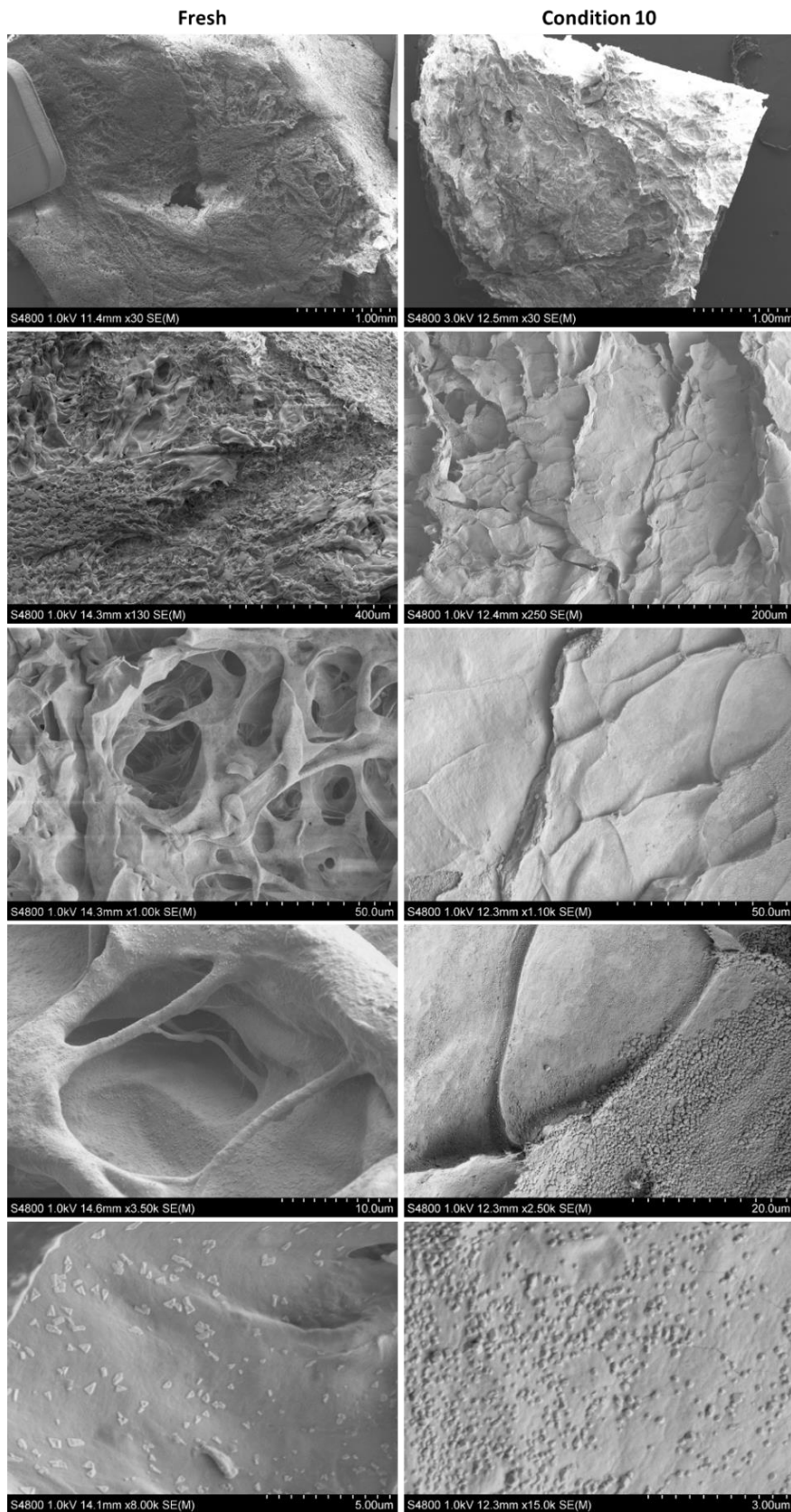
Figure 3.18: Scanning electron microscopy. Condition Fresh on the left and 10 (Freeze – Thaw + 0.05% SDS + Triton 0.5% (3x)) on the right (n=1).

3.3.3. Stage 4: Troubleshooting

In the following section can be found supplementary experiments to try to pinpoint the reason for the contradiction between the qualitative data, such as the bright field and fluorescence images and the quantitative data, regarding DNA, protein and GAGs quantification.

The first troubleshooting plot is presented in figure 3.19 and addresses the impact of the digestion and quantification method. As mentioned before in the methods section 3.2.4.1, was tested the effect of the papain digestion or protease K, on picogreen and nanodrop DNA quantification. From the plot is visible that DNA quantified with nanodrop is 10x higher than with picogreen. The orange and blue bars are ten times the grey, pink and green bars. In addition, it is also observed the tendency that the Papain + Picogreen protocol has more DNA than the Papain + QIAamp + Picogreen followed by the Protease K + QIAamp + Picogreen, grey, pink and green bars. The exception for this tendency is condition 4.

Just to bring to attention, the graph 3.14A) results from a Papain + Picogreen approach, and graph 3.14B) results from a Protease K + QIAamp + Nanodrop method, corresponding to grey and orange bar respectively.
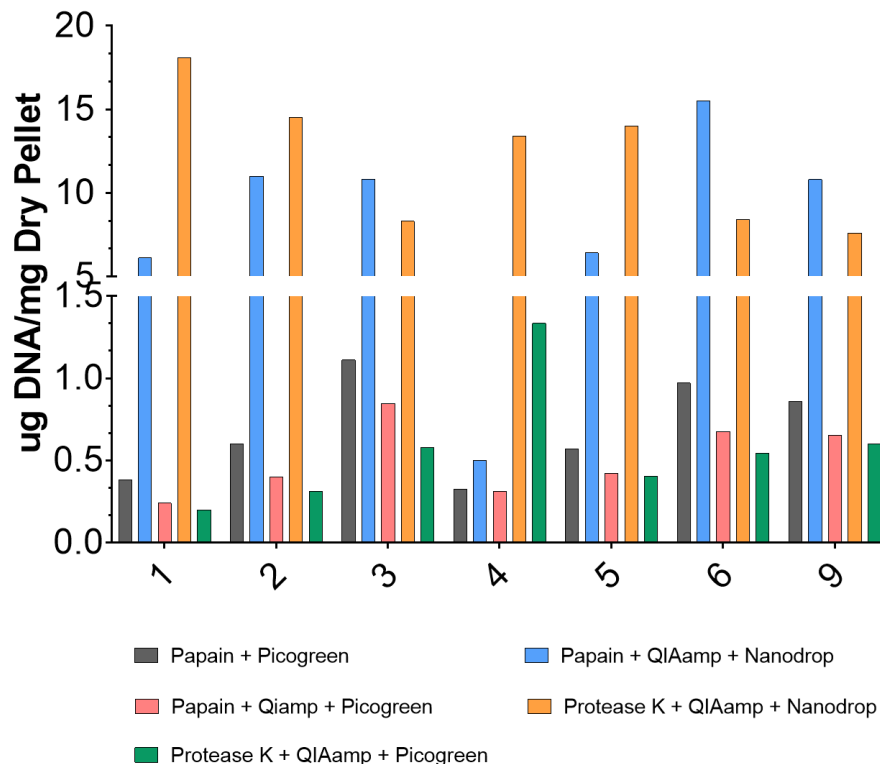
Figure 3.19: Digestion vs quantification method troubleshooting. DNA quantification by digesting dECM with papain or protease K, followed by DNA quantification using picogreen or nanodrop. The QIAamp kit is also used for DNA purification (n=1).

Then, it was evaluated the effect of SDS and triton residues on the quantification of DNA using picogreen kit (figure 3.20). For that, it was diluted 100, 10, 1 and 0.1 ng of dsDNA standard in the SDS and triton solutions used during the decellularization protocol. Looking at the SDS effect, both concentrations, 0.5% and 0.05% lead to a decrease in fluorescence signal throughout the DNA range. The 0.5% SDS has a much more visible effect. At the lowest DNA amount, 0.1 ng, the fluorescence values are negative for both SDS concentrations. On the other hand, triton leads to an increase in the fluorescence signal, but the interference in the signal is not as significant as the SDS. The exception is at the lowest 0.1 ng which leads to a decrease of the fluorescence signal in comparison to the papain. The combination of SDS and Triton also diminishes fluoresce signal, but the higher concentration of Triton, condition light green, almost eliminates the effect of SDS from 100 to 1 ng. In general, the deviation from the papain is greater at 0.1 ng of dsDNA. Can be found in appendix 7 the same study but with TE buffer as the control.

dsDNA (ng)	100	10	1	0.1
0.05% SDS	65% decrease (p=0.0328)	55% decrease	54% decrease	117% decrease (p<0.0001)
0.5% SDS	100% decrease (p<0.0001)	101% decrease (p<0.0001)	104% decrease (p<0.0001)	143% decrease (p<0.0001)
0.05% Triton	22% increase	29% increase	7% increase	73% decrease
0.5% Triton	14% increase	37% increase	33% increase	54% decrease
0.05 + 0.05	81% decrease (p=0.0044)	86% decrease (p=0.0022)	94% decrease (p=0.0005)	93% decrease (p=0.0117)
0.05 +0.5	19% decrease	11% decrease	25% decrease	84% decrease (p=0.0346)

Figure 3.20: SDS and triton effect on picogreen dsDNA measurements. Influence of SDS and Triton on DNA quantification with papain digestion solution as the control. The rows correspond to the fluorescence signal for each chemical tested divided by the fluorescence signal of papain. The columns correspond to 100,10,1 and 0.1 ng of DNA for the different chemical analyses, 0.05% SDS, 0.5% SDS, 0.05% triton, 0.5% triton, 1:1 ration of 0.05% SDS and 0.05% triton and 1:1 ration of 0.05% SDS and 0.5% triton. The error bars represent SEM and n=3 to 7.

In the next figure, the same data analysis was performed, but instead of diluting the ng of dsDNA standard in the decellularization solution SDS or Triton, was used the last PBS wash from the decellularization protocol. The graph in figure 3.20 shows the influence of the SDS and Triton solutions as they were used for decellularization. However, the dECM is washed three times with

PBS at the end of the method, as described in section 3.2.2. In this way, if there is interference from the chemicals on the assays, the residual concentration should be less. To address that, it was recovered the last PBS wash and the same protocol was applied as in figure 3.20. The last PBS wash from the different decellularization conditions was used to dilute 100, 10 and 1 ng of DNA.

The results presented in figure 3.21, show that by decreasing the ng of DNA the deviation from the papain digestion calibration curve increases, but also the variance in the data. The fluorescence decrease recorded before for SDS was not replicated in figure 3.21. The exception is 0.05% Triton (1x), that fluorescence decreases regarding papain values, which is not observed in the graph from figure 3.20.
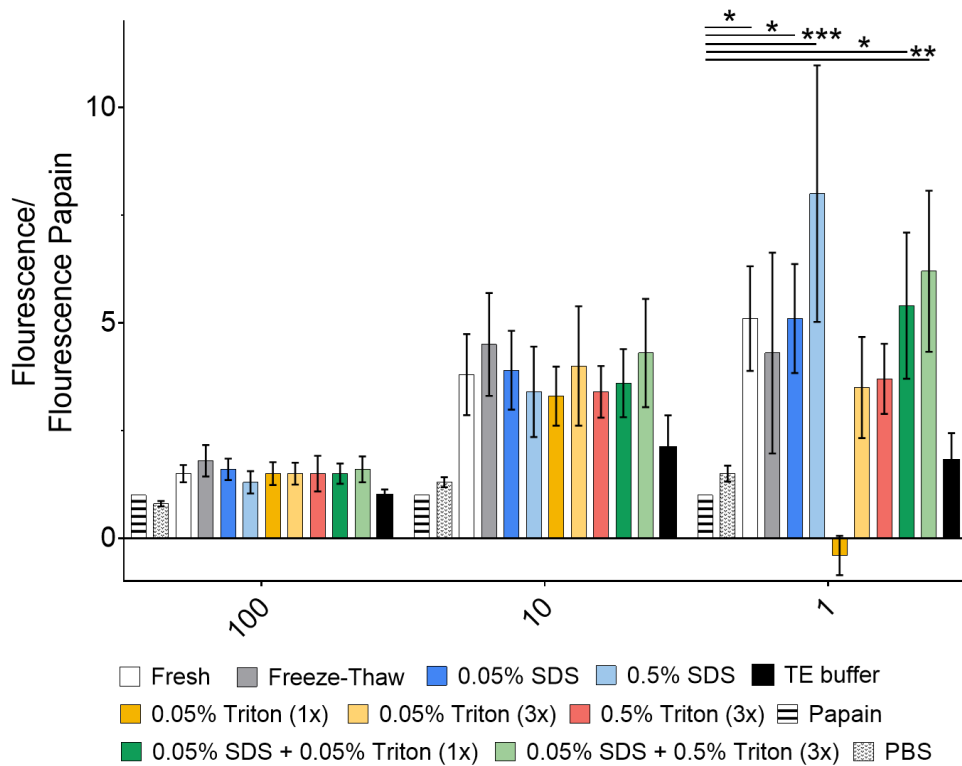
Figure 3.21: Effect on picogreen dsDNA measurements. Fluorescence values in comparison to papain digestion solution with 100, 10 and 1 ng of dsDNA added to the last PBS wash applied to the dECM. The asterisk symbols in the plot represent: *$p < 0.05$, ** $p < 0.01$, and ***$p < 0.001$. The error bars represent SEM (n=4).

To evaluate if supplementary washing reduces the surfactant effect in the assays, the dried dECM was washed with DMEM media during 48h at room temperature (figure 3.22). The dsDNA content is presented on left hand side graph, showing the same tendency and similar values as

in graph 3.14A), where no supplementary washing was done before quantification. The exception is condition 4, where dsDNA content increased with the washing. On the other hand, the protein content decreased in value for conditions 1,2,5,6 and increase for conditions 3 and 9.
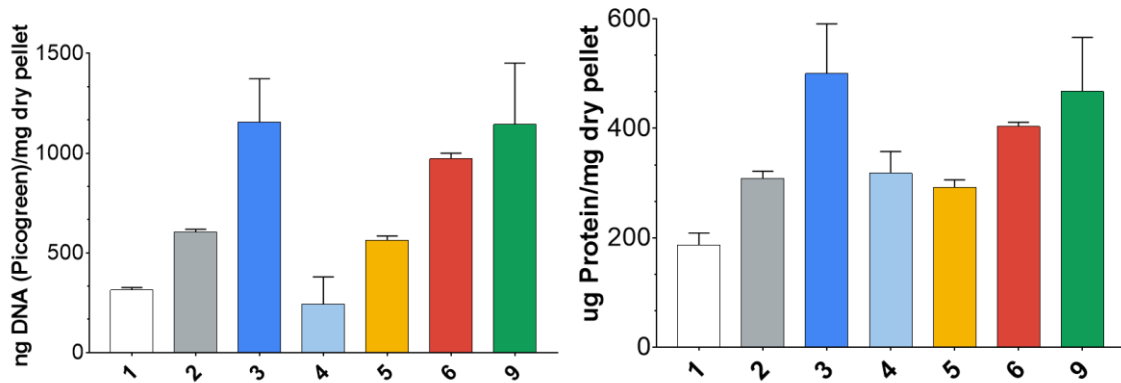
Figure 3.22: DMEM wash of dECM. The left side graph depicts the dsDNA content for decellularized conditions 1-6 and 9 when extra washing steps were applied. The right side graph shows the protein content for decellularized conditions 1-6 and 9 when extra washing steps were applied (n=2).

The last experiment from the troubleshooting section focuses on quantifying the residual amount of SDS. To address that, the methylene blue assay was used to determine the SDS percentage at three different time points, on steps 3, 6 and 8, highlighted by a black square in figure 3.8.

1. Step 3 – Last PBS rinse from conditions 1-10 after decellularization

2. Step 6 – 6 days wash after freeze-drying dECM scaffold from condition 10

3. Step 8 – Neutralized pepsin digested dECM from conditions 10 and 1 (with 48 hours wash on step 6).

Figure 3.23A) presents the data from point 1, where PBS was assayed as control. The graph shows that from conditions 1-8 the SDS concentration is compared to the PBS value (0.01%) and only conditions 9 and 10 show higher SDS percentages. However, all conditions show a lower percentage of SDS than the ones used during decellularization (conditions 3, 9 and 10 used a 0.05% SDS and condition 4, a 0.5% SDS solution). Despite higher values of SDS recorded for conditions 9 and 10, 0.022% and 0.036% respectively, is also noteworthy the big error bars.

Figure 3.23B) presents the data from points 2 and 3. The washing step was extended for 6 days, where can be seen a decrease in SDS percentage as the number of days increased. On the 6th day, the percentage of SDS is at the same level as the PBS. Another feature shown in figure 3.23B) are the values for dECM 10 and fresh that corresponds to neutralised dECM samples decellularized with conditions 10 and 1 (control) respectively. Note that both samples followed the standard protocol of 48 hours of washing on step 6. From the graph is visible that despite on day 2 only 0.012% SDS is recorded in the PBS wash, the dECM 10 has approximately double that amount, 0.026%, bound to its matrix. Note that the condition fresh has similar values of PBS, indicating that the high protein content does not interfere with the methylene blue assay.
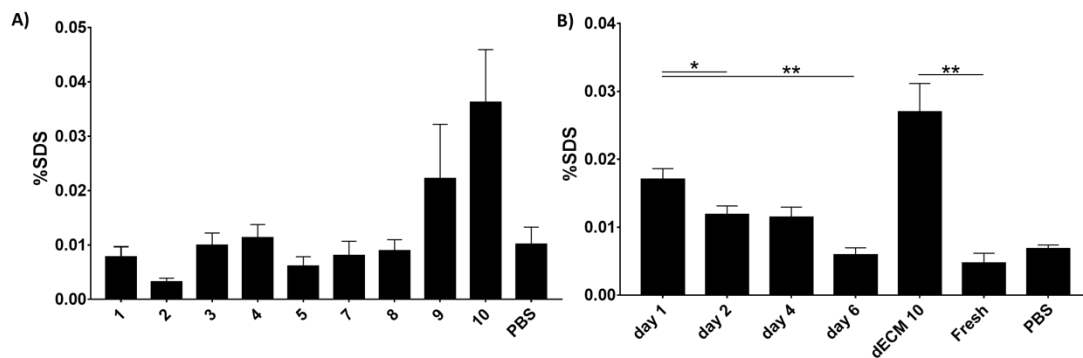
Figure 3.23: Methylene blue assay. A) The graph represents the percentage of SDS in the last PBS wash from sample fresh (1; n=5), freeze-thaw (2; n=3), 0.05% SDS (3; n=3), 0.5% SDS (4; n=3), 0.05% Triton 1x (5; n=3), 0.05% Triton 3x (7; n=5), 0.5% Triton 3x (8; n=4), 0.05% SDS + 0.05% Triton 1x (9; n=6), 0.05% SDS + 0.5% Triton 3x (10; n=18) and PBS (n=9). B) The plot represents the percentage of SDS in the PBS wash after membrane drying during 6 days: day 1 to 6. The dECM 10 represents the conditions number 10 after pepsin digestion and neutralization. The fresh represents the condition fresh after pepsin digestion and neutralization (n=10 for day 1 and 2, n=6 for dECM 10 and n=3 for the rest of the conditions). The asterisk symbols in the plot represent: *p < 0.05 and ** p < 0.01. The error bars represent SEM.

3.3.4 Stage 5: dECM Crosslink

Stage 5 of the biomaterial formation includes the several crosslinking strategies undertaken to prepare for the cell seeding stage, where more detail is given in chapter 4. During stage 5, only condition 10 of decellularization was used to generate the dECM. The first approach is referred as "No Crosslink" and corresponds to the dECM scaffold after the PBS (or specific cell media) washing from step 6 from figure 3.8. Then, it was evaluated the crosslink using temperature, after pepsin digested dECM, mentioned in the text as Temperature Crosslink. As a result of lack

of gelation, it was investigated the addiction of riboflavin and ascorbic acid to stimulate the collagen fibres to crosslink with light. However, the strategy did not work as well, which resulted in moving forward and polymerizing fibrin gel with neutralized dECM. Sections 3.3.4.1 to 3.3.4.4 present in more detail the results.

3.3.4.1 No crosslink

This section shows the no crosslink strategy where was analysed the potential of the dECM scaffold from step 6 (figure 3.8). In figure 3.24 is presented a series of dECM after freeze-drying, after the washing step and after applying an 8 mm puncher. The image also shows the shape variability after freeze-drying, even with the 10 mm PDMS ring as a mould, not all dECM adopt a uniform shape. In this way, is necessary an extra step where an 8 mm puncher was used. From the image is also noted the swelling capacity of the dECM scaffold.
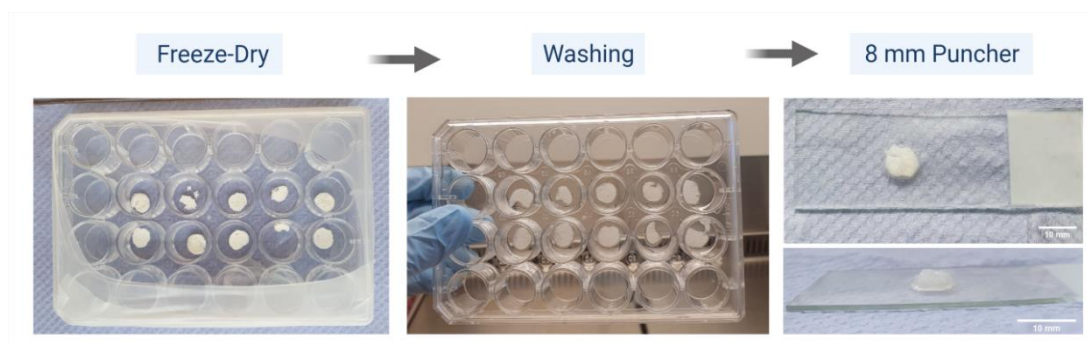
Figure 3.24: No crosslink dECM. The left image shows the top view of dECM after freeze-drying. The middle image shows the top view of the same plate but after the PBS washing step. The right image shows the top and side view of dECM after applying an 8 mm puncher (scale bar represents 10 mm). Created with BioRender.com

3.3.4.2 Temperature Crosslink

The efforts to crosslink the dECM with temperature are present in figure 3.25. However, even experimenting with different concentrations, the dECM gelation was not observed. The neutralized dECM remained liquid, which can be observed by tilting the plate at the horizontal position, the liquid accumulates at the bottom.
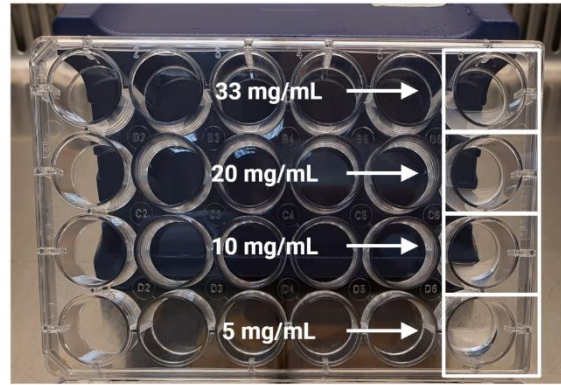
Figure 3.25: Temperature crosslink of dECM. The range of dECM concentrations tested were 33, 20, 10 and 5 mg/mL diluted with 10xPBS. Created with BioRender.com

3.3.4.3 Riboflavin Crosslinking

This section shows the apparatus when crosslinking the dECM with riboflavin and ascorbic acid under three different light sources (figure 3.26). The only condition that crosslink was 20% gelatin using the torch as the light source, where after light exposure the dECM, riboflavin and the ascorbic acid mixture was not able to be pipetted.

Given the lack of gelation, the activity of the riboflavin and the suitability of the light sources were assessed as potential reasons for the absence of crosslink. For that was evaluated if the riboflavin formulation was correct and if the power source was strong enough to reduce the riboflavin.
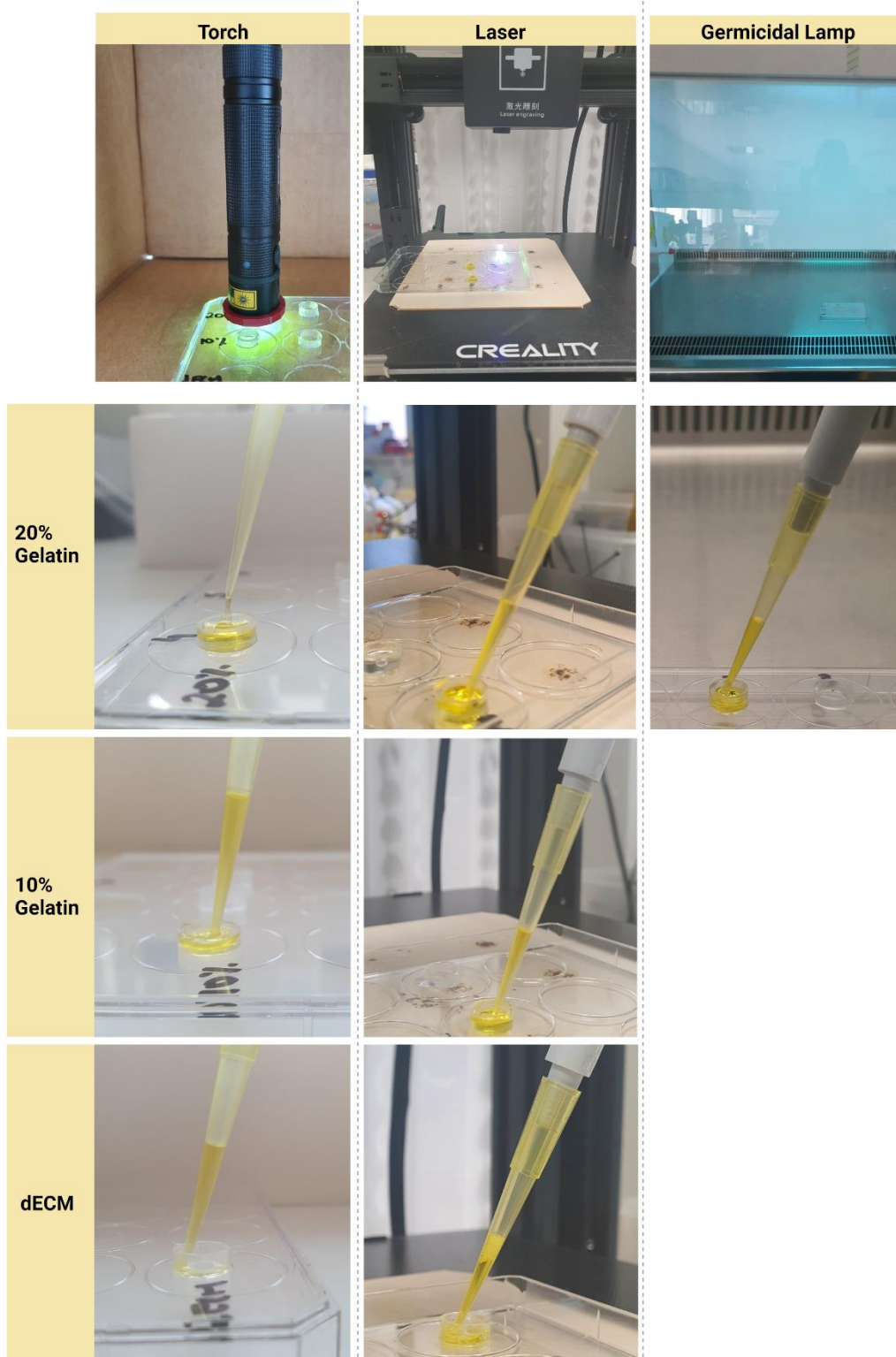
Figure 3.26: Riboflavin Crosslinking of dECM. Strategies applied for crosslink gelatin and dECM using a tourch (365 nm), laser (450.500 nm) and germicidal UV lamp (265 nm).

In figure 3.27 on the left hand side, is plotted the riboflavin absorbance spectrum at different pH values, from 6.07 to 8.16. The data shows that independently of the pH the riboflavin solution shows three absorbance peaks, one around 250-285 nm, a second one at 375 nm and the third one at 450 nm. The first range of absorbance coincides with the germicidal UV lamp, which has a maximum emission at 265 nm. The second absorbance peak can be excited with the torch at 365 nm. To excite the last peak, the laser with maximum emission in the range of 450-500 nm is suitable. The same figure, but the right hand side plot, shows the spectrum of 0.1 mg/mL riboflavin solution with pH 7 before and after light exposure with the 3 light sources. The graph shows that after exposure with the laser or torch the absorbance peaks at 375 nm and 450 nm are no longer present. On the other hand, exposure to the UV lamp does not change the absorbance spectrum.
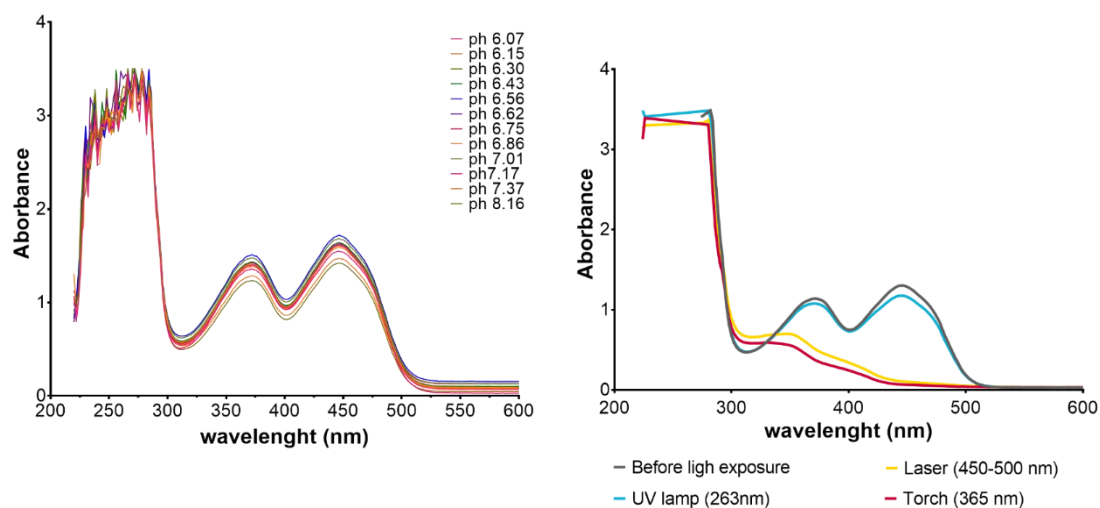
Figure 3.27: Riboflavin spectrum at different pH and before and after light stimulation. Left Plot: absorbance spectrum of a riboflavin solution containing 0.1 mg/mL at different pH values. The range of pH values are indicated in the plot with different colours, from 6.07 to 8.16 (n=3). Right plot: riboflavin spectrum of 0.1 mg/mL and pH 7 before and after light exposure. Before light exposure is represented by the grey line, the torch by the red, the laser by the yellow and the UV lamp by the blue. (n=3).

Then, it was considered the lack of collagen content as justification for the lack of gelation, since 20% gelatin was able to crosslink, but 10% not. The collagen content was determined with the Sircol kit from biocolor, used before in figure 3.14C). The samples analysed were: 20% gelatin, pepsin digested dECM during 24, 48 and 72 hours. For all the samples it was assayed 4 mg of dry content. The results are presented in the plot from figure 3.28, where it can be visualized the 100 times increase in collagen in the gelatin solution compared to dECM. It is also noteworthy

that longer digestion times does not lead to higher collagen extraction. Note that this data is only n=1, so is only suggestive.
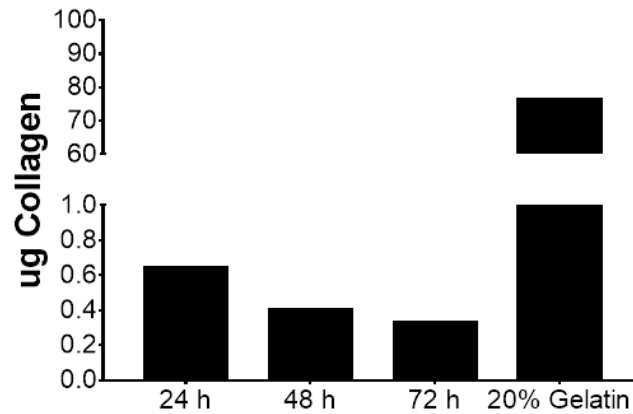
Figure 3.28: Collagen quantification. The samples plotted are: 4 mg gelatin, pepsin digested dECM for 24, 48 and 72 hours (n=1).

3.3.4.4 Fibrin Polymerization

The lack of gelation of dECM alone, resulted in the following strategy, mixing the dECM with fibrinogen and thrombin. The fibrinogen and thrombin polymerize into fibrin, which is a hydrogel extensively used and characterized in chapter 5 where the vasculature model is established on. In figure 3.29 is presented the dECM/fibrin hydrogel polymerized on a 3D printed part (make in TPU). More detail in chapter 4.

Figure 3.29: Fibrin crosslink of dECM. dECM/fibrin hydrogel polymerized in a 3D printed part. The hydrogel is situated in the central ring.

3.3.5 Stage 6.1: dTHP-1 Conditioned with Washing Waste Solution

To evaluate if the dECM could activate an inflammatory response, dTHP-1 cells were exposed to the washings from step 6 from the protocol illustrated in figure 4.2 (figure 4.8). In this way, dTHP-1 cells were exposed after 24 hours recovery period to RPMI used to wash the dECM scaffold. As control, was used fresh RPMI (referred as 0ng LPS) and RPMI supplemented with 1000 ng/mL of LPS (referred as 1000 ng LPS).
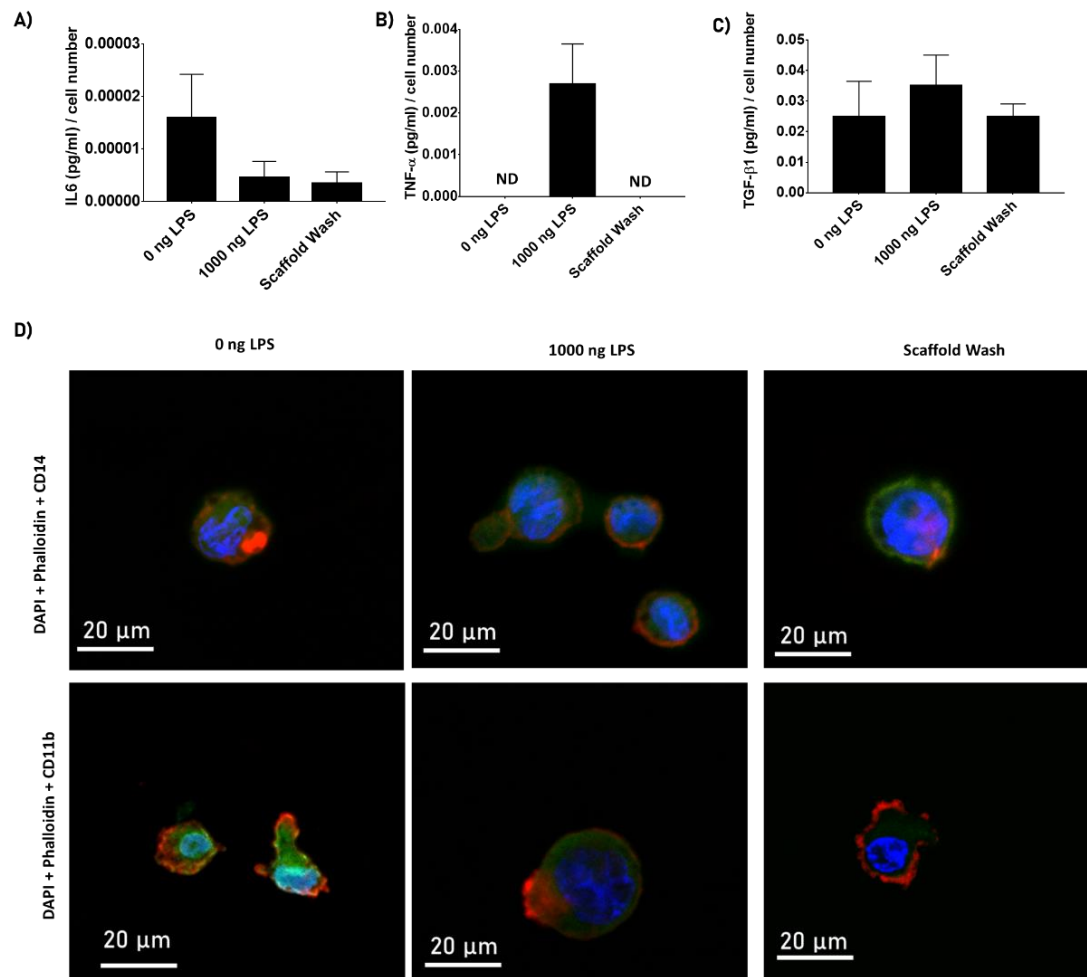
Figure 4.1: dTHP-1 Conditioned with Washing Waste Solution. PMA differentiated THP-1 and stimulated with 0 ng/ml of LPS, 1000 ng/mL of LPS and scaffold washing RPMI media. A) IL6 (n=2 and n=3 for 0 ng of LPS). B) TNF-α (n=3). C) TGF-β1 (n=3). D) Surface marker CD14 and CD11b expression showed in green, counterstained with DAPI in blue for nucleus and Phalloidin in red for F-actin (error bars represent 20 μm n=3). The legend ND represents absorbance values below the limit of detection. The error bars represent SEM.

The inflammatory response was evaluated by determining the IL6, TNF-α and TGF-β cytokines secretion as well as morphology assessment using confocal microscopy of CD14 and CD11b surface markers. The TNF-α was only detected on the wells exposed to LPS. The TGF-β shows a slightly higher value in LPS exposed samples, and scaffold wash and normal media present the same level of the cytokine. The IL6 highest value is from the normal media, but also the error bar. The LPS and scaffold wash present the same level of IL6 cytokine. Regarding the images on 8D), the cells show a nucleus that occupies most of the cytoplasm, visualised in blue from the DAPI stain and in red from the Phalloidin stain. The dTHP-1 does not show stress fibres, so the F-actin is presented outlining the cytoplasm. The cells also show CD14 and CD11b presented in green.

3.4 Discussion

The aim of chapter 3 was to present how the alveolar region biomaterial was developed, characterized and crosslinked. This was achieved in five different stages, illustrated in figure 3.1. The main findings in this chapter were first from stage 1, where the conditions to culture the HLF-1 to create the extracellular matrix were investigated. During the time in culture, the lung fibroblast showed an active proliferative profile, being selected 21 days as the time frame to produce the ECM derived biomaterial. Then, addressed in stage 2, was the establishment of the decellularization process using 10 different conditions. The characterization of the decellularized ECM, performed in stage 3, helped to narrow down the decellularization condition to create the alveolar biomaterial. The characterization used quantitative and qualitative methods to determine the DNA, protein, collagen and GAGs content. After analysing all the data, condition number 10 of the decellularization was selected to build the alveolar biomaterial. The next stage, number 4, originated from the need to understand how the assays used during dECM characterization were being affected by leftover residues of the surfactants (used during the decellularization protocols). This investigation helped to conclude that the surfactant of choice to perform the decellularizations, number of washing (and washing solutions) and assays selected for the characterization should be chosen with attention. Then in stage 5, can be found the different strategies for dECM crosslink. The main conclusion from this part of the chapter indicates that collagen production from a cell derived ECM technology needs to be maximized to be able to avoid external crosslinker agents. Lastly, in stage 6, the dTHP-1 were exposed to the last wash of the dECM scaffold to understand if residues of the surfactant could hinder cell viability. From the results, the cells were viable and the waste media did not induce any pro-inflammatory response. Below can be found in more detail a discussion of the results from stage 1 to 5.

3.4.1 Stage 1: 2D HLF-1 Characterization

The initial 2D characterization helped to determine if the HLF-1 could be cultured for 21 days while maintaining viability, function and morphology. Despite the trypan blue data showing a maximum of cell death of 25% on the 21st day, the number of live cells and dsDNA content increase during the culture time, indicating that cells are still actively dividing. In addition, the MTS plot shows that the metabolic activity per number of live cells fluctuates along the 21 days, from 0.0002 to 0.0005. If day 14 is ignored, MTS has its maximum on day 3 and then shows a slow decreasing slope until reaching 0.0002 on day 21. Comparing each data point to day 1, only day 21 shows a lower metabolic activity indicating that 21 days should be the optimal time

length to culture the HLF-1 before incurring in significant metabolic drops. Moving forward to the dextran blue data, the cells take 21 days to build a tight monolayer, especially between days 7 and 21, where the absorbance of dextran blue suffers a higher reduction. In terms of morphology, the cells maintain a very elongated shape during all culture time, as expected for fibroblast. Since with the higher confluency is not recorded any abnormal shape transition, it can be concluded that the cells are not affected by density. All this data supports the hypothesis that the HLF-1 continue viable and active during the 21 days. As a result, 21 days were used to develop the alveolar biomaterial through the decellularization of the HLF-1 cell sheet.

Conclusion	
HLF-1 Characterization	▪ The HLF-1 are viable and proliferative for 21 days The HLF-1 have the lowest metabolic activity on the 21st in culture ▪ The HLF-1 spindle shape morphology does not change with high confluency
Overall Project	▪ Selected 21 days, as culture time of HLF-1, to develop the alveolar biomaterial

3.4.2 Stage 3 and 4: dECM Characterization and Troubleshooting

In this section can be found the discussion of the DNA, GAGs, collagen and protein quantification from the dECM. To discuss the dECM characterization is going to be analysed the results together with the requirements introduced by Peter M. Crapo article[119] (presented in method section 3.2) and together with the results obtained from the troubleshooting section.

<50 ng dsDNA per mg ECM dry weight

The first requirement sets a limit of double strand DNA for below 50 ng per dry weight. In the thesis, two methods were used to quantify the DNA: picogreen and nanodrop (with previous nuclei acid purification with QIAamp kit). Before analysing the results, it is necessary to state some background knowledge that distinguishes both methods. For instance, the picogreen is a fluorescence reagent that binds only to double-stranded DNA. The presence of other nuclear material such as ssDNA and RNA only contributes to a 10% increase in the total fluorescence signal[136]. On the other hand, the nanodrop uses the absorbance at 260 nm to measure the nucleic acids, contributing to the signal: dsDNA, ssDNA and RNA. To ensure accurate results the nanodrop measures the 260/280 and 260/230 ratios. A ratio of around 1.8 is considered pure

DNA and around 2 is accepted as pure RNA for 260/280. In addition, the 260/230 ratio must be higher than the 260/280 to ensure pure nucleic acid and between 1.8 – 2.2. The ratios obtained for conditions 1 to 10 of dECM can be seen in appendix 1. The 260/280 ratio is higher than expected which indicates RNA contamination. On the other hand, the 260/230 ratio is within the range, indicating an absence of proteins as contaminants. The QIAamp kit used to purify the nucleic acids prior to nanodrop quantification was able to remove the protein, even on conditions 1 and 2, which have the highest amount of protein (from H&E characterization). However, regarding the nuclear acids, the manual instruction followed retrieved all genomic content, including RNA, which explains the higher 260/280 ratio. The fact that the nanodrop quantifies all DNA and RNA explains why this method quantifies 10x more nuclear content than the picogreen. In this way, picogreen or similar methods that just quantify the dsDNA would be better suited to meet the requirement above (less than 50 ng dsDNA per mg ECM dry weight) than QIAmp purification and nanodrop quantification, except if ensured only dsDNA purification.

The reason behind 10x more nuclear content measured with the nanodrop compared to picogreen, does not explain the abnormal tendencies observed in the graphs 3.14A) and 3.14B). In the case of picogreen, a table can be found in appendix 6 detailing the effect of SDS, triton and sodium chloride on the fluorescence signal (obtained from picogreen manual instructions). For QIAamp, contaminants that absorb at the same wavelength as 260 nm include free nucleotides, proteins, phenol and EDTA[136]. The effect of these contaminants is put aside after the 260/230 ration evaluation. If any of those contaminants were to be present, they would affect the ratio.

Regarding the picogreen assay, the documented effect, present in appendix 6, on SDS and triton interference in the fluorescence signal is in line with what was measured in figure 3.20. Note that this data was generated from the surfactant effects on 100 ng of DNA, but in figure 3.20, a range from 100 to 0.1 ng was analysed. The SDS decrease the signal, the same was observed in figure 3.20 and in figure 3.14A), where 0.5% SDS leads to a total signal elimination. Regarding the triton, the data from figure 3.20 is in line with the picogreen manual instruction (except for the low amount of dsDNA, 0.1 ng) as well as figure 3.14A), where except for the 0.05% (1x) triton, all conditions where triton alone was used show increase signal compared to the fresh condition. The combination of triton and SDS in figure 3.20 shows that the 0.5% triton cleans the effect of the 0.05% SDS (except for 0.1 ng DNA), which is also documented in other publications[137–139].

The same effect is not observed in plot 3.14A), with both conditions 9 and 10 having higher dsDNA quantification. An important chemical that should have been analysed as the SDS and triton in figure 3.20 is sodium chloride. The osmotic solution has 1M of NaCl and all the washing steps are performed with PBS with 155.1 mM, which would lead to a 150% and 23% fluorescence signal reduction respectively. To remove the effect of the salt, in future could be used distilled water for the washing steps. A more hypotonic environment would lyse the cells as well.

Noteworthy, that this data alignment does not happen in figure 3.21, where the last PBS wash for the several decellularization conditions was used to dissolve the dsDNA standard. The rationale to use the last PBS wash was that the residual concentrations found in the dECM matrix would be closer to the ones in the last PBS wash than on the fresh SDS or triton solutions. All the decellularization conditions lead to an increase in the fluorescence signal, including the fresh and freeze-thaw where no chemicals were added. This positive influence in the signal is higher as the DNA concentration decrease (except for 0.05% triton), which may indicate another contaminant as the reason for the signal disturbances. Note that for this data analysis, the fluorescence signal from 0 ng of dsDNA was removed from the data, which eliminates the signal from dsDNA already present on the last PBS wash.

In addition, to rule out the papain digestion solution as the reason for the picogreen fluorescence signal influence, is presented in appendix 7 the same study as in figure 3.20. But with TE buffer as the control condition, as recommended in the manual instructions. The papain solution throughout the dsDNA concentration range tested, does not lead to a signal influence more than 17% compared to TE. This indicates that does not interfere with the picogreen dye and subsequently the results from the dECM DNA characterization.

After making sure that papain does not interfere with the fluorescence signal, it was tested if it lead to total dECM digestion. In the troubleshooting section, graph 3.19 shows that when nanodrop is the quantification method, higher values of DNA are recorded, since nanodrop uses 260 nm absorbance as the quantification method as explained above. One thing that is noticed is that when picogreen method is used, samples digested with papain, have higher dsDNA values than protease K digestion samples. This situation is even more visible if QIAamp is used as an intermediate step to purify the nucleic acids. This concludes that from n=1 data, papain digestion is a good method to disrupt the dECM.

<200 bp DNA fragment length

To quantify the DNA fragment size of dECM, an agarose gel was used to separate the fragments and syber safe dye to stain them. The samples used to run the gel, were the same presented in plot 3.14B). The sybr safe is able to stain DNA as well as RNA, so the total nucleic content purified from the QIAmp is stained. In this way, the gel in figure 3.16 shows total nucleotide content. From decellularization condition 1-10 was loaded 1 µg of total nucleotides. In this way, it was expected the same band intensity. However, conditions 3,4,9, and 10 have higher band intensity. The documentation indicates that triton residues do not interfere with the sybr safe dye, but SDS reduce staining efficacy. However, the opposite was observed, conditions where SDS was used during the decellularization procudure had stronger band signal. To address this issue, was tested supplementing conditions 1 and 4 with 0%SDS, 0.05%SDS and 0.5%SDS. The results can be found in appendix 2. It is observed that the higher the SDS supplementation, the less intense is the band. This helps to conclude that SDS contamination is not the cause for the higher band intensity found in conditions 3,4,9, and 10.

To further investigate the reason why those bands have higher intensity, it was tested to load the same volume of sample straight from the eppendorf (20 µL of the sample), instead of loading the same amount of DNA. The results are in appendix 3. The same group of samples was used to run the gel in figure 3.16 and appendix 3. The idea behind this test was to observe on the gel a correlation between concentration and band intensity. However, looking at samples 1 and 3, 1 has 3 times more nucleotides concentration and has less band intensity.

It was last tested the effect of AE buffer, since from figure 3.16, AE buffer shows a visible band (appendix 4). In appendix 4 from supplementary data can be found 3 repeats of condition 1 (condition 1 was used, since has the highest nucleotide concentrations and where residual AE buffer would have the smallest effect). It was loaded 1 µg of nucleotides either diluted in water or AE buffer, where it can be concluded that AE buffer does not increase the signal or change fragment size.

In DNA gel electrophoresis two features can be analysed, the band intensity for determining the relative amount and fragment size. The nanodrop, as mentioned before, measures all types of nucleic acids as well as syber safe, so a correlation should exist between nanodrop determined concentrations and band intensity. However, visually that does not happen.

Regarding the length of the fragments, the required limit for a decellularized tissue is the presence of fragments with a maximum 200 pb. The fragments detected on the agarose gel have around 1kb in size, much higher than the requirements to consider the cell sheet decellularized.

For higher specificity toward detecting double strand DNA in the agarose gel, SYBR® Green should have been used. The syber safe links to all nucleic acids while SYBR Green I is an ultrasensitive stain for dsDNA.

Lack of visible nuclear material in tissue sections stained with DAPI or H&E

Regarding the third requirement, dECM condition 1-10 was stained with H&E and DAPI, figure 3.12 and 3.13. Analysing the bright filed H&E images under triton treatment, is observed a correlation between a higher concentration of detergent or the number of treatment repeats with less nuclear content. The nucleus is no longer oval, and the purple colour is associated with string-like structure. The SDS treatments cause a clear elimination of dark purple, associated with DNA, when concentration increases to 0.5%. The combined treatments of SDS and triton as expected show more nuclear clearing than its individual counterparts. Using DAPI is more visible the effect of the SDS, the nuclei look more like a diffuse smear. The treatment with both detergents caused a further DNA reduction as parallel to what is seen for H&E. Looking at the triton effect, 10x higher concentration of triton and treatment repeats also show a progressive reduction of organized nuclear content. Both stains, show results similar to what was excepted, in terms of harsher treatments containing less visible nuclear content. Although, comparing both methods, DAPI seems to bind more to DNA than *H&E.*

In conclusion, from the 3 requirements introduced by Peter M. Crapo article[119], only the last one was achieved, lack of visible nuclear material. The requirements regarding the dsDNA content and the fragment size were not fulfilled. To quantify the dsDNA more accurately it could be used the QIAamp to purify the DNA together with the picogreen to quantify only dsDNA[137]. Alternatively, the Qubit™ 1X dsDNA Assay Kits (from Invitrogen) could be used, which documents no interference to the fluorescence signal when 0.01% SDS is used.

To induce fragmentation of DNA, an extra step in the decellularization protocol with endonucleases and exonucleases, such as DNase (or RNase) and benzonase respectively, would enzymatically degrade the DNA[140–142].

Glycosaminoglycan Characterization

The discussion so far has focused on the DNA characterization of the decellularized ECM, with qualitative data not following quantitative approaches. The same problem was encountered

when determining GAGs using the Glycosaminoglycan Blyscan Assay or Alcian blue staining. The quantitative measurements with the Blyscan kit were able to quantify total, O-sulfated and N-sulfated GAGs. The data does not follow the tendency expected, with harsher decellularization treatments having higher total or O-sulfated GAGs. The N-sulfated GAGs is determined by subtracting the total from O-sulfated GAGs, which originated only negative values as observed in the plot from figure 3.15C). The same tendency is seen in the GAGs graph, with µg of GAGs increasing with higher concentrations of SDS or Triton and number of treatments. After contacting customer service, was suggested to further dilute the samples to prevent surfactant cross reaction with the blyscan dye.

To overcome the blycan dye limitation, the dECM was stained with alcian blue. The triton treatments retain more glycosaminoglycan than SDS. From conditions 5-8, a visible blue structure is observed. While during SDS, or combined treatments a more diffuse blue is present. Regarding preserving GAGs in the matrix, triton treatments would be beneficial, the same conclusion was found in other research articles[119,143]. A substitute for the blyscan assay could be the dimethylmethylene blue assay for total GAGs determination[144,145].

Collagen Characterization

The collagen quantification was the only feature quantified that followed the trend expected. In figure 3.14C), harsher treatments have a more negative effect on collagen levels. In addition, join treatments seem to have an accumulative effect on collagen elimination, observed in conditions 7,8 and 10. The collagen quantification follows the tendency of the eosin Y stain, except for conditions 6 and 7, from the images looks like more pink is observed on condition 7, but the plot is observed a negative slope from conditions 5-8. From the collagen point of view, the more the better for the matrix formation, however, a balance situation needs to be met, between DNA removal and ECM conservation.

Protein Characterization

The protein quantification present in figure 3.14D) also follows an abnormal tendency, the method used to quantify the protein was the DC assay from Bio-Rad, which stands out for Detergent Compatible assay. However, the company has also available a reducing agent and detergent compatible assay: RC and DC assay which will be a good alternative. The reducing

agents present are in the papain digestion solution, such as DTT and EDTA, which could be interfering with the results.

To complement the quantitative protein characterization, the total dECM protein content was visualized on an SDS page gel. In figure 3.17 is found repeat 1 for conditions 1 and 9 and two biological repeats for condition 10. The third repeat for condition 10 and the second for condition 1 are present in appendix 5. The variability between the repeats indicates that a more standardized mg of dry dECM needs to be established. Despite adjusting the pepsin and acetic acid volume for different dry dECM weights, 24 hours digestion can lead to complete fragmentation of the dECM[146]. This is shown in the SDS-PAGE gel where the band is located at the end of the gel. If excluding the condition where digestion was excessive, condition 10 in figure 3.17 show band A, B and C highlighted, which compared to other research papers, these 3 bands may indicate respectively β, α1 and α2 chains from collagen[108,147]. The addiction of a collagen SDS-PAGE standard would confirm this statement. The gel also shows with less intensity a band around 50 kD and a smear from 25kD until the end, which indicates the presence of other metabolites. The SDS-PAGE on appendix 5 also shows a very intense band between 75 and 50kDa. This band is not characteristic of pepsin digested collagen, so another protein is being secreted from the HLF-1 in high amounts. To elucidate the total protein content of the dECM a technique as mass spectrometry could help to identify proteins in the bands.

Scanning Electron Microscopy

To finalize the dECM characterization, the surface was imaged with scanning electron microscopy, since fibre arrangement is important for cell adhesion and viability[148,149]. The SDS is reported to significantly alter the dECM surface[148,143], which is confirmed by the images in figure 3.18. The comparison between the fresh with condition 10, shows visible surface alteration by the lack of porous in condition 10.

SDS Quantification with Methylene Blue

The traces of the different chemicals used along the decellularization and digestion process of the dECM impact the assays in different ways, so a careful selection of the assays and stains needs to be done in future. Nevertheless, guaranteeing extensive washings steps to remove most of the residual contaminants should be a priority as well. The contaminants not just interfere with the assays but also with cell viability. With this in mind, the SDS content was

quantified with the methylene blue assay. The dECM is washed 3 times before being stored at -80° C. The washing steps are enough for conditions 1-8 where the percentage of SDS is at the same level as PBS. However, for conditions 9 and 10, extra washing steps until the percentage of SDS decrease to PBS levels should be introduced in future. Noteworthy that was expected conditions 9 and 10 to benefit from the triton cleaning effect, but maybe this cleaning effect is not detected on methylene blue assay as is on picogreen.

The methylene blue assay could be introduced to guarantee SDS levels below control levels, between washing steps. This could also be introduced on the washing step after dECM freeze-dry, figure 3.8 step 6. Where extending the washing for 6 days reduced the SDS content on the washing to PBS levels.

However, further analysis on correlating the SDS content from the washings and the one that is bound to the dECM matrix needs to be established. The extra washing steps either before or after drying does not necessarily ensure reducing the SDS content bound to the dECM matrix to the levels of the washings. Is visible that dECM washed 3 times after decellularization and 2 days after drying contains bound to the matrix double the amount determined after the 2 days washing.

This may indicate that extra washing steps before freeze-drying may be more significant in lowering the SDS content. The SDS is an anionic surfactant and an amphipathic molecule with a high affinity to proteins, especially to the lysine amino acid. A successful strategy to remove SDS is to apply a washing step with a solution with pH = 9 or 75% ethanol as shown by the publication of Terence Woods and collegues[148]. In conclusion, the addiction of SDS quantification after each wash to guarantee control levels together with washing with pH = 9 buffer solution or 75% ethanol could help reduce SDS content on dECM matrix.

The effect of the extra washing step is visible in figure 3.22, where dsDNA value from condition 4 increased after 48 hours wash with media. The same effect was not visible at the protein level, the use of the RC and DC assay would be a better suit for protein quantification if the contaminates are not just detergents as explained before.

In conclusion, after the characterization of the dECM, was chosen condition number 10 to produce a matrix to seed the alveolar model. It was taken into account the qualitative characterization of the dECM together with the collagen quantification from plot C) in figure 3.14. The condition that led to more DNA removal was 0.5 %SDS, but also more ECM damage. Then it was evaluated side by side conditions 9 and 10, on average condition 9 has 12 times

more collagen but visually looks like retaining more DNA so it was selected condition 10 to move forward as a compromise scenario between DNA removal and ECM preservation.

Conclusion	
dECM Characterization: Main Conclusions	- dsDNA, protein and GAGs content not quantified accurately - DNA fragments lengths above requirement - Visual reduction in nuclear content and ECM with decellularization - Collagen content determined accurately
dECM Characterization: Alternative Methods	- dsDNA: Qubit™ 1X dsDNA Assay - DNA Gels: SYBR® Green - Collagen: add collagen marker for SDS PAGE Gel - Protein: RC and DC assay - GAGs: Dimethylmethylene blue assay
dECM formation: Protocol Improvements	- Add a fragmentation step with a DNase (or RNase) - Distilled water as washing step - SDS content control over the entire dECM formation process - Add wash with pH=9 solution or 75% ethanol to remove SDS - Create SOP for dECM pepsin digestion - Test condition Freeze-Thaw + 0.5% Triton (>3x)
Overall Project	Decellularization condition 10 - Freeze -Thaw + 0.05%SDS + 0.5% Triton (3x) - was selected to create the alveolar biomaterial

3.4.3 Stage 5: dECM Crosslink

No Crosslink

The no crosslink strategy corresponded to the dECM scaffold from step 6, figure 3.8. From figure 3.24 is observed high variability of fragments shape, although an 8 mm puncher was used to uniformize the shape, the membranes still have different heights. The freeze-dry used was composed of a vacuum pump connected to a reservoir that achieved -110°C, not allowing further optimizations. In addition, the SEM image (from figure 3.18) of the scaffold surface indicates a lack of porous. Despite the enumerated limitations, cells were seeded on the dECM scaffold, which data is present in chapter 4.

Temperature Crosslink

To address the problem above and to prevent scaffold to scaffold variability the dECM was digested with pepsin. The pepsin cleaves the collagen carboxyl bounds making it soluble. After the digestion, with pH and temperature adjustment, the collagen in the digested dECM should crosslink, as described in different literature articles[106–108,114,150]. However, gelation was not observed.

Riboflavin Crosslink

With the lack of gelation from the temperature crosslink approach, was tested stimulating collagen bound with riboflavin supplementation and light stimulation. However, no polymerization was observed as well, with images from figure 3.26 showing the unsuccess of the experiment as well. At this point, three major features were highlighted as possible contributors to the lack of polymerization:

1. Inactive riboflavin or inadequate light source
2. Insufficient power from light source
3. Low collagen content, riboflavin and ascorbic acid to start the reaction

To investigate the riboflavin activity, was determined the absorbance spectrum of 0.1 mg/mL riboflavin solution at different pH values (higher concentrations of riboflavin lead to signal saturation). To all conditions, the riboflavin shows a similar spectrum as reported in others literature articles[151,131], with peaks at 275 nm, 375 nm, 450 nm. The peaks coincide with UV germicidal lamp from the hood, torch and laser, the light sources used to excite the riboflavin. This finding indicates adequate riboflavin formulation and light source.

To address if the light sources had sufficient power to reduce the riboflavin, was determined the spectrum before and after light exposure. The spectrum shows that after exposure with the torch and laser the peaks at 375 nm and 450 nm reduced, concluding that the molecule is no longer active. This experiment excludes point two as the reason for the lack of polymerization.

Regarding point number 3 of the troubleshooting presented above, the only condition that polymerized was a mixture with 100 µL of 20% gelatin, 10 µL of riboflavin (10 mg/mL stock) and 10 µL ascorbic acid (10 mg/mL stock). It was also tried to supplement 20% gelatin, with 1 and 0.1 µL riboflavin and ascorbic acid, but these conditions did not polymerize. Indicating an optimal concentration of 1 mg/mL of riboflavin or ascorbic acid to achieve polymerization. The

absence of polymerization when using 10% gelatin it was a first indication that the lack of collagen may be the cause of the crosslink absence. To investigate it further, it was determined the collagen content of 20% gelatin and dECM digested during 24, 48 and 72 hours. The results from one biological repeat show around 100 times more collagen in 20% gelatin than 24 hours digested dECM, suggesting once more that the absence of polymerization may be a result of a lack of collagen. Despite the lack of success on crosslinking the dECM with riboflavin, this agent has been used to improve the mechanical properties of decellularized tissues, such as vascular grafts[133] or porcine heart[109]. Other crosslinkers have also been documented[152], such as genipin, a naturally-derived agent used to crosslink a rat trachea[153]. Or glutaraldehyde and carbodiimide used for crosslink a decellularized meniscus[154]. So, in future, other agents can be investigated as well to promote dECM crosslink.

Taking a brief look at collagen composition and its biosynthesis, the fibres are composed of a repetition of glycine amino acidic every third position (Gly$n$ – X-Y), with proline and lysine often occupying the X and Y position. To these amino acids are then added hydroxyl groups by the enzymes prolyl hydroxylase and lysyl hydroxylase. These enzymes require ascorbic acid as a cofactor to function and lysyl requires as well Cu^{2+}. The next post-translation modification is the glycosylation of the hydroxyl lysine by adding glucose and galactose[155].

Given the high content of proline in collagen (20%), is considered an important amino acid in collagen biosynthesis. Proline can be synthesized from arginine, glutamate and glutamine[156]. Fibroblast in low glutamine media shows a lower capacity of proline synthesis[157]. Lung fibroblast required glutamine for inducing collagen through TGF-β pathway[158]. However, collagen is secreted in higher amounts in proline supplementation than in glutamine[159]. The DMEM media used to culture HLF-1 contains glutamine and arginine but lacks proline. An alternative media is RPMI1640 which contains 20 mg/mL of proline.

In addition, after realizing the crucial role of ascorbic acid, preliminary tests on increasing ascorbic acid from 500 µM to 5 mM were done, resulting in an increase of dECM weight of 4 times. The 10x increase in ascorbic acid supplementation in association with proline could boost collagen production. In this way, future work should investigate media composition and extra supplementation for promoting collagen biosynthesis and in this way be able to crosslink dECM alone. This could be confirmed by 7 days culture of HLF-1 and PCR quantification of genes of interest for collagen production, such as for the most common collagen type, collagen 1 (COL1A1/2), but also lung specific collagens as collagen III (COL3A1), VI (COL6A1/2/3), XIV (COL9A1), XIII (COL13A1) and XVIII (COL18A)[155].

Fibrin Polymerization

The alveolar model is going to be placed on top of the vasculature model, which is created using fibrin gel. In this way, due to the lack of collagen to initiate polymerization with riboflavin, it was used the neutralized dECM as a supplement for fibrin gels with 1.25 mg/mL fibrinogen and 5 U/ml thrombin. This combination was selected as is the concentration that led to the more elastic gels, results in data chapter 5. The dECM/fibrin gel was tested for supporting cell growth, which data can be found in chapter 4.

Conclusion	
dECM crosslink	▪ Test extra supplementation of ascorbic acid and proline during HLF-1 growth to increase collagen biosynthesis
Overall Project	▪ No crosslink dECM scaffold and dECM/fibrin gel were used further in chapter 4 to test the capacity in supporting a cell population

4.4.1 Stage 6.1: dTHP-1 Conditioned with Washing Waste Solution

The dTHP-1 were exposed to dECM wash (2 days RPMI wash) to have preliminary data on the impact that SDS could have on cell viability. The measurement of SDS content on such a wash is present in chapter 3, figure 3.28, which determined the SDS content of 0.012%. This means, dTHP-1 under condition media were exposed to approximately 0.012% SDS. For the dTHP-1 seeded on stage 6.1 that concentration did not appear to interfere with cell viability, with cells presenting normal morphology.

Alighting with this rationale is the presence of TNF-α only on the samples stimulated with LPS[160]. The LPS is also known to stimulate IL6[160], but such pronounced stimulation was not seen. Taking into account the variability of the normal media, all conditions secrete IL6 approximately at the same level. Regarding the TGF-β, its secretion is associated with M2 macrophages. This type of macrophage has high phagocytosis capacity, is able to produce ECM, angiogenic and chemotactic factors and IL-10[160]. The concentration is slightly higher in LPS supplementation than in without LPS supplemented or scaffold washing media, but is not statistically significant. Indicating that what was measured may be the TGF-β baseline value.

This preliminary study demonstrated that dTHP-1 are able to tolerate the 0.012% SDS.

.

Chapter 4

Alveolar Region Cell Culture
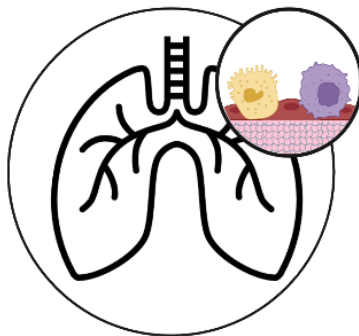
4.1 Introduction

In chapter 3, the focus was selecting the biomaterial to resemble the alveolar region extracellular matrix. The solution was to decellularize a human lung fibroblast cell sheet, retrieve 21 days of ECM secretion and transform it into a biomaterial. In this chapter, the attention lays on which cells to populate the alveolar biomaterial with, an aspect as important for the model outcome. With that in mind, two questions were made:

1. Choose between cell lines or primary cells?
2. How diverse needs to be the cell population?

The primary cell lines are patient specific, which could be beneficial for personalized medicine. However, to develop high throughput models, donor heterogeneity and tissue availability could make an extra challenge. As an alternative, there are human pluripotent stem cells (hPSCs), which include both embryonic stem cells (ESCs) and induced pluripotent stem cells (iPSCs). These cells have the capacity to differentiate into a more committed cell state and recapitulate embryo development *in vitro*, examples of these are when incorporated in organoid *in vitro* models. The ESCs share the same limitations as with primary cells, with the addition of ethical issues. On the other hand, the iPSCs don´t have a controversial origin, but research is still ongoing on protocol optimization for the different lung epithelial cells[161]. Despite the pros and cons, the lack of possibility to work with primary or hPSCs cells on this project, makes the cell source restricted to cell lines. The following reviews from Sebastian G. Klein *et al* (2011)[162] and Nichols, J *et al* (2104)[163] list in a table the most common cell lines used in the lung *in vitro* models. In addition to the cells listed in the reviews, the hAELVi cell line derived in 2016 was also considered for the alveolar type I cell line[96].

After selecting cell lines as the target for the cell source, was evaluated the diversity of the cell population of the alveolar region. Section 1.1.3 in the introduction already detailed the alveolar epithelium composition but in brief, is composed of alveolar type I and II that have a barrier and secretory function respectively. The alveolar type I cells are in direct contact with the endothelial cells and actively participate in the gas transfer. The alveolar type II cells are responsible for surfactant, from secretion until recycling and are mostly found in the septal areas of the alveoli. In these areas are also mostly found supportive cells such as fibroblast and smooth muscle cells in a rich ECM environment. The immune cells are the alveolar macrophages, that move within the hypophase across the alveolar surface[11]. This brief overview of the alveolar region cell population demonstrates the importance to have epithelial, immune and supporting cell representation in the models. The immune cell presence becomes even more relevant with the fact that the model aims to be used for risk assessment of inhaled particles.

Then, the information of the commercially available cell lines, was crossed with the cell diversity aimed in this project, as well as with the cell lines which the lab had experience working with. As a result, was selected the monocyte cell line THP-1, that was differentiated with PMA into macrophage as representative of the immune system. Representing the epithelial cells were tested: A549, H441 and hAELVi. Lastly, the human lung fibroblast from chapter 3 were also tested, to play a role of supporting cells.

In conclusion, this chapter used the biomaterials derived in chapter 3, the dECM scaffold and the dECM/fibrin gel, as a substrate to build on the alveolar model. As mentioned above, five cell lines were tested from epithelial, immune and stromal origin to make the model more relevant regarding cell diversity in the alveolar niche. The cell's viability was analysed in terms of morphology with bright or fluorescence microscopy and cytokine secretion. At the end of this chapter, was selected which biomaterial and cells would be used to build the alveolar region model presented in Part 1 from figure 1.9. This alveolar model was then used in chapter 7 to build the full model, where vasculature and bioreactor are included as shown in figure 1.10.

4.2 Methods

Chapter 3 focused on showing the stages undertaken during the development and characterization of the biomaterial for the alveolar region. This chapter tested the biomaterial from two different steps of the process in supporting cell attachment and proliferation (from steps 6 and 9.3 illustrated in figure 3.8). In figure 4.1, such seeding strategies are illustrated by stages 7.2 and 7.3 in the dECM scaffold and in the dECM/fibrin gel respectively. To be able to seed the cells in the biomaterial was required to design and 3D print two parts, that resemble a transwell and the respective well, to support air liquid interface.
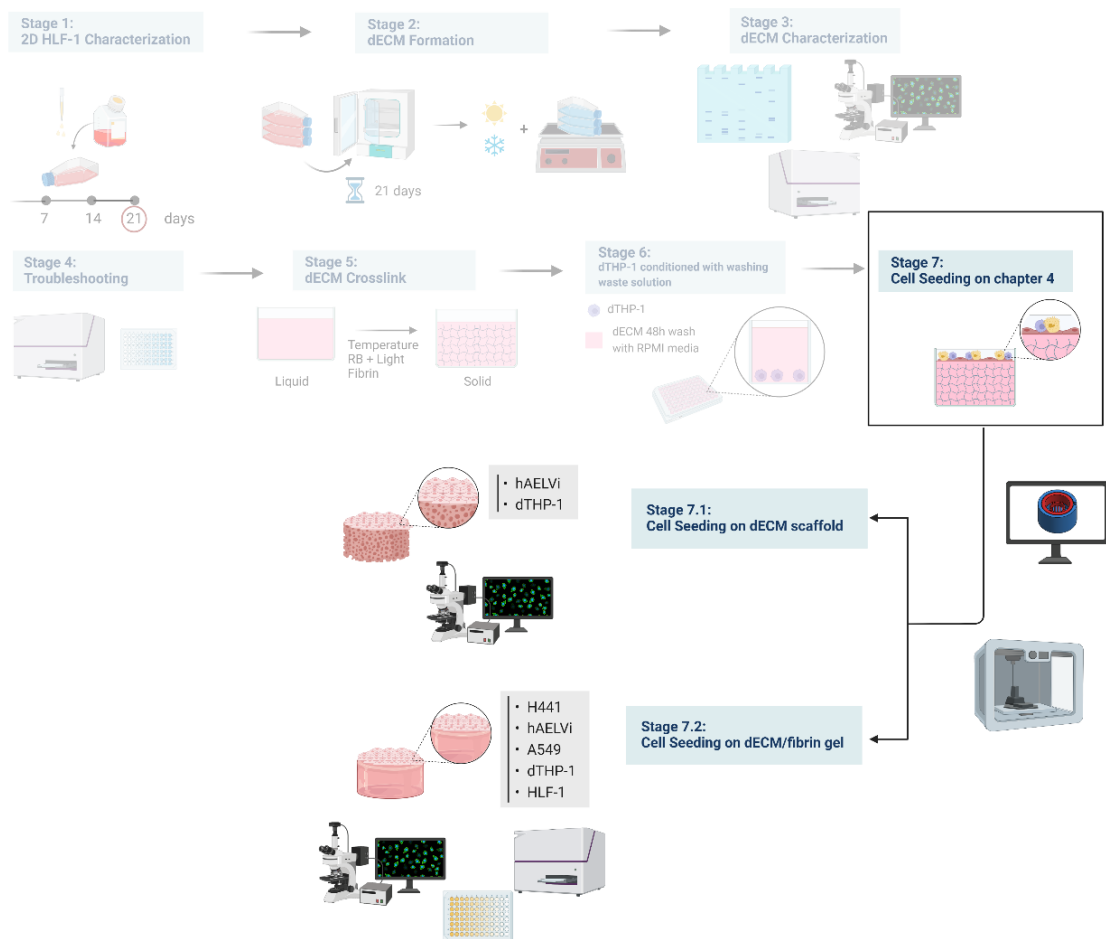
Figure 4.1:Overview of the tasks included in chapter 4. This chapter follows the biomaterial formation presented in chapter 3. Stage 7 refers to cell seeding strategies undertaken, that are performed in the dECM scaffold in stage 7.1 and the dECM/fibrin in stage 7.2. The cells seeded on stage 7.2 were the hAELVi and dTPH-1 and seeding success was evaluated by confocal microscopy. On stage 7.3, were additionally seeded H441, A549 and HLF-1. The cells were also evaluated by confocal microscopy and the A549 and dTHP-1 for cytokine presence in the media. Created with BioRender.com

The two seeding strategies from stages 7.1 and 7.2 originate from two different steps of the decellularization process. The illustration of figure 4.2 helps to pinpoint from each step of the protocol the dECM scaffold and the dECM/fibrin are from.
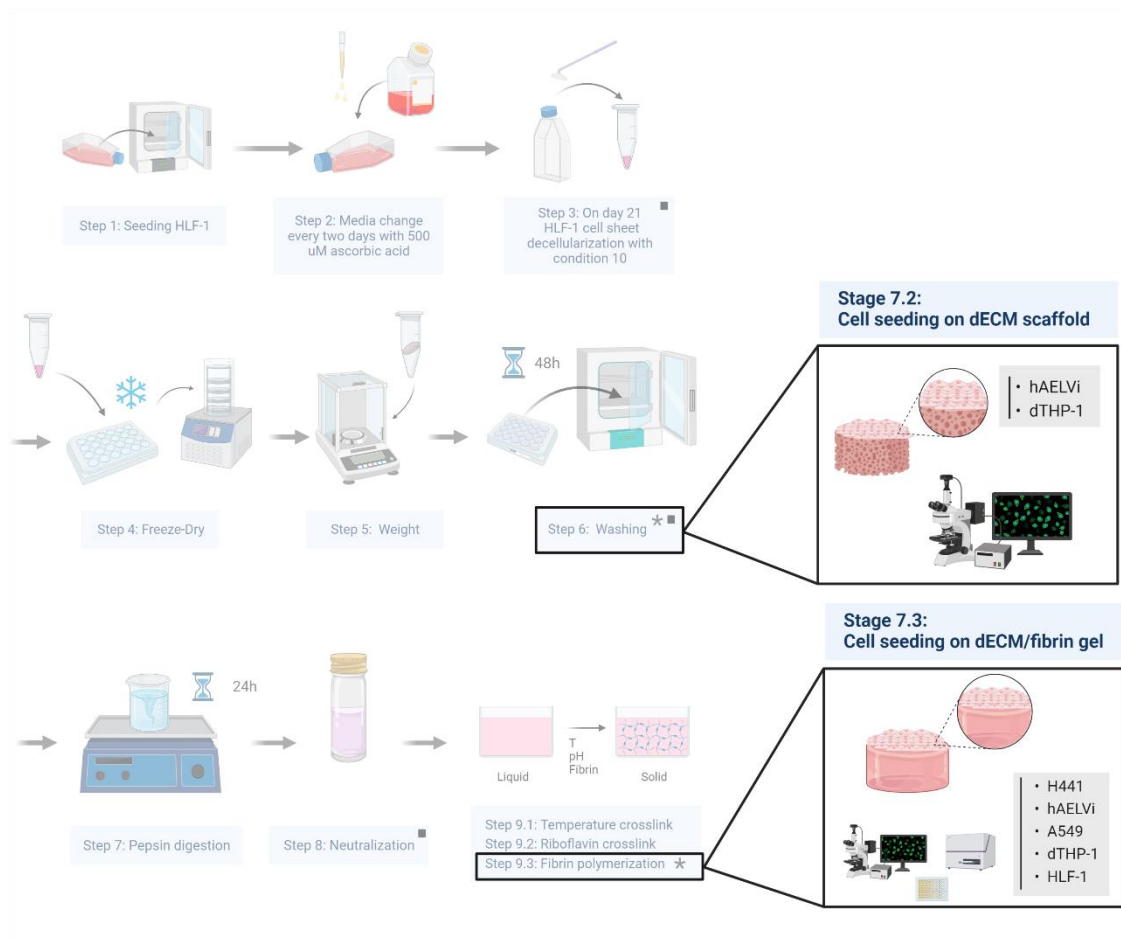
Figure 4.2: Link between stages 7.1 to 7.2 and dECM formation procedure. Stage 7.1 derivates after the washing step (step 6). Stage 7.3 derivates from the polymerization of fibrinogen and thrombin together with papain digested dECM. Created with BioRender.com

4.2.1 Stage 7.1: Cells Seeding on dECM Scaffold

The first seeding strategy on the dECM biomaterial, was after the washing step, illustrated in figure 4.2 by step 6. The wash was performed with PBS or cell line specific media. To address the irregular geometry, was used an 8 mm puncher to remove the excess dECM scaffold as already mentioned in figure 3.24.

To seed the cells in the scaffold, the Autodesk Inventor® program was used to draw the scaffold and media holder that then 3D printed in polyurethane (TPU). Both parts fit into a 12 well plate and allow an air liquid interface. In figure 4.3 can be found the technical sketches and images of the printed parts.

The scaffold holder has a lattice at the bottom from where the biomaterial contacts with media and stoppers on the side to prevent the scaffold to float under submerged conditions. The bottom compartment holds 350 µL and the top one 100 µL. For sterilization, the printed parts were placed in 70% ethanol during 24 hours. Prior to cell seeding, the parts were left in the hood to dry and rinsed with media three times.
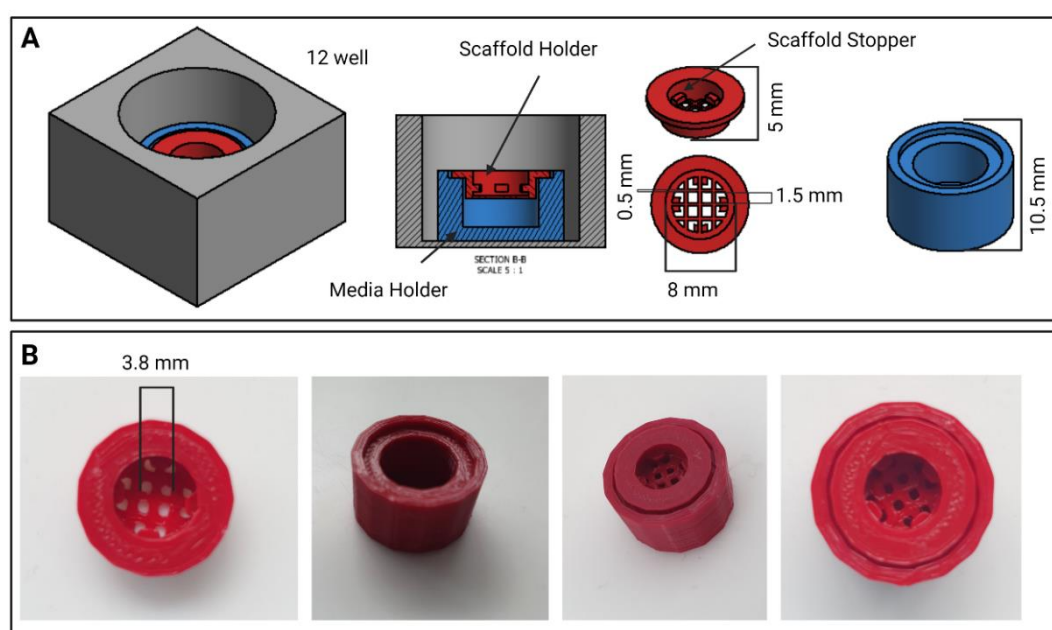
Figure 4.3: dECM scaffold 3D printed support. A) Technical sketches from the Autodesk Inventor® program of the scaffold and media holder. B) Image of the 3D printed parts. Dimensions annotated are in millimetres (mm). Created with BioRender.com

4.2.1.1 dTHP-1 dECM scaffold Seeding

The THP-1 were handled as detailed in section 2.3.3 and differentiated as mentioned in section 2.3.3.1. Then, the cells were seeded at 40 000 cells/cm^2 (20 000 cells per dECM scaffold) in the dECM scaffold at a total volume of 50 µL, with the bottom compartment containing 350 µL of RPMI media. After 24 hours, the scaffold was either kept in submerged conditions (where 50 µL was top up) or brought to ALI. For the latter, it was removed the media from the top compartment of the scaffold holder. Then, after 24 hours it was stimulated the cells with 1000 ng/mL of LPS. For the submerged condition, the media was removed and added 2.57 µL of the LPS stock solution with 175 µg/mL into a 450 µL of fresh media. The media was distributed to the top and bottom, 100 µL and 350 µL respectively. Regarding the ALI condition, 2.09 µL of LPS stock was added to 365 µL of fresh media. The media was distributed to the top and bottom, 15

μL and 350 μL respectively. The cells were exposed to LPS for 24 hours before stopping the experiment. At this point, the cells were processed for confocal microscopy imaging. The timeline of the experiment is present in figure 4.4.
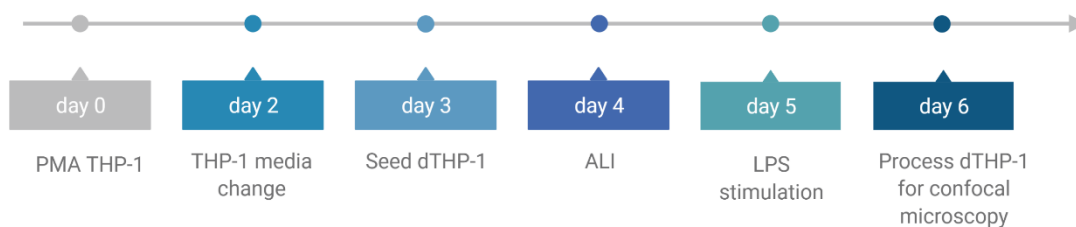
Figure 4.4 Timeline of the dTHP-1 seeding on the dECM scaffold. Created with BioRender.com

4.2.1.1.1 dTHP-1: CD11b Fluorescence Staining

Regarding dTHP-1 processing for confocal microscopy, the cells and scaffold were fixed with a 4% PFA solution for 15 minutes at room temperature. Then, was blocked for one hour at room temperature with 1% BSA solution in PBS. Next, CD11b primary antibody (#ab269676 from abcam) was added in 1:1000 dilution in 1% BSA solution overnight at 4°C. Then, the scaffold was washed three times with PBS for one minute each wash before adding the secondary antibody solution. The latter contained the secondary antibody Alexa Flour 555 donkey anti-rabbit at 1:1000 dilution, together with DAPI (2 μg/mL) and Phalloidin (1:200). The incubation lasted for one hour at room temperature and was protected from light. After the incubation period, the scaffold was washed three times with PBS with one minute between washes. A total of 100 μL was added to each scaffold of the primary and secondary antibody solution. The scaffold was imaged using a Zeiss LSM 710 with 405 nm laser to excite DAPI, 543 nm laser for the CD11b and 633 nm laser for the Phalloidin.

4.2.1.2 hAELVI dECM scaffold Seeding

The hAELVi were handled as detailed in section 2.3.4. The cells were seeded on the scaffold, at 200 000 cells/cm^2 [164] (100 000 cells per dECM scaffold) in a total volume of 50 μL with 350 μL of media in the bottom compartment of the media holder. After 24 hours the top compartment of the scaffold holder was topped up with 50 μL. The cells were under submerged conditions until day 2, when half of the samples were brought to ALI and the other half were kept under submerged conditions as a control. The culture lasted for 14 days, with fresh media added on days 4, 7 and 10 of the culture. The cells were analysed on days 2, 7 and 14 at the confocal microscopy.

4.2.1.2.1 hAELVi: ZO-1 and Occludin Fluorescence Staining

The cells and scaffold were fixed for 15 minutes with 4% PFA at room temperature. After two times washing with PBS for 1 minute each, the scaffold was either stored at 4°C with 0.1M of glycine or stained. The scaffold was stained with ZO-1 (#33-9100 from Invitrogen) or occludin (#33-1500 from Invitrogen), where the same protocol was applied. To commence the stain, the scaffold was permeabilized with 0.1% triton solution for 5 minutes at room temperature. Then, washed two times with PBS for 1 minute each, before blocking for 1 hour at room temperature with 10% FBS in PBS. The scaffold was then washed two times with PBS for 1 minute each, before being added to the first antibody solution. This solution contained the first antibody (Z0-1 or occludin) diluted in PBS at 1:200. Each scaffold was incubated with 50 μL of the first antibody solution overnight at 4°C in the shaker[164]. On the following day, the scaffolds were washed two times with PBS for one minute each before being added the secondary antibody solution containing 1: 100 secondary antibody (Goat anti-Mouse Alexa Flour Plus 488), 1:200 Phalloidin and 2 μg/mL DAPI. The secondary antibody solution (50 μL per scaffold) was incubated for 1 hour at room temperature and protected from light. After incubation time, the scaffolds were washed one last time for 3 times with PBS for one minute each before imaging on a Zeiss LSM 710 using laser the 405 nm for DAPI, 488 nm for ZO-1 and 633 nm for imaging Phalloidin.

4.2.2 Stage 7.2: Cell Seeding on dECM/fibrin Gel

The second seeding strategy consisted of adding to digested dECM, fibrinogen and thrombin following the protocol illustrated in figure 4.2, step 9.3. For more detail on dECM/fibrin polymerization refer to section 3.2.5.7 in chapter 3.

Parallel to seeding the cells in the dECM scaffold, a gel and media holder were designed in the Autodesk Inventor® program and 3D printed in TPU. The media holder supports 650 μL or 350 μL depending on the height of the media holder being 10.5 mm or 8 mm. Then, more 100 μL are able to fit on the gel holder for submerged experiments. For sterilization, the prints were autoclaved. The sketches and images are in figure 4.5, where can be seen that the media holder is similar to the one presented in figure 4.3. But the gel holder suffered some adjustments. The central ring is where the polymerization of the dECM/fibrin takes place, and the media contacts with the gel from the lattice in the bottom. The central ring has 0.3 cm^2, so the area available for seeding is 0.3 cm^2 instead of 0.5 cm^2 as in figure 4.3. In this set up, in submerged conditions the media contacts with the cells, if the media holder is fully filled. Another feature is the facility in accessing the media level from the media holder, which is especially important when air-liquid interface is established.

Regarding the cell seeding, after 75 µL of dECM, fibrinogen and thrombin mixture polymerize in the central ring, the gels stay undisturbed for 15 minutes in the hood and then 2 hours in the incubator (humidified 37°C, 18% oxygen and 5% CO_2). After this period, the gels are ready to be seeded. Note that when diluting the d ECM from 33 mg/mL to 20 mg/mL it was used cell line specific media.
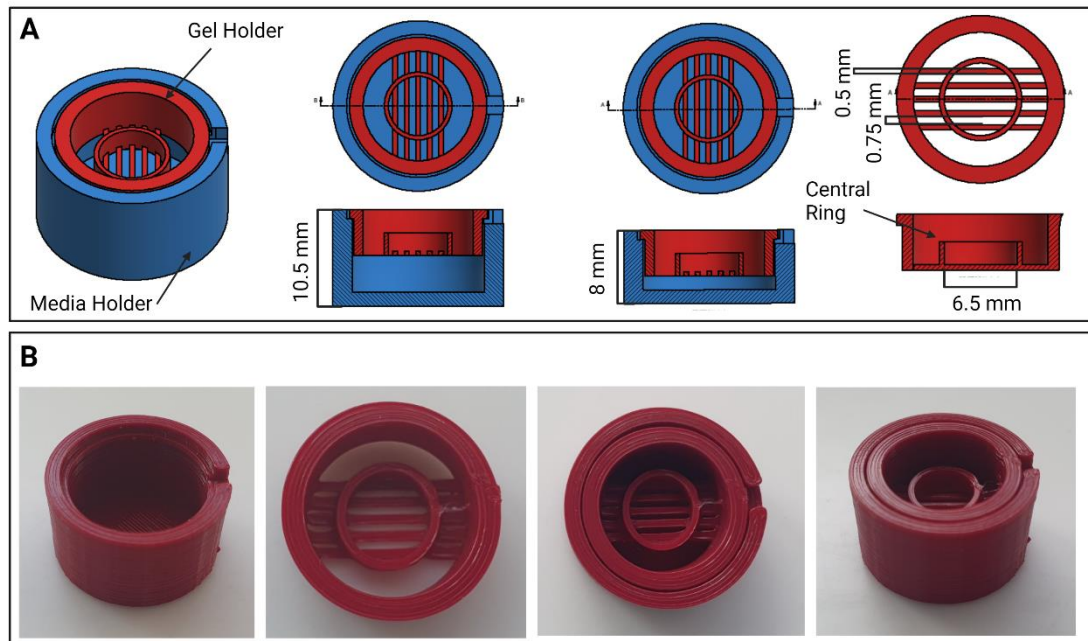
Figure 4.5: dECM/fibrin 3D printed support. A) Technical sketches of the gel and media holder for the dECM/fibrin gels with 10.5 or 8 mm in height. B) Image of the 3D printed parts. Dimension noted in milometers (mm). Created with BioRender.com

4.2.2.1 hAELVI seeding on dECM/fibrin gel

To investigate the ability of the hAELVi cells to grow on dECM/fibrin gel, the cells were seeded on the 3D printed gel holder for ALI experiments using the 10.6 mm media holder. For submerged conditions, the dECM/fibrin was polymerized in an 8 mm PDMS ring (with 0.5 cm^2). For comparative reasons, the cells were also seeded on commercially available Transwells. In figure 4.6 is depicted the experiment timeline.

The cells were handled as described in section 2.3.4. On day 0, the cells were seeded at two different seeding densities: 100 000 cells/cm^2 and 50 000 cells/cm^2 in a total volume of 50 µL. On the following day, 650 µL of media were added to the bottom compartment and 100 µL to the central ring. The experiment lasted for 7 days and air liquid interface was established on the second day. At this point, the 100 µL were removed from the central ring. On the 4th day of culture, 100 µL media were added to the media holder for media replenishment.

For cells seeded on Transwells, the same seeding density and experimental protocol was followed. However, note for successful cell attached in Transwell the PET membrane needed to be coated with a huAEC Coating Solution as described in section 2.3.4. The insert size used was a 12 well, with 1.12 cm^2 cell growth area. The apical side took 0.5 mL media and the basolateral 1.0 mL. On the second day, half of the samples were brought to ALI and the other half remained in submerged conditions. On the 4th day, fresh media was added, 100 µL in both the top and bottom compartments for submerged conditions and 100 µL in the bottom compartment only for ALI experiments. For the ALI experiment, in addiction, every day was removed the excess media from the apical side.

For morphological assessment the cells were imaged following the protocol from section 4.2.1.2.1. In addition, the media was analysed for IL6 and IL8 ELISAs following the method described in sections 2.5.1 and 2.5.4 respectively. For data analysis, in addiction to what is described in the protocol, the values were divided by the cell number. The cell number was determined by following the protocol in section 2.7. The results from hAELVi characterization on the Transwells can be found in appendix 11 to 13.

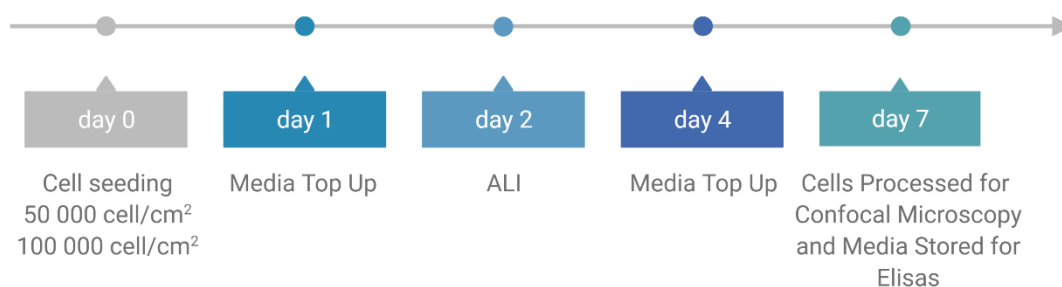**Figure 4.6: Experiment timeline of hAELVi seeded on dECM/fibrin gel.** Created with BioRender.com

4.2.2.2 H441 seeding on dECM/fibrin gel

To investigate the H441 growth in the dECM/fibrin gel, the cells were seeded in the gels and in Transwells as described in protocol 4.2.2.1. The H441 cells were handled as specified in section 2.3.5. The results from H441 characterization on the Transwells can be found in appendix 8 to 11.

4.2.2.3 HLF-1 seeding on dECM/fibrin gel

To evaluate the growth of HLF-1 on the dECM/fibrin gel, the cells were seeded during 7 days. The HLF-1 were cultured as in section 2.3.1. The dECM/fibrin gel was polymerized in the central ring of the gel holder, and it was used the 8 mm in height media holder. The cells were seeded at 5000 cells/cm^2 (1500 cells per dECM/fibrin gel) in a total volume of 50 µL. On day 1, the bottom compartment was filled with 350 µL of DMEM media and more 100 µL was added on top. The media was supplemented extra with aprotinin at 20 µg/mL. This supplementation comes from knowledge of the fibroblast culture in fibrin gels from chapter 5. The cells were in submerged cultured during the seven days, with media top up on day 4 of culture. The total volume of 100 µL was added to the media and central ring with aprotinin supplemented.

On day 7th the cells were processed for staining by fixing them with 4% PFA solution for 15 minutes. After removing PFA with two cycles of washing with PBS one minute each, a solution containing 1:200 Phalloidin and 1 µg/mL DAPI in PBS was added to the dECM/fibrin gel. A total of 100 µL of staining solution was added to each gel. The staining solution was incubated for one hour at room temperature. To remove the excess staining, three cycles of PBS wash were applied before imaging the gels on the Zeiss LSM 710 using the laser 405 nm for DAPI and 633 nm for Phalloidin.

4.2.2.4 A549s seeding on dECM/fibrin gel

The A549 cells were cultured as specified in section 2.1.6. The dECM/fibrin was polymerized on the central ring of the gel holder and the media holder use had 8 mm in height. The cells were seeded at 2.79 x10^5 cells/cm^2, the gel has 0.3 cm^2, so a total of 83 400 cells per gel were seeded. On day 1, the bottom compartment was filled with 350 µL of RPMI media and more 100 µL was added on top of the central ring. The cells were in submerged conditions during four days, when half of the samples were brought to ALI by exposing the gel to the air, while the other half continue submerged[165]. On the 4th day of culture, 100 µL of media was added to the media holder of the ALI experiment. For submerged it was added 100 µL to the bottom compartment and 100 µL on top of the cells. The experiment was stopped on days 4 and 7, where cells were processed for confocal microscopy and the media collected for cytokine quantification. The timeline of the experiment is present in figure 4.7.
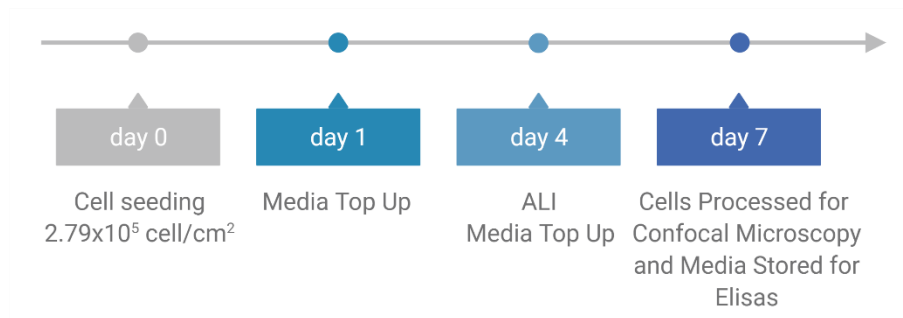
Figure 4.7: Experiment timeline of A549 seeded on dECM/fibrin gel. Created with BioRender.com

The same experimental protocol was followed when A549 were seeded in the transwell for comparative studies. The insert size used was the 12 well, with 1.12 cm^2 cell growth area. The apical side took 0.5 mL media and the basolateral 1.0 mL. On the 4th day, fresh media was added, to both top and bottom compartments 100 µL for submerged and 100 µL in the bottom compartment for ALI experiments. For ALI experiments, media was collected daily from the apical to maintain the air liquid interface.

For morphological assessment, the cells were imaged following the protocol from section 4.2.1.2.1. In addition, the media was analysed for IL6 and IL8 ELISAs following the method described in sections 2.5.1 and 2.5.4 respectively. In addiction, was also quantified the LDH in the media using the protocol described in section 2.6. For data analysis, in addition to what is described in the protocol, the values were subtracted by the value of plain media, divided by the cell number and multiplied by the volume of the sample. In this way, it was possible to compare samples with different cell numbers and total volumes, such as the ones seeded on the gel and on the transwell. The cell number was determined by following the protocol in section 2.7.

4.2.2.5 dTHP-1 seed on the dECM/fibrin gel

To evaluate if the dECM/fibrin gel could initiate an immune response, differentiated THP-1 were seeded on the gel. It was used the 3D printed media holder with 8 mm in height to make the study. The same experimental design was used as described in figure 4.4. The THP-1 were handled as described in section 2.3.3 and differentiated as mentioned in section 2.3.3.1. The cells were seeded on day 0 at 40 000 cells/cm^2 (12 000 cells per gel). On the following day, 350 µL of media was added to the bottom compartment of the media holder and the cells were either brought to ALI or keep in submerged (top up with 100 µL of media). After 24 hours period, media was removed and fresh media with 1000 ng/mL of LPS was added. For ALI conditions, 350

µL was added to the bottom compartment and 15 µL on top of the cells. For submerged conditions, 350 µL was added to the bottom compartment and 100 µL to the top.

On the following day, the media was collected for IL6, TNF-α and TGF-β ELISAs following the protocol described in sections 2.5.1 to 2.5.3. In addition to the data analysis described, the values were also divided by the cell number. The cell number was determined by following the protocol in section 2.7. In addition, the cells were prepared for imaging as described in section 4.2.1.1.1.

4.3 Results

In this result chapter, can be found the cell seeding experiments on the dECM scaffold and dECM /fibrin gel, present in sections 4.3.1 and 4.3.2 respectively. The cell lines used to test the capacity of the biomaterials to support cell attachment and proliferation were from lung epithelial (A549s and H441), stromal (lung fibroblast) and immune (differentiated TPH-1). The data from this chapter will help to narrow down the biomaterial and which cell lines to build the alveolar model.

4.3.1 Stage 7.1: Cells Seeding on dECM Scaffold

This section shows the results when hAELVi and dTPH-1 cells were seeded on the dECM scaffold. In figure 4.8 is presented the scaffold placed on the 3D printed parts under ALI and submerged conditions.
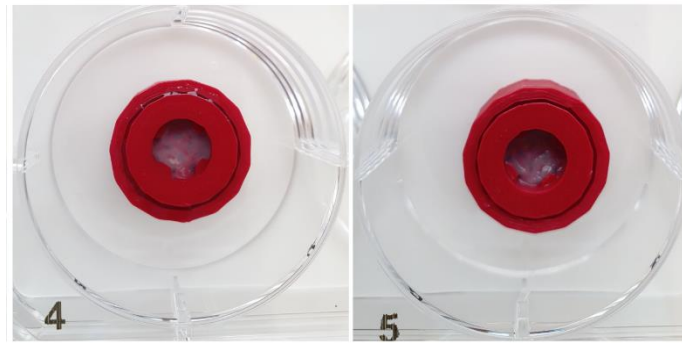
Figure 4.8: dECM Scaffold positions on the 3D printed support. The left side image shows the dECM scaffold under submerged conditions. The right hand side image shows the dECM scaffold on ALI.

4.3.1.1 dTHP-1 dECM scaffold Seeding

In figure 4.9 is presented images of dTHP-1 seeded in the dECM scaffold under submerged and ALI conditions with 0 or 1000 ng/mL LPS. The nucleus is shown in white and the CD11b in green, however, the cells were found in low numbers through the scaffold surface.
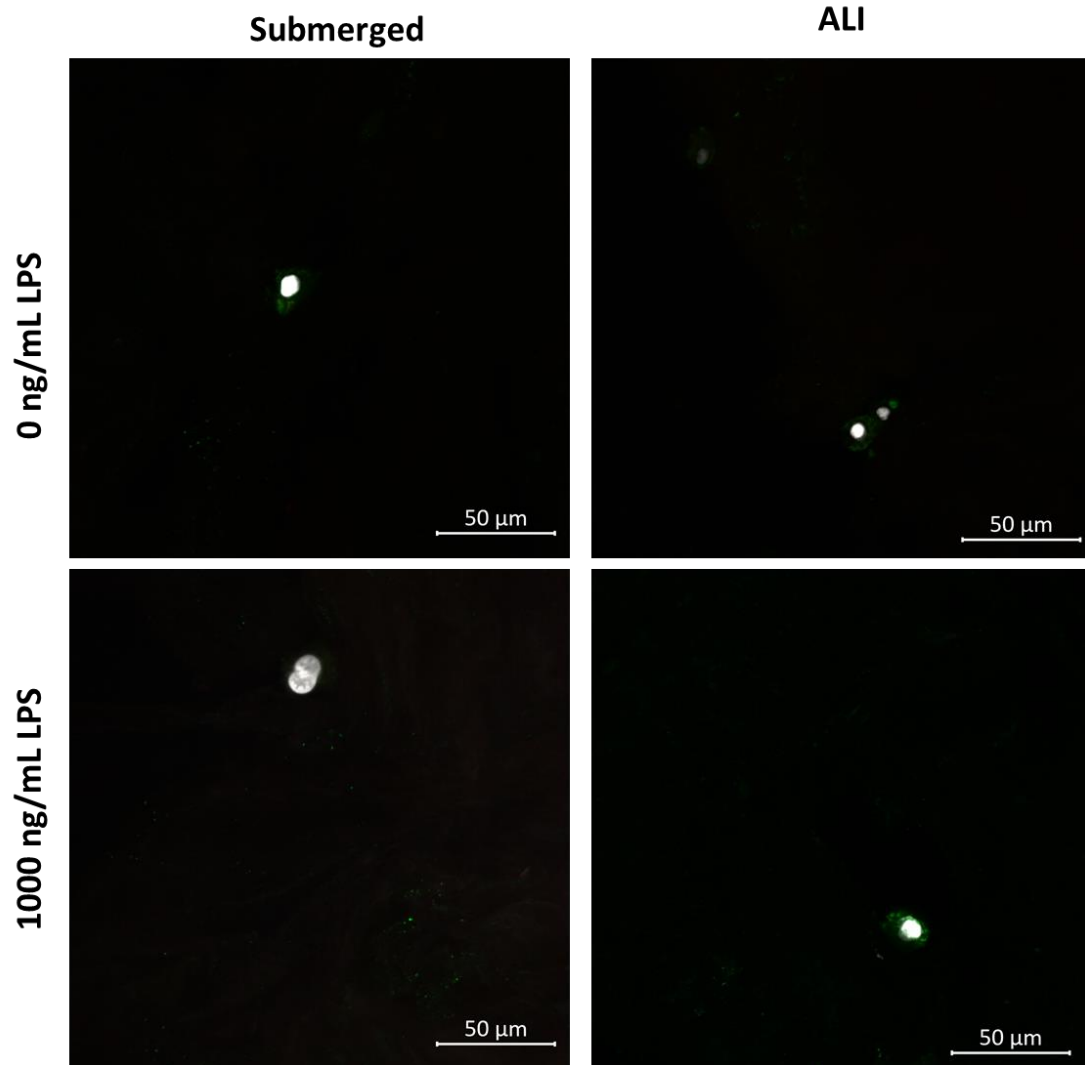
Figure 4.9: dTHP-1 seeded on dECM scaffold. The nucleus is showing in white and the CD11b in green. (n=2 and scale bar represent 50 µm).

4.3.1.2 hAELVi dECM scaffold Seeding

In figure 4.10 is presented images of the hAELVi cells seeded on the dECM scaffold under submerged and ALI conditions at time point day 2, 7 and 14. The cells on day 2 of culture are covering the entire scaffold area on the occludin stain. However, for the Z0-1 stain, cells were not found. On day 7, were only found cells in submerged condition, but given the poor staining quality of DAPI and Phalloidin, the cells don´t look viable. On day 14 is found cells with a blue nucleus, but just in some parts of the scaffold under ALI.
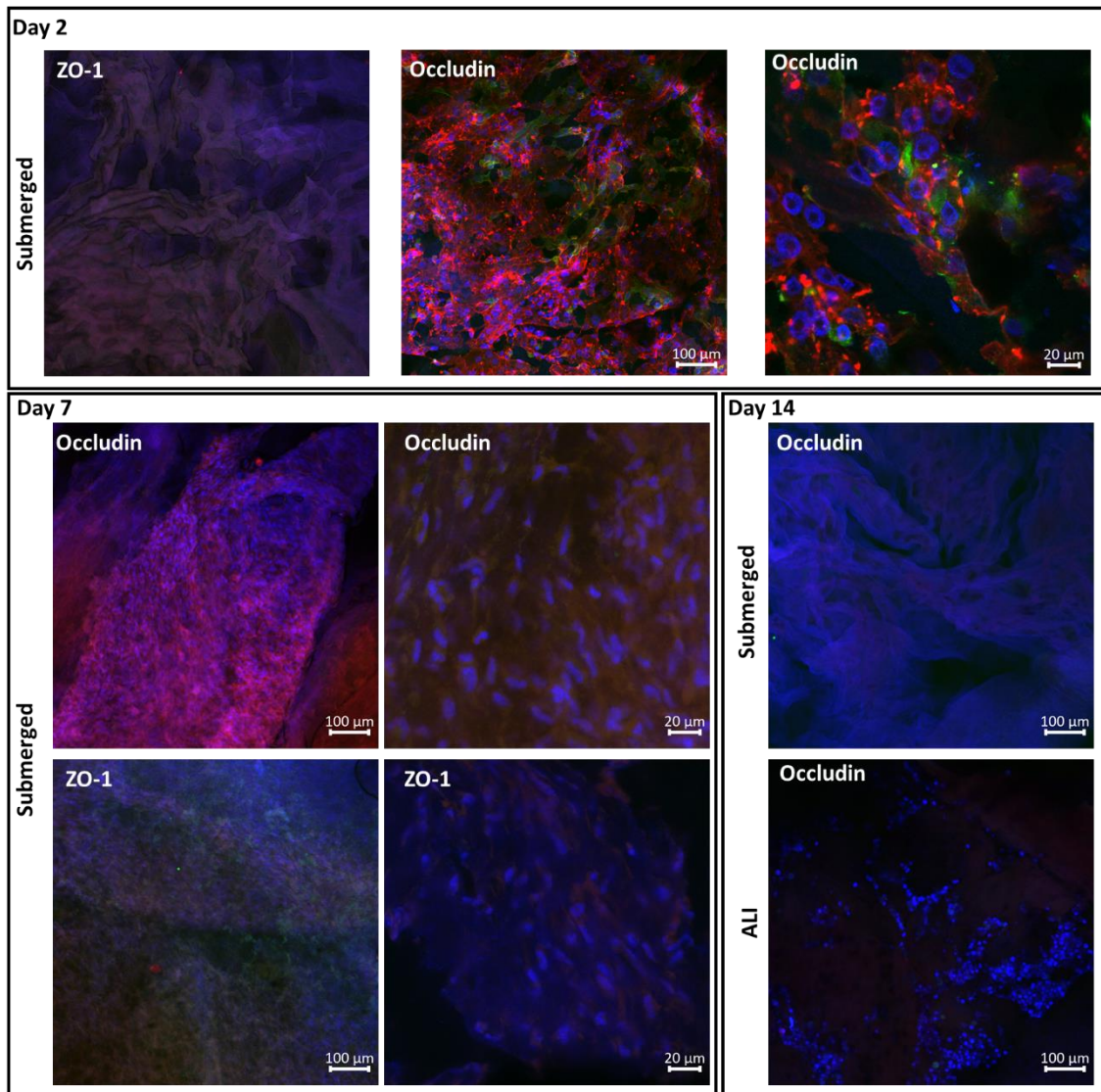
Figure 4.10: hAELVi seeded on dECM scaffold. The nucleus is showing in blue, the red F-actin and green occludin or ZO-1. (n=1 scale bar represents 100 or 20 μm).

4.3.2 Stage 7.2: Cell Seeding on dECM/fibrin Gel

The following section shows the results when H441, hAELVi, HLF-1 and A549 cells were seeded in the fibrin/dECM gel. In figure 4.11 is presented the gel in submerged conditions or under ALI when polymerized on the central ring of the gel holder.

Figure 4.11: Fibrin/dECM gel polymerized on 3D printed support. The gel is under submerged conditions on the left side of the image, and at ALI on the right hand side of the picture. Created with BioRender.com

4.3.2.1 H441 dECM/fibrin Gel Seeding

The H441 were seeded on fibrin/dECM gel as described in section 4.2.2.2 However, the cells were not able to be cultured on the gels during the 7 days. On the 2^{sd} day of culture, the cells were suspended in a mixture of digested gel and media, with total gel degradation occurring on the 4th day (figure 4.12). In appendix 8-10 can be found H441 characterization on Transwells.
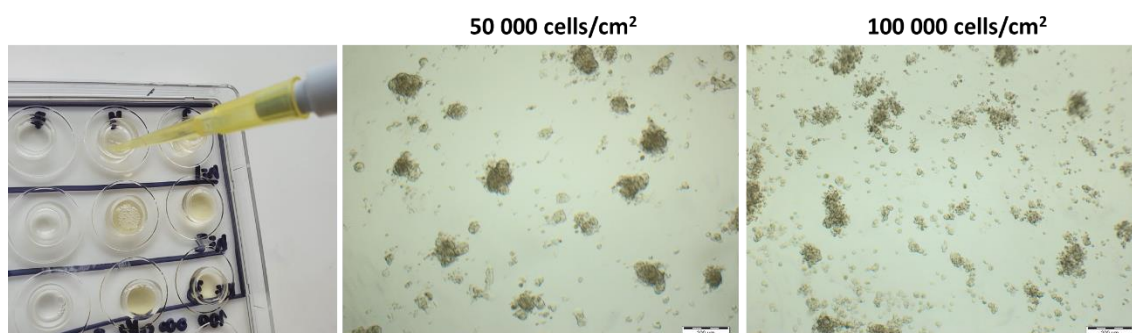
Figure 4.12: H441 cells seeded on fibrin/dECM gel. The images correspond to the 4th day of culture under submerged conditions. The left side image depicts the digested gel, the image in the middle the cells at 50 000 cells/cm^2 seeding density and the right hand side image the cells at 100 000 cells/cm^2 cell density (n=3 and the scale bar represents 200 μm).

4.3.2.2 hAELVi dECM/fibrin Gel Seeding

Contrary to the H441 seeding results, the gel did not degrade when hAELVi cells were present (figure 4.13). However, the cells were poorly attached, showing a round morphology and lack of ZO-1 expression. In addition, on the tile scan images can be found cells outside the gel, that were dragged with PBS wash. In the appendix 11-13 can be found hAELVi characterization on Transwells.
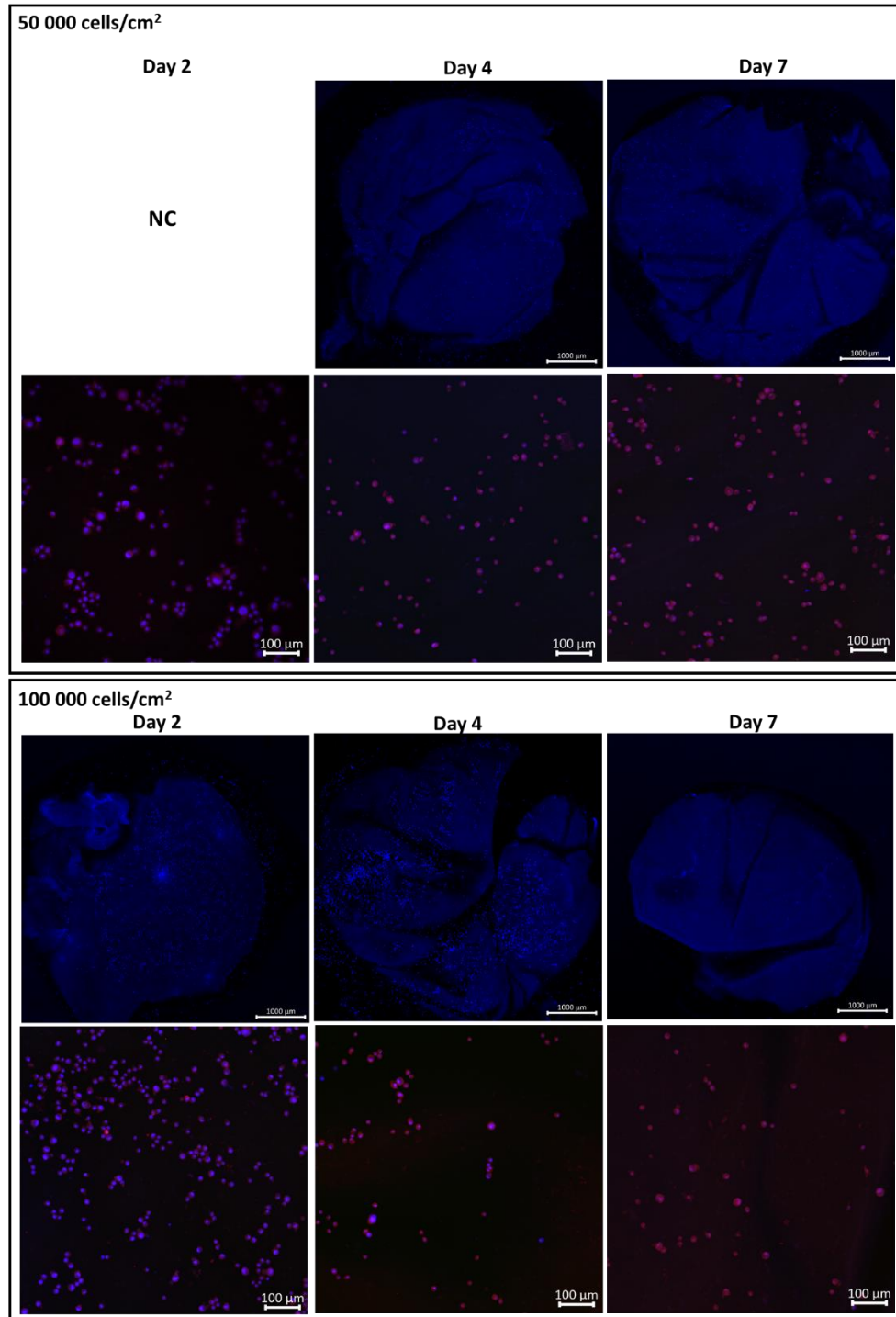
Figure 4.13: hAELVI seeded on fibrin/dECM gel. The images correspond to cells seeded at 50 000 and 100 000 cell/cm^2 on time point day 2 (submerged), day 4 and 7 under ALI. Represented in blue is DAPI staining the nucleus and in red, the Phalloidin staining for the F-

actin. The top line image is a tile scan of the entire gel (1000 µm scale bar) and below is a 10x image (100 µm scale bar) (n=3). The NC legend means image not captured.

4.3.2.3 HLF-1 dECM/fibrin Gel Seeding

The HLF-1 cells were seeded on the fibrin/dECM gel as described in section 4.2.2.3 (figure 4.14). On the 7th day of culture, the images show a mixture of live cells, with a round nucleus and F-actin fibres, together with fragmented nucleus, indicating cell death.
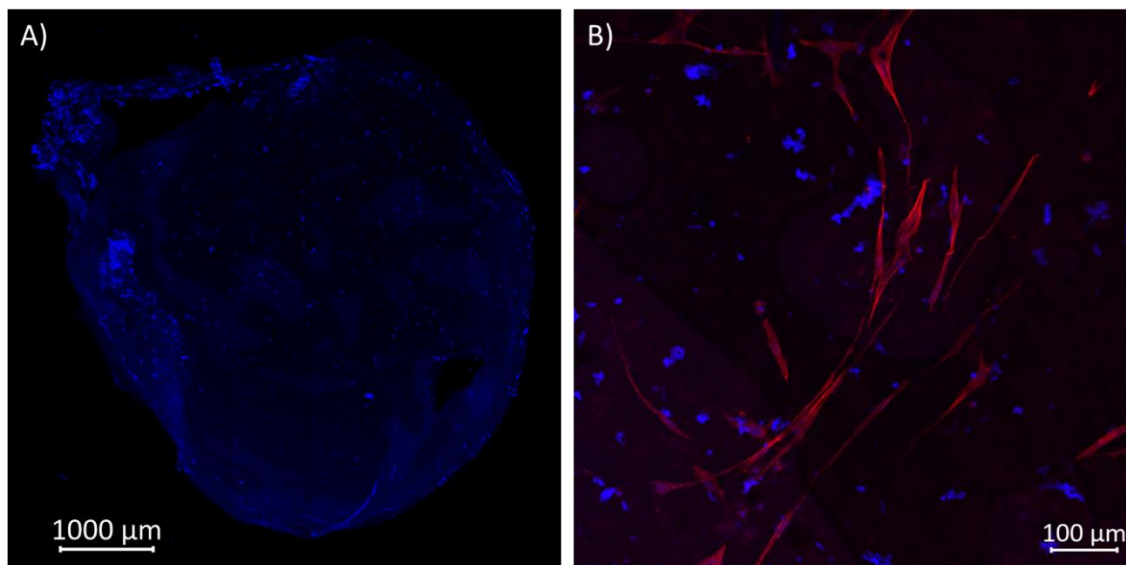
Figure 4.14: HLF-1 seeded on fibrin/dECM gel. The images correspond to cells seeded at 5000 cells/cm^2 on the 7th day of culture. Represented in blue is DAPI staining the nucleus and in red, the Phalloidin staining the F-actin. The image on the left is a tile scan of the entire gel (1000 µm scale bar) and image on the right used a 10x objective (100 µm scale bar) (n=3).

4.3.2.4 A549 dECM/fibrin Gel Seeding

The A549 cells were seeded in the fibrin/dECM gel and Transwells for comparative studies (figure 4.15). Contrary to what was observed for hAELVi, H441 and HLF-1, the A549 were able to attach to the dECM/fibrin gel and be in culture for 7 days in submerged or ALI. Regarding the IL6 and IL8 secretion, the cells secrete higher amounts of those cytokines when seeded on the gels than on the Transwells. The LDH follows the same tendency as the ELISAs.
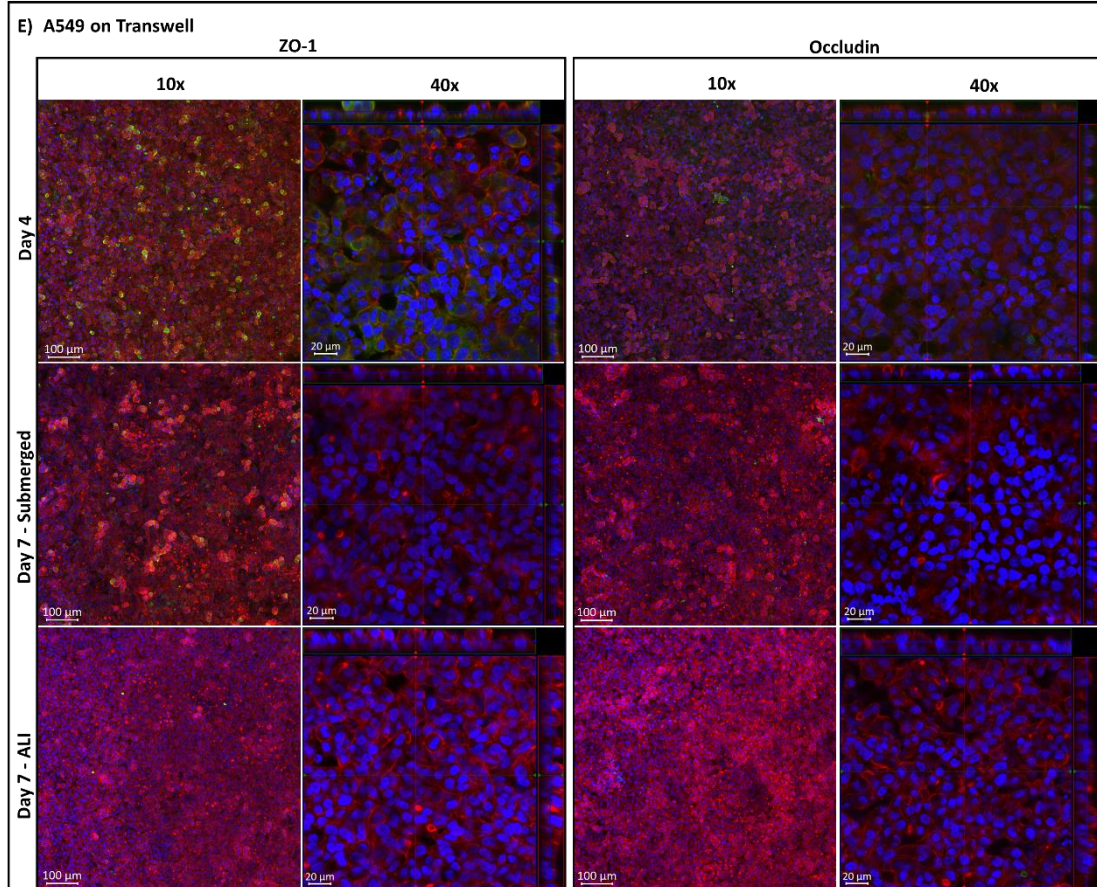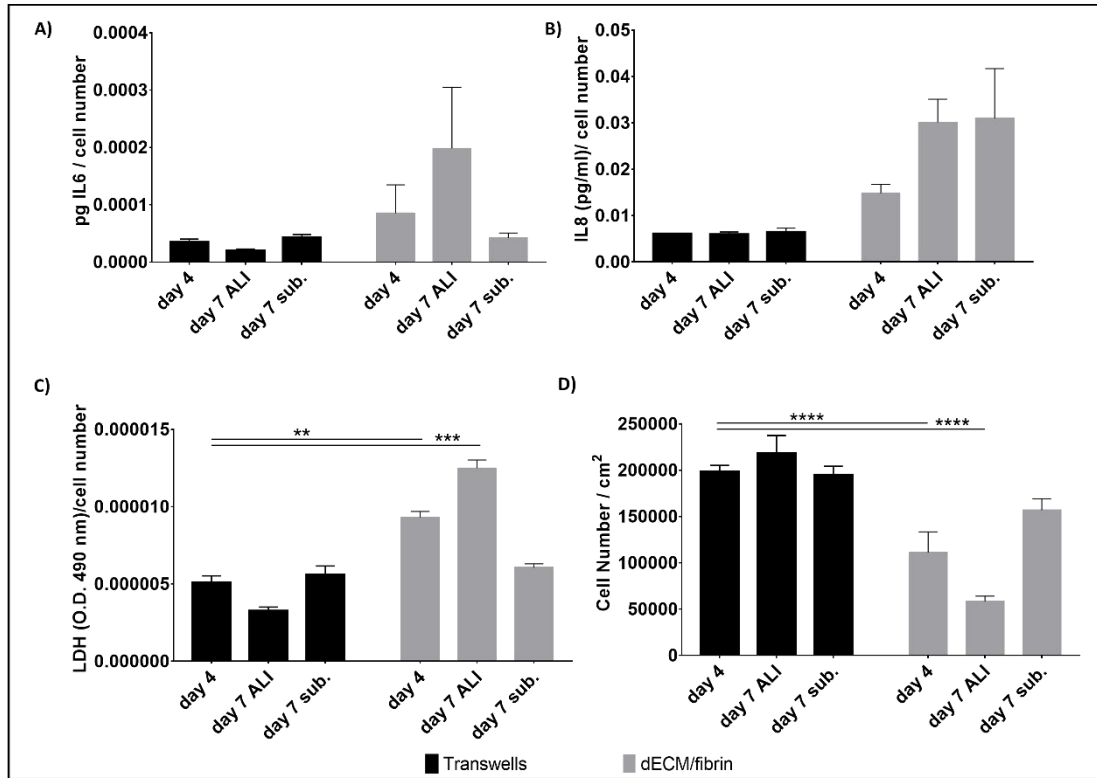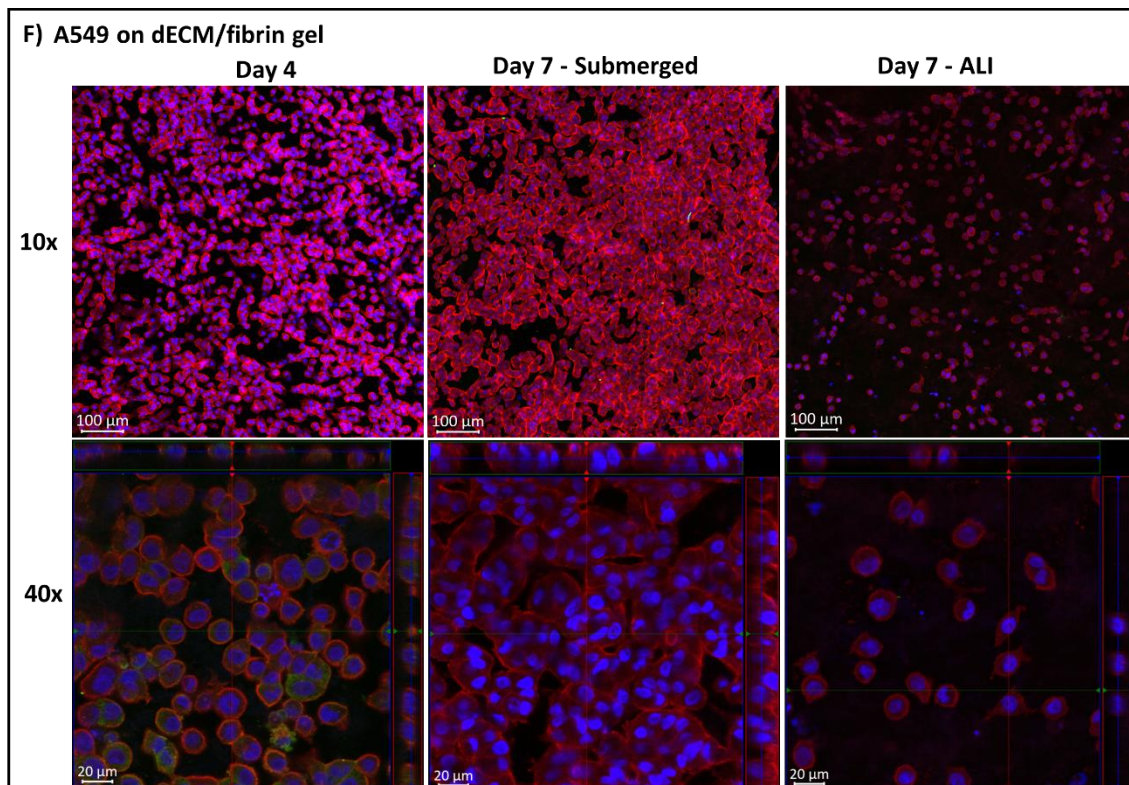
Figure 4.15: A549 cells seeded on Transwells and on the dECM/fibrin gel. The time points analysed are day 4 and 7 under submerged and ALI seeded on fibrin/dECM gel. A) IL6 cytokine quantification normalized by the cell number (n=3). B) IL8 cytokine quantification normalized by the cell number (n=3). C) LDH quantification normalized by the cell number (n=3). D) Cell number (n=4 to 11). E) A549s cell morphology seeded on Transwells. F) A549s cell morphology seeded on the d ECM/fibrin gel. The nucleus is represented in blue stained with DAPI, F-actin in red stained with Phalloidin and in green is showed the surface marker ZO-1 (n=3). The indication of 10x and 40x corresponds to the objective used to acquire those images. The asterisk symbols in the plot represent: ** $p < 0.01$, *** $p < 0.001$ and **** $p < 0.0001$. The error bars represent SEM.

The confocal images, show the nucleus presented in blue with an oval shape and F-actin delineating each cell. Regarding the surface markers ZO-1 and occludin, the first is found on day 4 but is not present on day 7 for all conditions. The occludin surface marker is not found. The difference between Transwell and dECM/fibrin seeding is found in the cell density. For both conditions, the cells were seeded at 2.78×10^5 cells/cm², but cells seeded on the transwell show higher confluency and the presence of ALI on the 7th day does not have an impact on cell number. However, the cells seeded on the gel do not show complete confluency on days 4 and 7. On ALI, the impact is much higher, when it was quantified fewer cells than on day 4, figure 4.15D).

153

4.3.2.5 dTHP-1 dECM/fibrin Gel Seeding

To evaluate if the dECM/fibrin gel could activate an inflammatory response, dTHP-1 cells were seeded on the gel (figure 4.16). After 24 hours recovery period, the cells were brought to ALI or kept in submerged conditions. On the following day, it was added to the cells fresh media or media supplemented with LPS. The previous conditions were evaluated by determining the IL6, TNF-α and TGF-β cytokines secretion as well as morphology assessment using confocal microscopy of CD11b surface markers. The TGF-β shows negative values except for the LPS stimulation under ALI. Regarding the IL6 and TNF-α, the submerged condition has higher cytokines values than ALI. The cell morphology inspection using confocal microscopy shows white nucleus in all the conditions tested, but lacks in general Phalloidin and CD11b. Phalloidin was only found in the submerged condition and CD11b in submerged with LPS.
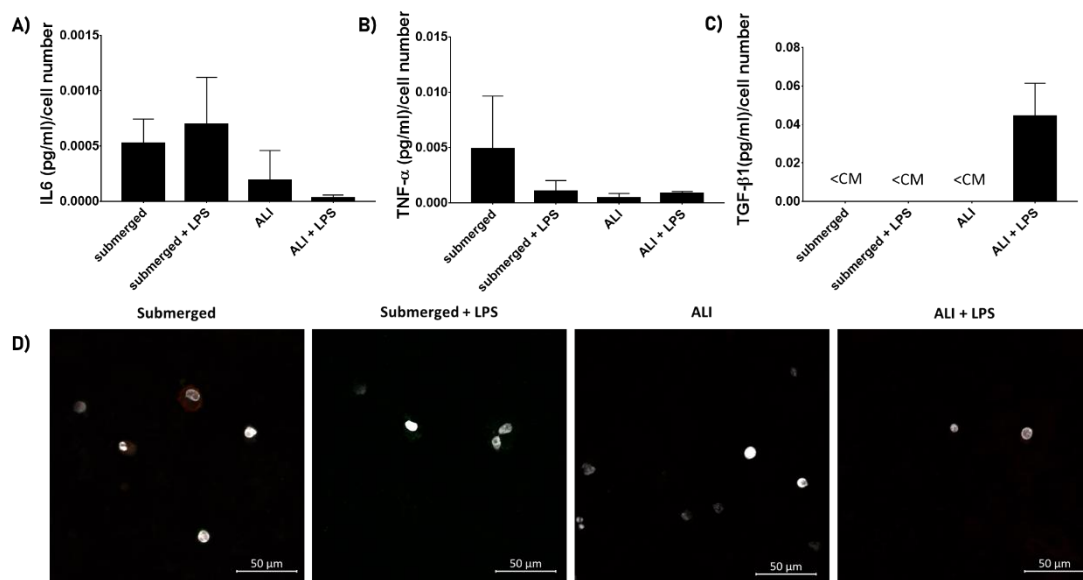
Figure 4.16: dTHP-1 cells seeded on dECM/fibrin gel. The conditions analysed are submerged or air-liquid interface (ALI) with and without LPS supplementation (1000 ng/mL). A) IL6 cytokine quantification normalized by the cell number (n=3). B) TNF-α cytokine quantification normalized by the cell number (n=3). C) TGF-β1 cytokine quantification normalized by the cell number (n=3). D) Fluorescence microscopy images showing the nucleus in white stained with DAPI and F-actin in red stained with Phalloidin. Conditions submerged with LPS also show green fluorescence from CD11b (n=3). The legend < CM indicates sample concentration below the concentration in the media.

4.4 Discussion

The aim of chapter 4 was to access which cells line were able to attach and proliferate in the dECM scaffold and dECM/fibrin gel, the alveolar biomaterials derived in chapter 3. This is illustrated in stages 6.1 and 6.2 from figure 4.1. Regarding the study of the dECM scaffold, the cells (dTHP-1 and hAELVi) did not show the capacity to attach and proliferate, which may be a result of residues of SDS bound to the surface that can become cytotoxic to the cells. This together with the damage of the surface from the effect of SDS and Triton, can prevent the cells from attaching in the first place. On the other hand, the A549s and dTPH-1 were able to tolerate the dECM/fibrin gel, being in this way, the cell lines selected to build the alveolar co-culture in chapter 7. Below can be found a more detailed discussion of stages 7.1 and 7.2 of chapter 4.

4.4.1 Stage 7.1: Cell Seeding on dECM scaffold

The first seeding attempt on the alveolar biomaterial was on the dECM scaffold. For that, was designed and printed two parts to support scaffold use under ALI and enable submerged culture without it floating. These requirements were achieved and demonstrated in figure 4.8 where the scaffold does not float under submerged conditions and on ALI continues in contact with the media. This gave the flexibility to use the scaffold in submerged conditions, which is necessary during seeding but also to proportionate a more physiological environment to the cells when ALI is established. Another feature to mention is the facility to add and remove the scaffold. The stoppers are only 4 and are position at a level where scaffold deformation by compression does not occur.

Regarding cell seeding, the first cells seeded were dTHP-1 to analyze the possible immune response triggered by the biomaterial. The cells were in low numbers and in this way difficult to find in the image. The hAELVi were not found in all experimental conditions and from day 2 onwards don´t appear viable by the poor staining.

In chapter 3, section 3.4.4, was discussed that the percentage of SDS in the last PBS/media wash on the dECM scaffold (step 6 from figure 4.2) was 0.012%. Indicating that the cells may be exposed to this percentage of SDS. This fact together with the known surface alteration after SDS treatments, as seen in chapter 3 figure 3.18, could impact of cell's capacity to adhere and proliferate in the dECM scaffold.

4.4.2 Stage 7.2: Cell Seeding on dECM/fibrin Gel

As an alternative to dECM scaffold, the cells were seeded in the dECM/fibrin gels. For that, was also designed and 3D printed two parts to support gel polymerization and cell seeding. The new parts showed more control of media volumes during submerged and ALI experiments, since the gel holder does not occupy all the area of the media holder. A feature that could be improved in the next version is the height of the central ring. If increased, could easily accommodate more than 100 µl and in this way, facilitate cell seeding and leave the cells less susceptible to evaporation under submerged experiments.

Regarding the test of the biomaterial with cells, from the range of cells tested, different outcomes were obtained. The H441 completely digested the gel, which in future could be overcome with the addition of aprotinin. The aprotinin is used in chapter 5, since it reduces fibrin gel degradation by the fibroblast. Despite the H441 were not able to be cultured on the dECM/fibrin gel, the cells were characterized using a Transwell as substrate. The results are in appendix 8-10. The IL6 and IL8 graphs show base line secretion of these cytokines along the time and on ALI or submerged. The fluorescence images show the cell's morphology with DAPI and Phalloidin and Z0-1 and occludin expression, especially on day 7.

The HLF-1 seeded on the dECM/fibrin gels, despite being supplemented with aprotinin, which prevented gel degradation, the images showed a mixture profile of viable and cell debris. This cell line is able to proliferate during 21 days on fibrin gels, data shown in chapter 5, indicating the neutralized dECM as the potential cause for the lack of cell viability.

Regarding the hAELVi, despite lower catalytic activity towards the gel, the cells show very round morphology and were easily washed away, indicating low adherence toward the dECM/fibrin gel. For comparison, the hAELVi were also seeded on Transwells to have a baseline of IL6 and IL8 secretion, as well as morphology. The results are in appendix 11-13. The occludin is detected only on day 7. On the other hand, the ZO-1 shows some signal on day 2, but higher expression is observed on the 7th day. The hAELVi cells were able to grow on Transwells following manufacture instructions, but not on the dECM/fibrin gel, indicating once more the biomaterial as the reason for the lack of cell viability.

Contrary to what was observed for the H441, hAELVi and HFL-1, the A549 and the dTHP-1 were successfully seeded on the dECM/fibrin gel. The A549 showed a more pro-inflammatory response when cultured in the dECM/fibrin gel compared to Transwells. The IL6 and IL8 secretion was detected in higher values when the gel was the substrate (except on day 7 submerged IL6). The same is observed with LDH, this metabolite is higher in cells seeded in

dECM/fibrin gel, suggesting cytotoxicity. In addition, the cells do not have the same growth tendency as in Transwells. This indicates, that despite able to attach and survive for 7 days under submerged or ALI conditions, the cells in Transwells have a less inflammatory profile, the cell membrane is more intact and are more proliferative.

Regarding the dTHP-1, the cells were present in the numbers excepted but the stain apart from DAPI was not satisfactory, the Phalloidin was present in just one condition, and CD11b was lacking. About the cytokines, the TGF-β is only determined on ALI with LPS stimulation, all the other conditions the concentration determined for the sample was below the concentration of plain media. For TNF-α, if taking into consideration the high variability of the submerged condition, all samples do not express much of this cytokine. If for the dTHP-1 seeded on stage 6.1 the LPS stimulated the TNF-α, for the cells seeded on the gel that did not occur. Regarding the IL6, in general, the cells under submerged have higher values of this cytokine, but the high variability of the results does not allow any conclusion. Noteworthy, dTHP-1 show in stage 6.1 and 6.3 the ability to attach and last in culture, but when seeded in the dECM scaffold no. This may suggest, once more surface topology as one of the reasons for unsuccessful cell culture on stage 6.2 (section 4.4.2).

Next, going into more detail for discussing the lack of viability of some cells (H441, HLF-1 and hAELVi) when cultured on the dECM/fibrin gel. For this biomaterial, the residual SDS concentration may be the factor as well. It was mentioned in section 4.4.1 that the cells seeded on the dECM scaffold may be exposed to 0.0012% SDS. However, on the digested dECM the percentage of SDS determined was higher, approximately 0.027% (step 9.3 from figure 4.2). The cells seeded on the dECM/fibrin are exposed to even more SDS concentration, contributing for the lack of cell's viability.

A study where it was investigated the cytotoxic thresholds of SDS and Triton on human bronchial epithelial cells, human pulmonary vascular endothelial cells (CBF12), human lung fibroblasts and human mesenchymal stem reveal a range between 0.0078% to 0.016% for SDS and for Triton a concentration between 0.0031% to 0.0063%[129]. If the last PBS wash detains a concentration of 0.012% SDS and in this way within the range, the concentration bound to the dECM matrix is above the range. This further validates the necessity of controlling the residual content of SDS (figure 3.23).

Other research articles also documented the negative impact of residual SDS on cell viability. Cornea tissue treated with Triton, freeze-thaw and native without decellularization treatment showed viable primary human corneal stromal cells, when hydrogel derived ECM was reseeded.

But no viable cells were found on SDS treated cornea tissues. SDS measurement with methylene blue confirmed the residual surfactant concentration as the cause of hydrogel cytotoxicity[108]. The same was found during the SDS decellularization of porcine small intestine segments, which documented SDS to be bound to the matrix even with extra washing steps applied. The residual SDS concentration influenced the survival of porcine endothelial primary cells reseeded on the ECM derived hydrogel. Further tests also showed that the toxicity derived from the surfactant was influenced by the culture medium on which the endothelial cells were cultured on and additional BSA or fetal calf serum could eliminate SDS negative effect[166]. This latter strategy could be added to the one already advanced in chapter 3 discussion, were washing with a solution with pH = 9 or 75% ethanol reduced between 8 and 23 times the SDS content below cytotoxic levels. However, despite such strategies could lower SDS concentration, the level of repopulation and viability was still low, indicating surface damage as the cause[148].

The examples above show that the SDS's negative impact on decellularized matrixes has also been reported in the literature. In future, reducing the SDS content using extra washing steps with some of the solutions shown above, together with tight monitoring of its content throughout the decellularization process would be essential. But may not be a guarantee of scaffold suitability for supporting cell growth, as SDS has the capacity to significantly alter ECM content[167]. At that time, a rethink of a decellularization strategy without SDS entirely may be the solution. The alternative could be Triton treatments alone together with an additional fragmentation step with a DNase/RNase, as already advance in the chapter 3 discussion.

Conclusion	
From the chapter	▪ dECM scaffold surface does not promote cell attachment and proliferation ▪ dECM/fibrin gel does not promote H441, hAELVi and HLF-1 attachment and proliferation, but supports A549 and dTHP-1
Overall Project	▪ A549 and dTHP-1 seeded on dECM/fibrin gel chosen as cells lines and biomaterial to build the full model

Chapter 5

Vasculature Model
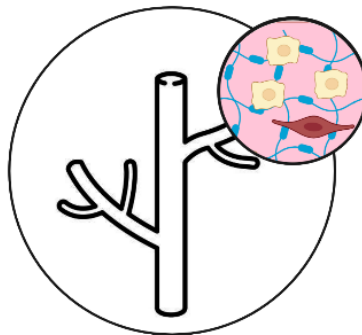
5.1 Introduction

The absence of integrated *in vitro* models of vasculature is one of the major limitations in the field. Namely, in order to mimic physiological conditions, cells would need to be less than 100 µm from a capillary, high oxygen source[56]. In the capillaries near the alveoli, this corresponds to 100 mmHg of oxygen partial pressure, but at tissue level can drop to 40 mmHg. Regarding the *in vitro* scenario, the oxygen concentration in a humidified incubator (5% CO_2 and 37 °C) is 18.6%, which at sea level corresponds to an oxygen partial pressure of 141.1mmHg (or 7.23 mM). Then, considering the properties of the media, oxygen dissolved at interface air-media is around 3.5 mmHg (or 0.181mM). But this is still far away from the oxygen concentration that the cells are exposed to, since oxygen consumption rate and media thickness determines the oxygen gradient[168]. If for cells seeded on a flask, the oxygen concentration is already limited, is an extra challenge, when moving on to the third dimension, where oxygen diffusion into the scaffold needs to be considered.

For a better understanding of vasculature formation, section 1.1.4.2 from the introduction describes the process of *de novo* blood vessel formation. Section 1.1.4.2 also defines angiogenesis, the formation of blood vessels from pre-existing ones, where in the beginning, endothelial cells differentiate into tip and stalk cells. The tip cells develop filopodia and are the ones that define the direction of the new blood vessel, while the stalk cells, with a high proliferative profile, follow them forming the cord. The cord later develops a lumen that is going to be perfused, before final vessel maturation, by pericytes or smooth muscle cells. All the actions described before, are coordinated with basement membrane degradation[81]. Thus, angiogenesis is the process aimed to be recreated in this chapter.

In the literature, two main strategies exist in order to form blood vessels *in vitro*. Either cell can be seeded in organ-on-a-chip or 3D bioprinted models, achieved by coating the fluidic channels. The endothelial cells are seeded on a hollow tube that is perfused, and in this way, mimics the *in vivo* blood vessel, where cells are exposed to dissolved oxygen and nutrients.

Alternatively, cells can be seeded on a 3D scaffold, that promotes cell organization in the different steps of angiogenesis described above. This strategy has the capacity to recapitulate angiogenesis, though, is not without challenges. When cells are seeded within a biomaterial, oxygen, nutrients, growth factors and waste products become limited by diffusion. This creates a heterogeneous environment, where depending on the cell position to the media source, they are subjected to a different concentration of the same factor. In angiogenesis, a gradient from vasculature endothelial growth factor (VEGF) is known to guide the tip cells[81], with hypoxia also

stimulating this process[169]. Thus, this project was tried to use the limitations of working with scaffolds to promote angiogenesis.

In this way, a specifically selected fibrin gel was used as the scaffold to direct angiogenesis. Fibrin is a reaction between fibrinogen and thrombin, which is the base of a blood clot. After the formation of a blood clot, endothelial cells degraded it in the process of wound healing. During this phase, products of the degradation stimulate angiogenesis in positive feedback[170,171]. This makes the use of a fibrin gel as a biomaterial physiologically relevant and enables angiogenesis *per se*.

As a final remark, the cells selected to be seeded on the fibrin gel were lung microvascular endothelial cell line (HULEC-5a), which are more physiologically and anatomically relevant cell[12] than the most widely used HUVECs. These cells were co-cultured with lung fibroblast as supporting cells.

In conclusion, this chapter focus on Part 2 of the project presented on figure 1.9, aiming to recreate angiogenesis. Two biomaterials were tested, a fibrin gel and very briefly a gelatin and alginate mesh. There are several articles in the literature with proven record vasculature-like formations[88–90,172,173], where fibrin was the biomaterial selected. The idea behind this chapter was to induce endothelial cells organization in 3D structures that could sprout towards a gradient of angiogenic factors. An additional cells line, fibroblast, was also added to study its presence on guiding angiogenesis. Parallel to the cellular work, in this chapter can be also found the biomaterials characterization, as it was considered important to be able to link cellular behaviour with biomaterial architecture.

5.2 Methods

To facilitate the reading of this chapter an overall image of the four stages taken to build the vasculature model are shown in image 5.1. Stage 1 refers to the initial 2D cell characterization of the endothelial cells (ECs). This stage helped to understand the endothelial cells' behaviour prior to attempting to culture them in a 3D micro-environment. Stage 2 mentions the brief work performed with the gelatin gel. Stages 3 and 4 consider the work completed with the fibrin gel regarding the characterization and the several strategies to promote cell growth.
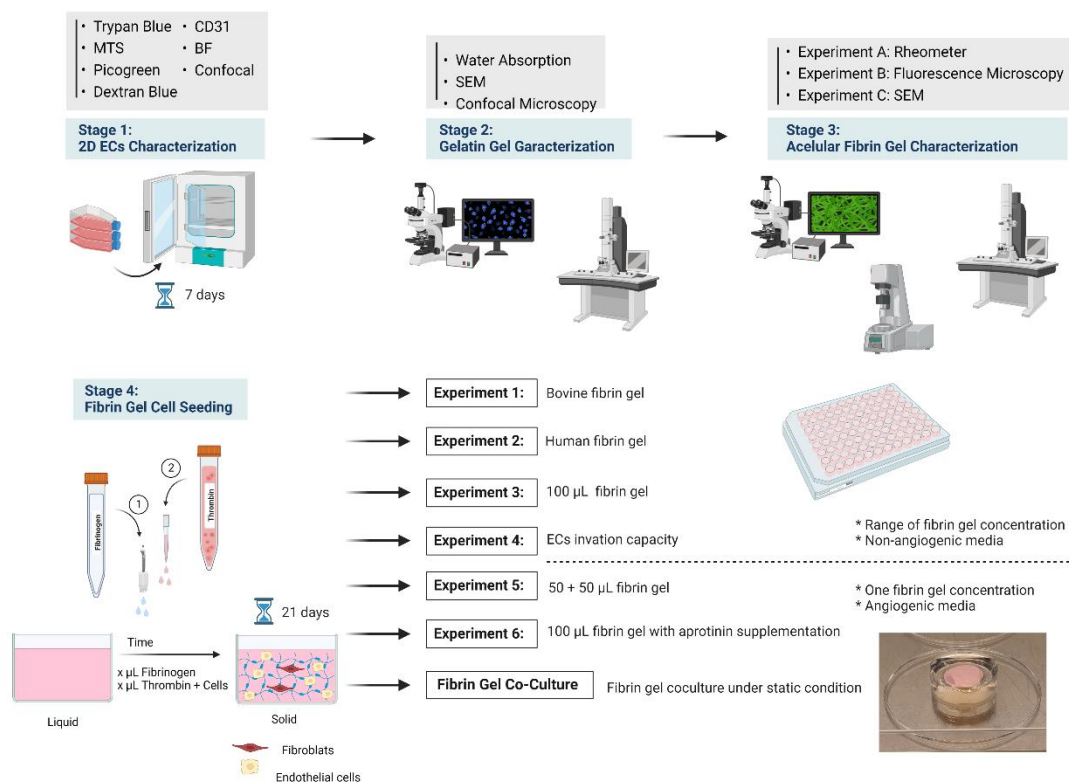
Figure 5.1: Overview of the chapter 5 stages. Stage 1 illustrates the endothelial cell's 2D characterization, with the assay performed on the grey box. Stage 2 refers to the characterization of the gelatin gel. Stage 3 includes the rheological characterization of the fibrin gel as well as fibre's network visualization with confocal and scanning electron microscopy (SEM). Stage 4 illustrates the procedure for cell seeding on the fibrin gel. To evaluate the suitability of the fibrin gel to support cell growth, seven experiments were performed, from 1 to 6 monocultures of endothelial or fibroblast and the 7th as static co-culture. The experiments vary on the origin of the fibrinogen and thrombin, the total volume of gel, if cells were seeded as scattered cells or as spheroids, the plastic wear where polymerization occurred and extra supplementation to induce angiogenesis and prevent gel degradation with aprotinin. Legend: BF refers to bright field microscopy. Created with BioRender.com

162

5.2.1 Stage 1: 2D ECs Characterization

5.2.1.1 Cell Culture

The human lung fibroblast (HLF) and endothelial cells (ECs) were sub-cultured as described in section 2.3.1 and 2.3.2 respectively.

5.2.1.2 2D Cell Characterization

For all the assays present in general methods 2D Cell Characterization (section 2.4), the ECs were seeded at 5000 cells/cm^2. The characterization lasted for 7 days, the time points analysed were from day 1 to 7.

5.2.1.2.1. Trypan Blue Exclusion Assay

The protocol followed is previously described in section 2.4.1.

5.2.1.2.2 CellTiter 96® AQueous One Solution Cell Proliferation Assay

The protocol followed is previously described in section 2.4.2

5.2.1.2.3. Quant-iT™ PicoGreen™ dsDNA Assay Kit

The protocol followed is previously described in section 2.4.3.

5.2.1.2.4 Dextran Blue

The protocol followed is previously described in section 2.4.4. For the endothelial cells was additionally determined the dextran blue value when seeding in the 12 well transwell 25000, 50000, 100000 and 500000 cells. After 24 hours of the seeding the dextran blue assay was performed as described in 2.4.4.

5.2.1.2.5. Flow Cytometry

The protocol followed can be found on section 2.4.5, where cells were tested for the presence of the surface marker CD31 (#303103FITC from biolegend). The total of 1x10^5 viable cells were diluted in 1 mL of PBS with 2.5 μL of the CD31.

5.2.1.2.6. Bright Filed Microscopy

The protocol followed can be found on section 2.4.6 from general methods.

5.2.1.2.7. Fluorescence Microscopy

The protocol followed can be found on section 2.4.7 from general methods.

5.2.1.2.7.1 DAPI and Phalloidin Staining

The protocol followed can be found on section 3.2.1.7 from chapter 3.

5.2.1.2.7.2 DAPI, Phalloidin and CD31

After removing the glycine solution, the cells were blocked with blocking buffer (5 % FBS in PBS) during 1 hour at room temperature. After washing three times with PBS, the primary antibody solution was added to the cells. The CD31 (#MA5-13188 from Invitrogen) was diluted in 1:100 in 1% BSA in PBS and incubated overnight at 4°C in the dark (plate was sealed to avoid drying of the well). On the next day, the plate was at room temperature for 1 hour before washing three times with PBS. Then, the secondary antibody (1:1000 dilution in 1% BSA in PBS) was added together with the phalloidin (1:200 dilution in 1% BSA in PBS) for 2 hours at room temperature in the dark. After washing three times with PBS the slides are stained with DAPI (1 µg/mL in PBS) for 15 minutes at room temperature in the dark. The cove slip was mounted to the glass slide as detailed in section 2.2.7. The DAPI was excited with a 405 nm laser and detected from 410-481 nm range. The Phalloidin was excited with a 633 nm laser and the emission signal was captured from 638-759 nm range. The CD31 was excited with a 488 nm laser and detected from 492-560 nm range using a ZEISS LSM 710.

5.2.1.2.7.3 DAPI, Phalloidin and VE-Cadherin

The same protocol was followed as in 5.2.1.2.7.2 but, the VE-cadherin primary antibody was added in a dilution of 1:400 in 1% BSA in PBS and the secondary was Alexa Flour 555 donkey anti-rabbit in 1:1000. The VE-Cadherin was excited with a 555nm laser and detected from 521-579 nm range using a ZEISS LSM 710.

5.2.2 Stage 2: Gelatin Gel Characterization

The gelatin gels were composed of 6% gelatin, 4% alginate and 0.9% NaCl. Firstly, the gelatin was dissolved in MCDB131 media at 50°C. Following the complete dissolution of the gelatin, was added the alginate and NaCl powder. Then, the unpolymerized gelatin mixture was stored at 4°C until further use. On the day of the experiment, the gelatin mixture was allowed to warm in the water bath at 37°C prior to crosslinking with calcium chloride. Two concentrations of calcium chloride were used during crosslink 150 or 300 mM. The protocol for polymerization can be seen in figure 5.2. The acellular gelatin gels were characterized through Scanning Electron Microscopy and water porosity. The gelatin gels were also seeded with endothelial cells and the seeding efficacy was evaluated through DAPI stain. For detailed protocols please refer to sections 5.2.2.1. to 5.2.2.3.
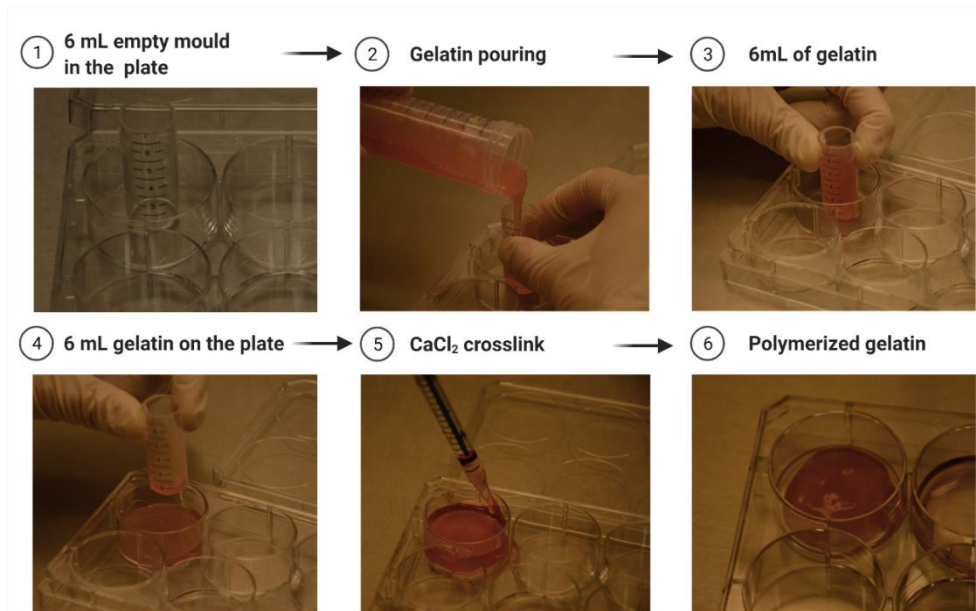
Figure 5.2: **Gelatin and alginate mesh crosslink protocol.** On point 1 is shown the 6 mL mould used for volume accuracy, which is being full on point 2. On point 3 the mould is lifted and the gelatin falls downs into the plate. Afterwards the calcium chloride (CaCl$_2$) is added on top to crosslink the alginate illustrated on point 5, which after 5 minutes is removed as shown on point 6. Created with BioRender.com

5.2.2.1. Scanning Electron Microscopy

The gelatin gel was polymerized in a 6 well plate as illustrated in figure 5.2 from steps 1 to 6. Before pouring the unpolymerized gelatin mixture, 0, 1 or 2 mL of CaCl$_2$ (with 150 mM or 300 mM) was added to the bottom of the plate. Afterwards, with a help of a mould (shown in figure 5.1, step 1), 6 ml of the unpolymerized gelatin mixture was added to each well. Then, was added 4.5 mL of CaCl$_2$ on top of the gel for 5 minutes. After polymerization time, the CaCl$_2$ was

removed. Next, the gel was cut into smaller pieces and dried using a freeze-dry machine (Scanvac CoolSafe Freeze-dryer) and stored at 4°C until imaging. The gels were visualized using a Hitachi S-4800 Scanning Electron Microscope (no coating was applied). For data analysis, using ImageJ software was manually measured at least 3 porous in each image.

5.2.2.2. Water Porosity

The same protocol was followed as for the SEM in section 5.2.2.1 until the freeze-drying step. Then, the pieces of the gel were weighed and added to water until completely submerged. After 2 or 24 hours, the gel was tap dried with paper and weighed a second time. The difference between the weight wet and dried weight corresponds to the water that was absorbed.

5.2.2.3. Endothelial cells seeding on gelatin and alginate gel mixture

The gel was polymerized as shown in figure 5.2, but a 6 well Transwell was used instead of a 6 well plate and it was tested the formation of gels with 4, 5 and 6 mL. Firstly, the unpolymerized gelatin mixture was added to each well with the help of the mould. Then, 3 mL of MDCB131 media with 180000 endothelial cells and 300 mM of $CaCl_2$ was added on top. To the basolateral side of the Transwell membrane was added more 2.5 mL of 300 mM of $CaCl_2$ solution dissolved in MDCB131 media. The plate was moved to the incubator (humidified 37°C with 21% oxygen and 5% CO_2). The next day, the seeding efficacy was evaluated with a DAPI stain. The gel was fixed with 10% paraformaldehyde solution for 24 hours at 4°C, before being stained for 30 minutes with 1 µg/mL of DAPI solution. After three times PBS wash, with 5 minutes in between the washes the gel was imaged on an inverted Olympus IX 51, with a black and white camera XM 10. The halogen light source is an Olympus TH4 - 200 and the fluorescent light source is a Prior Lumen 200.

5.2.3 Stage 3: Acellular Fibrin Gels Characterization

On stage 3 is included the acellular characterization of the fibrin gel with a rheometer, fluorescence and scanning electron microscopy. For this section, the fibrin gel was polymerized by dissolving an equal volume of fibrinogen solution (10 mg/mL stock solution in PBS) and thrombin solution (40 U/mL stock solution in MDCB131 media all supplemented except FBS). Both solutions were sterile filtered with a 0.2 µm porous filter before use. In table 5.1 can be

found the details of the experiments performed to characterize the acellular fibrin gel, experiments A. to C.

Table 5.1: Summary of experiments performed for the acellular fibrin gel characterization. The table contains details of thrombin and fibrinogen origin. The volume refers to the total fibrin gel volume. Then, is referred the fibrinogen and thrombin concentration used, the experiments performed and in what set up. Legend: SEM, scanning electron microscopy. PDMS, Polydimethylsiloxane.

Experiment	Origin	Total Volume (µL)	Fibrinogen (mg/mL)/ Thrombin (U/mL)	Assays	Set Up
A. Section 5.2.3.1	Human	78	5,2.5,1.25/5,1,0.1	Rheometer	Rheometer
B. Section 5.2.3.2	Human	200	5,2.5,1.25/5,1,0.1	Fluorescence Microscopy	8 mm PDMS ring
C. Section 5.2.3.3	Human	200	5,2.5,1.25/5,1,0.1	SEM	8 mm PDMS ring

5.2.3.1: Experiment A: Acellular Fibrin Gel Rheologic Characterization

The instrument used to record the fibrin gel rheology was an ARG2 from TA instruments. It was followed the instrument SOP during turning on, calibrations, cleaning and turning off. The geometry used during the measurements was a 40 mm parallel plate, Peltier plate steel, with a gap of 78 µL. First, 39 µL of fibrinogen were pipetted in the rheometer bed, then 39 µL thrombin were added on top of the fibrinogen drop. The geometry was mediately lower and rotated to ensure mixture of the fibrinogen and thrombin. The procedure applied 2% strain at 37 °C. The rheology of the gels was recorded until the storage (G') and loss modulus (G'') reached the plateau, where it was left to record at least 1000 points used to perform the data analysis. For data analysis, the excel sheet generated was imported in MATLAB R2019B (licence number 92345). After plotting the graph of the storage and loss modulus over time, it was identified the time points of the plateau and selected 1000 points that were averaged to calculate the storage and loss modulus of the fibrin gel. The MATLAB script can be seen below together with an example of script output (figure 5.3).

```
%1. HOME --> Import Data to load excel sheet.
%2 Select only numbers and choose column vector from output type
a = size(StepTime)
b = (a-1000)
lm = sum(LossModulus(b:a,1))/1000;
Sm = sum(StorageModulus(b:a,1))/1000;
T = table (lm, Sm)
 figure ('DefaultAxesFontSize',22)
subplot(1,2,1)
plot (StepTime,LossModulus)
xlabel('Time (s)')
ylabel('Loss Moludus (Pa)')
subplot(1,2,2)
plot (StepTime, StorageModulus)
xlabel('Time (s)')
ylabel('Storage Moludus (Pa)')
```
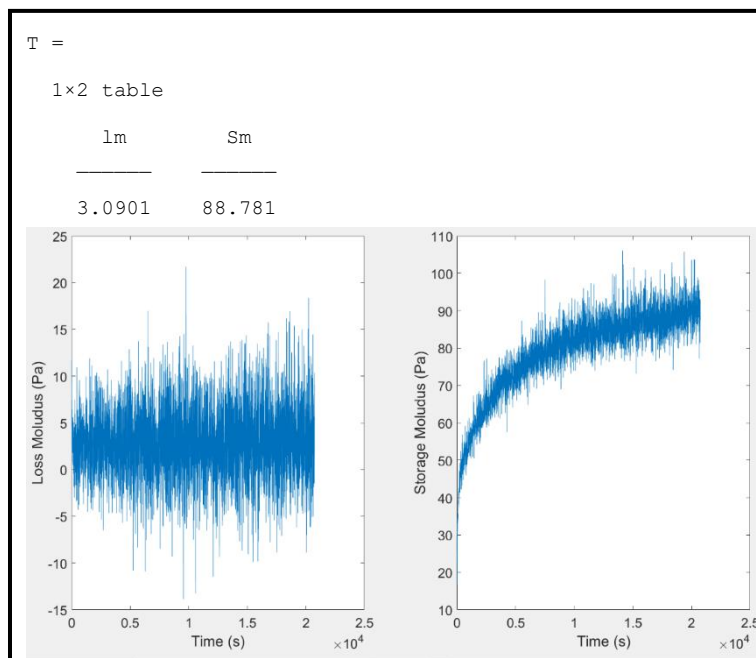

Figure 5.3: Output from the MATLAB script. The condition present corresponds to 2.5 mg/mL fibrinogen and 5 U/mL thrombin as an example. The lm indicates loss modulus and Sm storage modulus.

5.2.3.2. Experiment B: Acellular Fibrin Fluorescence Microscopy and Image Analysis

Equal volumes of fibrinogen and thrombin were added until making a total volume of 200 µL. To ensure fibre visualization, 4% of the fibrinogen was substituted with 488 conjugated fibrinogen. After gel formation in the hood, the gels were incubated for 24 hours to ensure complete polymerization. Afterwards, the gels were processed In the Singleton Hospital Pathology Department for paraffin embedding and slice (8 µm thick). The slides were imaged on Zeiss LSM 710 with a 488 nm laser excitation. Each slide was imaged in four different fields of

168

view, plus a z -stack using 10, 40 and 60x objectives. For data analysis, the images were processed using ImageJ batch process function. The code is presented below, first, the images were imported, then converted to 8-bit (greyscale), then a threshold was applied, converting the images to their mask counterparts using the Huang algorithm (other two methods were used for comparison reasons, the Default and the Percentile). Finally, by clicking the measure option, a percentage of the area covered in black pixels is given. This area corresponds to the porous. An example of the input and output image is shown below (figure 5.4)

```
setBatchMode(true);
run("8-bit");
run("Bandpass Filter...", "filter_large=160 filter_small=3 suppress=None tolerance=5 autoscale saturate");
setAutoThreshold("Huang");
//run("Threshold...");
setAutoThreshold("Huang");
setOption("BlackBackground", false);
run("Convert to Mask");
run("Measure");
```
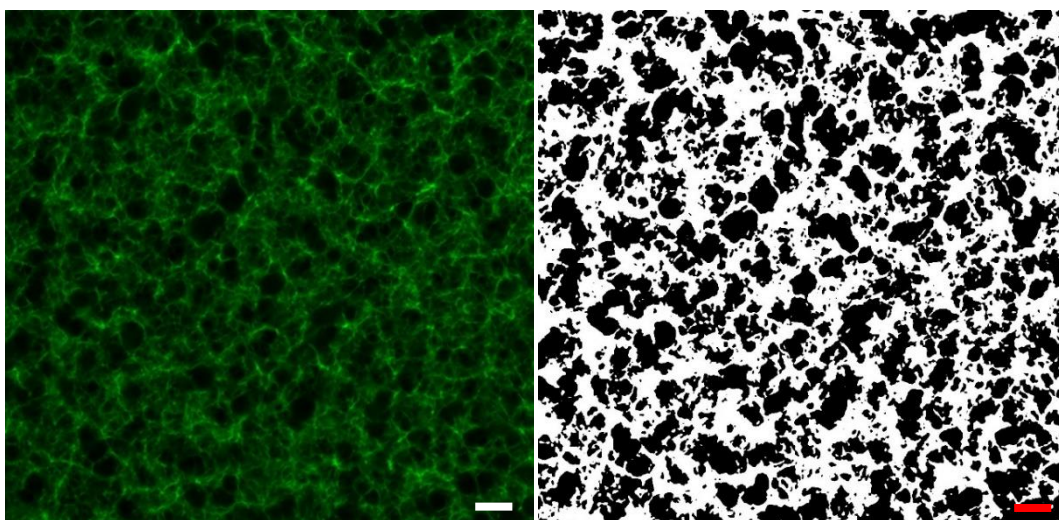

Figure 5.4: Acellular fibrin fluorescence microscopy and image analysis Image on the right represents the green fluorescence image imported into the ImageJ programme, with the fibrin fibres in green (scale bar represents 10 μm). On the left is represented the image after the threshold (Huang algorithm), with the fibrin fibres in white and porous in black pixels (scale bar represents 10 μm). The fibrin gel depicted is the polymerization of 2.5 mg/mL of fibrinogen and 0.1 U/mL of thrombin with 4% 488-labelled fibrinogen.

5.2.3.3. Experiment C: Acellular Fibrin Scanning Electron Microscopy

After imaging the slides from section 5.2.3.2, the slides were dewaxed. The removal of the paraffin started with rinsing the slides in Xylene, then in 95% ethanol, 70% ethanol followed by 50% ethanol. Every rinse took 3 minutes. Prior to drying the slides in the desiccator, they were

rinsed in tap water to remove ethanol traces. The slides were coated with 2 nm chromium with a Q150TE coater from Quorum Technologies, before imaging on the Hitachi S-4800 Scanning Electron Microscope. For data analysis, it was determined manually using imageJ the diameter of the fibres. For that, the image was first loaded into the program, then was set up the scale, then was measured manually the fibre diameter. The number of slides imaged were 3 corresponding to n=3 (except for 5mg/mL + 0.1 U/mL where n=1). Each slide was imaged at least 3 times and for each image, a total of 5 different places were measured.

5.2.4 Stage 4: Fibrin Gel Cell Seeding

This stage focus on seeding the endothelial and fibroblast cells in the fibrin gel. A total of 7 experiments were performed, with a summary presented in table 5.2.

Table 5.2: Summary of experiment for fibrin gel cell seeding. The table contains details of thrombin and fibrinogen origin. The volume refers to the total fibrin gel volume. Then, is referred the fibrinogen and thrombin concentration used, the experiments performed and in what set up. From experiments 1. to 6. the ECs and HLF-1 were seeded as monocultures. In experiment 7 ECs and HLF-1 cells were seeded in co-culture. Legend: ECs represent endothelial cells, HFL-1, human lung fibroblast, dsDNA, double strand DNA.

Experiment	Origin	Total Volume (µL)	Fibrinogen (mg/mL)/ Thrombin (U/mL)	Assays	Set Up
1. Section 5.2.4.1	Bovine	200	5 / 10, 5, 2.5, 0.5	dsDNA	96 well Plate
2. Section 5.2.4.2	Human	200	5,2.5,1.25/5,1,0.1	dsDNA and DAPI	96 well Plate
3. Section 5.2.4.3	Human	100	5,2.5,1.25/5,1,0.1	dsDNA	96 well Plate
				DAPI and Phalloidin Haematoxylin	8 mm PDMS ring
4. Section 5.2.4.4	Human	spheroids	5,2.5,1.25/5,1,0.1	Hoechst and PI Haematoxylin	8 mm PDMS ring
5. Section 5.2.4.5	Human	50 + 50	2.5/5	DAPI and Phalloidin	8 mm PDMS ring
6. Section 5.2.4.6	Human	100	2.5/5	DAPI and Phalloidin	8 mm PDMS ring
7. Section 5.2.4.7	Human	100 Co-culture	2.5/5	DAPI and Phalloidin	8 mm PDMS ring

5.2.4.1 Experiment 1: Bovine Fibrin Gel

Equal volumes of fibrinogen and thrombin were added until making a total volume of 200 μL. First, the fibrinogen was added to the bottom of the plate ensuring that all surface is wet. The 10 mg/mL stock solution was dissolved in PBS. Then, the ECs were harvested as in section 2.1.2. and added to a new vial the right volume to make 25000 cells per number of gels seeded. Then, the cells were centrifuged again, the supernatant was removed and was added the right amount of thrombin solution for the number of gels seeded. The thrombin solution was made by diluting the 40 U/mL stock (previously thrombin powder dissolved in complete MDCB131 media without FBS) in complete MDCB131 without FBS. The 10% FBS was supplemented afterwards in the final volume thrombin with cells. Then, the cell solution in thrombin was added to the 96 well. The mixture was pipetted up and down to homogenise the fibrinogen, thrombin and the cells, but only twice to prevent polymerization to occur on the tip. The gels were left in the hood for 15 minutes before moving to the incubator (humidified 37°C, 18% oxygen and 5% CO_2). After 24 hours, 100 μL of complete MDCB131 media was added to each well. The cellular growth was compared in the fibrin gel (3D) and well as in 2D, where the fibrinogen was replaced by PBS. To evaluate the cellular growth from both conditions, the dsDNA was determined using the Picogreen Kit on day 1, 3 and 7

5.2.4.1.2 Picogreen dsDNA Quantification

A total of 100 uL of papain digestion (0.3 mg/mL papain digestion, 2 mM DTT, 20 mM NaAc, and 1 mM EDTA) was added to each well of the 96 well plate. For the cell culture in the fibrin gels (in 3D), the plate was sealed and placed in the oven at 50°C overnight to ensure total gel digestion. To the cells seeded in 2D, the papain solution was added for 15 minutes with constant pipetting to help disrupt the cell membrane. Afterwards, the protocol followed was the same as in section 2.4.3. Note that the calibration curve was dissolved in papain digestion instead of TE Buffer. For data analysis, was used the calibration curve to determine the ng of DNA, which is plotted as ng DNA/per fibrin gel.

5.2.4.2 Experiment 2: Human Fibrin Gel

The protocol followed was previously described in section 5.2.4.1, except for the fibrinogen and thrombin used are of human origin and the concentration of both components also changed as shown in table 5.1. An extra condition tested was the absence of FBS during polymerization, with 10% FBS being added or not, to the thrombin solution used to dissolve the cells. Note that

the volume corresponded to the 10% FBS was removed from the volume of media needed to dilute the thrombin from stock concentration into working concentration. The endothelial cellular growth in the 3D fibrin gel was evaluated by dsDNA and the protocol followed is previously detailed in section 5.2.4.1.2. The dsDNA quantification was done on days 1,3,7,14, and 21 for all conditions. In addition, the cells on day 21 (No FBS) were also stained with DAPI. To the wells was added a 10% PFA solution for 30 minutes, followed by 1 µg/mL of DAPI solution for 1 hour, at room temperature protected from the light. After three PBS washes, with 5 minutes each, the plate was ready to be imaged on Zeiss LSM 710 with a 405 nm laser.

5.2.4.3 Experiment 3: 100 µL Fibrin Gel

The protocol followed was previously described in section 5.2.4.1, except for the fibrinogen and thrombin used being of human origin, the concentration of both components also changed (detailed in table 5.2) and the final fibrin gel volume is 100 µl. The polymerization of the fibrin gel in experiment 3 did not include FBS. Two experimental set ups were used, 96 well plate for dsDNA quantification and an 8 mm PDMS ring for cell staining with DAPI and Phalloidin or Haematoxylin. To determine the proliferation of the endothelial cells the dsDNA was determined on days 7, 14 and 21 and the protocol followed was previously described in section 5.2.4.4 1. The morphological assessment of the endothelial cells occurred on days 7, 14 and 21. In section 5.2.4.3.1 below is described the protocol for DAPI and Phalloidin stain and section 5.2.4.3.2 for Haematoxylin stain.

5.2.4.3.1 DAPI and Phalloidin Stain

The cell culture media was removed and 100 µL of 10% paraformaldehyde solution was added to each gel for 30 minutes. Then, the gels were removed from the PDMS ring and added to a new well with 10% paraformaldehyde. The second fixing step took 30 minutes as well. At this stage, the gels were either stored at 4°C in PBS or proceeded to stain. To commence the stain, 250 µL of the stain solution containing DAPI (2µg/ml), Phalloidin (1:200) with 0.1% Triton in PBS was added to each fibrin gel for 1 hour at room temperature and protected from the dark. Afterwards, the gels were washed three times with PBS for one minute between washes. At this point, the gels were stored at 4°C in PBS or imaged on a Zeiss LSM710. The DAPI was excited at 405 nm and Phalloidin at 633 nm.

5.2.4.3.2 Haematoxylin Stain

After imaging the gels from section 5.2.4.3.1, 100 μL of Haematoxylin solution was added for 30 minutes to each gel at room temperature. After incubation time, the gels were washed five times with PBS, before placing them on a shaker where PBS was added fresh every hour until no traces of the dye is seen. The gels were imaged using an Olympus BX51 microscope with cellsens software.

5.2.4.4 Experiment 4: Endothelial Cells Invasion Capacity

To evaluate the capacity of the endothelial cells to migrate across the fibrin gel, the cells were seeded to form a spheroid. Afterwards, fibrinogen and thrombin were pipetted, and the spheroid was embedded in the fibrin gel as it polymerized. Then was monitored the capacity of the ECs to come out of the spheroid and migrate in the fibrin gel. This experimental design is used to test the capacity of cancer cells to invade tissues, which is considered a key hallmark of malignant tumours, but instead of Matrigel, in this thesis is was used the fibrin gel.[174–176].

5.2.4.4.1 Spheroids Formation

The spheroids were initially formed by the hanging drop technique, which consisted of pipetting 20 μL drop of complete MCDB131 media, with 10% FBS extra supplementation and with 3000 cells on the lid of a 48 well plate. After 3 days in the incubator (humid 37°C, 18% oxygen and 5% CO_2) the spheroids were formed. Before proceeding to spheroids embedding in fibrin gel, bright field pictures were taken using the Olympus BX51 to evaluate spheroid geometry.

5.2.4.4.2 Spheroids Fibrin Gels Embedding

After inspecting spheroid's geometry, it was added fibrinogen and thrombin to embed the spheroids. For that, the plate was flipped and to the 20 μL drop where the spheroid was formed, it was added 10 μL of fibrinogen and 5 μL of thrombin. The plate was left undisturbed for 15 minutes, before being moved to the incubator (humidified 37°C, 18% oxygen and 5% CO_2). After 24 hours, it was placed around each spheroid an 8mm in diameter PDMS ring to contain 100 μL of complete MCDB131 media. On day 2 after embedding, the media was removed from the rings and was added a 4% paraformaldehyde solution to fix the spheroids for 30 minutes. Then, the spheroids were stained with Haematoxylin, Hoechst and Propidium Iodide as described in sections 5.2.4.4.3 and 5.2.4.4.4.

5.2.4.4.3 Hoechst and Propidium Iodine

After spheroid fixation, 100 µL of a staining solution containing 30 mg/mL Hoechst (1000 mg/mL stock solution) and 30 mg/mL PI (12300 mg/mL stock solution) was added to each spheroid. The solution was incubated for 30 minutes at room temperature in the dark. Afterwards, the spheroids were washed 3 times with PBS and imaged on a ZEIS LSM 710 using 405 nm laser for Hoechst and 633 nm laser for PI. In total were imaged 5 biological repeats with 3 to 4 technical repeats each.

5.2.4.4.4 Haematoxylin Stain

After Hoechst and PI imaging, 100 µL of haematoxylin solution was added to each spheroid for 10 minutes at room temperature. Afterwards, the spheroids were washed with PBS until no traces of dye was present in the washings. Then, the spheroids were imaged on an Olympus BX51 microscope (software cellsens). For the data analysis, the images were loaded on ImageJ software. Then, using the free hand tool was outlined the initial area of the spheroid and then the total area of cell migration. Afterwards, the invasion area was determined by subtracting the spheroid area from the area of cell migration. In total were analysed 5 independent repeats with 3 to 4 technical repeats each. Below can be found an example of the ImageJ procedure (figure 5.5).
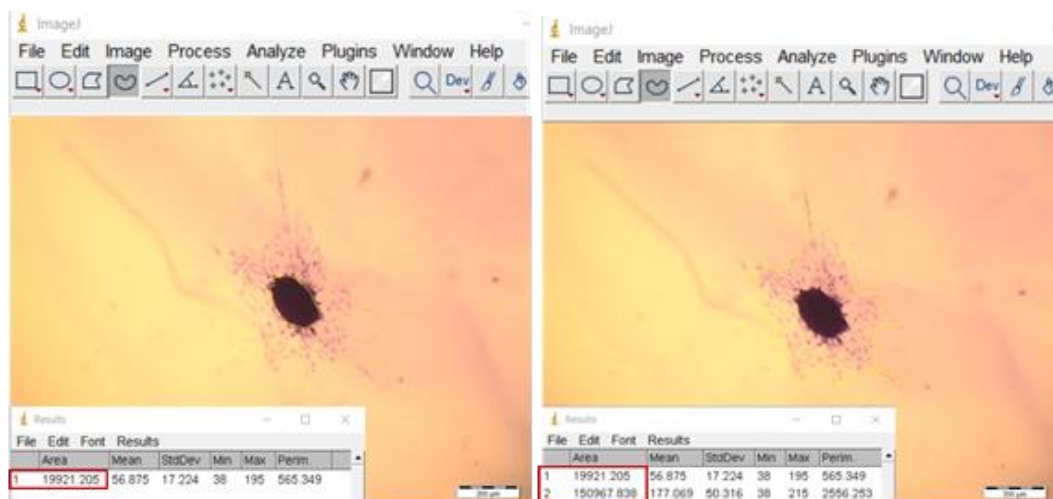
Figure 5.5: Image analysis of endothelial cells invasion area. The left side image corresponds to a representative spheroid stained with haematoxylin and imaged with a bright field microscope. The image was loaded in imageJ outlining the initial area of the spheroid in a yellow line. The right side image corresponds to the same spheroid but with the total area of cell migration outlined in yellow. (fibrin polymerization condition: 1.25 mg/ml + 1 U/ml No FBS).
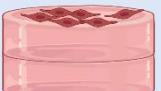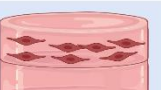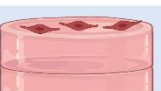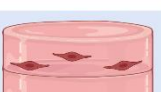
5.2.4.5 Experiment 5: 50 µL + 50 µL Fibrin Gel

To test the effect of extra supplementation to induce angiogenesis, monocultures of human lung fibroblasts and endothelial cells were seeded on fibrin gels. The gels were polymerized as described in section 5.2.4.3, but the total of 100 µL gel was divided into the upper and bottom gel with 50 µL each. The specifications of the polymerization can be found in the bullet points below and the list of angiogenic supplements in table 5.3. For more detail on monoculture seeding refer to sections 5.2.4.5.1 to 5.2.4.5.6 and figure 5.6.

- 2.5 mg/mL Fibrinogen

- 5 U/mL Thrombin

- 100 µL total fibrin gel volume divided into 50 µL upper and 50 µL bottom gel

- Polymerization in MCDB131 media supplementation from section 2.1.2 except FBS

- 8 mm PDMS rings used as scaffolds

Table 5.3: List of supplements used to induce angiogenesis. Supplements to promote angiogenesis, added fresh, on complete media from section 2.1.2. All supplements listed were aliquoted in the stock concentration, except the ascorbic acid that was always prepared fresh.

Supplements	Stock Concentration	Working Concentration
Ascorbic acid	1 mg/mL in water	1 µg/mL
bFGF	50 µg/mL in water	50 ng/mL
PMA	10 µM in water	2 ng/mL
VEGF	50 µg/mL in 0.1% BSA	50 ng/mL
S1P	1 mM in methanol	500 nM

Seeding Strategy		Upper Gel	Bottom Gel
A		-	ECs 25000 cells
B		-	ECs 32 spheroids
C		HLF-1 On Top 1250 cells	-
D		HLF-1 1250 cells	-
E		HLF-1 On Top 250 cells	-
F		HLF-1 250 cells	-

Endothelial Cells (ECs)   Spheroids   Fibroblats (HLF-1)

Figure 5.6: Experiment 5 seeding illustration. Illustration of the 50 + 50 µL seeding strategy of endothelial and fibroblast cells monocultures with supplements to induce angiogenesis. Created with BioRender.com

5.2.4.5.1 Seeding Strategy A

Strategy A commenced with pipetting 25 µL of 5 mg/mL fibrinogen solution to the 8 mm diameter PDMS ring. Then, was added 25 µL of the cell solution in 10 U/mL of thrombin as detailed in section 5.2.4.2. The 50 µL gel solution was left in the hood for 15 minutes before being placed in the incubator (humid 37°C, 21% oxygen and 5% CO_2). After 2 hours of incubation to ensure complete gel polymerization, 100 µL of MCDB131 media was added to each gel. The plates were in the incubator for 30 minutes more before adding the second layer of gel. For that, first was removed the media, then was pipetted 25 µL of fibrinogen (5 mg/mL) followed by 25 µL of thrombin (10 U/mL). After 15 minutes in the hood, the gels were moved to the incubator. The fully supplemented media (as detailed in table 5.2) was added after 24 hours and changed 2 in 2 days. The experiment lasted for 21 days, but on timepoints 7, 14 and 21 days, the gels were imaged with DAPI and Phalloidin. The protocol for staining was the same as followed in section 5.2.4.3.1.

5.2.4.5.2 Seeding Strategy B

For this experiment, it was used a 96 well plate lid and was followed the protocol from section 5.2.4.4.1 for spheroid formation. Then, the plate was flipped and with the plate at a 45° angle was pipetted MCDB131 media on top of each column of the plate. This made the spheroids drop to the bottom side of the 96 well plate lid along with the media. The spheroids were collected in a falcon tube and centrifuged at 300xg for 5 minutes. Each 96 well plate was collected in a separate falcon tube. The media was removed and 75 µL of 10 U/mL thrombin solution was added to each falcon tube. The spheroids from one 96 well plate were used to form 3 gels. To start the fibrin gel formation, 25 µL of 5 mg/mL fibrinogen solution was added to the 8 mm diameter PDMS ring. Then, was pipetted 25 µL of the spheroid solution in thrombin. The second layer of fibrin was formed as described in section 5.2.4.5.1 as well as the rest of the experiment.

5.2.4.5.3 Seeding Strategy C

Strategy C started with pipetting 25 µL of 5 mg/mL fibrinogen solution to the 8 mm diameter PDMS ring. Then, was added 25 µL of the 10 U/mL thrombin solution. The 50 µL gel solution was left in the hood for 15 minutes before being placed in the incubator (humid 37°C, 21% oxygen and 5% CO_2). After 2 hours of incubation time to ensure complete gel polymerization 100 µL of MCDB131 media was added to each gel. The plates were in the incubator for 30 minutes before adding the second layer of gel. For that, first was removed the media, and repeated the same as before 25 µL of fibrinogen (5 mg/mL) followed by 25 µL of thrombin (10 U/mL). After 15 minutes in the hood, the gels were moved to the incubator. After 2 hours incubation period was added 100 µL of MCDB131 media containing 1250 fibroblasts. The fibroblasts were handled as I section 2.1.1. The rest of the protocol is the same as in section 5.2.4.5.1

5.2.4.5.4 Seeding Strategy D

Strategy D started with pipetting 25 µL of 5 mg/mL fibrinogen solution to the 8 mm diameter PDMS ring. Then, was added 25 µL of the 10 U/mL thrombin solution. The 50 µL gel solution was let in the hood for 15 minutes before being placed in the incubator (humid 37°C, 21% oxygen and 5% CO_2). After 2 hours of incubation to ensure complete gel polymerization 100 µL of MCDB131 media was added to each gel. The plates were in the incubator for 30 minutes before adding the second layer of gel. For that, first was removed the media, and was added 25 µL of fibrinogen (5 mg/mL) followed by 25 µL of the cell solution in thrombin (10 U/mL). For that, the fibroblasts were handled as in section 2.1.1 and after cell count, was pipetted the volume that

would contain 1250 fibroblast/gel. The cell solution was centrifuged, and the thrombin solution was added, 25 μL/gel. After 15 minutes in the hood, the gels were moved to the incubator. The rest of the protocol is the same as in section 5.2.4.5.1

5.2.4.5.5 Seeding Strategy E

The protocol followed was the same as in 5.2.4.5.3, but only 250 fibroblasts/100 μL of MCDB131 media were seeded on top of the gel.

5.2.4.5.6 Seeding Strategy F

The protocol followed was the same as in 5.2.4.5.4, but 250 fibroblasts/gel were seeded.

5.2.4.6 Experiment 6: 100 μL Fibrin Gels with Aprotinin Supplementation

To prevent fibrin gel degradation by the fibroblasts, it was added to the list of supplements from table 5.3 aprotinin. The aprotinin stock concentration is 20 mg/mL in water and the working concentration is 20 μg/mL. In addition, with a lack of invasion of the cells from the upper or bottom gel in the 50 + 50 μL approach, the fibrin gel configuration returned to a single gel with a 100 μL total volume. For more detail on monoculture, seeding refer to sections 5.2.4.6.1 to 5.2.4.6.5 and figure 5.7.

5.2.4.6.1 Seeding Strategy A

The protocol followed was the same as in 5.2.4.5 but the gel was formed with only one layer of fibrin, where 50 μL of ECs solution in 10 U/mL thrombin was added to 50 μL of 5 mg/mL fibrinogen. The fully supplemented media, as detailed in table 5.3 plus aprotinin was added after 24 hours and media changed 2 in 2 days. The experiment lasted for 21 days, but on timepoints 7, 14 and 21 days the gels were imaged with DAPI and Phalloidin. The protocol for staining was the same as followed in section 5.2.4.3.1.

	Seeding Strategy	Fibroblasts	Endothelial Cells
A		-	25000 cells
B		On Top 1250 cells	-
C		1250 cells	-
D		On Top 250 cells	-
E		250 cells	-

Endothelial cells   Fibroblats

Figure 5.7: Experiment 6 seeding illustration. Illustration of the 100 µL seeding strategy of endothelial and fibroblast cells monocultures with supplements to induce angiogenesis plus aprotinin. Created with BioRender.com

5.2.4.6.2 Seeding Strategy B

Strategy B commenced with pipetting 50 µL of 5mg/mL fibrinogen solution to the 8 mm diameter PDMS ring. Then, was added 50 µL of the 10 U/mL thrombin. The gel solution was left in the hood for 15 minutes before being placed in the incubator (humid 37°C, 21% oxygen and 5% CO_2). After 2 hours of incubation to ensure complete gel polymerization 100 µL of MCDB131 media was added to each gel for 30 minutes. Then, the media was removed and was added 100 µL of MCDB131 media containing 1250 fibroblasts. After 15 minutes in the hood, the gels were moved to the incubator. The rest of the protocol is the same as in section 5.2.4.6.1

5.2.4.6.3 Seeding Strategy C

First in strategy C was pipetted 50 µL of 5 mg/mL fibrinogen solution to the 8 mm diameter PDMS ring. Then, was added 50 µL of fibroblast cell solution in 10 U/ml thrombin as described in section 5.2.4.8.4 with 1250 cells/ 50 µL of thrombin. The gel solution was left in the hood for 15 minutes before being placed in the incubator (humid 37°C, 21% oxygen and 5% CO_2). The rest of the protocol is the same as in section 5.2.4.6.1

5.2.4.6.4 Seeding Strategy D

The protocol followed was the same as in 5.2.4.6.2, but only 250 fibroblasts were seeded on top of the gel.

5.2.4.6.5 Seeding Strategy E

The protocol followed was the same as in 5.2.4.6.3, but only 250 fibroblasts were seeded scattered in the gel.

5.2.4.6.6 DAPI, Phalloidin and fibrin gel staining

For experiment 6, 4% of the fibrinogen was substituted by 488-labelled fibrinogen as already described in section 5.2.3.2. The staining protocol with DAPI and Phalloidin was the same as mentioned in section 5.2.4.3.1. The imaging of the gels on the ZEIS LSM 710 used the 405 nm laser to excite the DAPI, to visualize the nucleus, the 488 nm laser to visualize the fibrin gel and the 633 nm laser to excite the Phalloidin and in this way visualize the F-actin.

5.2.4.6.7 ELISA

The media was analysed for angiogenesis-related proteins, such as interleukin 1β (IL-1β), interleukin 8 (IL8) and interleukin 6 (IL6). The protocols are detailed in sections 2.5.5, 2.5.4 and 2.5.1. respectively

5.2.4.7 Experiment 7: Fibrin Gel Co-culture under Static Conditions

To build the co-culture in fibrin gels, endothelial and fibroblasts were seeded together using strategies A and E from figure 5.7. The model assembly started with pipetting 50 μL of 5 mg/mL fibrinogen solution to the 8 mm diameter PDMS ring. Then, was added 50 μL of the 10 U/mL thrombin with 250 fibroblast and 25000 endothelial cells. After 15 minutes in the hood, the gels were moved to the incubator (humid 37°C, 21% oxygen with 5% CO_2). The fully supplemented media with aprotinin was added 24 hours and media changed 2 in 2 days. The experiment lasted for 21 days, but on timepoints 7, 14 and 21 days the gels were imaged and ELISAs were performed. The protocols are in sections 5.2.4.7.1 and 5.2.4.7.1. An illustration of the seeding strategy can be found in figure 5.8.

Seeding Strategy	Fibroblasts	Endothelial Cells
	250 cells	25000 cells

Endothelial cells ⬤   Fibroblats ⬛
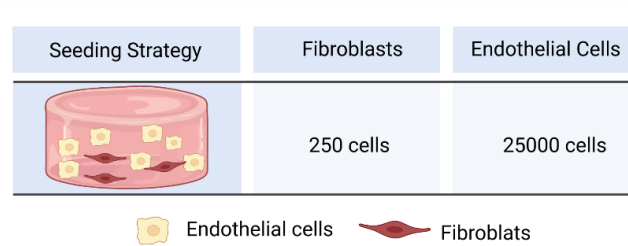
Figure 5.8: Experiment 7 seeding illustration. Illustration of the 100 µL seeding strategy of endothelial and fibroblast cells cocultures with supplements to induce angiogenesis plus aprotinin. Created with BioRender.com

5.2.4.7.1 DAPI, Phalloidin and CD31 Stain

First, was remove the cell culture media and 100 µL of 10% paraformaldehyde solution was added to each gel for 30 minutes. Then, the gels were removed from the PDMS ring and added to a well with 10% paraformaldehyde. The second fixation step took 30 minutes as well. At this stage, the gels were either stored at 4°C in PBS or proceeded to stain. To commence the stain, the gels were first permeabilized with 0.1% Triton solution in PBS (1 mL/ gel) in a shaker at room temperature. Then, washed two times with PBS for one minute between washes before the blocking step. This step consisted of 1% BSA solution in PBS that was added to each gel for 1 hour in a shaker at room temperature (1 mL/ gel). Then, the gels were washed two times with PBS for one minute between washes before adding mouse anit-CD31 (#ab9498 from abcam) solution. The first antibody was added in a dilution of 1:500 in PBS (100 µL/gel), overnight at 4°C in a shaker. On the following day, the plate was moved to the shaker at room temperature while the secondary antibody solution, Goat anti-Mouse Alexa Flour Plus 488 (1:100) containing DAPI (2 µg/mL) and Phalloidin (1:200) was prepared. The same washing step with PBS was applied, before adding to each gel 100 µL of the secondary antibody solution. The plate was moved to the shaker during 1 hour at room temperature. The gels were washed one last time for three times with PBS with one minute between washes. At this point, the gels were stored at 4°C in PBS or imaged on a Zeiss LSM710. The DAPI was excited at 405 nm, CD31 at 488 nm and Phalloidin at 633 nm.

5.2.4.7.2 ELISA

The supernatant harvested from the cell cultures was analysed for angiogenesis-related proteins, including IL6 and IL8. The protocols are detailed in sections 2.5.1 and 2.5.4 respectively.

This result section focuses on showing the efforts to create the vasculature-like model, in four different stages, presented in figure 5.1. For that, first was tested the suitability of the endothelial cell line selected, the HULEC. Then, was briefly tested a gelatine and alginate mesh as a biomaterial to support the endothelial cells (in stage 2). Given the results, was chosen to move forward with a more suited biomaterial, the fibrin gel. The characterization of the fibrin gel was done in stage 3 before cell seeding. That part of the work is presented in stage 4 and includes a total of 7 experiments (summarized in table 5.2).

5.3.1 Stage 1: 2D Endothelial Cells Characterization

The endothelial cells were firstly characterized in normal 2D cultures (figure 5.9). The trypan blue data, graph 5.9A) shows an exponential growth over 7 days. The curve fitted is the following $y=5381e^{0.2741x}$, with an initial value of 5381 and a constant rate of 0.2741 day^{-1}. With this data, then it was determined a time constant of 3.6 days (equation 6) and a doubling time of 2.5 days (equation 7). The trypan blue data was also used to generate graph 5.9B) which shows the live and dead ratio. During the 7 day period, the percentage of dead cells was always below 10%, the higher values are from days 1 and 2 of 8% and 9% respectively. Another indication that the cells are dividing during the seven days is the statistical significance of the increase of dsDNA shown in graph 5.9C). Along with this data is the MTS, which shows that the metabolic activity per number of live cells, also increases during the 7 days. Moving forward, graph 5.9D) shows the percentage of CD31 quantified through flow cytometry. From day 5 to 7 increases the number of cells expressing CD31, with a respective decrease of CD31 negative cells. Finally, both graphs 5.9E) and 5.9F) show dextran blue data, the first indicates dextran blue absorbance over 7 days fluctuating around the negative control. On the other hand, when reading the absorbance after 24 hours with higher seeding densities it was noticed that a significant decrease in the dextran blue intensity. Regarding the morphology of the cells, 5.9G) shows the cell shape and confluency on days 1, 3, 5 and 7. At lower density, as on day 1, some cells adopt an elongated shape, and others appear circular. With the increase of confluency, the cell monolayer shows a more uniform cobblestone appearance. In section 5.9H) can be found a more detailed characterization of the cell morphology on day 7. The stain only with DAPI shows cell uniform distribution along the imaged area, then the presence of Phalloidin shows visible complete confluency of the cell monolayer. In addition, the staining of CD31, localized preferentially on the cell membrane, visually confirms the flow cytometry data, that the HULEC cells line expresses the endothelial cells CD31 characteristic marker. The presence of VE-cadherin, also

the green fluorescence on the cell membrane, but in the far-right image, indicates that the cell monolayer is able to establish adherent junctions.
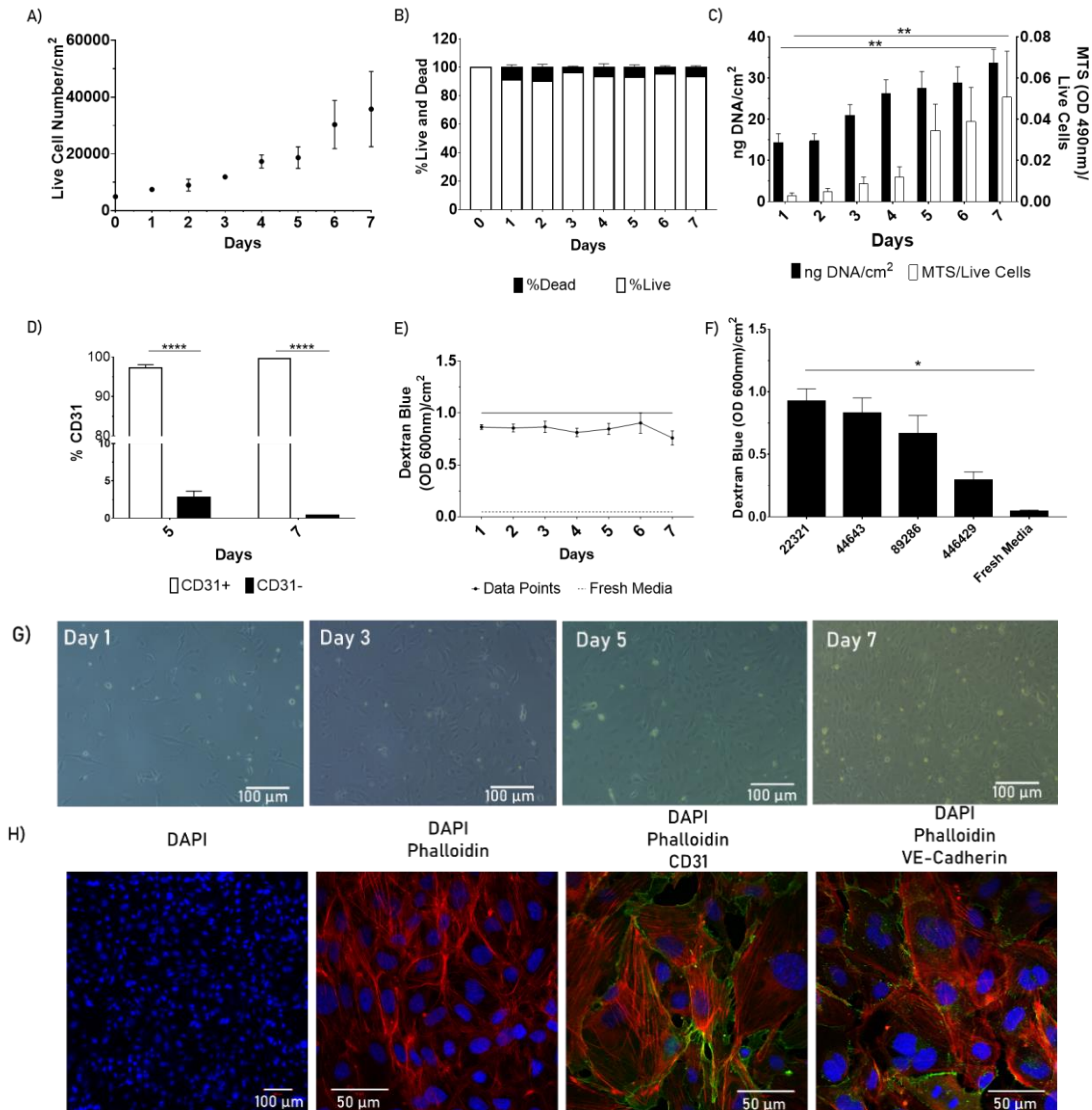
Figure 5.9: Endothelial cells 2D characterization. A) Live cell quantification with trypan blue over 7 days (n=3). The cell growth fits the following exponential curve $y=5381e^{0.2741x}$. B) Live and dead cells ratio using trypan blue assay (n=3). C) dsDNA quantification using picogreen for 7 days on the left y-axis (n=3 and ** represents p= 0.0070) and MTS absorbance over the number of live cells on the right y-axis (n=3 and ** represents p= 0.0040). D) Expression of the CD31 marker on day 5 and 7 (n=3). E) Dextran blue absorbance along 7 days (n=3). F) Dextran blue absorbance in function of the cells number (n=3 and * represent p=0.0195). G) Inverted bright field images of endothelial cells on day 1,3,5 and 7 (n=3 and scale bar represent 100 μm). H) Fluorescence images of endothelial cells on day 7 (n=3). From left to right, the first image shows the nucleus in blue stained with DAPI (scale bar represents 100 μm). The second image shows the cells stained with DAPI and in red, Phalloidin for F-actin (scale bar represents 50 μm). Next, the endothelial cells are stained with DAPI, Phalloidin and CD31 in green (scale bar represents 50 μm). The far-right image depicts the ECs stained with DAPI, Phalloidin and VE-Cadherin in green (scale bar represents 50 μm). The error bars correspond to SEM.

5.3.2 Stage 2: Gelatin and Alginate Gel Characterization

The next section shows the brief characterization of a mesh of 6% gelatin and 4 % alginate as a scaffold for endothelial cell growth. The scanning electron microscopy (SEM) images (figure 5.10) show the porosity of the scaffold depending on the polymerization conditions. The calcium chloride ($CaCl_2$) concentration was 150 or 300 mM and the volume of media at the bottom of the plate was between 0 and 2 mL.
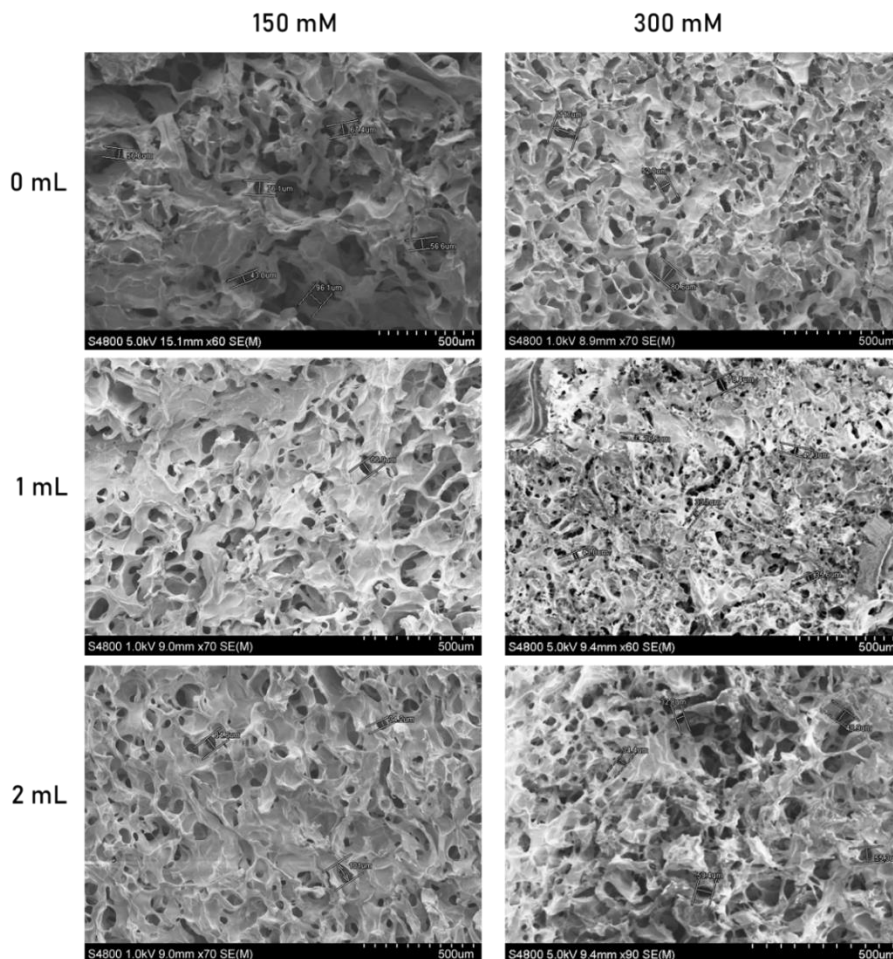
Figure 5.10: Gelatin gel scanning electron microscopy images. Scanning electron microscopy representative images of the 6% gelatin and 4% alginate gels depending on the polymerization conditions. Calcium chloride concentration 150 mM or 300 mM and volume of calcium chloride on the bottom of the plate, 0 to 2 mL. Annotated can be seen measurements of the porous in micrometers (n is between 3 and 16 and scale bar represents 500 μm).

The analysis of the SEM images is plotted in figure 5.11A), which shows the lowest diameter porous size of 16 μm when 150 mM of $CaCl_2$ is used together with 0 mL of crosslinker in the plate in the beginner of the experiment. Then, when using 1mL and 2 mL the diameter of the

184

porous size increase to 65 and 50 μm respectively. When using 300 mM of $CaCl_2$ for the polymerization, it was determined gels with the average pore size of 105, 65 and 72 μm when 0, 1 and 2 mL of crosslinker was present in the bottom of the plate. Figure 5.11B) shows the volume of water absorbed at time point 2h and 24h. From the graph is noticed that after 24 hours the gel still has capacity of absorbing water. Regarding cell seeding on the gelatin and alginate gels, the control condition where no cells were seeded showed unspecific biding and uniform blue fluorescence from the DAPI stain, figure 5.11C). When cells are seeded, figure 5.11D) to 5.11F), agglomerated cell nucleic are observed in very small numbers.
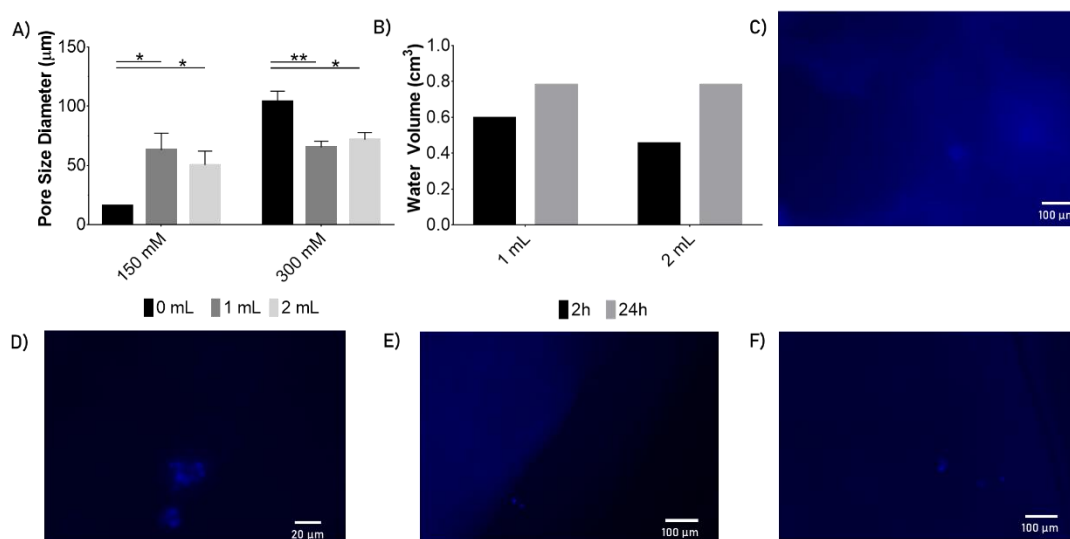
Figure 5.11: Gelatin gel characterization. A) Pore size diameter depending on crosslink condition, $CaCl_2$ concentration and initial volume (n=3 to n=16). B) Water volume depending on initial volume of $CaCl_2$ (300mM $CaCl_2$) (n=1). C) to F) DAPI stain on day 1 after gel crosslink. C) Control gel without cells (n=1). D) 4 mL gel with cells (n=1). E) 5 mL gel with cells (n=1). F) 6 ml gel with cells (n=1). The asterisk symbols in the plot represent: *p < 0.05** and ** p < 0.01. The error bars represent SEM.

5.3.3 Stage 3: Acellular Fibrin Gel Characterization

5.3.3.1. Experiment A: Acellular Fibrin Gel Rheologic Characterization

This section includes the rheological characterization of the fibrin gels, the results of loss and storage modulus can be found in figure 5.12. The fibrinogen (human origin) conditions used are 5, 2.5 and 1.25 mg/ml. The thrombin (human origin) concentrations are 5,1 and 0.1 U/ml. From the analysis of figure 5.12, the storage modulus is higher than the loss modulus for all the fibrinogen conditions. More specifically, both moduli follow the trend that the values are higher for 0.1 U/ml of thrombin, then for 1 U/ml and followed by 5 U/ml. In addition, looking at the y-

axis, the figure also shows that the values are higher for 5 mg/ml, decreasing in magnitude with the decrease of fibrinogen concentration. In this way, the increase of fibrinogen leads to an increase in the storage and loss modulus. On the other hand, the increase in thrombin leads to a decrease in both modules.
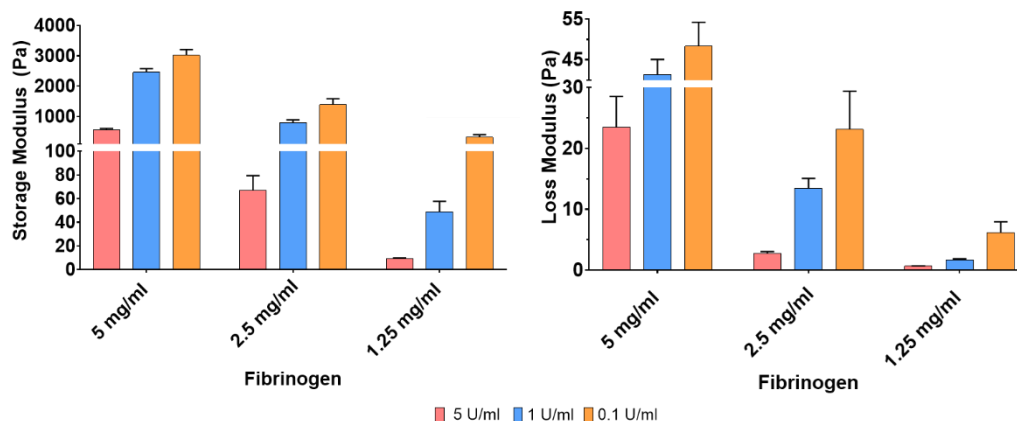
Figure 5.12 Storage (G') and loss modulus (G'') of fibrin gel in Pascal (Pa). The fibrinogen conditions used are 5, 2.5 and 1.25 mg/ml. The thrombin concentrations are 5,1 and 0.1 U/ml (n=3 to 5, each repeat is one run of the rheometer). The p values are presented on appendix 15. The error bars represent SEM.

To better understand the relationship between both moduli, the loss tangent was analyzed. This corresponds to the ratio between the loss and storage modulus in each cyclic deformation (tan δ = G''/G'). For all conditions tested, in table 5.4, the ratio is below zero, indicating the storage modulus is higher than the loss modulus (14-62 times higher), indicating the dominance of solid-like behaviour and that the gel polymerized. From the analysis of table 5.3, where similar values of loss tangent are highlighted in colour, is concluded that despite the increase of fibrinogen leading to an increase in the storage and loss modulus, the loss tangent decreases, indicating that the storage modulus increase more than the loss modulus. On the other hand, thrombin increase is associated with a decrease of G' and G'', however, the loss tangent increased, concluding that the storage modulus decreased more than the loss modulus. This indicates, that both phenomena, increase of fibrinogen or decrease of thrombin contribute to lower G'' and increase G'. This makes the loss tangent decrease and originates more rigid gels. On the contrary lead to more elastic gels.

186

Table 5.4: Loss tangent values. Loss tangent values for the fibrin gels with 5, 2.5 and 1.25 mg/ml of fibrinogen and 5, 1, 0.1 U/ml of thrombin. The colour scheme highlights values in the same range (n=3 to 5, each repeat is one run of the rheometer).

Fibrinogen/Thrombin	5 U/ml	1 U/ml	0.1 U/ml
5 mg/ml	0.041	0.017	0.016
2.5 mg/ml	0.041	0.017	0.017
1.25 mg/ml	0.070	0.034	0.019

5.3.3.2 Experiment B and C: Acellular Fibrin Fluorescence Microscopy and SEM Characterization

In this section is visualized the structure of the fibres composing the network of the fibrin gel, achieved by SEM and fluorescence images, where 488-labelled fibrinogen was added to the gel. (figures 5.13 to 5.15)
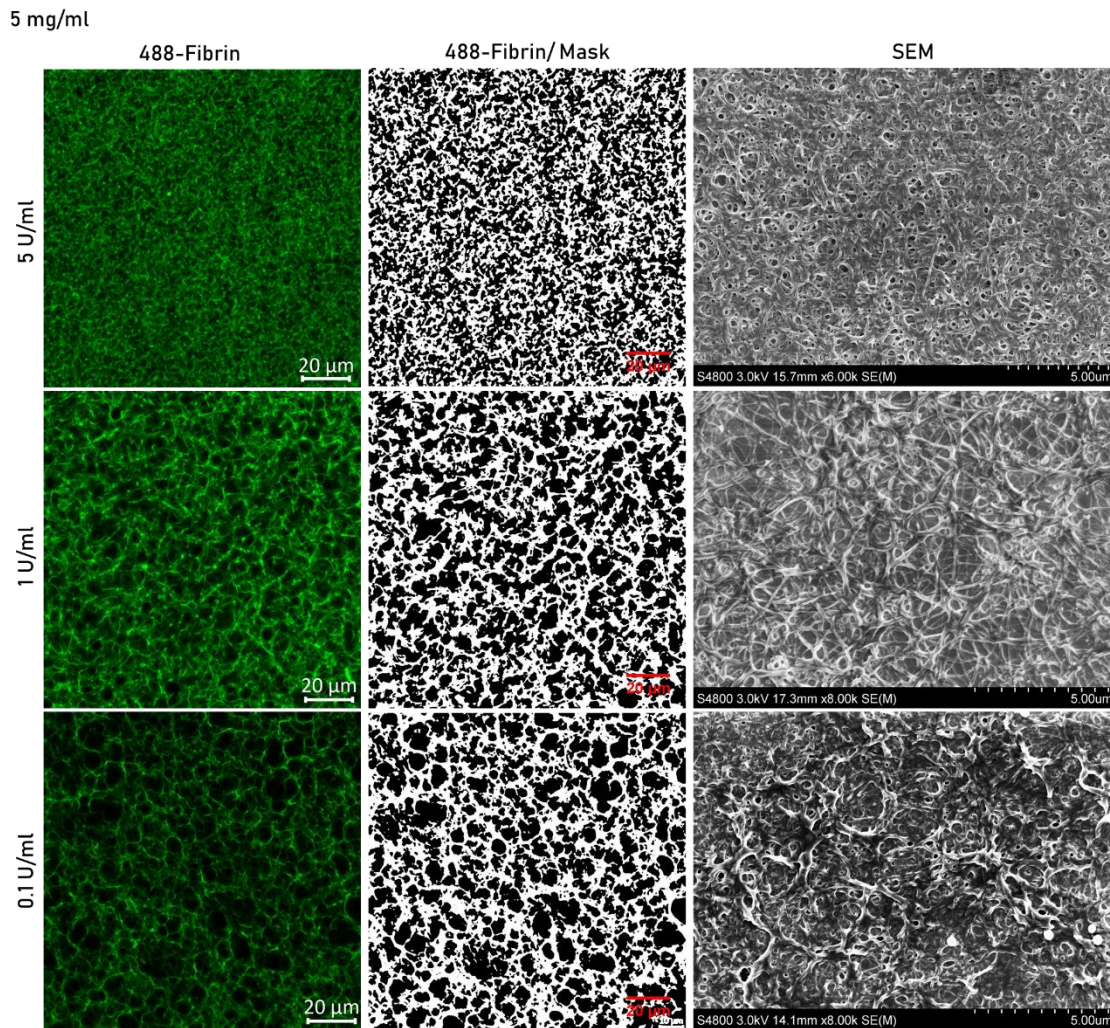
Figure 5.13: Fluorescence and scanning electron microscope images of fibrin gel polymerized with 5 mg/mL of fibrinogen and 5, 1 and 0.1 U/mL of thrombin. Left: Fluorescence image of

fibrin gel with 4% of 488-labelled fibrinogen (scale bar represents 20μm). Middle: threshold image generated by ImageJ (scale bar represents 20μm). Right: SEM image (the scale bar represents 5μm). (For condition 5 U/ml n=3, and a total of 38 images, 1 U/ml n=3 and a total of 31 images, 0.1 U/ml n= 3 and a total of 26 images).

From figures 5.13 to 5.15 the column at the felt hand side the show the fluoresce images. In the middle column, the threshold images that imageJ used to determine the white pixels (the fibres). On the right hand side column is present the SEM images. The most visible effect is the one from thrombin, which is observed on the confocal images but also on the SEM, where there is an increase in porous size and fibre length as the thrombin concentration decreases.
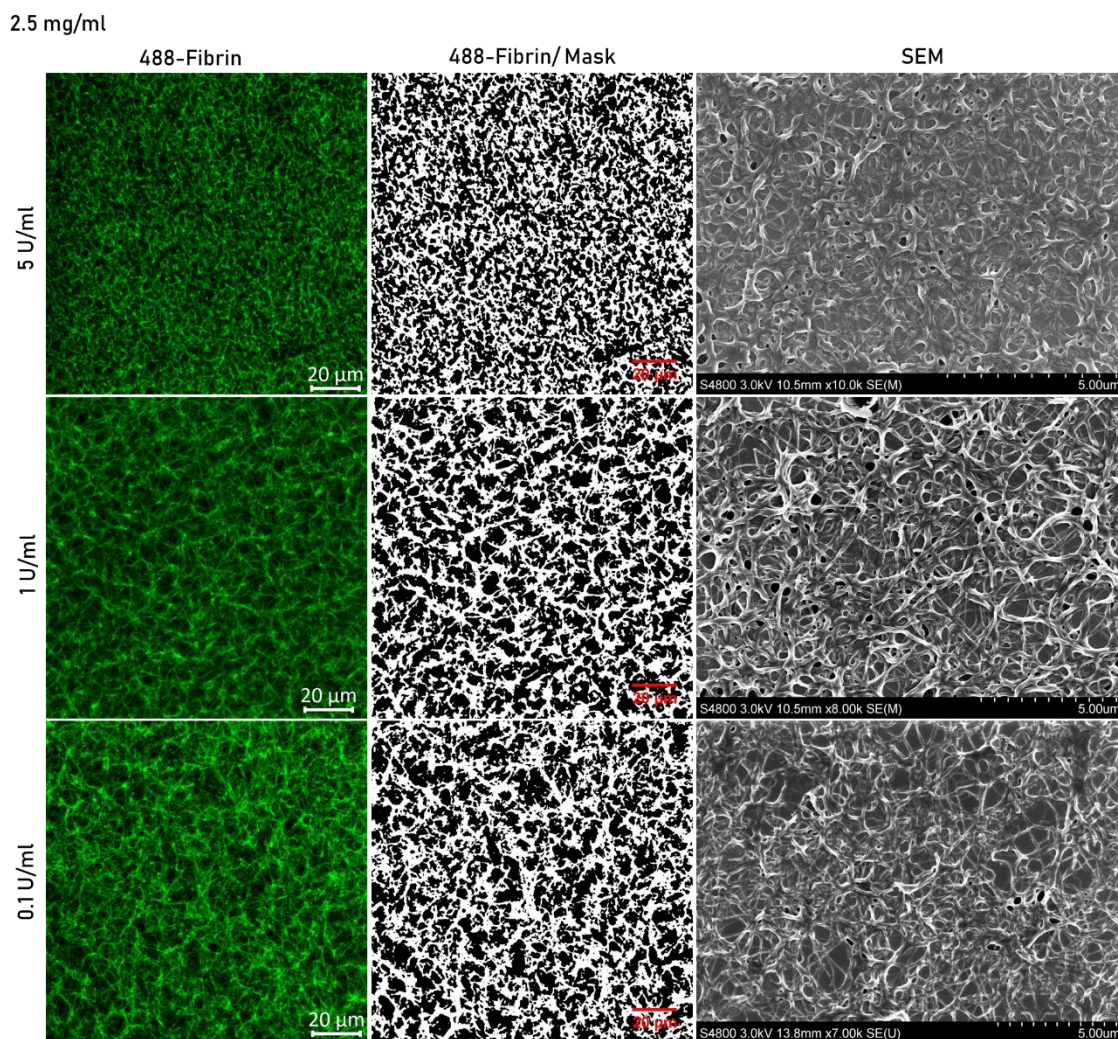
Figure 5.14: Fluorescence and scanning electron microscope images of fibrin gel polymerized with 2.5 mg/mL of fibrinogen and 5, 1 and 0.1 U/mL of thrombin. Left: Fluorescence image of fibrin gel with 4% of 488-labelled fibrinogen (scale bar represents 20μm). Middle: threshold image (scale bar represents 20μm). Right: SEM image (scale bar represents 5μm). (For condition 5 U/ml n=3 and a total of 34 images, 1 U/ml n=3 and a total of 36 images, 0.1 U/ml n= 3 and a total of 27 images).
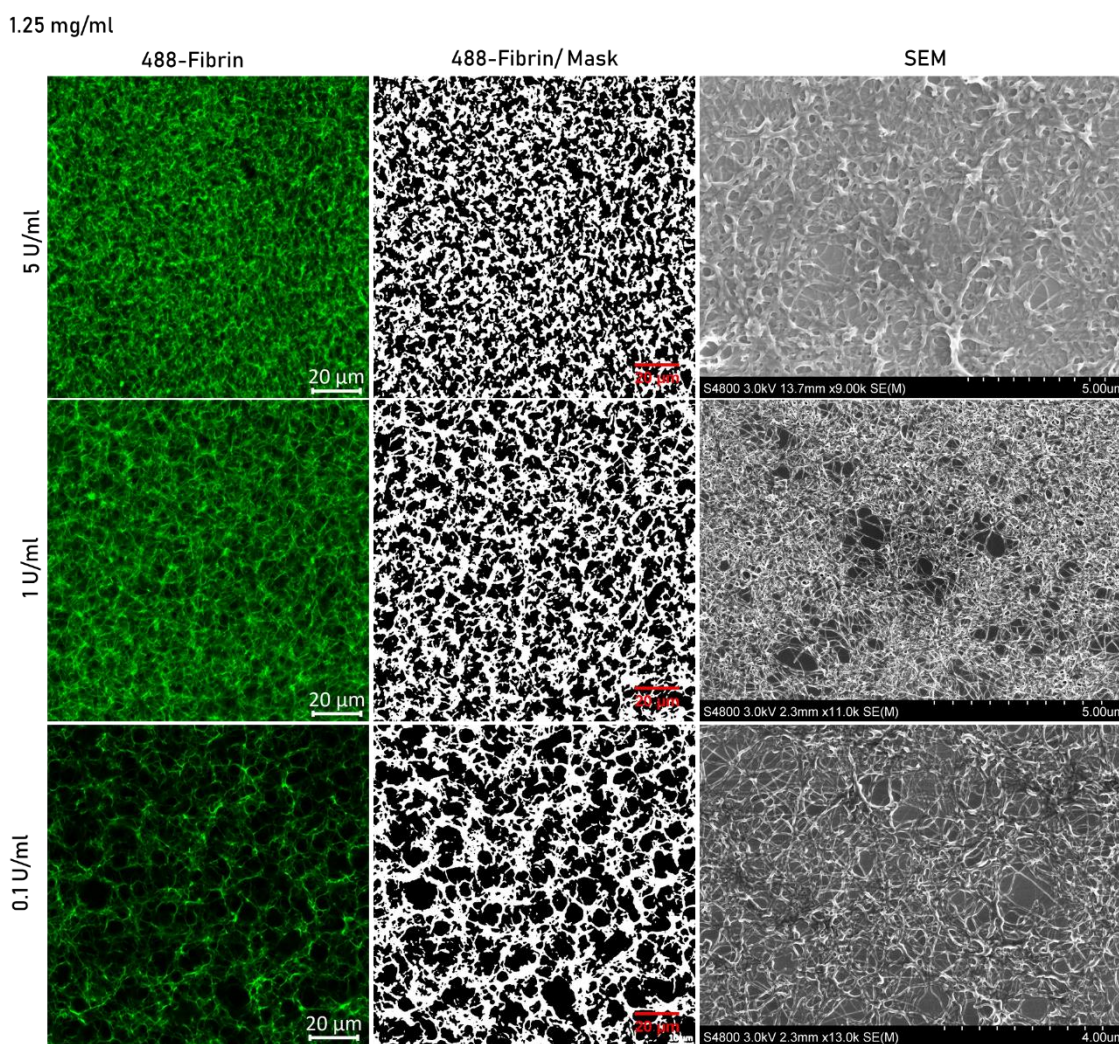
1.25 mg/ml

Figure 5.15: Fluorescence and scanning electron microscope images of fibrin gel polymerized with 1.25 mg/mL of fibrinogen and 5, 1 and 0.1 U/mL of thrombin. Left: Fluorescence image of fibrin gel with 4% of 488-labelled fibrinogen (scale bar represents 20μm). Middle: threshold image (scale bar represents 20μm). Right: SEM image (scale bar represents 5μm). (for condition 5 U/ml n=2 and a total of 18 images, 1 U/ml n=3 and a total of 30 images, 0.1 U/ml n= 2 and a total of 23 images).

The fluorescence images of the fibrin gel shown on the left hand side column from figures 5.13 to 5.15 were further analysed to determine the percentage of area occupied with porous. The images presented in the middle column from figures 5.13 to 5.15 correspond to that analysis. Where ImageJ converted the colour image in black and white to be able to quantify black and white pixels that match porous versus the fibres respectively. This using the script presented in section 5.2.3.2. (figure 5.16 left hand side plot). The increase of the thrombin concentration creates gels with more branching points and smaller porous, which led to gels with a lower percentage of the area associated with porous. However, an overall note is that the porosity

does not differ much between the conditions, the y axis from figure 5.16 is from 40% to 60% and the plot does not follow the porosity expected. In addiction to porosity, figure 5.16 on the right hand side includes the fibre diameter depending on fibrinogen and thrombin concentration. This data analysis shows a decreased tendency in fibre thickness as fibrinogen concentration decrease. Comparison within the same fibrinogen concentration but across thrombin concentration only shows a visual trend downward for 1.25 mg/mL.
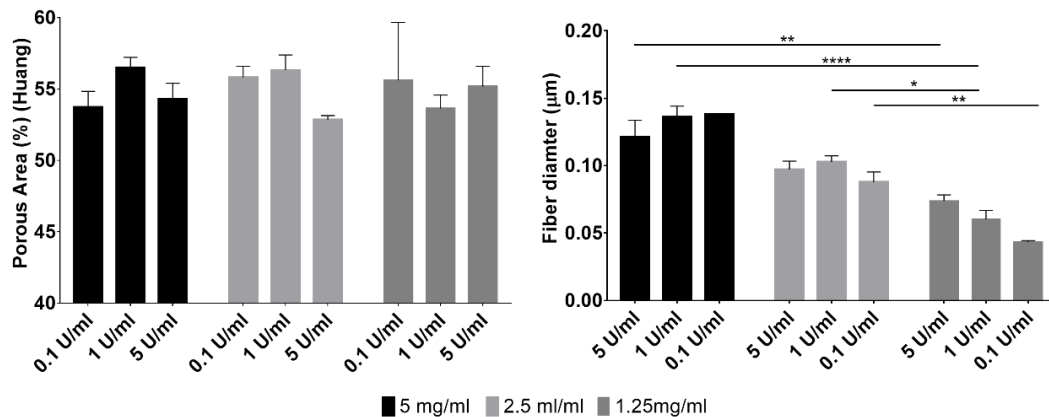
Figure 5.16: Fibrin gel porosity and fibre diameter. On the left, percentage of area corresponded to porous in the fibrin gel using confocal images depending on fibrinogen and thrombin concentration (n=3 except for 1.25mg/ml + 5 mg/ml and 1.25mg/ml + 0.1 mg/ml which is n=2, however the number of images analysed range from 36 to 18). On the right, fibre diameter in micrometres (μm) using SEM images depending on fibrinogen and thrombin concentration (n=3 except for 5mg/mL + 0.1 U/mL that is n=1). The asterisk symbols in the plot represent: *$p < 0.05$** and ** $p < 0.01$. The error bars represent SEM.

5.3.4 Stage 4: Fibrin Gel Cell Seeding

5.3.4.1 Experiment 1: Bovine Fibrin Gel

The first trial of seeding endothelial cells in the fibrin gel used fibrinogen and thrombin of bovine origin and a 96 well plate as the platform to polymerize 200 μL of gel (table 5.1, experiment 1). The fibrinogen concentration was 5 mg/mL and thrombin was tested 10, 5, 2.5 and 0.5 U/mL. The dsDNA was determined on days 1,3, and 7 to follow endothelial cells proliferation inside the gel. To compare the growth of the endothelial cells seeded in the gel and in 2D, the same experimental protocol followed to seed the cells in the gel was followed but PBS (media where fibrinogen stock is diluted) was added instead of fibrinogen. The results can be found in figure 5.17A), for the cells grown in 3D cells and 5.17B) for the cells in 2D. To facilitate graph comparison the y-axis was kept constant, which highlights the higher values recorded for cells seeded in the fibrin gels than in 2D seeding. Nevertheless, both graphs show a growing tendency from day 1 to day 7, with exception of the 10 U/mL thrombin condition in 3D. This condition,

from day 3 to day 7 the dsDNA amount decrease. The graph 5.17A) does not only displays a trend between the days, but also within the same day, higher amounts of dsDNA are quantified for lower thrombin concentrations. A similar tendency is observed on plot 5.17B) where cells are seeded in 2D, and the difference is the extra thrombin supplementation. These conclusions are only visual since there is no significant increase between the days for both graphs. One last feature that stands out in both graphs is related to the high standard deviation observed on day 7.
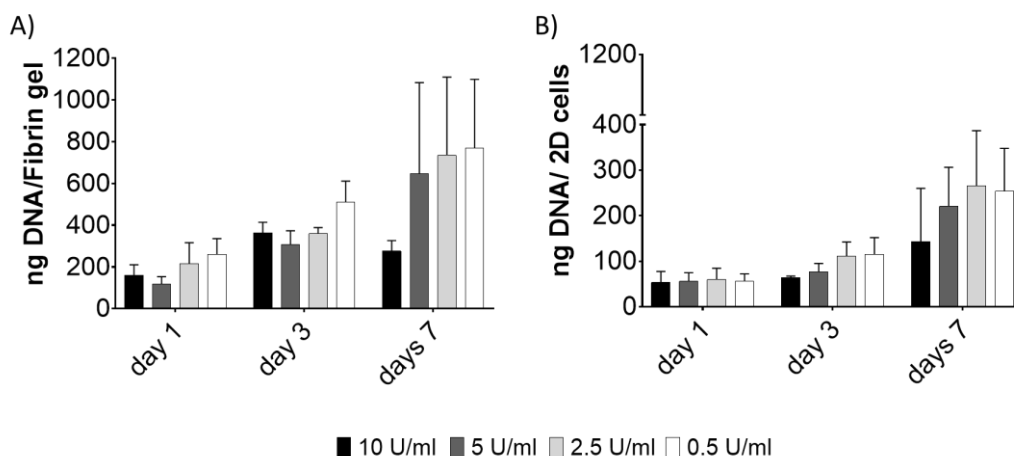
Figure 5.17: Experiment 1: bovine fibrin dsDNA quantification. dsDNA quantification of endothelial cells cultured with fibrinogen and thrombin from bovine origin. The fibrinogen concentration is 5 mg/ml and thrombin are 10, 5, 2.5 and 0.5 U/ml. The left side graph shows the DNA quantification of endothelial cells grown in 200 µL fibrin gels on days 1,3, and 7 after polymerization. The right-side graph shows the DNA quantification on days 1, 3 and 7 of endothelial cells grown in 2D, where the fibrinogen was substituted by PBS (n=3 except for 3D cells days 7, 10 U/mL, 2D cells day 3 and 7 for 10 U/mL that is n=2). The error bars represent SEM.

5.3.4.2 Experiment 2: Human Fibrin Gel

The experiment 2, as detailed in table 5.2, used fibrinogen and thrombin of human origin and a 96 well plate as platform for the 200 µL gel polymerization. However, the concentrations of fibrinogen and thrombin slightly changed to be within the physiologic levels. In this way, the fibrinogen concentrations tested were 5, 2.5 and 1.25 mg/mL and thrombin 0.1, 1 and 5 U/mL. In figure 5.18 is present the dsDNA quantification from days 1,3,7,14 and 21 with and without FBS during polymerization. On day one, was expected more a less the same dsDNA content, however, gels with FBS show higher dsDNA content. From day 1 to 3, conditions with FBS saw the dsDNA content decrease, the condition with 0.1 U/mL (No FBS) did not change and only conditions 5 and 1 U/ml of thrombin (No FBS) show double DNA content. From day 3 to 7 there is not much change, values of DNA are around 100 ng with FBS condition being slightly higher.

From day 7 to 14 there is a general drop for all conditions, from 100 ng to around 50 ng. However, from day 14 to 21, the tendency is inverted, and the values are similar to day 7, values of DNA are again around 100 ng with FBS condition being slightly higher.
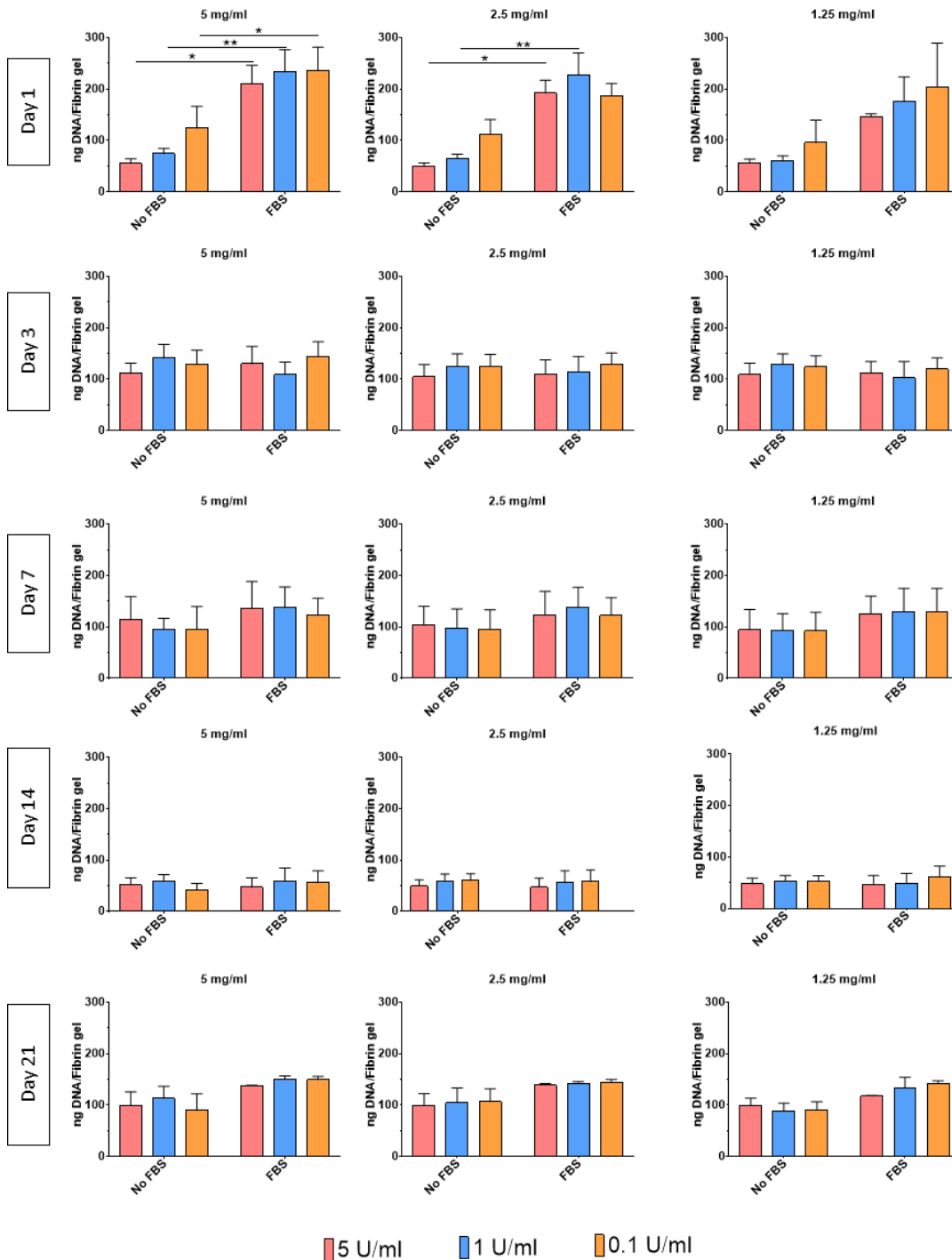
Figure 5.18: Experiment 2: human fibrin gel dsDNA quantification. dsDNA quantification of endothelial cells cultured with fibrinogen and thrombin from human origin dsDNA quantification of 200 μL fibrin gels on days 1, 3, 7, 14 and 21 with and without FBS during gel formation. The

fibrinogen concentrations are 5, 2.5 and 1.25 mg/mL. The thrombin conditions are 5, 1 and 0.1 U/mL (day 1, 3 are n=3, day 7 is n=6 for No FBS and n=4 for with FBS, day 14 and 21 are n=4 for No FBS and n=2 for with FBS). The asterisk symbols in the plot represent: *$p < 0.05$** and ** $p < 0.01$. The error bars represent SEM.

The endothelial cells from day 21 (No FBS) from figure 5.18 were imaged using DAPI (figure 5.19). The condition where is observed a higher number of distributed cells is when 1.25 mg/mL fibrinogen is crosslinked with 0.1 U/mL of thrombin. For the rest of the conditions, the cells are found in small clusters across the gel.
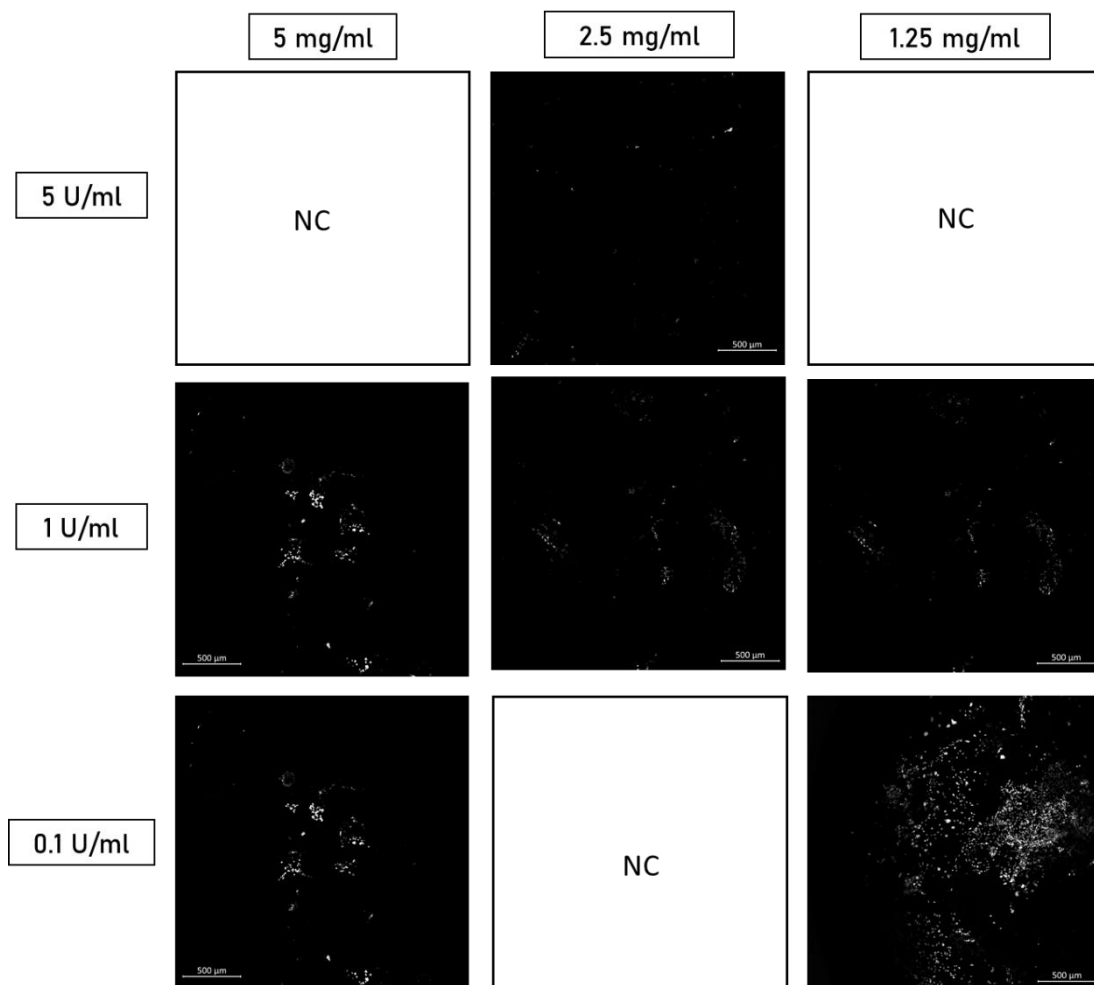
Figure 5.19: Experiment 2: human fibrin gel DAPI stain. Endothelial cells cultured in fibrinogen and thrombin of human origin stained with DAPI, showing the nucleus in white. The images correspond to 200 µL fibrin gel on day 21 without FBS. The fibrinogen concentrations are 5, 2.5 and 1.25 mg/mL. The thrombin conditions are 5, 1 and 0.1 U/mL. The scale bar corresponds to 500 µm. The NC corresponds to conditions not imaged (n=1).

5.3.4.3 Experiment 3: 100 µL Fibrin Gel

To improve endothelial cell seeding on the fibrin gels, it was polymerized in the 96 well plate 100 µL instead of 200 µL. This adjustment changes the ratio diameter/height from 1.2 found for 200 µL gel to 2.2. In this way, in 200 µL gel both height and diameter were similar. However, to improve oxygen and nutrients diffusion across the height of the gel it was tested seeding the endothelial cells in 100 µL gel, where the diameter is twice the height. In figure 5.20 can be found the dsDNA quantification of 100 µL gel on days 7, 14 and 21 without FBS. From day 7 to day 21 there is a slight tendency where a lower concentration of fibrinogen has higher ng dsDNA. Regarding the impact of thrombin, does not seem to influence cell growth.
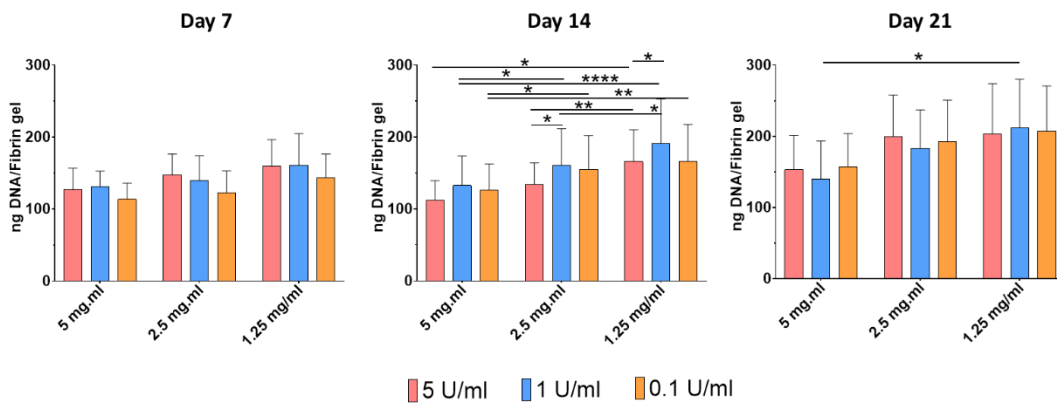
Figure 5.20: Experiment 3: 100 µL fibrin gel dsDNA quantification. Endothelial cells seeded on 100 µL fibrin gel. The dsDNA was determined on days 7, 14 and 21. The fibrin gel polymerization occurred without FBS. The fibrinogen concentrations are 5, 2.5 and 1.25 mg/mL. The thrombin conditions are 5, 1 and 0.1 U/mL (n=4). The statistics are only shown for conditions with the same fibrinogen or thrombin. The asterisk represents *p < 0.05, ** p < 0.01 and ****p < 0.0001. The error bars represent SEM.

To have a visual distribution of the cells when seeded on 100 µL fibrin gel, figure 5.21 comprehends haematoxylin stain (within two magnifications) and DAPI and Phalloidin stain of gels from days 7, 14 and 21. On day 7 it is observed that a higher number of cells are found in gels with 5 U/mL of thrombin, then 1 U/mL, followed by 0.1 U/mL. Indicating that independent of the fibrinogen conditions the cells prefer higher thrombin concentrations. On day 14, cells start to acquire a more 3D structure instead of being evenly distributed across the gel as seen on day 7. This results in 2D images where round structures emerge, since the all structure is distributed across the z stack. These features are not observed on condition 1.25 mg/mL, where cells proliferate a lot but do not sustain complex 3D structures. These gels are soft, collapse and support only 2D cell proliferation. On day 21, the 3D round structures are even more developed, except again for 1.25 mg/mL.

5 mg/ml

5 U/ml

1 U/ml

0.1 U/ml

2.5 mg/ml

5 U/ml

1 U/ml

0.1 U/ml

.

195

1.25 mg/ml

5 U/ml

1 U/ml

0.1 U/ml

5 mg/ml

Day 14

5 U/ml

1 U/ml

0.1 U/ml

2.5 mg/ml

5 U/ml

1 U/ml

0.1 U/ml

1.25 mg/ml

5 U/ml

1 U/ml

0.1 U/ml

5 mg/ml

Day 21

5 U/ml

1 U/ml

0.1 U/ml

2.5 mg/ml

5 U/ml

1 U/ml

0.1 U/ml
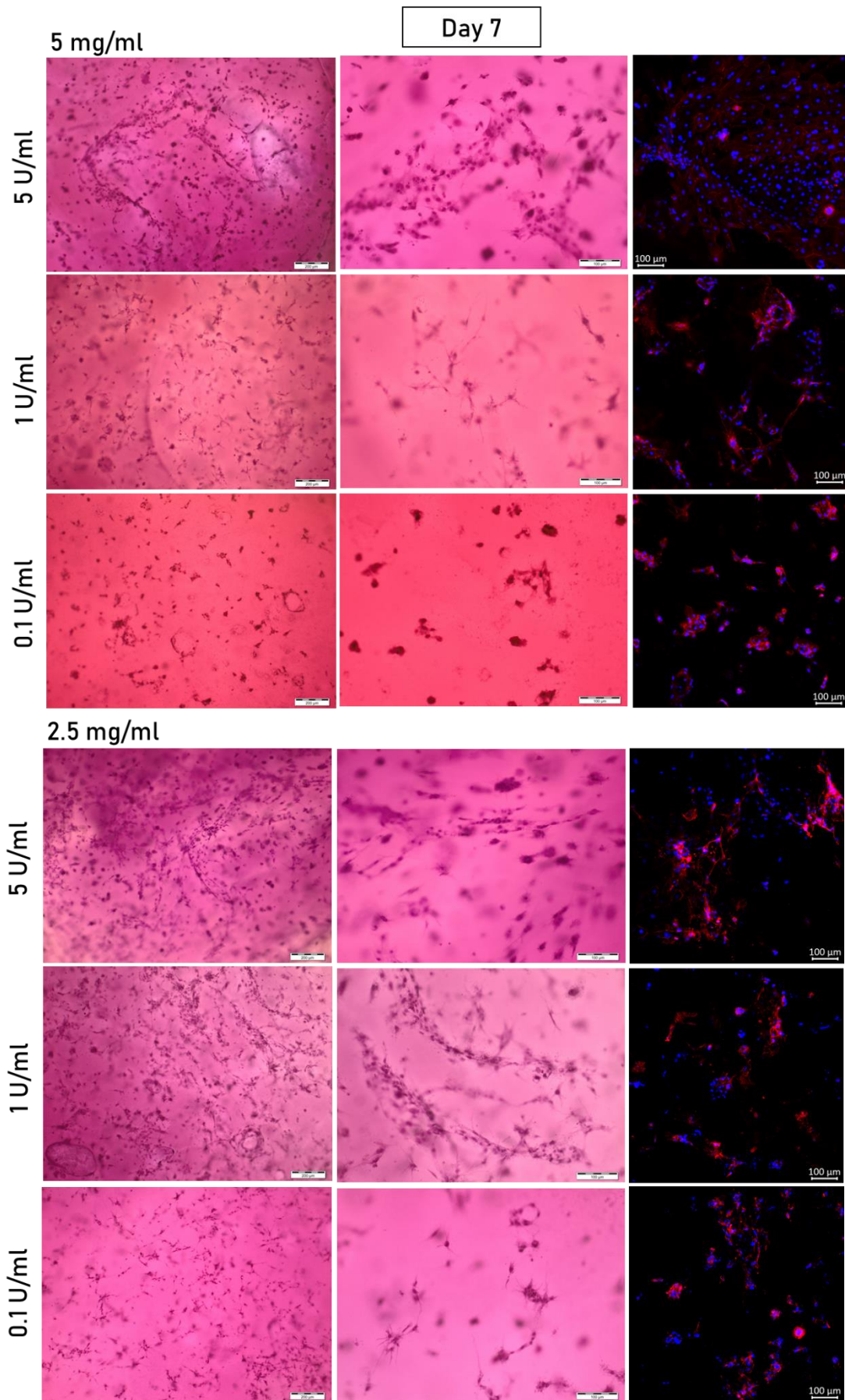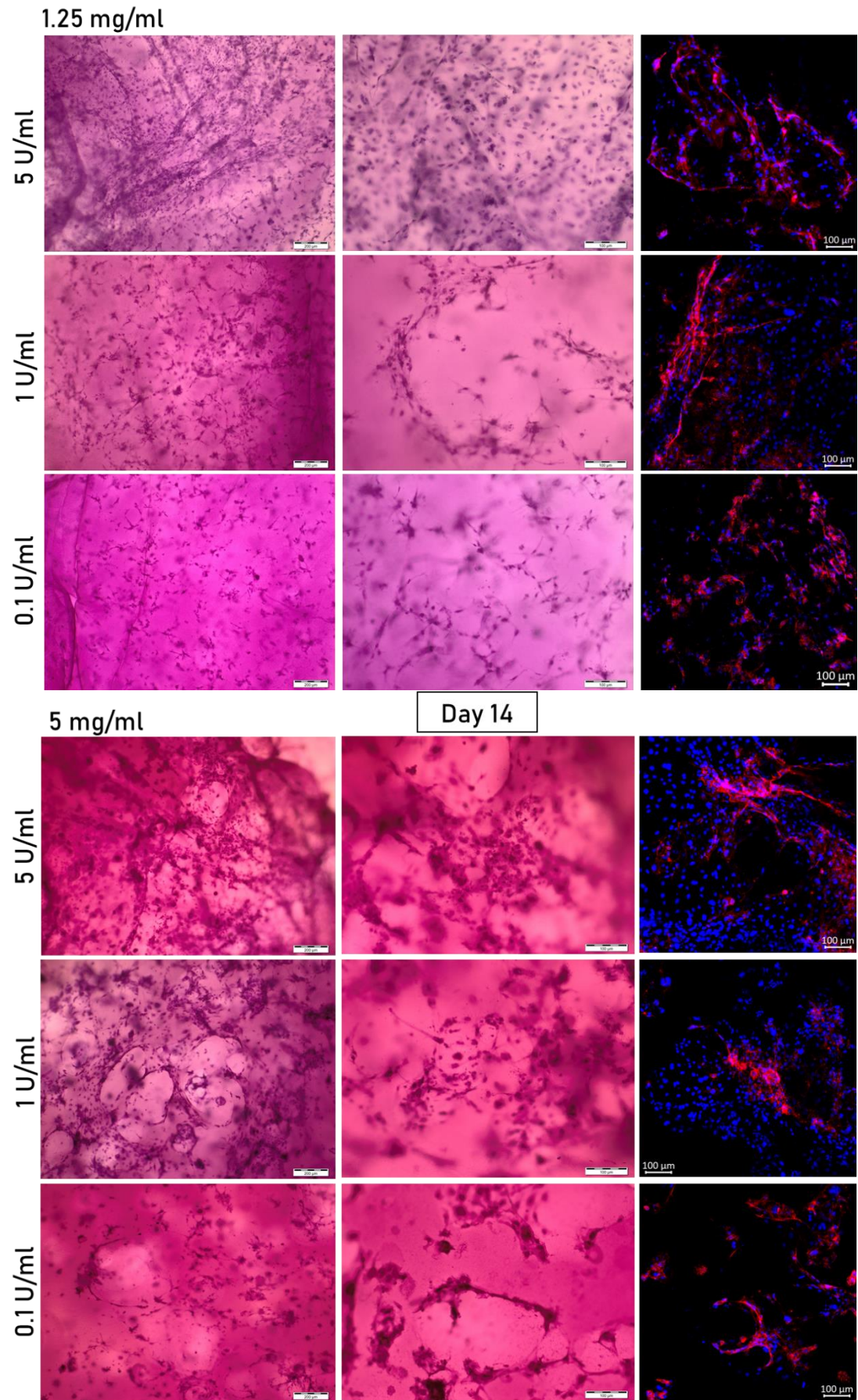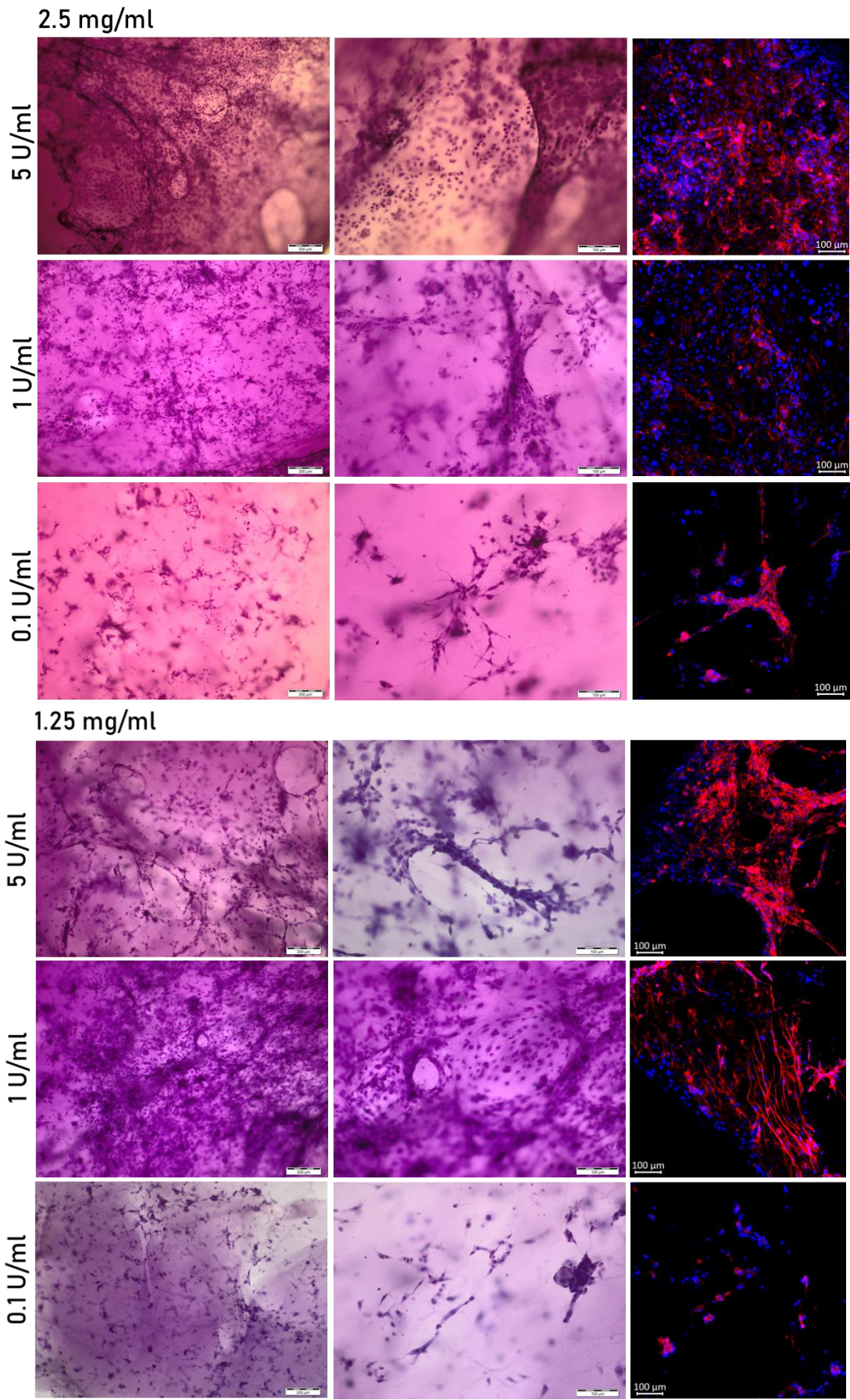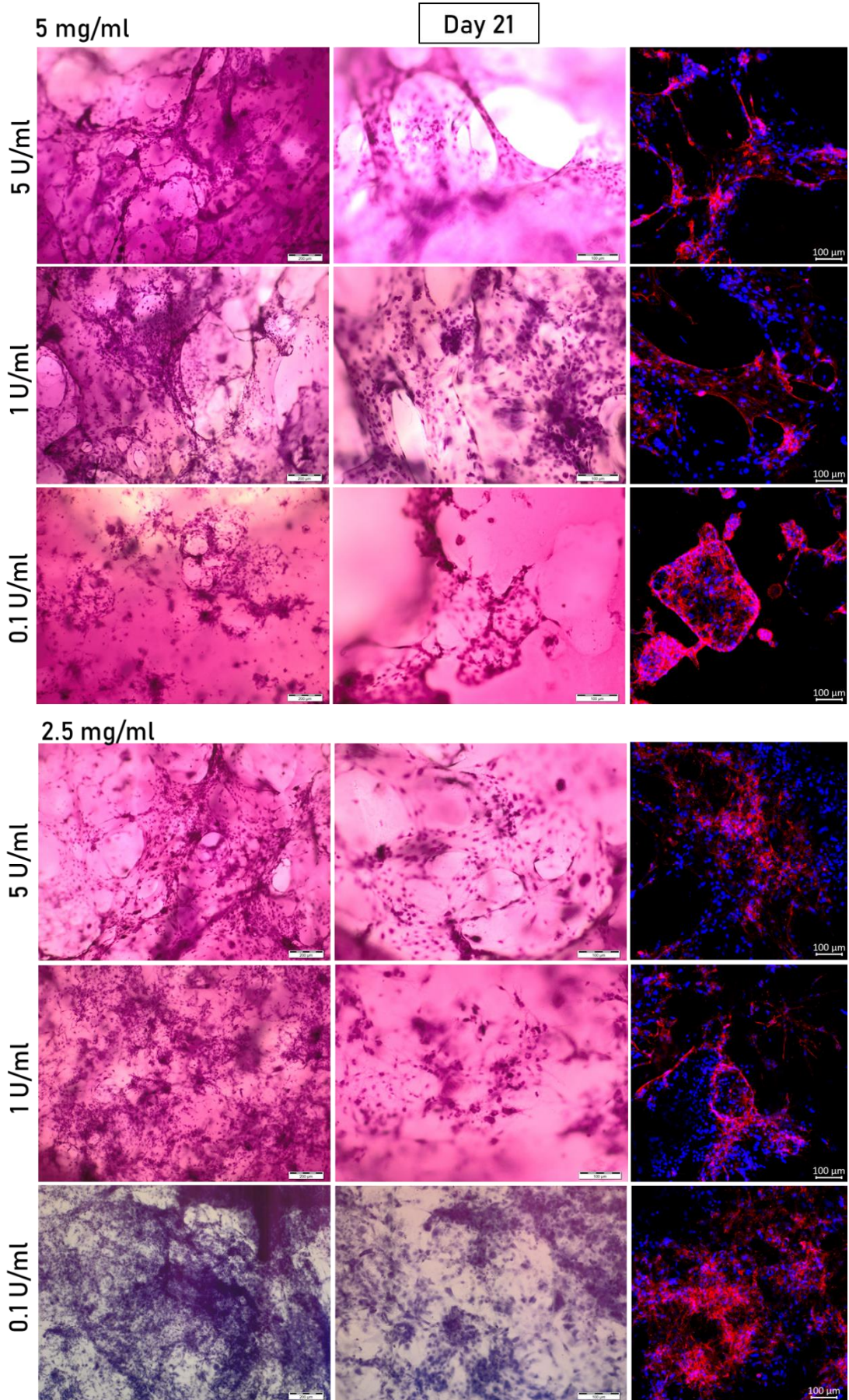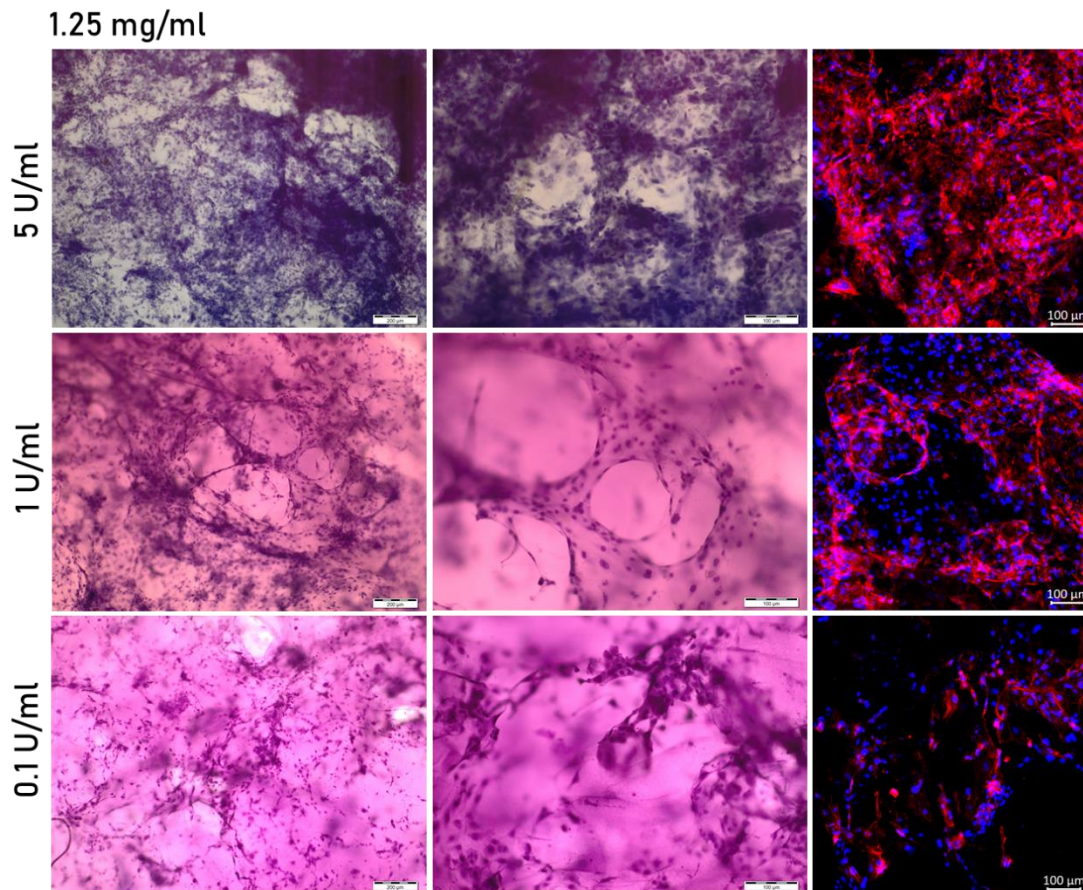
Figure 5.21: Experiment 3: 100 µL fibrin gel bright field and fluorescence images. Endothelial cells seeded on 100 µL fibrin gel. Images on the left-hand side as well as in the middle column correspond to gels stained with Haematoxylin, where the scale bar (white bar) corresponds to 200 µm and 100 µm respectively. The right-side images correspond to gels stained with DAPI and Phalloidin. The scale bar represents 100 µm (n=3 for day 7 and n=2 for day 14 and 21). The fibrin gel polymerization occurred without FBS and was imaged on day 7,14 and 21 of culture. The fibrinogen concentrations are 5, 2.5 and 1.25 mg/mL. The thrombin conditions are 5, 1 and 0.1 U/mL.

The reduction in half of total fibrin gel volume from 200 µL to 100 µL, from experiment 1. or 2. to experiment 3, has an impact on the diameter/height ratio of the gel. The volume reduction in the 96 well pate resulted in a double in the ratio from 1.2 to 2.2. This means that the diameter of the gel is two times bigger than the height. This change is even more pronounced when using the 8 mm PDMS ring, where the diameter is 4 times bigger than the height. This data is shown in table 5.5.

Table 5.5: Diameter/height ratio of fibrin gel polymerized on 96 well plate or 8 mm PDMS ring. Diameter/height ratio of endothelial cells cultured on 96 well plate in a total volume of 200 or 100 µL of fibrin gel. The ratio is also determined for the cell cultured on the 8 mm PDMS ring with a total volume of 100 µL. The 96 well plate specifications were available on the ThermoFisher Technical Data Sheet for Nunc 96-Well, PS, Flat Bottom Plate, Pinch Bar.

Volume (µL)	Height (mm)	Diameter (mm)	Ratio (diameter/height)
96 well plate			
0	0	6.1	-
400 (max volume)	11.3	7.0	-
200	5.65	6.5	1.2
100	2.83	6.3	2.2
8 mm PDMS ring			
0	0	8	-
100	1.99	8	4

5.3.4.4 Experiment 4: Endothelial Cells Invasion Capacity

To support the selection of the fibrinogen and thrombin concentration to move forward with, it was measured cell invasion capacity. Contrary to results before, where the cells were evenly dispersed in a fibrinogen and thrombin solution that when polymerizes solidifies incorporating the scattered cells. For the cell invasion assay, the cells were embedded in the fibrin gel as spheroids, table 5.1 experiment 4. Very briefly, after following the hanging drop technique to form the spheroids, it was pipetted into the drop, the fibrinogen and thrombin solution, which lead to the embedding of the spheroid in the fibrin gel. On day 2 of being embedded in the gels, the spheroids were fixed and imaged. Figure 5.22 represents the invasion area (determined as described in section 5.2.4.4.4) and in figure 5.23 the images of the spheroids stained with Hoechst and PI and Haematoxylin.

The plot exhibits a trend where higher thrombin concentration led to higher migration of the cells independently of the fibrinogen concentration. It is noticed as well that the presence of FBS during polymerization does not increase cell invasion. The higher capacity to invade the gel is found when thrombin concentration is 5 U/mL with and without FBS for 2.5 and 1.25 mg/mL of fibrinogen, as well as for 1.25 mg/mL combined with 1 U/mL and no FBS.
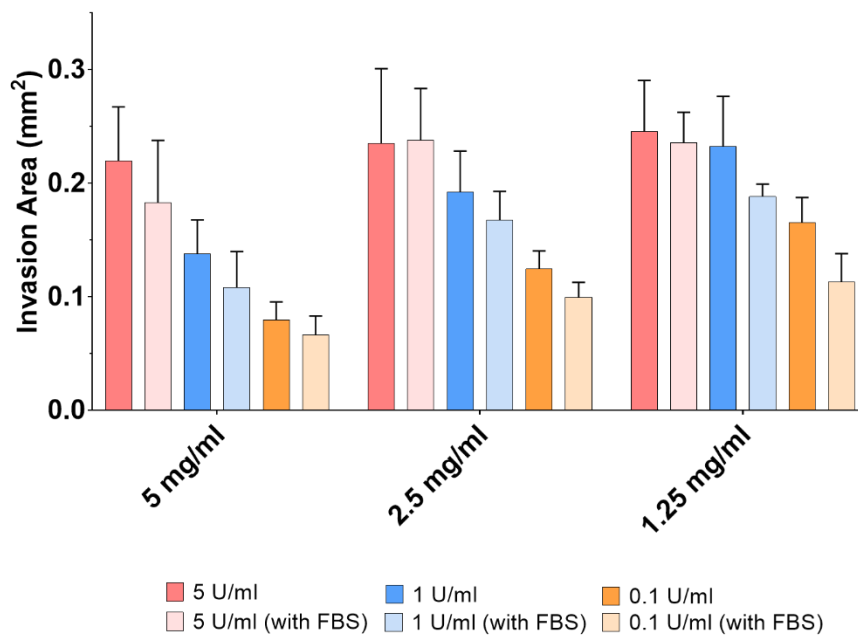
Figure 5.22: Experiment 4: endothelial cell spheroids invasion area. Plot of the invasion area on day 2 after fibrin embedding with and without FBS during gel formation. The fibrinogen concentrations are 5 mg/ml, 2.5mg/ml and 1.25 mg/ml. The thrombin conditions are 5 U/ml, 1 U/ml and 0.1 U/ml. (n=5, expect condition 5 mg/ml, 5 U/ml with FBS where n=4, each biological repeat is the average of 2 to 4 spheroids). Error bars represent SEM.

Figure 5.23 depicts a representative image of haematoxylin stain, as well as Hoechst and PI, of a spheroid depending on thrombin and fibrinogen conditions. The haematoxylin images were the ones used to generate the plot in figure 5.22 with images showing the trend in the graph. The Hoechst and PI show live and dead cells respectively, with dead cells mostly restricted to the spheroid centre.

After evaluating experiments 3 and 4, was selected the 2.5 mg/mL fibrinogen and 5 U/mL thrombin as the concentrations to move forward to develop the vasculature model. The dsDNA quantification from experiment 3 does not show a condition where more DNA is present and consequently more cells. However, the fluorescence and bright field images role out 1.25 mg/mL of fibrinogen as not supportive of 3D cells rearrangement as 5 or 2.5 mg/mL do. In addition to the fact that the gels are softer and too fragile to handle. The spheroid data allow for narrowing the thrombin condition to 5 U/mL, which independent of the fibrinogen concentration led to a higher invasion area, but with 2.5 and 1.25 mg/mL being slightly higher. In this way, was selected 2.5 mg/mL and 5 U/mL as polymerization conditions to move forward and build the coculture.
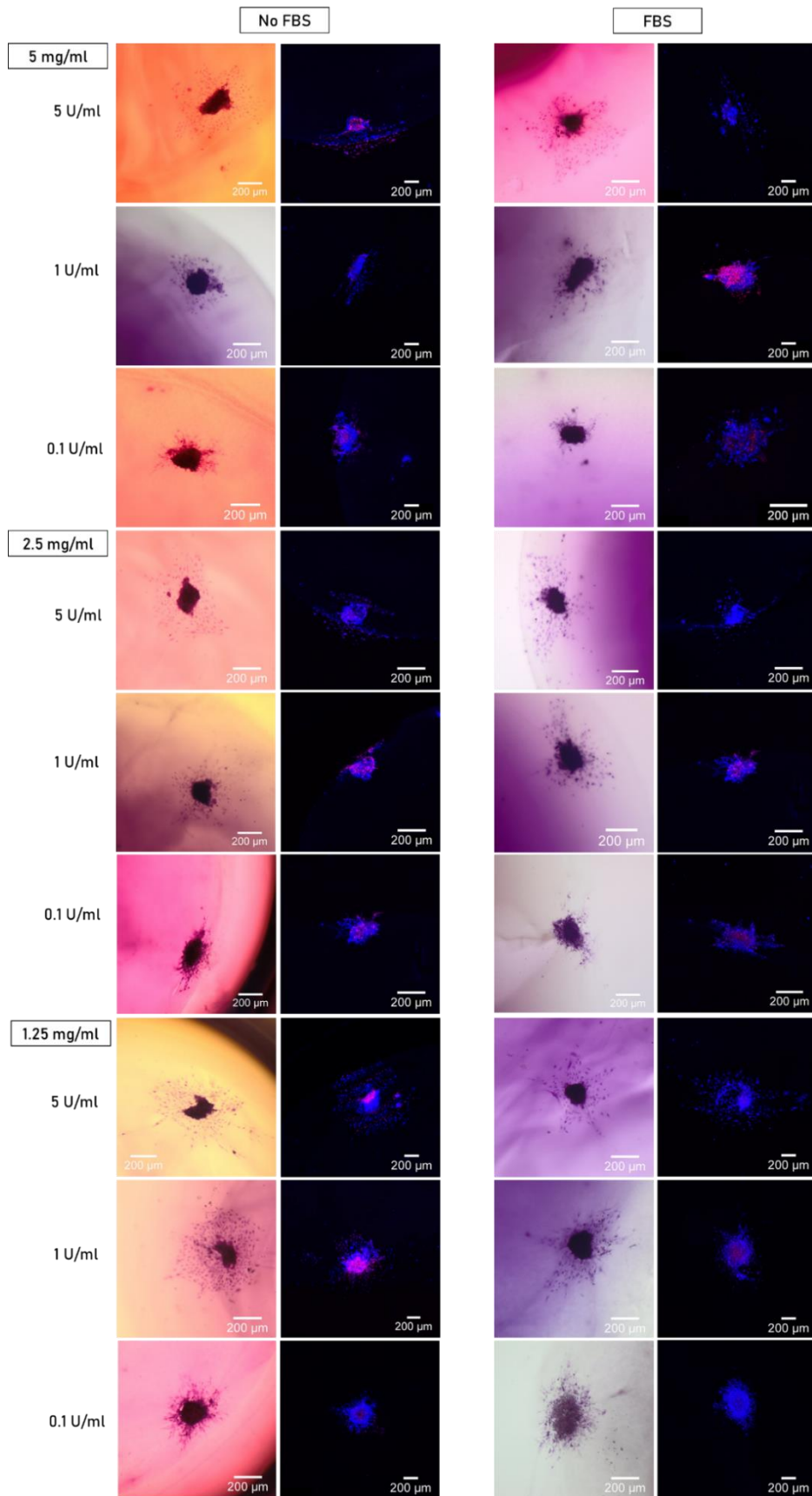
Figure 5.23: Experiment 4: endothelial cell spheroids bright and fluorescence staining.
Spheroids on day 2 after fibrin embedding with and without FBS during polymerization. The

column on the left represents Haematoxylin stain and on the right Hoechst and PI. The scale bar represents 200 μm (n=5, expect condition 5 mg/ml, 5 U/ml with FBS where n=4).

5.3.4.5 Experiment 5: 50 μL + 50 μL Fibrin Gel

After selecting the fibrinogen and thrombin conditions to move forward with, experiment 5 tested the proliferation of the endothelial and fibroblasts cells in 50 + 50 μL gels under angiogenic induction media. The endothelial cells were seeded scattered or as spheroids and in figure 5.24 are representative images of the culture on days 7,14 and 21. Note that these images correspond to the seeding strategy A and B from figure 5.6. The endothelial cells seeded as scattered show similar morphology and distribution as already documented before in figure 5.21, as the days in culture increase the cells organize in 3D structures. On the other hand, as spheroids, the round 3D structures associated with the spheroid formation and previously recorded in figure 5.23 are not visible. The DAPI stain of the entire gel shows small numbers of isolated cells.

Regarding the fibroblast seeded on the fibrin gels, figure 5.25 is shown from A) to D) the conditions illustrated in figure 5.6 C to F respectively. The cells are represented with a blue nucleus and in red the F-actin filaments. The cells seeded on top or inside the gels show in both conditions elongated morphology, very similar to what was seen in data chapter 1 on the 2D characterization of the lung fibroblast. However, the fibroblast over time degraded the gel, with higher catalytic capacity with higher cell number, the reason for the missing images on days 14 and 21.
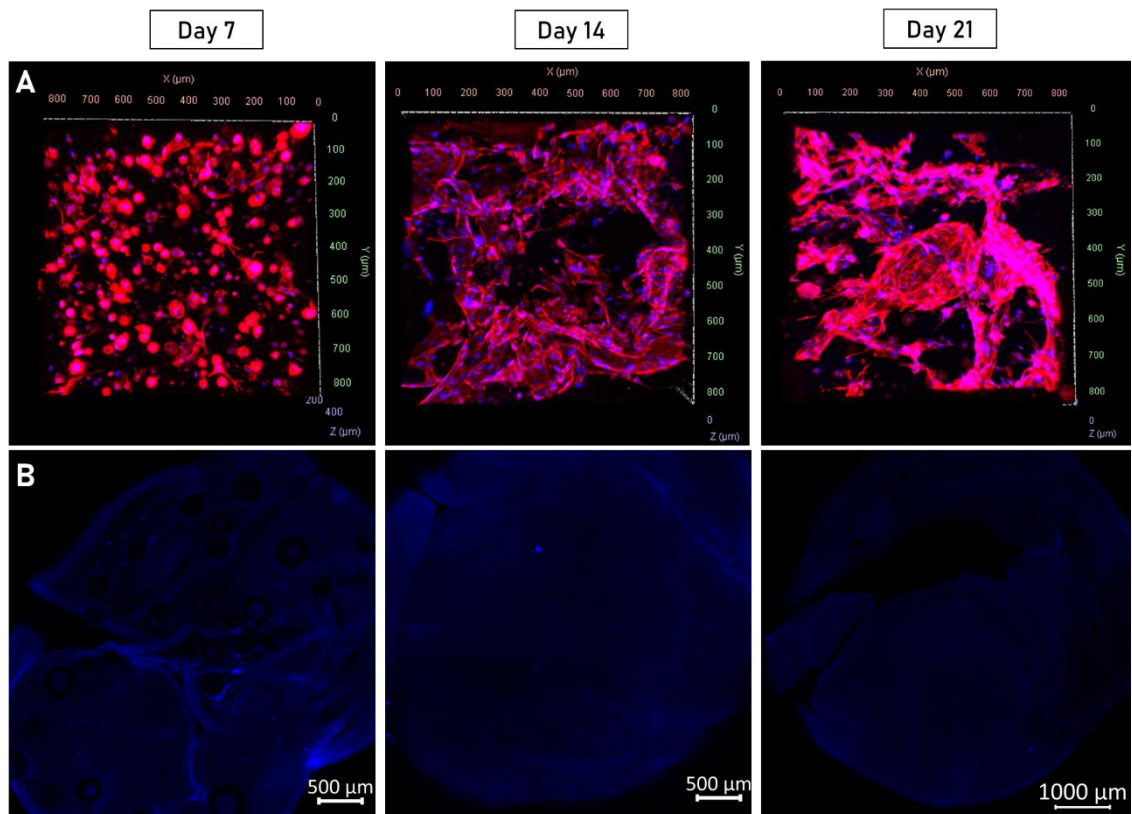
Figure 5.24: Experiment 5: endothelial cells seeded on 50 + 50 µL fibrin gel. A) Top images correspond to endothelial cells scattered seeded on 50 + 50 µL gel. B) Bottom images correspond to spheroids on 50 + 50 µL gel. In blue is represented the nucleus and in red the F-actin filaments. The scale bars represent 500 µm or 1000 µm (n=2).

204
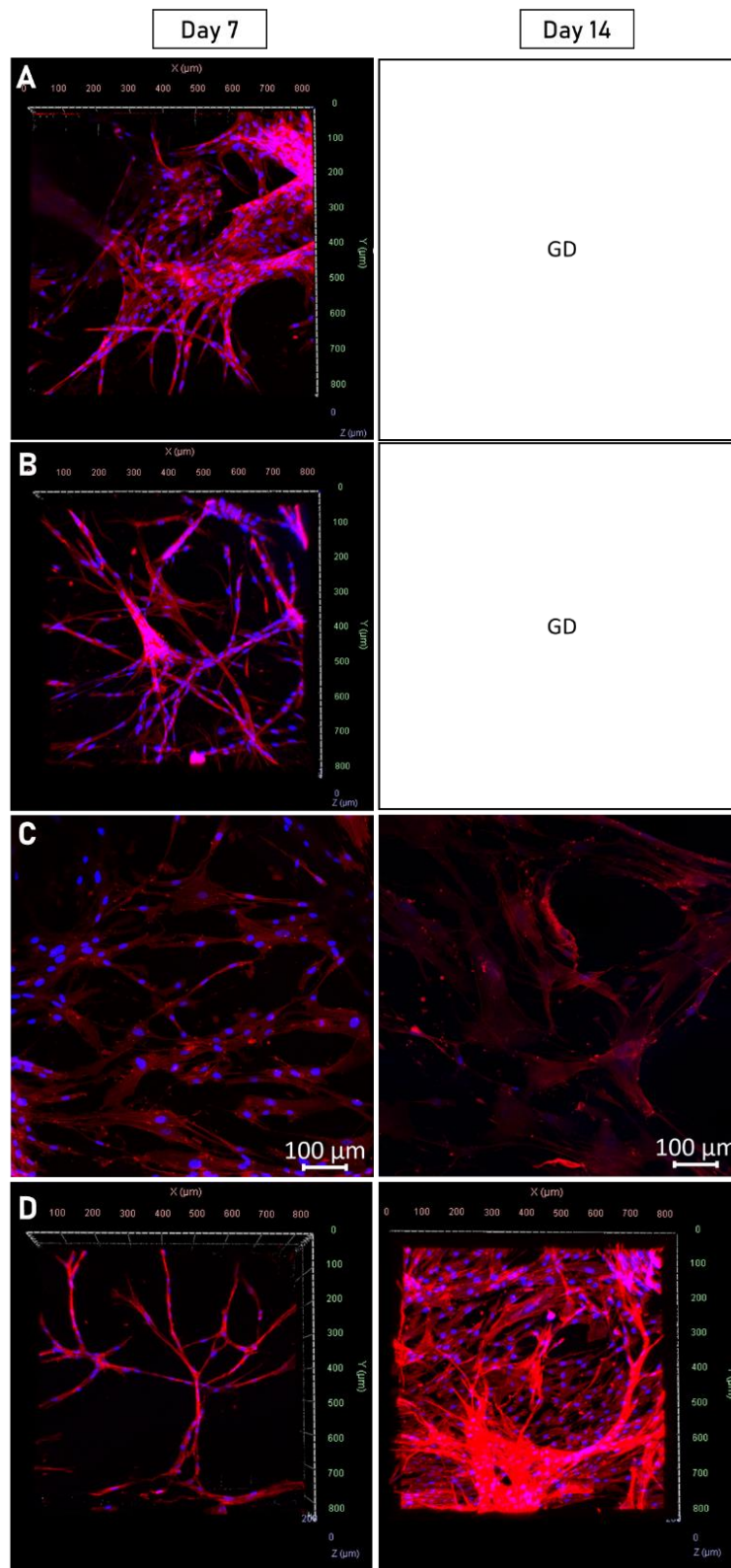
Figure 5.25: Experiment 5: fibroblast seeded on 50 + 50 µL gel. A) Corresponds to illustrated on C in figure 5. B) Illustration D. C) Illustration E. D) Illustration F. In blue is represented the nucleus and in red the F-actin filaments. The scale bars represent 100 µm. The legend GD corresponds to gel degraded (n=1).

5.3.4.6 Experiment 6: 100 μL Fibrin Gels with Aprotinin Supplementation

In experiment 6 was addressed the high catalytic capacity of the fibroblasts by adding aprotinin to the list of the angiogenic supplements to prevent gel degradation. In addition, the fibrin gels instead of being composed of two 50 μL gels stacked one on top of the other, were composed of one single 100 μL gel. The results are shown in figure 5.26, where is represented the images of the endothelial or fibroblasts seeded as illustrated in figure 5.7. In addiction was also quantified the presence in the media of IL6 and IL8 cytokine (figure 5.27).

In figure 5.26A) the endothelial cells look the same as in figure 5.24A), regarding proliferation and capacity to form 3D structures. This indicates, that visually the aprotinin does not have an impact on cell's viability. Regarding the fibroblasts, the cells were able to grow during 21 days and show similar spindle shaped morphology as in figure 5.25 without gel degradation. This indicates the suitability of the aprotinin to block the cell's catalytic effect. On conditions 5.26B) and 5.26D), the fibroblasts were seeded on top of the gel at 1250 and 250 cells/gel respectively, which despite initial seeding density, on day 21, the cells show similar confluency. In addition, the cells do not penetrate the gel, during the 21 days the cells only proliferate on the gel surface. This is observed by the layer of cells on the surface of the gel in green. On the other hand, conditions 5.26C) and 5.26E) the fibroblasts were seeded inside the gel at 1250 and 250 cells/gel respectively. The cells, in these two conditions, also show spindle shaped morphology and the ability to proliferate during 21 days in the total volume of the gel. After looking at the fibroblast conditions, it was selected the condition 5.26E), where 250 fibroblasts were seeded inside the gel to make the co-culture with the endothelial cells.

Regarding the IL8 and IL6 cytokine quantification, in figure 5.27A) is observed that IL6 is not secreted by the endothelial cells in complete media. But when is switched the media for the angiogenic one with the aprotinin, figure 5.27B), the secretion of IL6 increases. The same is shown for IL8, which under complete media, figure 5.27D), from day 7 to 21 the cells secrete less IL8, but on angiogenic media with aprotinin, figure 5.27E), the IL8 levels are higher and approximately the same during the 21 days. Noteworthy, that the same protocol is followed, such as seeding density, gel and media volume, as well as, visually, the cells present the same proliferation, indicating that under angiogenic media each cell secretes more IL6 and IL8. The fibroblast from condition 5.26E), which is the condition to move forward in the co-culture, secrete IL6 in very little amounts but IL8 secretion increase with time in culture, figure 5.27C) and D respectively. In addiction, was also quantified IL-1β, however was not detected.
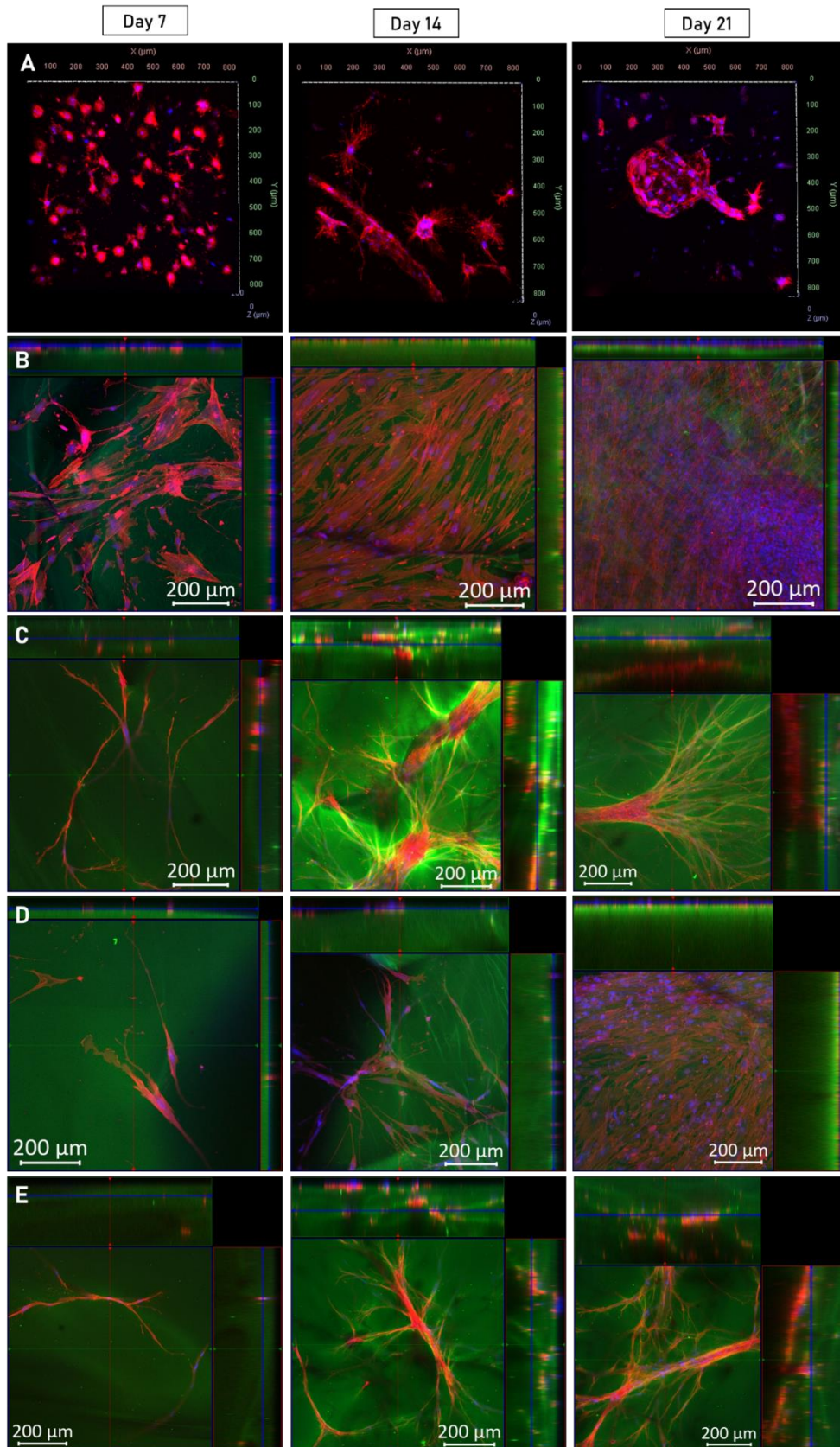
Figure 5.26: Experiment 6: endothelial and fibroblasts seeded on 100 μL gels with aprotinin. A) Endothelial cells seeded in 100 μL fibrin gels with angiogenic supplements plus aprotinin (illustration A figure 6). B) Fibroblasts seeded on top of 100 μL fibrin gels (1250 cells) with

angiogenic supplements plus aprotinin (illustration B figure 5.7). C) Fibroblasts seeded in 100 μL fibrin gels (1250 cells) with angiogenic supplements plus aprotinin (illustration C figure 5.7). D) Fibroblasts seeded on top of 100 μL fibrin gels (250 cells) with angiogenic supplements plus aprotinin (illustration D figure 5.7). E) Fibroblasts seeded in 100 μL fibrin gels (250 cells) with angiogenic supplements plus aprotinin (illustration E figure 5.7). In blue is represented the nucleus stained with DAPI, in red the F-actin with Phalloidin and in green is stained the fibrin gel. The scale bars represent 200 μm (n=3).
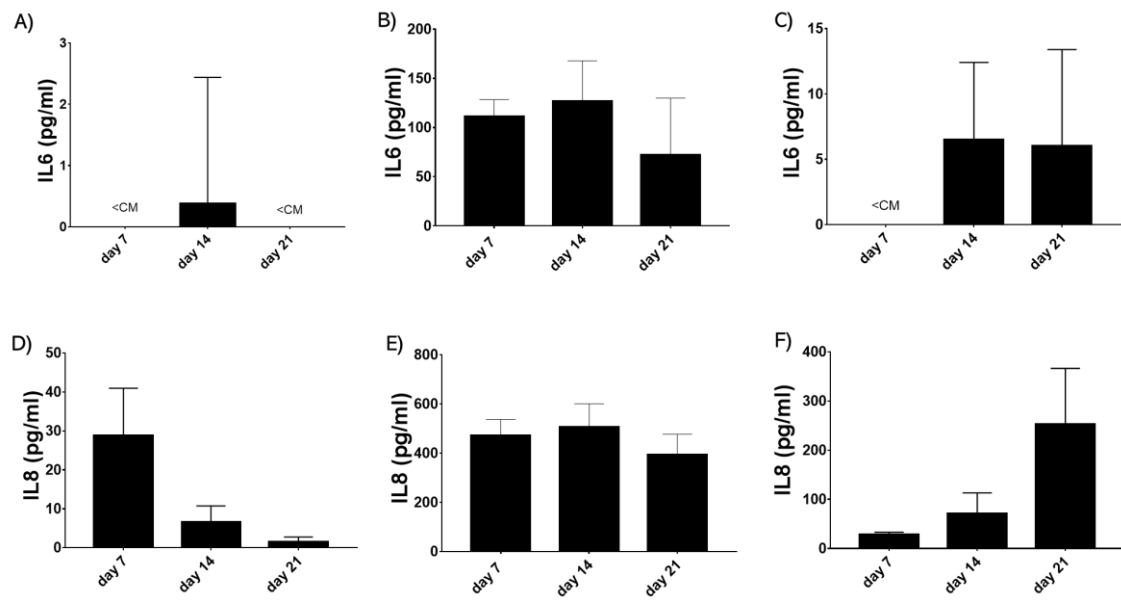
Figure 5.27: Experiment6: cytokine quantification of endothelial and fibroblasts seeded on 100 μL gels with aprotinin. A) to C) IL6 secretion. D) to F) IL8 secretion. A) and D) Endothelial cells cultured on complete media. B) and E) Endothelial cells cultured in angiogenic media plus aprotinin and C) and F) Fibroblast from condition E from figure 5.26. The legend: < CM indicates sample concentration below the concentration in the media. The error bars correspond to SEM (n=3, except day 21 for A) which is n=5, day 21 for D) which is n=4, and day 14 for D), E) and F) which is n=2).

5.3.4.7 Experiment 7: Fibrin Gel Coculture under Static Conditions

This result section includes the coculture of endothelial and fibroblast on 100 μL fibrin gel with angiogenic inducing media plus aprotinin. Figure 5.28 shows a representative image of days 7,14 and 21 of the coculture, and in figure 5.29 is plotted the IL8 and IL6 cytokine quantification.

The endothelial cells on figure 5.28 are represented in green by the CD31 surface marker and counterstaining with DAPI and Phalloidin, in blue and in red, representing the nucleus and F-actin respectively. The fibroblasts, that don´t express CD31, are visible as a result of DAPI and Phalloidin staining and the absence of green. In addiction, the morphology also helps to differentiate both cell lines, with fibroblasts presenting a spindle-shaped and endothelial cobblestone with cytoplasm projections (filopodia). The co-culture during the 21 days shows an

over proliferation of the fibroblasts in comparison with single culture control presented on condition E from figure 5.26. The endothelial cells are able to proliferate and organize in 3D structures, but the fibroblasts occupy a lot of the space. The fibroblasts organize in clusters of cells that contact with each other. In addition, both cell types are also able to establish cell-cell contact.

Regarding the cytokine expression in figure 5.29, both IL6 and IL8 have maximal secretion on day 14. In addition, in terms of value, the IL6 and IL8 concentrations are below what was recorded on the single culture of endothelial and fibroblast in figure 5.27, except for day 14.
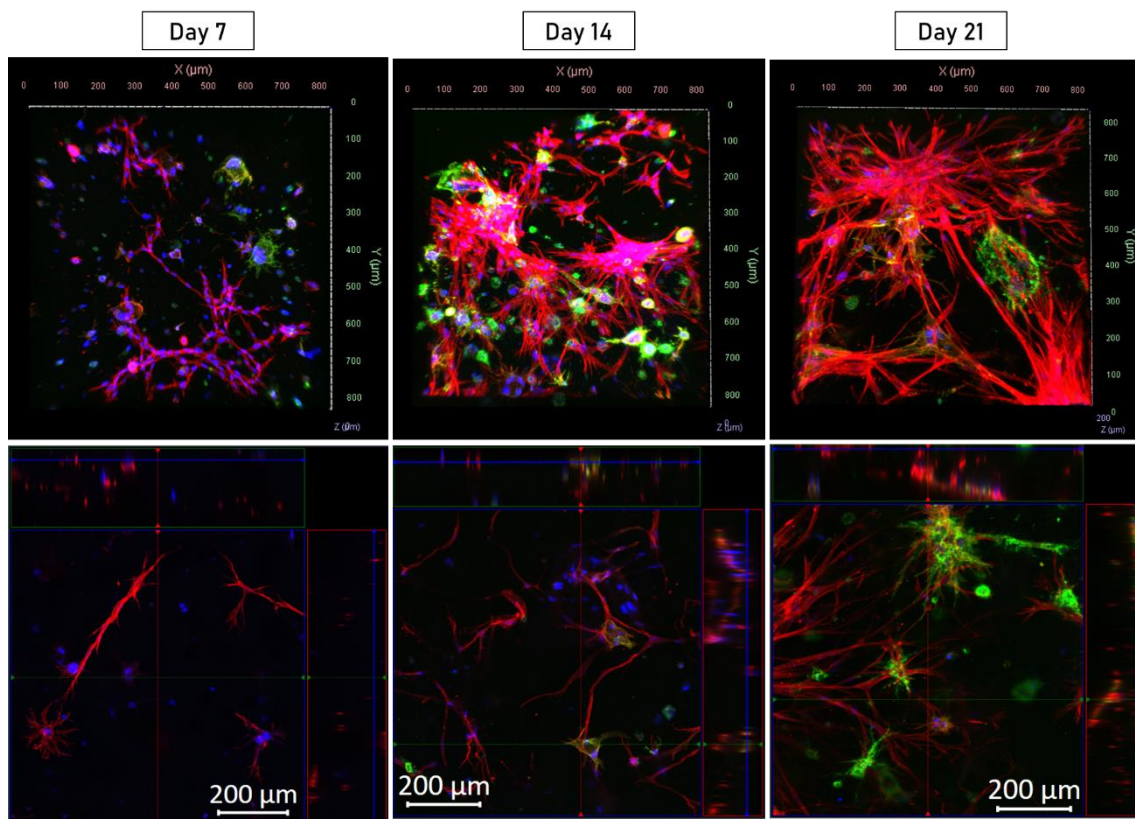
Figure 5.28: Experiment 7: endothelial cells and fibroblast coculture. The top image represents the top view of the z-stack. The bottom image represents an ortho view to show cell-cell contact. In blue the nucleus is stained with DAPI, in red the F-actin with Phalloidin and in green CD31 staining the endothelial cells. The scale bars represent 200 μm (n=3).
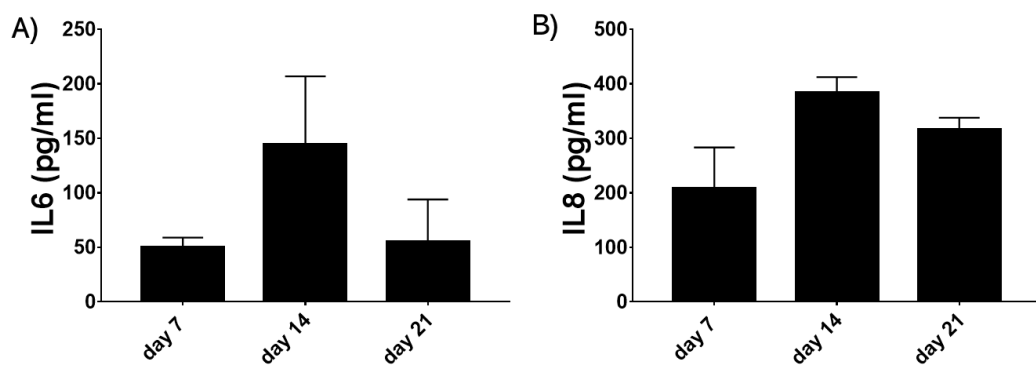
Figure 5.29: Experiment 6: cytokine secretion of endothelial and fibroblasts coculture. A) IL6 and B) IL8 cytokine quantification of endothelial and fibroblast co-culture of 100 μL fibrin gel under angiogenic media plus aprotinin. (n=3, except for day 14 of IL8 that is n=2). The error bars correspond to SEM.

5.4 Discussion:

The aim of chapter 5 was to present the data collected from Part 2 of the project (figure 1.9), which addressed the vasculature model. This was broken into four stages presented in figure 5.1. In stage 1, the endothelial cells were characterized in normal 2D cell culture conditions to evaluate the cell line suitability before seeding them in 3D. The cells were able to proliferate for seven days and expressed specific surface markers. Stage 2 was presented the brief work using the gelatine and alginate mesh to investigate its suitability to support EC growth. The high viscosity presented by the gelatine and alginate mesh made it difficult to handle it and seed cells on it, the reason for looking for an alternative biomaterial. The selected biomaterial to substitute the gelatin was the fibrin gel, extensively characterized in stage 3. The fibrin reaction showed a high dependence on the thrombin concentration, that when increased created gels with higher branching points and more elasticity. Finally in stage 4, was addressed the capacity of the endothelial cells to grow, organize and invade the fibrin gel. A total of 7 experiments were performed varying the fibrinogen and thrombin concentrations, the origin of the fibrin, the total volume of the gel, the way the cells were seeded (scattered or spheroids) and the presence of extra angiogenic factors. This helped to narrow down one polymerization condition that better promoted vasculature-like formation. This condition was presented in experiment 7 under static conditions and applied in chapter 7 underflow. Below, can be found more detail on the discussion from stages 1 to 4.

5.4.1 Stage 1: 2D Endothelial Cells Characterization

The 2D characterization of endothelial cells, found in figure 5.9, helps to describe the cell line before attempting the culture in 3D gels. During the 7 days of characterization, the cells are in the exponential phase, without significant cell death and with high metabolic activity. As confluency increases the specific marker CD31 also increases and after 7 days of culture the cells don´t present an intact monolayer. Only by seeding a higher number of cells, where cells are stacked on top of each other the dextran blue absorbance decrease. The endothelial cells used are from human lung microvasculature, that do not form an intact barrier. This feature is seen to promote the transport of nutrients and gases in the alveolar region. This explains why the cells don't form an intact barrier when confluent, even when forming more than one layer. Moreover, the cells present as expected a cobblestone appearance and express specific endothelial markers, such as CD31 and VE-cadherin.

Conclusion	
From the chapter	- HULEC endothelial cell line show in 2D characterization exponential growth and high metabolic activity for 7 days. - Express on the 7th day, a monolayer of cells with CD31 and VE-cadherin surface marker.
Overall Project	Use of HULEC cell line to develop the *in vitro* model of angiogenesis

5.4.2 Stage 2: Gelatin and Alginate Gel Characterization

After complete 2D characterization, the ECs were seeded on two different scaffolds, a mesh of 6% gelatin and 4% alginate or fibrin gels. The initial tests with the gelatin gel did not lead to successful cell seeding and proliferation, which determined its short investigations. The gelatin mesh before polymerization was very viscous which impaired an adequate homogenization of cell solution with pre-gel form. Therefore, the seeding strategy focused on adding the cells with the calcium chloride, however, after 24h of polymerization very few nuclei were stained with DAPI. The pore size of the gelatin and alginate mesh determined after the SEM images, lead to different conclusions. When using 150mM of $CaCl_2$ higher initial volumes in the bottom of the well detain porous with bigger diameters. The opposite tendency was found when using 300mM of $CaCl_2$. Note that the SEM image help to determine the porous size, smaller porous does not indicate more porous. That analysis was not performed.

5.4.3 Stage 3: Acellular Fibrin Gel Characterization: Experiments A to C

In this way, it was selected fibrin gel to move forward as a scaffold for the vasculature formation. Regarding the characterization of the fibrin, was applied confocal and SEM techniques as well as rheological measurements. This helped to visualize the fibrin network and understand the impact of the fibrinogen and thrombin on it, but also on the elasticity of the gel. The clot formation in static conditions will occur until all soluble fibrinogen is converted into insoluble fibrin. Two phenomena influence polymerization, lateral aggregation or branching of the fibres. The fibrin fibres thicken and elongate by lateral aggregation. However, if fibrinogen is cleaved at a fast rate, lateral and length fibre growth is slower compared to branching. This results in a network of thin and short fibres and gels with higher density and smaller pores. While if later aggregation is dominated fibrin fibres thicken, branching points are reduced and create gels with higher porous. The competition between a branching or lateral aggregation depends on the

thrombin activity, higher thrombin activity promotes branching, on the contrary, low thrombin activity promotes lateral aggregation[177]. The theory explained before is aligned with the images from figures 5.13 to 5.15. The conditions with higher thrombin concentration show gels with higher branching density, reduce fibre length, smaller porous and fibre thinning. The same effect is observed as the fibrinogen concentrations raise, but to a much less extent. Higher fibrinogen concentrations are responsible for increasing the number of monomer formation contributing to accelerate the branching reaction[178]. Despite that, the thrombin concentration is the one dominating polymerization reaction and defining the fibrin network.

The images from 5.13 to 5.15 were subjected to imageJ threshold using the Huang algorithm to quantify the percentage of the area associated with porous. The most general conclusion is that independently of the polymerization condition, the percentage of the porous area does not change much, is between 50-60%. This conclusion was observed as well when subjecting the data to the other two algorithms of the ImageJ, such as the Default and the Percentile. The plots can be found in appendix 20 showing the Default plot with areas between 60-70% and the Percentile with around 50%. (49-50%) The three algorithms vary on the threshold criteria when identifying the pixel associated with fibre (white pixel) and the pixel associated with porous (black pixel). This has an impact on the percentage of areas allocated to porous/fibre. However, from the three algorithms is not possible to have a trend between the different conditions of thrombin and fibrinogen, which may indicate the balance between a network of thicker fibres with bigger porous versus thin fibres and smaller porous may lead to the same area occupied with fibres.

The mechanical properties of fibrin showed that the gel acts as a viscoelastic material (more detail in appendix 14), meaning that the gel assumes a behaviour between an ideal elastic material (Hooke's Law) and a viscous material (Newton's Law). The elasticity, or rigidity, is characterized by a reversible mechanical deformation, when the stress is removed the material returns to its original position. The viscosity is characterized by an irreversible mechanical deformation, all energy applied is dissipated in the flow of the material. The elastic component of the gel is measured by the storage modulus (G'). The loss modulus measures the viscous component of the material (G''). The results shown in figure 5.12 show that with the increase of fibrinogen, the gels become more rigid (increase G') but also more viscous (increase of G''). More energy is stored, and more energy is dissipated. This is associated with gels with higher branching density, smaller porous and fibre thickness, which can be confirmed by figures 5.13 to 5.15. On the other hand, rising thrombin concentration, parallel to the fibrinogen, also leads to gels with higher branching density. However, the storage and loss modulus decrease,

exhibiting less elasticity and less viscosity. Concluding that, for the same deformation (2% strain), less energy is stored, and less energy is dissipated. The same results are shared in the work of Ryan et al (1999)[178] which concluded that higher branching originates more rigid clots, however, the combination of high branching with low fibre diameter leads to a decrease in clot rigidity. From the data gathered on fibre's diameter, this one decreases as the fibrinogen concentration decrease (figure 5.16 plot on the right). Lower fibrinogen is associated with a higher loss tangent, which is a better variable to show the relationship between the storage and loss modulus. Higher loss tangent, corresponds to more elastic gels as mentioned in the result section. In this way, the characterization also linked lower fibres diameters to decrease clot rigidity, but associated with little branching. The high loss tangent is also associated with high thrombin that favours branching. But no trend in fibres diameter was observed when analysing thrombin.

Continuing analysing the loss tangent, when this variable decreases the gels are more rigid and associated with higher fibrinogen or lower thrombin. The higher gel rigidity is associated with a lack of ability to network rearrangements after stress. This gel behaviour is associated with higher fibre diameter and branching (despite branching and lateral aggregation are driven more by thrombin concentration) when fibrinogen is high. Regarding low thrombin values, this is associated with lateral aggregation.

To conclude, this makes the conditions 1.25mg/mL + 5 U/mL highlighted in red in table 5.3 the most elastic gel. On the opposite side of the table, in green, the condition 5 mg/mL + 0.1 U/mL is the most rigid. Together with this condition, also highlighted in green are the rest of the conditions with a similar value of rigidity. Showed in yellow are the values with intermediate rigidity.

To complement fibrin gel characterization, an apparatus to measure the gel permeability was set up. This can be found in appendix 21 but little success was found. The apparatus was based on water flow rate through the gel as seen in some publications[179,180]. With the water flow rate, it can be determined the permeability using the Darcy law. However, the gel frequently detached from the PDMS ring which ended the experiment. In future to improve the setup, the fibrin gels could be polymerized on a Transwell and measured the diffusion from top to bottom compartment of Dextran Blue, similar to what was done on the 2D characterization of fibroblast and endothelial cells.

Conclusion	
From the chapter	▪ Higher thrombin promotes branching and increased loss tangent (more elastic gels) ▪ Low thrombin promotes lateral aggregation and decreases loss tangent (more rigid gels) ▪ Higher fibrinogen promotes branching (to a less degree to thrombin), a decrease of loss tangent (more rigid gels) and higher fibre diameter ▪ Low fibrinogen promotes lateral aggregation (to a less degree to thrombin), an increase of loss tangent (more elastic gels) and lower fibre diameter

5.4.3 Stage 4: Fibrin Gel Sell Seeding Cellular: Experiments 1 to 4

Regarding the cell viability in the fibrin gels, the initial tests, experiment 1, were done in 200 μL gels polymerized on a 96 well plate, with fibrinogen and thrombin of bovine source. The results in figure 5.17 show an increase in dsDNA indicating cell proliferation. On top of that, the cells seeded in the fibrin gels show more dsDNA on the 3rd and 7th days than in 2D. Indicating that the gels have the ability to support more proliferation of viable cells over the course of 7 days than normal plastic plates.

Then the research moved to more physiological conditions, switching the bovine origin fibrinogen and thrombin to human enzymes and using concentrations within the ones present in the human blood. Fibrinogen physiological value in the blood is between 2.0 to 4.5 mg/mL, considering a critical concentration below <1.0 mg/mL[181]. The fibrinogen concentration used were 1.25, 2.5 and 5 mg/mL. The thrombin physiological value in the blood is between 5-10 nM[182], which converting 0.1, 1 and 5 U/mL to concentration using the characteristic units/mg corresponds to 1,10 and 50 nM. Experiment 2 also seeded the ECs on 200 μL gel and on a 96 well plate, however, the cells did not proliferate as seen before in experiment 1. The same value of dsDNA is quantified on days 3 and 21. Differences in the percentage of fibrinogen that is clottable and units/mg of thrombin may explain the lack of cell proliferation. The bovine fibrinogen only 65-85% of the protein is clottable compared to the 95% of the human. There are also differences in the thrombin, the bovine only has 40-300 units/mg, while the human has 2700 units/mg. The DAPI images in figure 5.19 also support that the cells are not growing, since only some cell agglomerates were imaged. Note that the acellular fibrin characterization discussed above was done using the human origin fibrinogen and thrombin.

To improve cell proliferation, experiment 3 seeded the same number of ECs (25000 cells/gel) in 100 µL gel and on a 96 well plate for the dsDNA quantification. The volume reduction changed the diameter to height ratio from 1.2 to 2.2. The 2.2 ratio means that the diameter is two times larger than the height. This has an impact on nutrients and gas diffusion across the total depth of the gel. In addition, the same number of cells were seeded in half volume, doubling the initial cell confluency. Both strategies lead to results in figure 5.20, where is observed a visual increase from day 7 to day 21 of dsDNA, especially with fibrinogen decrease. The corresponded images, in figure 5.21, reveal more detail on how cells are distributed and organised during the 21 days. The images are aligned with the DNA data, showing cell proliferation from day 7 to 21 across fibrinogen and thrombin conditions. From the images, conditions that used 5 and 1 U/mL seemed better to support the cell 3D organization. In addition, gels with 1.25 mg/mL fibrinogen were quickly discarded since the gels were very soft and hard to handle.

To help to narrow down the fibrinogen and thrombin condition to build the vasculature model, experiment 4 was performed. The spheroid method was introduced to help determine which gel conditions the cells show higher migration capacity. Noteworthy, that the invasion area calculated for the different polymerization conditions is a two dimensions migration. The results in figure 5.22 show a very reproducible trend across the fibrinogen and thrombin conditions. After 2 days on the fibrin gels the spheroids that show the highest invasion area are the ones embedded on 1.25 mg/mL + 1 U/mL (without FBS) and polymerized with 5U/mL of thrombin independently of the fibrinogen concentration. Linking the spheroid data with the rheologic characterization of the gels, more thrombin results in less rigid gels, which is aligned with the higher invasion area. Also, the conditions where was seen most invasion corresponds to conditions highlighted in red and yellow from table 5.3, gels with higher loss tangent and consequently more elastic. To determine the best gel to continue the studies, the conditions enumerated before were crossed to the gel conditions that supported globular cellular rearrangements from figure 5.21. In this way, crossing the information from figures 5.21 and 5.22 was chosen condition 2.5 mg/mL and 5 U/mL to move forward with to build the vasculature model.

Conclusion	
From the chapter	▪ Experiment 1: 3D scaffolds support more cellular proliferation than 2D normal plastic wear. ▪ Experiment 2: fibrinogen and thrombin origin/manufacture influence enzyme activity. ▪ Experiment 3: 100 µL fibrin gel promotes cell proliferation and 3D organization. ▪ Experiment 4: higher invasion area is determined when 5 U/mL of thrombin is used.
Overall Project	▪ Total gel volume of 100 µL polymerized in 8mm PDMS rings with 2.5 mg/mL and 5 U/mL of fibrinogen and thrombin respectively selected to develop the *in vitro* model of angiogenesis.

5.4.3 Stage 4: Fibrin Gel Sell Seeding Cellular: Experiments 5 to 7

After narrowing down the fibrinogen and thrombin concentration to use further, the angiogenic inducing media was tested. Together with the 50 + 50 µL gel strategy to induce endothelial cells morphogenesis.

The 50 + 50 µL gel rationale was supported by literature articles, such as from Steven C. George group[89,92] and the paper from V. van Duiden *et al* (2018) using a MIMETAS platform[173]. Where the cells migrate from a side position into an empty gel with the possibility to differentiate into stalk and tip cells. In this project, the idea was to seed the endothelial cells in the bottom gel, for them to migrate and invade the top gel in the direction of a higher concentration of the angiogenic supplements. However, the endothelial cells were not able to migrate to the adjacent gel. As well as the fibroblasts were not able to migrate from the top gel to the bottom one or invade the top gel when seeded on top of it. The confocal images in figure 5.13 to 5.15 show porous gels, but correspond to middle slices and the technical repeats are 3 adjacent slices. In future, slices from the middle of the fibrin gel need to be included to better understand the complete gel structure.

Regarding the angiogenic media, several factors are documented in the literature as having a role in the angiogenic process, such as promoting endothelial cells proliferation, migration, morphogenesis, branching, lumen formation and ECM degradation. The most known is the vascular endothelial growth factor (VEGF), but also the family of fibroblast growth factor (FGF) plays an important role, epidermal growth factor (EFG), platelet derived growth factor (PDGF), angiopoietins, ephrins, matrix metalloproteinases (MMP), nitric oxide synthase (NOS), insulin,

ascorbic acid and interleukins such as IL-1β, IL6 and IL8[170,183,85,184,169]. However, as not all factors could be introduced in the media, it was followed the combination of angiogenic factors present in the paper from V. van Duiden et al (2018)[173]. The essential supplements are PMA, S1P, VEGF and bFGF. Table 5.6 presents the functional role of each supplement, the ones indicated before plus hydrocortisone and EFG already present in the complete media, as well as ascorbic acid and aprotinin (note that aprotinin was not present in the angiogenic media in the 50 + 50 μL experiment).

In the 50 + 50 μL experiment, the endothelial cells were seeded as spheroids or scattered. The first seeding strategy was not successful, the spheroids disintegrated and only cell fragments were seeded. The spheroid structure is not robust, the pipette handling and centrifuge may have disrupted the spheroids. However, given the results from the spheroid invasion area, would be interesting to incorporate in future experiments the replication of the same experiment but with angiogenic media and extent the culture during more days. On the other hand, the ECs seeded scattered were able to change during the 21 days, on the 7th day, the cells look very round and with small cytoplasm to nucleus ratio. This feature changes on day 14, when cells spread and contact with each other. On day 21, the cells were able to organize and form 3D structures. However, one feature that stands out is the lack of directionality from those structures, since the angiogenic media was added on top it was expected that the endothelial cells would prefer to migrate towards it. In addiction, is also not known if the 3D structures have a lumen or not. For that is suggested to add to the media labelled dextran and visually follow its diffusion.

Regarding the fibroblast seeding, the cells show a high catalytic effect, and the culture was not able to last for 21 days before gel degradation. To address this problem was added aprotinin in experiment 6.

Experiment 6 differs from the one before in the extra supplement but also the cells were seeded on a single 100 μL gel, since cell invasion towards adjacent gels was not successful. The endothelial cells seeded in this condition, show the same morphology evolution from day 7 to 21, as mentioned before. However, it looks like the gel is populated with fewer cells on days 14 and 21 and the 3D structures on day 21, despite present, look like they are in fewer numbers. The fibroblasts were successfully cultured during the 21 days, the images show proliferation and cell migration, indicating the benefit of the aprotinin supplementation.

Table 5.6: Supplements used to induce angiogenic with its functional role.

Supplements	Function	References
Complete Media		
Hydrocortisone	Potent anti-inflammatory Mitogen inducer Promotes glucose and amino acid update Enhance barrier function Inhibit tube formation	[185]
hEGF	Upregulates VEGF secretion	[183]
Angiogenesis Inducing Media		
Ascorbic acid	Promotes cell proliferation by activating an ERK1/2 controlled pathway	[186]
	Promotes collagen type IV synthesis, necessary for basement membrane formation	[187]
bFGF	Strong mitogen Heparan sulfate binding protein Urokinase type plasminogen activator, resulting in fibrin degradation Up-regulation of VEGF	[170]
PMA	Lumen formation	[188]
	Activate protein kinase C, resulting in lumen formation	[189]
	Activate protein kinase C, inducing migration, proliferation and vessel formation	[190]
	Activate protein kinase C, promoting expression of MMP2 and 9	[191]
VEGF165 (VEGF-A)	Inducer of the angiogenic cascade Heparin binding protein Regulates vascular permeability Induced by hypoxia	[183,192]
	Binds to VEGF-receptor 1 (VEGFR1), VEGFR2, Neuropilin-1 and Neuropilin-2 on EC	[170]
S1P	Pericytes recruitment and association to vessels through N-Cadherin	[193]
	Promotes ECs migration, proliferation and morphogenesis	[194]
	Regulates lymphocyte trafficking	[195]
	Regulates endothelial cell barrier function, vessel stability and angiogenesis by cross talking to PDGF and VEGF receptors	[85]
Aprotinin	anti-fibrinolytic	[196]

The supplementation of aprotinin in the media or added during polymerization is a common strategy when using fibrin gels. Several authors document that aprotinin prevents the degradation of the gel and in this way preserves its 3D structure[197,198,199,89]. Aprotinin is an inhibitor of serine proteases such as trypsin, chymotrypsin, kallikrein and plasmin. The latter is a known enzyme responsible for fibrin degradation[196]. The reduction of the fibrin gel

degradation when supplemented with aprotinin in the media indicates the involvement of the plasmin enzyme secreted by the fibroblast.

In this way, the aprotinin was well applied and solved the problem of the gel degradation, however, the small fragments from the fibrin degradation are a signal for neovascularization and the presence of anti-plasmin molecules, such as aprotinin (or aminocaproic acid) reduce cellular invasion, matrix degradation and angiogenesis[199,200].

In conclusion, future work should optimize the aprotinin, to find the minimum concentration to eliminate the visible fibroblasts catalytic effect and consequently induce the minimum impact on angiogenesis. In addition, could be tested by adding the aprotinin to the fibrinogen or thrombin solution for the molecule to be incorporated into the matrix, as chosen in several research articles[201,202,203], instead of diluting it in the media, the solution used. Another alternative could be the use of pericytes instead of fibroblasts, which is the supportive cell line for microvasculature[204]. Pericytes cover 26% of the alveoli capillary in mature bovine lung[205].

To analyse the response to angiogenic media, endothelial cells grown with and without angiogenic supplements were tested for the cytokines IL-1β, IL8, IL6. In addition, fibroblasts from condition E from figure 5.26, were also analysed with the same cytokines as a control for the co-culture. The IL-1β is involved indirectly in angiogenesis by stimulating VEGF production in smooth muscle cells and promoting angiopoietin-1 secretion[169], nonetheless, was not detected in any sample tested. The IL6 can also promote VEGF secretion[169] and was detected in higher quantities in endothelial cells under angiogenic media. The IL8 shows a downward trend for ECs without angiogenic media from day 7 to day 21. Note that the concentration of the cytokine was not divided by cell number, so the IL8 per cell number decreased during the weeks. On the other hand, the cells with angiogenic media show much higher IL8 production over the weeks. This cytokine is involved in several roles, such as cell proliferation, increase blood vessel permeability and increase production of matrix metallopeptidase 9 and 2[169]. IL8 is preferentially secreted during hypoxia and is an angiogenic factor secreted by macrophages[169]. The fibroblasts do not show IL6 secretion, but show increased concentration of IL8 as the weeks pass.

To finalize the chapter, the endothelial cells and fibroblast from condition 5.26E) were seeded together. The images show high proliferation of the fibroblast, higher than recorded before in single culture, consequently the endothelial cells had less space to invade and form 3D structures. Nonetheless, both cells seem to establish cell-cell contact but not as documented before where the supporting cell lay next to the endothelial cell when the tubular structures are formed for vessel maturation[188,206,207]. Regarding the cytokine expression, both IL6 and IL8 have

220

a maximum on day 14. This maximum is more explicit for IL6, where day 14 co-culture is higher than ECs single culture with angiogenic factor, which is not observed for days 7 and 21. For IL8, all values are lower, compared to monocultures, but day 7 suffers the higher reduction. The fibroblast's monoculture secreted IL8, which was expected to sum to the IL8 secreted from the ECs when in coculture, but that was not observed.

Conclusion	
From the chapter	▪ Experiment 5: ECs and HLF-1 do not invade adjacent fibrin gels. The fibroblasts have high catalytic activity towards fibrin gels. ▪ Experiment 6: Aprotinin supplementation reduced fibrin gel degradation. ECs do not seem significantly affected by aprotinin ▪ Experiment 7: coculture shows high fibroblast proliferation and reduced ECs 3D organization
Overall Project	▪ 25000 ECs together with 250 HLF-1 seeded on 100 µL fibrin gels with 2.5 mg/mL and 5 U/mL fibrinogen and thrombin respectively selected to perform underflow experiments.

Chapter 6

Bioreactor Development and Simulations
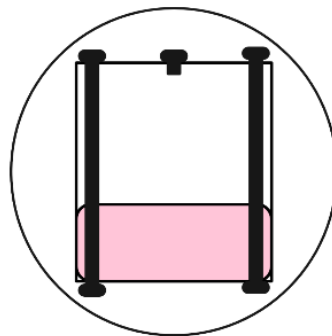
6.1 Introduction

The term bioreactor in the literature comprises a range of applications and geometries in which a bioreactor has been used to support cells or a tissue construct in their biological functions. It has the ability to create a physiological environment, deliver mechanical stimulations and monitor the culture[208,209].

One of the most recent applications is the use of bioreactors to support decellularization and recellularization of lungs[80,210,211,212]. Where the main features included are the circulation of surfactants during decellularization and cells during recellularization. In addition, some applications, also support air to stimulate the lung, mimicking inhale and exhale. To support this line of research, a large number of cells need to be available, especially in all whole organ's reimplementation, and bioreactors have been part of the solution supporting iPSC expantion[213,214,215]. These type of bioreactors have also been able to keep viable lungs in *ex vivo* for transplantation[216,217]. Or used during maturation steps before tissue implantation[40].

Another type of bioreactor also found in the literature to support lung bioengineering models, is the rotary bioreactor, where a cell monolayer coated around the cylinder is exposed cyclically to air to media[218]. These types of bioreactors have also been used to guide iPSC[219] or ESC[220] differentiation and model disease[221]. This type of bioreactor is able to support air-liquid interface (ALI), which is closer to physiological conditions than submerged cultures.

Other strategies use a Transwell to develop the cellular model that is then integrated into a bioreactor. The porous membrane of the Transwell act as the substrate for cells to grow, which can be perfused with media from the bottom compartment and air through the top on, allowing in this way air-liquid-interface. Lab-made bioreactors that use this strategy can be found in William W. Hope group[222,223] that developed a stainless steel bioreactor to study the isavuconazole and voriconazole kinetics in a dynamic in vitro model where a co-culture of HPAECs (an endothelial cell line) and A549S cell line was used. Another example of a lab-made bioreactor that used a Transwell as the model substrate is present in the work of Cornelia Blume for pollen exposure[224]. This kind of strategy can also be found commercially, supplied by Kirkstall, explored already to investigate aspergillus infections in human bronchial or small airway epithelial under ALI and perfusion,[225] branching morphogenesis[226] and nanoparticles toxicity screening in endothelial cells[227,228].

Together with ALI, another important mechanical stimulation for the lungs is the ability of the substrate to stretch and compress as the lungs do when inhaling and exhaling occur. To mimic this process, in the literature can be found several examples of lab-made devices[229,230,231] and

commercially available systems, such as the Flexcell Strain Unit[232,233,234] that support culturing the lungs cells in a mechanical relevant environment.

Regarding this PhD thesis, the bioreactor needs to be designed to hold the alveolar and vascular tissues representatives and allow media and air perfusion. The alveolar needs to contact with air, and the vasculature with the perfused media only. Making a parallelism between the features needed and the physiological environment, regarding the vasculature, the blood flows in the capillaries between 4.5 mL/min and 8.5 mL/min and imposes a shear stress on the endothelial cells in the range of 0.5 a 1 Pa[22]. The introduction of air would make the substrate where the cellular model is to be compressed and, in this way, apply displacement of the model, 5-12% strain (every 5 seconds)[235]. The air would not just be passive as seen for example when a transwell is at air liquid interface but would apply mechanical stimuli as well. Note, that despite the bioreactor has been designed to hold all these components, the dynamic air was not established. In this project, the alveolar region model is subjected to continuous flow and passive air.

To conclude, this chapter focus on completing Part 3 of the project, illustrated in figure 1.9. With the requirements set above, to design the bioreactor was established a cylindrical vessel with a lid where the air can be introduced through the top, two lateral openings on the vessel wall, where the inlet and outlet of the media could occur. The bioreactor was designed to fit a 6 well insert, to adapt to various types of alveolar models. The optimization of the bioreactor took four major stages, which are described and characterized more in detail below.

6.2 Methods

The optimization of the bioreactors includes four different versions. On figure 6.1 can be found an outline of the specifications for each version. The first version of the bioreactor was composed of a lid and a body, both manually machined by the physics workshops in acrylic. The inlet and outlet are placed on opposite sides of the body for media delivery and exit. The lid has also an opening for future air application. The bioreactor then is sealed with six screws on a side flap. Version 2 was already machined on an automatic Computerized Numerical Control (CNC). For this version, two biocompatible and transparent materials were tested: acrylic and polycarbonate. The inlet and outlet were moved tangent to the bioreactors body and the lid was redesigned to occupy less space. Then, it was reconsidered the bioreactor geometry to fit the alveolar and vasculature model. With this in mind, versions 3 and 4 were created, which are a combination of a lid, body and base in acrylic together with a PDMS disk. The PDMS part supports the inlet and outlet of media as it holds the place where the cellular model is going to lay. The rest of the acrylic structures create a close and sterile environment that will as well support dynamic air intake in future updates. Sealing between all the parts is maintained with four top and four bottom screws tight into the bioreactor's body. From versions 3 to 4, the PDMS disk was improved fitting three gel holders, where the cellular model is placed. Section 6.2.1 can be found in more detail the technical drawings of each version.
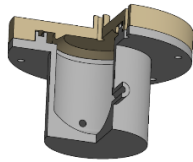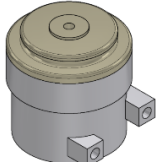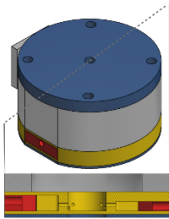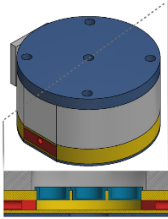
	Version 1	Version 2	Version 3	Version 4
Material	Acrylic	Acrylic Polycarbonate	Acrylic PDMS	Acrylic PDMS
Fabrication	Manually Machined	CNC Machined	CNC Machined Mould Casting	CNC Machined Mould Casting
Geometry				
Description	1. Bioreactor body with one inlet and outlet on opposite sides. 2. Lid with one inlet. 3. Bioreactor body and lid seal with 6 screws.	1. Bioreactor body with tangent inlet and outlet. 2. Lid with one inlet. 3. Bioreactor body and lid seal with a thread.	1. Parts: bioreactor body, lid and base in blue, PDMS in yellow, inlet and outlet fittings in red. 3. The parts are sealed together with 4 screws on top and base.	1. Parts: bioreactor body, lid and base in blue, PDMS in yellow, inlet and outlet fittings in red. 2. Gel holder in light blue. 3. The parts are sealed together with 4 screws on top and base.

Figure 6.1: Specifications of the bioreactors from versions 1 to 4.

6.2.1 Bioreactors Technical Drawings

6.2.1.1 Bioreactor: version 1

On figure 6.2 is presented the technical drawings with annotated dimensions of the first version of the bioreactor using the Autodesk Inventor® program.
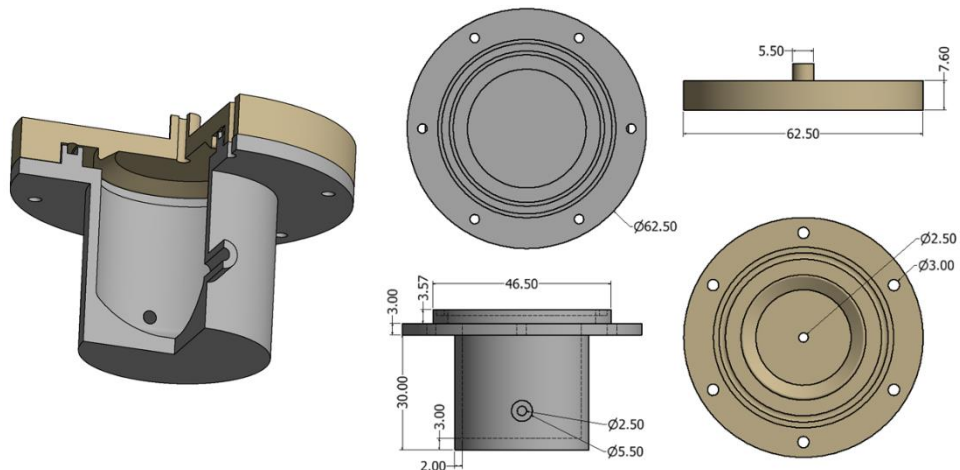
Figure 6.2: Bioreactor version 1 technical drawings with dimensions in mm. The lid is presented in light brown and the body in grey.

6.2.1.2 Bioreactor: version 2

On figure 6.3 is presented the technical drawings with annotated dimensions of the second version of the bioreactor using the Autodesk Inventor® program.

Figure 6.3: Bioreactor version 2 technical drawings with dimensions in mm. The lid is presented in light brown and the body in grey.

6.2.1.3 Bioreactor: version 3

On figure 6.4 is presented the technical drawings with annotated dimensions of the third version of the bioreactor using the Autodesk Inventor® program.

Figure 6.4: Bioreactor version 3 technical drawings with dimensions in mm. The lid and base are represented in blue, the body in grey, the PDMS disk in yellow and the inlet and outlet fittings in red.

6.2.1.4 Bioreactor: version 4

On figure 6.5 is presented the technical drawings with annotated dimensions of the fourth version of the bioreactor using the Autodesk Inventor® program.

Figure 6.5: Bioreactor version 4 technical drawings with dimensions in mm. The lid and base are represented in dark blue, the body in grey, the PDMS disk in yellow, the inlet and outlet fittings in red and the gel holder in light blue.

6.2.2 PDMS Mould Casting

PDMS is a biocompatible transparent silicone base material used in the project to build the part where the media gets into contact with the cells. The PDMS disk is found between the base and bioreactor body, represented in yellow in figure 6.1 in versions 3 and 4, figures 6.4 and 6.5. The material is also used to build the inlet and outlet fittings represented in red in figures 6.1, 6.4 and 6.5. The moulds to fabricate the PDMS parts were 3D printed in two types of material, in TPU (thermoplastic polyurethane) or PLA (polylactic acid). The PDMS is a two-component mixture added in the ratio of 1g Elastocil RT 601 B to 15.7g Elastocil RT601 A (from Wacker). After weighing both components, they were hand mixed for 5 minutes before being placed on a desiccator. The degassing step took at least 3 cycles of 5 minutes under vacuum, until no visible bubbles were observed. Then, to fill the moulds, the uncured PDMS was added to a syringe. Noteworthy, that the moulds were covered with a thin layer of vaseline to facilitate the demoulding afterwards. The sketches of the moulds are present in figure 6 and 7 for bioreactor 3 and 4 respectively. The PDMS polymerization took 24 hours at room temperature. On the following day, the moulds were disassembled, the solid PDMS was carefully removed, washed with detergent and autoclaved before used.

6.2.2.1 PDMS Mould: version 3

On figure 6.6 is presented the technical drawings with annotated dimensions of the PDMS mould for version 3 using the Autodesk Inventor® program. The moulds were then fabricated in PLA or TPU using the 3D printer.
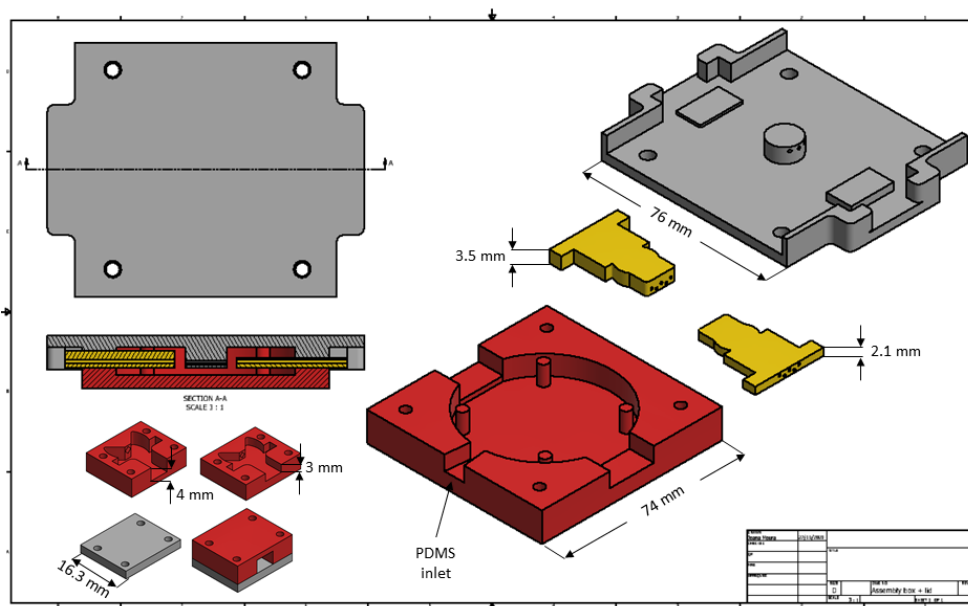
Figure 6.6: PDMS mould for version 3 of the bioreactor. On the right side of the image can be found the 3 components of the mould: the bottom view of the lid in grey, in red the box and in

yellow the channels models. On the top left side of the image is represented the assembly of the closed mould, top and side view. On the bottom left can be found the moulds of the inlet and outlet fittings, a grey base and a red top.

6.2.2.2 PDMS Mould: version 4

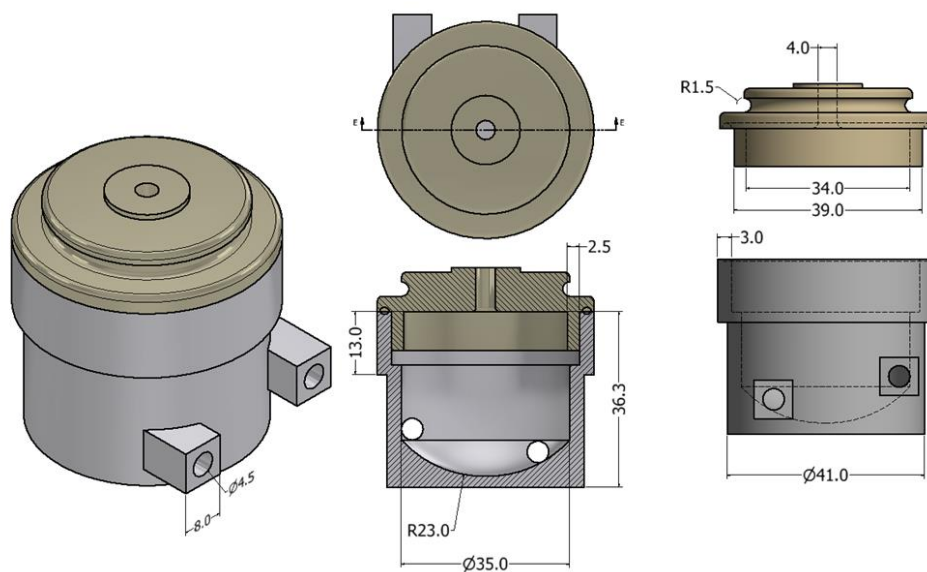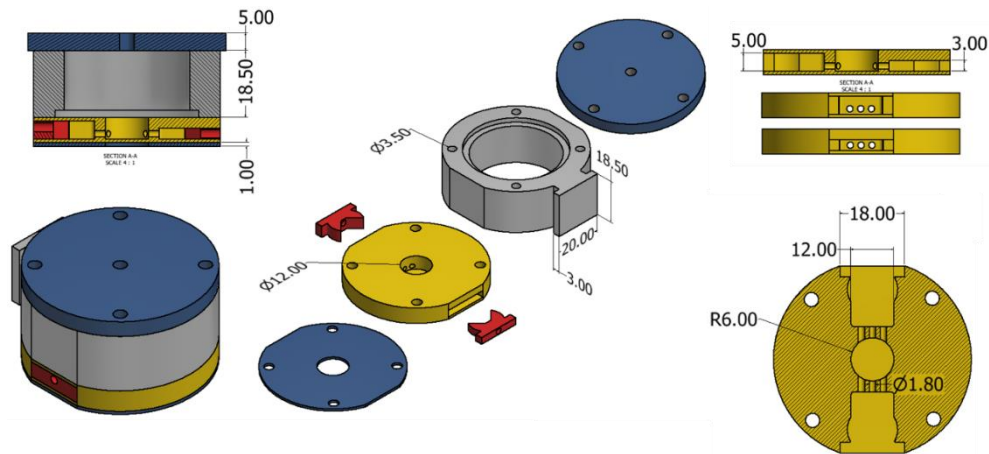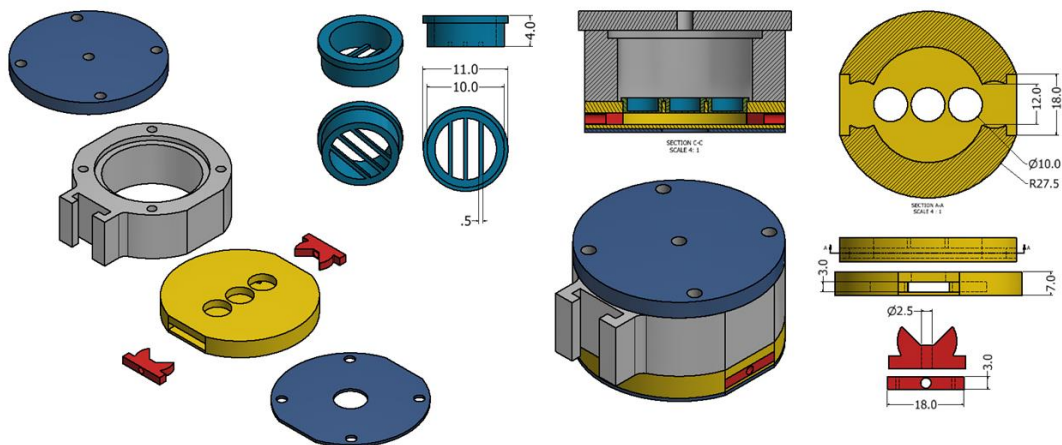On figure 6.7 is presented the technical drawings with annotated dimensions of the PDMS mould for version 4 using the Autodesk Inventor® program. The moulds were then fabricated in PLA or TPU using the 3D printer.
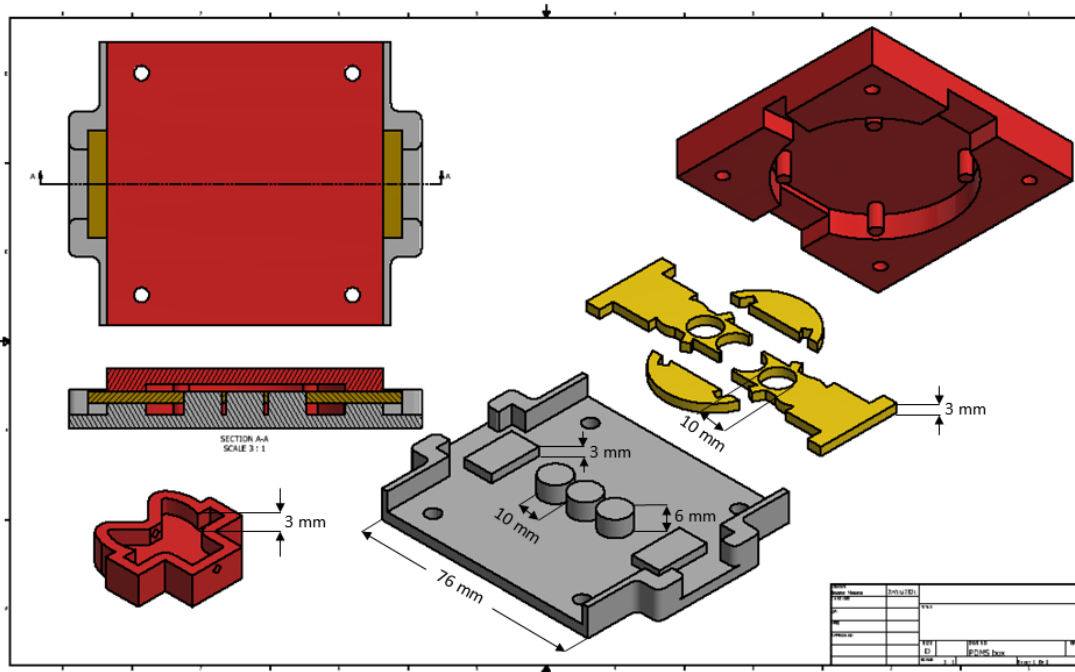
Figure 6.7: PDMS mould for version 4 of the bioreactor. On the right side of the image can be found the 3 components of the mould: the lid in grey, in red the box and in yellow the channels models. On top left side of the image is represented the assembly of the closed mould, top and side view. On bottom left can be found the mould of the inlet and outlet fittings.

6.2.3 Software

6.2.3.1 Autodesk Inventor® program

Inventor® program is a software provided by Autodesk that allows professional grade 3D mechanical design. The license type was: 1 seat, education and single-user.

6.2.3.2 Cura

Cura is an open source slicing software for 3D printers from Ultimaker. This software allows the upload of geometries developed in the Autodesk Inventor® program (in STL extension). The

229

software works by slicing the geometry in x-y layers to generate a g-code, which instructs the printer of the path to follow in each layer and other features such as, temperature of nozzle and bead, speed and layer thickness in the different geometry domains. During the course of the thesis the materials used were TPU and PLA. Different settings were applied for each material, which is outlined in table 6.1

Table 6.1: PLA and TPU settings in Cura. The default settings for standard quality were used except for the conditions bellow.

	TPU	PLA
Standard Quality	0.2mm	0.2mm
Top/Bottom layers	10	10
Nozzle Temperature	210	220
Bed Temperature	70	70
Retraction Distance	1mm	6.5mm
Support Structure (if applicable)	-	tree
Build Plate Adhesion	Brim (4-8mm)	Brim (2-4mm)

6.2.3.3 COMSOL®

COMSOL® 5.6 (license number 7075619) is a multiphysics simulation software that allows to simulate on top of parts designed on the Autodesk Inventor® program. In the context of this thesis, the software was used to simulate the flow in the bioreactor using the Laminar Flow Physics module. This physics has three major assumptions: the fluid is Newtonian, no-slip boundary condition (approximation that can be applied to fluids with Reynolds Number smaller than 2000) and the fluid is incompressible. The simulation uses the Navier-Stokes model at stationary state, using water at 37°C (Newtonian fluid) as the fluid perfused. The inlet used a parametric sweep to test 1.5 mL/min, 3 mL/min, 9 mL/min and 15 mL/min, as initials flow rates. However, the boundary condition was normal inflow velocity, so the flow rate was converted to velocity depending on the bioreactor inlet diameter using the expression: flow equals to inlet area times velocity (flow in mL/min, inlet area in cm^2 and v in cm/min). The outlet boundary condition was pressure, consider to be 0 Pa. The mesh used was normal course and the solver was the PARDISO. In addition, it was tested different solvers, such as MUMPS and SPOOLES as direct solvers and GMRES with smooth aggregation AMB (GMRES_SAAMG) and geometric multigrid (GMRES_GM) as interactive solvers. This helps to prove that the solution converges independently of the solver, proving the simulation is numerically valid. The simulations output contained the velocity, pressure and shear stress profiles. In addiction, was determined the

Reynolds number in 3 different points of the geometry, inlet, outlet and bioreactor midpoint. The Reynolds number is a dimensionless number that helps to describe the flow profile, is described by the ration of inertia and viscous forces.

$$Re = \frac{pvD}{\mu} \text{ (Eq. 6.1)}$$

Where ρ is the density, v the velocity, μ the viscosity and D_H the diameter. For non-circular geometries the diameter is given by the hydraulic diameter given by:

$$D_H = \frac{4 \times Area}{Perimeter} \text{ (Eq. 6.2)}$$

When Re << 1 COMSOL® suggests using the Creeping Flow physics. For higher Reynolds number the flow is firstly laminar and then can becomes turbulent. The transition between laminar and turbulent flow is not immediate and both flow regimes can exist. This transition was study in circular tube to happen between Reynolds number of 1800-2300[236]. The simulation determined the velocity profile which then allowed to calculate the Re in three points of the geometry and confirm the flow regime. In addition, the COMSOL® also determines the Reynolds number where the characteristic length is removed from the mesh.

6.3.1 Bioreactor Simulations: version 1

The following section shows the image of the first version of the bioreactor and the simulation outputs on different planes, lines and points of its geometry. This version was manually machined and the images in figure 6.8A) show similar geometry and dimensions to the ones presented in figure 6.2. Inside can be also observed a 6 well transwell. Regarding the simulations, the velocities input were 0.005, 0.01, 0.03 and 0.05 m/s. In figure 6.8B), is showed the sketch of the geometry used in the simulation where is highlighted in red the xz plane, in grey the yz, in black a line from inlet to outlet and 3 black dots in the middle of the inlet, body and outlet. These planes, line and points are used to show the simulations results. The Reynolds number (Re), on figure 6.8C), is determined on the 3 black points. Re is higher than 1 and inferior to 2300, indicating a laminar flow regime[236] for inlet and outlets. The laminar regime is maintained as the inlet velocity increases to 0.05 m/s. However, in the body the Re>> 2300 indicating turbulent flow. The velocity, pressure and shear stress simulation outputs are presented in figure 6.8D), 6.8E) and 6.8F) respectively. The outputs contain a top graph where the variable values are determined along the inlet and outlet, black line. Then, the middle and bottom images show the results for 1.5 mL/min (0.005 m/s) on the grey and red plane respectively. To compare the different solvers, in appendix 16 can be found a table with the velocity value at the inlet midpoint when the initial flow rate is 15mL/min (0.05 m/s).
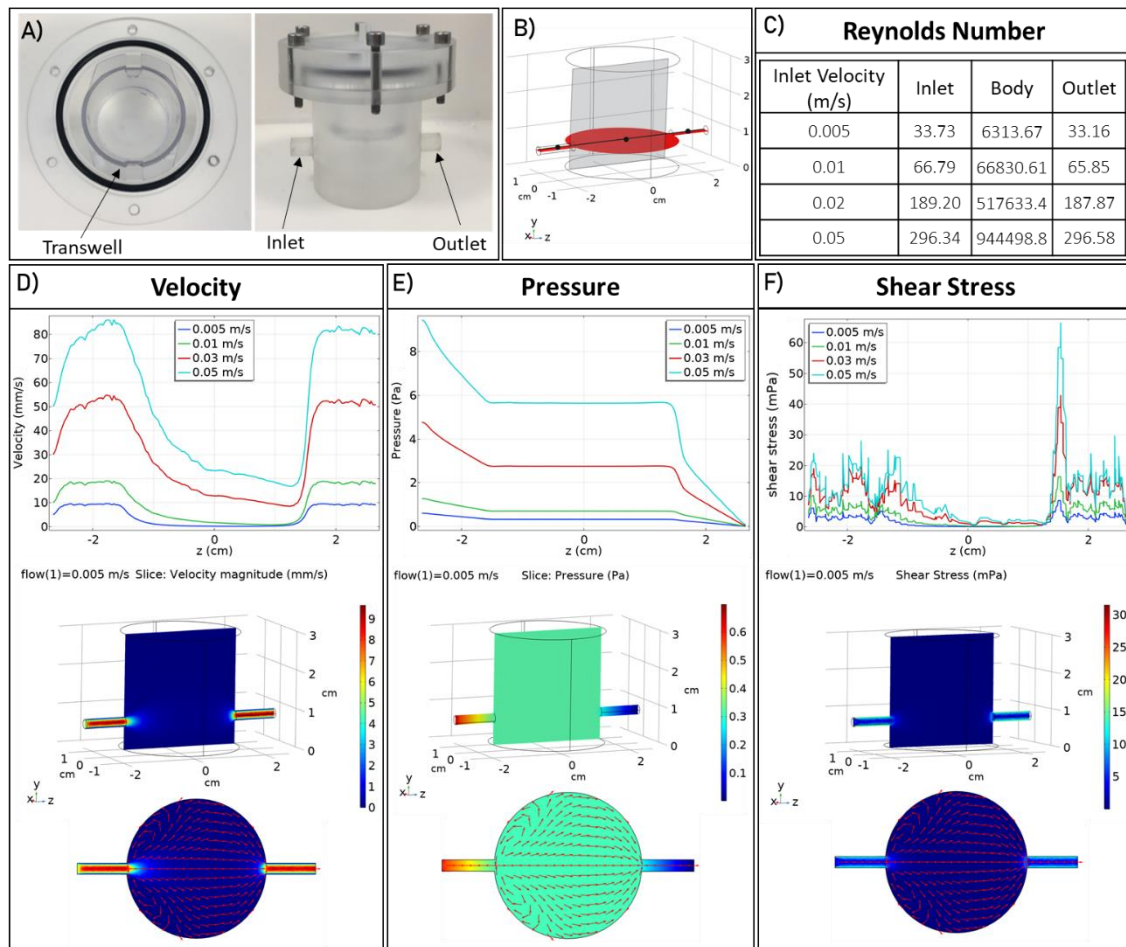
Figure 6.8: Version 1 simulation outcome. A) Bioreactor version 1 top and side images, where is highlighted the transwell, inlet and outlet. B) Bioreactor sketch geometry highlighting the xz plane represented in red, yz plane in grey, line from inlet to outlet in black and 3 black dots in the inlet, body and outlet midpoint. C) Table with Reynold number calculated at inlet, outlet and body midpoint (black dots in B)) at different initial velocity values. D) Velocity simulation output. Top graph represents the velocity in function of the z coordinate (black line from B)) at 0.005, 0.01, 0.03 and 0.05 m/s velocity at inlet. Middle image shows the velocity magnitude in colour scheme on the grey plane from B) at 0.005 m/s (1.5 mL/min). Bottom image shows the velocity magnitude in colour scheme on the red plane from B) at 0.005 m/s (1.5 mL/min). E) Pressure simulation output. F) Shear stress simulation output. Simulations performed with COMSOL Multiphysics ®, Laminar flow physics.

6.3.2 Bioreactor Simulations: version 2

The next version of the bioreactor focuses on turning it more compact, in this way, the fastening between lid and body was design to be by the inside wall of the bioreactor 's body, switching fixation from screws to thread. To experiment with the inlet and outlet, the diameter was increased (from 2.5 mm to 4.5 mm) and placed tangent to the bioreactor's body. The second version was machined on an automated lathe, however, due to construction limitations, the inlet and outlet could not be milled on the same part as the body. To address this issue, it was machined two parts, the bioreactors body and the inlet/outlet piece. Then, both pieces were glued together (using PecFix glue with activator). The image of both components is presented in figure 6.9A). This process was improved on the 3rd version of the bioreactor since is not ideal for cell culture the presence of glue. Similar to what was presented on the first version of the bioreactor, the output of the simulations contains the Reynolds number, in figure 6.9. The table shows numbers between 1 and 2300, indicating laminar flow regime at inlet and outlet, except in the body the Re>> 2300 indicating turbulent flow. In addition, velocity, pressure and shear stress profiles are present in figure 6.9C), 6.9D) and 6.9E) respectively. The top graph shows the variable in function of the z coordinate. On the same graph are represented the values at the inlet level, highlighted with a full line, and at the outlet, highlighted with a dotted line. Noteworthy, the inlet and outlet region are comprised between 2.5 and 1 cm. The image in the middle and bottom shows the profile at 0.0015 m/s (1.5 mL/min).
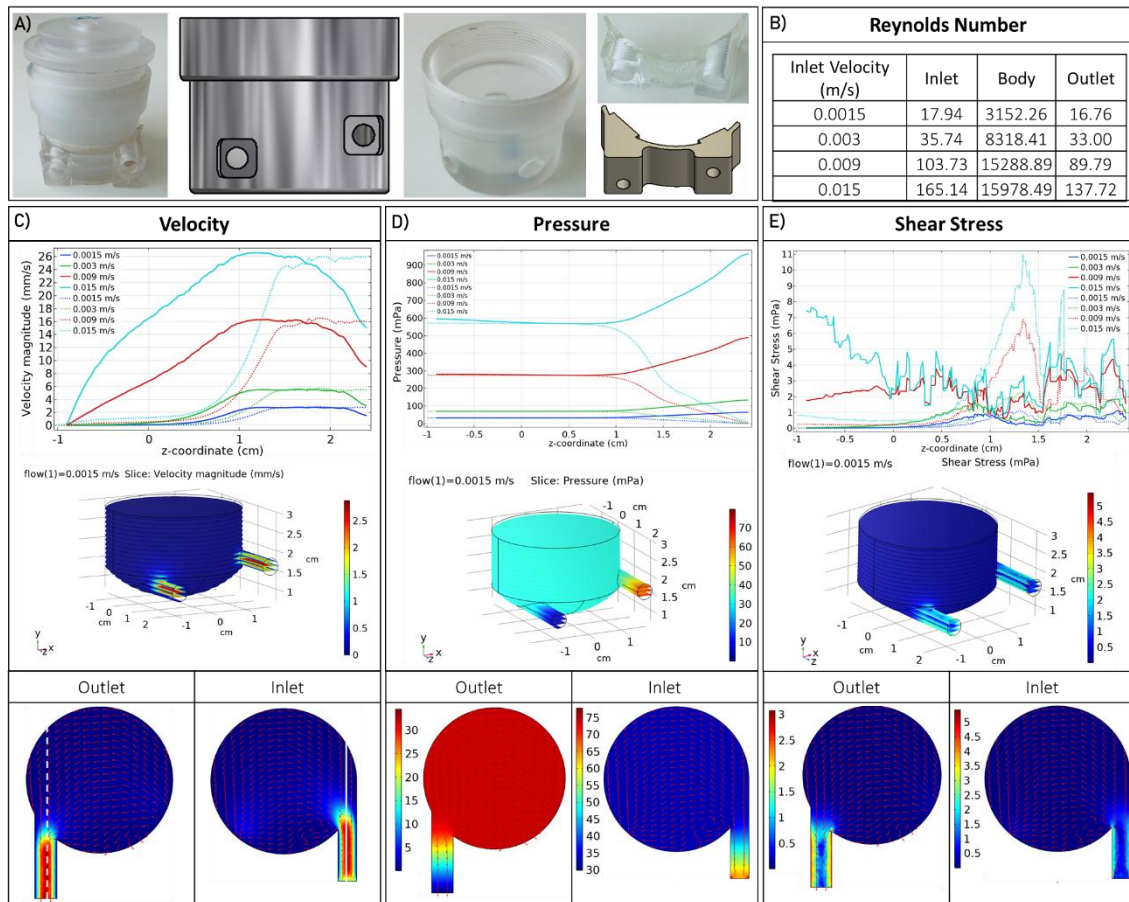
Figure 6.9: Version 2 simulation outcome. A) From left to right is represented the second version of the bioreactor, a technical sketch and image of the body piece and a technical sketch and image of the inlet/outlet piece. B) Table with Reynold number calculated at inlet, outlet and body midpoint at different initial velocity values. C) Velocity simulation output. Top graph represents the velocity in function of the z coordinate at 0.0015, 0.003, 0.009 and 0.015 m/s velocity at inlet. The full line represents the velocity at the inlet level and the dotted line at the outlet level. Representation of those line is in white in the bottom image. The middle image shows the velocity magnitude in a colour scheme at 0.0015 m/s (1.5 mL/min). The bottom image shows the velocity magnitude in a colour scheme on xz plane at inlet and outlet level at 0.0015 m/s (1.5 mL/min). E) Pressure simulation output. F) Shear stress simulation output. Simulations were performed with COMSOL Multiphysics®, Laminar flow physics.

The second version of the bioreactor was further improved in the physics workshop. The bottom of the vessel was etched to be able to fit a ring. The function of the ring was to support the alveolar and vasculature models. Figure 6.10 shows the technical sketches and images. The ring was 3D printed in the physics workshop in PLA.
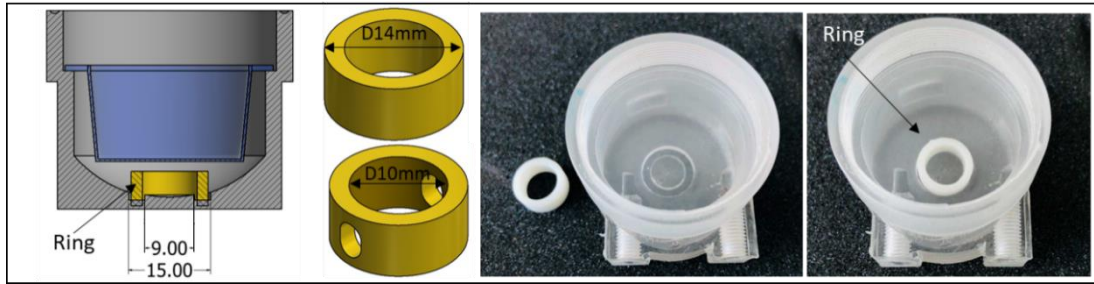
Figure 6.10: Improved geometry from version 2. A) From left to right: bioreactor's technical drawing side view with ring highlighted in yellow with dimensions annotated in mm. Image of the bioreactor without and with the ring in position.

There were several issues found in the second version of the bioreactor, with and without the ring. The fixation of the lid with the thread does not give the same close-fitting compared to the screw. The inlet/outlet needed to be machine apart and glued to the body. The fixation of the ring is not perfect since the ring leaks underneath. These problems were tackled in the third and fourth versions of the bioreactor.

6.3.3 Bioreactor Simulations and PDMS Mould Formation: version 3

One of the major problems to solve in the third version is the fixation of the ring to the bioreactor. The ring should be positioned and removed easily, but at the same time prevent leakage. In addiction should be able to separate the vasculature, which is irrigated with media, from the alveolar model, that needs to be in contact with air. With these constraints in mind, figure 6.11 depicts from A) to E) the evolution of the ring design. The material selected to create the ring was PDMS, which is a transparent and biocompatible silicone base material that secures a tight and leakage free fit. The first approaches, figure 6.11A) and B), focused on fixating the ring in the centre of the geometry. However, the tightness of the ring to the geometry in a pumping flow scenario may continue to be compromised. The next geometry, present in figure 6.11C) solved that problem by expanding the ring to the full length of the bioreactor's diameter. With the leakage problem resolved, the following designs focused on bringing media in contact with the vasculature model only. These efforts can be found in figure 6.11D) and E). The media enters through the part represented in red and is directed to a rectangular geometry, the reservoir, then perfuses through the channels that directs the flow to the central ring, where the cellular model is going to be positioned. When leaving the central ring the flow passes again through the rectangular reservoir before exiting through the outlet. Between geometry D and E, the latter was easier to fabricate by casting mould so was the one selected. In this way, the

236

third version of the bioreactor was composed of 6 parts, sketched in figure 6.4, one lid and base presented in blue, the bioreactors body in grey, the PDMS disk in yellow and the inlet and outlet fittings in red, also fabricated in PDMS by casting mould. The bioreactor is then sealed with 4 screws on top, that join the lid to the body and more 4 screws in the base, that pass though the PDMS disk and thigh on the body. In this way, the lid can be opened without disassembling the entire bioreactor. The internal dimensions of the bioreactor continue the same, where a 6 well insert fits in, to continue to ensure bioreactors flexibility. The bioreactors lid, base and body were laser cut in acrylic to give complete transparency to the bioreactor and facilitate external assessment.
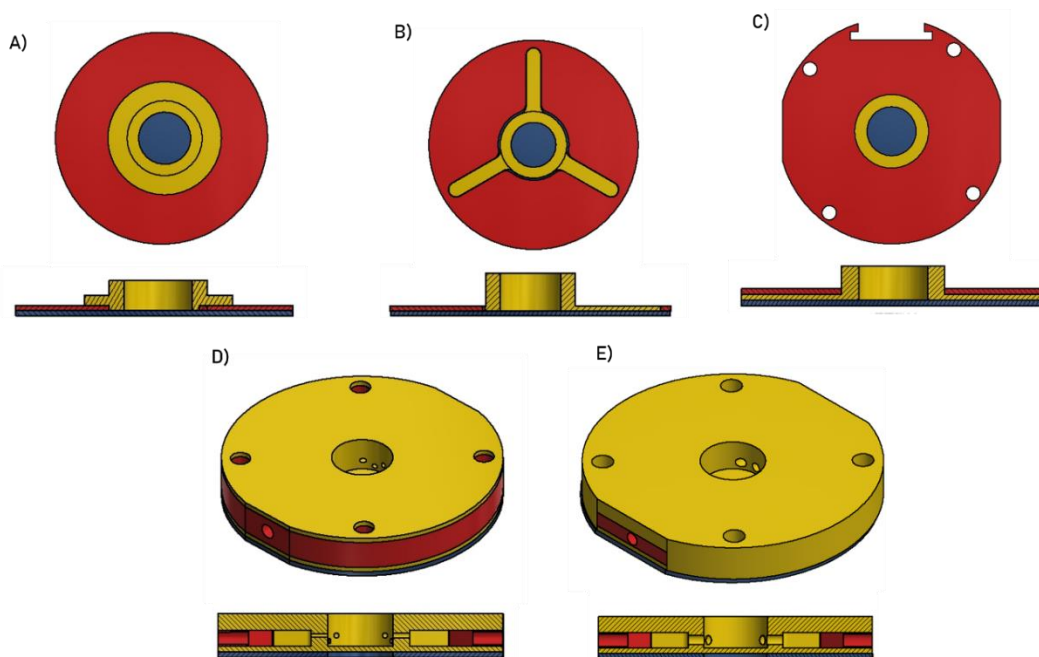
Figure 6.11: PDMS part. A) to E) Top and side view of the strategies designed to fix the PDMS piece to the geometry. In yellow is represented the PDMS piece. In blue the bioreactor base made of in acrylic. In red are represented the extra pieces to support the geometry, fabricated in acrylic from A) to C) and in PDMS in D) and E).

The geometry presented in figure 6.11E) was further modified, the inlet and outlet were positioned in slope and the reservoirs increase in height. The technical drawings can be found in figure 6.12. The geometry in A is the same presented in figure 6.11E), with both inlet and outlet at the same level and the reservoirs have 3 mm in height. However, in geometries B and C, the media enters the PDMS disk at a higher level than it leaves. The difference between B and C lays on the height of the reservoir closer to the outlet, for B has 3 mm and for C 5 mm. In figure

6.12 is also visible the central ring where the alveolar model is placed, the V shows the vasculature position and the A the alveolar.

.
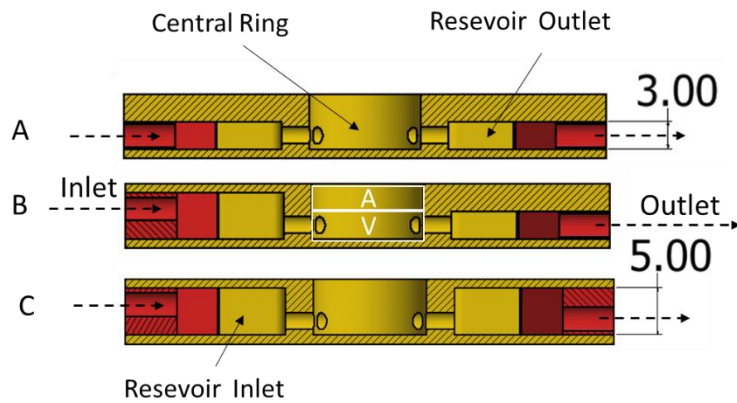
Figure 6.12: Side view sketch of the 3 PDMS part geometry. A-C, originated from figure 6.11E). Highlighted are the inlet and outlet, the reservoirs and the central ring (units in mm). On the central ring the V highlights the place for the vasculature model and the A the alveolar.

The three different geometries presented in figure 6.12 were fabricated by mould casting. The images of the different parts of the mould can be found in figure 6.13. The parts have similar geometry and dimensions to the ones presented in figure 6.6.
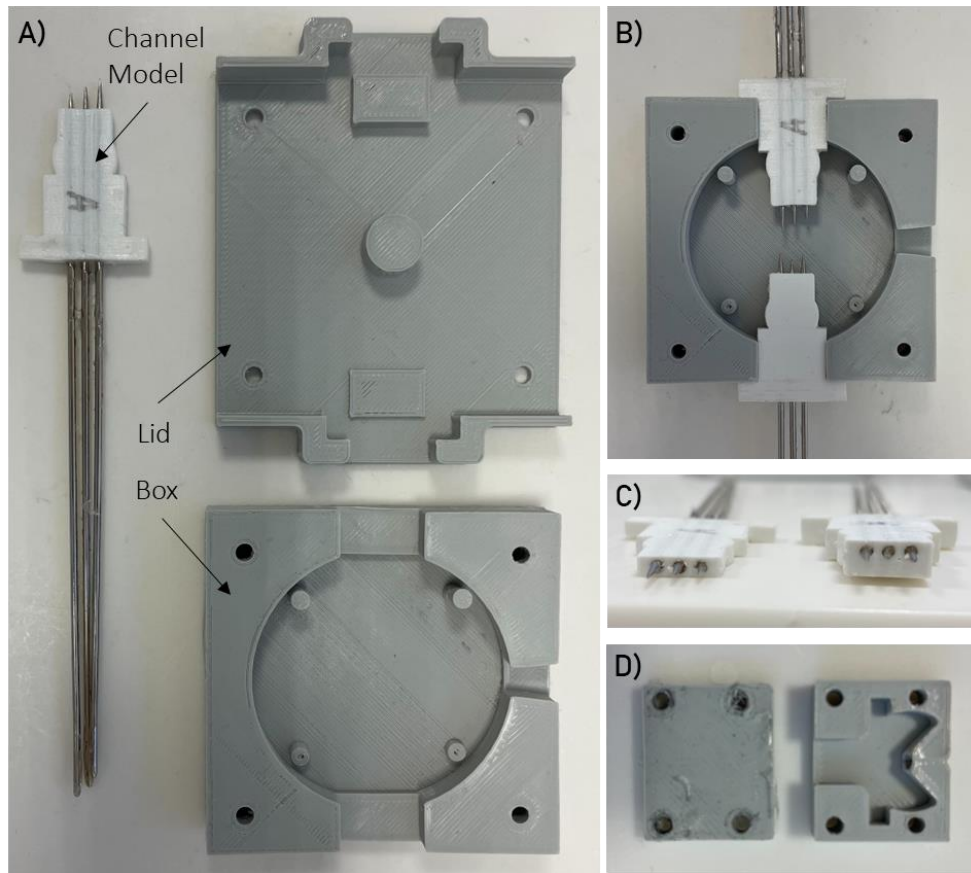
Figure 6.13: PDMS part 3D printed mould. A) Top view of the 3 components of the PDMS mould for the third version of the bioreactor. B) Representation of the fitting between the box and the channel model. C) Side view of the channel's models with 3 mm and 5 mm height respectively on the left and right side of the image. D) Mould of the stoppers, on the left the lid and on the right the base. A needle similar to the one in the channel model in A) is introduced in the base to make the stopper channel

The three different geometries presented on figure 6.12, were simulated similar to what was done for version 1 and 2. The simulation was done without the fibrin gel present, since the only physiscs available was the laminar flow. On figure 6.14 is presente the velocity simulation output for the 3 geometries, and on the supplementary information appendix 17 and 18 the pressure and shear stress respectivaly. The top graph shows the velocity along the inlet and outlet levels for different input velocities. The middle image shows the velocity profile on the yz plane from inlet to outlet at 0.022 m/s (corresponding to the flow of 1.5 mL/min) and the table the reynolds number. The Reynolds is below 2300 for inlet and outlet (computed with equation 6.3), indicating laminar flow. The reynolds on the ring was determined using the hydraulic diameter from equation 6.4 (height 3 or 5 mm and length 12 mm) and shows values higher than 2300, suggesting a transition to turbulent regime. The velocity simulations indicate similar flow profiles for the 3 geometries at inlet and outlet in the range of initial velociteis tested. The diference is

on the central ring where geometry A reaches higher velocities and consequenlty higher Reynolds. This feature may help to drain the media easly when the fibrin gel is in place. In addiction, geometry A is also easy to fabricate, reason for what was selected as the geometry to move further and test the fibrin gel on.

In the third version, the vasculature would be polymerized in the first 3 mm of the central ring to contact with the media and the alveolar on top. However, the media did not flow easily overflowing the central ring. In addiciton, the fibrin gel polymerized on the central ring and on the outlets of the channels that make a connection between the reservoirs and the central ring. This obstructed the channels making the flow between the 3 channels uneven. One last consideration is related to particles testing, which would require the model to be removed from the bioreactor and added to the exposure system. Since the model would be built on the central ring, removing it would collapse it and was not going to be possible to assemble it again on the PDMS once exposure was finished. To adress to these problems, a forth version of the PDMS disk was designed.
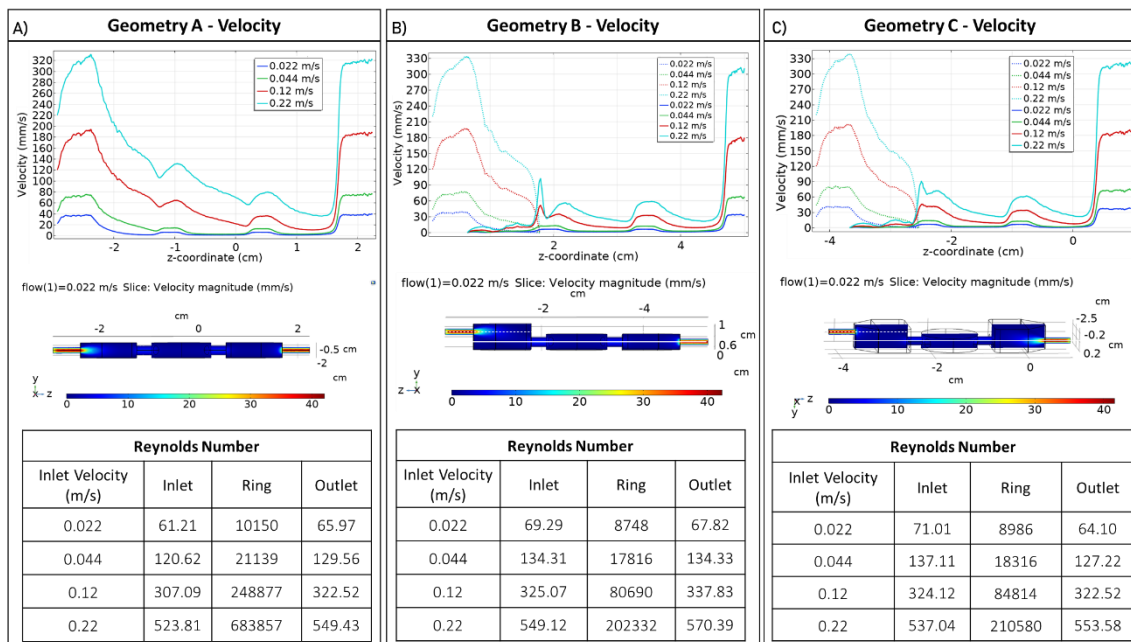
Figure 6.14: Version 3 simulation outcome. A) Velocity simulation output for geometry A. The top graph represents the velocity in function of the z coordinate from inlet to outlet with initial velocity of 0.022, 0.044, 0.12 and 0.22 m/s at the inlet. The middle image shows the velocity magnitude at zy plane that passes from inlet to outlet in colour scheme at 0.022 m/s (corresponding to the flow of 1.5 mL/min). Table on bottom represents Reynolds number at different velocity inlets and in 3 points of the geometry. B) Velocity simulation output for geometry B. The dotted line represents the velocity in function of the z coordinate at the inlet level and the full line at the outlet level. The lines can be found represented in white in the middle image. C) Velocity simulation output for geometry C. Simulations performed with COMSOL Multiphysics®, Laminar flow physics.

6.3.4 Bioreactor Simulations and PDMS Mould Formation: version 4

The fourth version of the bioreactor maintains the same lid, base and body from version 3, only the PDMS disk suffers improvements. The improved PDMS geometry allows three repeats per bioreactor and the gives flexibility to add and remove the model since is constructed in the gel holder. In Figure 6.15 can be observed an image from the entire moulding process, assembly and feeding of the PDMS disk and stoppers in figure 6.15A) and B respectively and the demoulding of the PDMS disk in 6.15C). The representation of the PDMS disk continues in figure 6.16A) where can be found the top and side view, with gel holder. The gel holder sits in the PDMS disk, and its bottom is tangent to the channel where media is pumped through. In figure 6.16A) is also represented an image of the bioreactor without a lid where can be seen the fitting of the 3 gel holders. The image on the far right from figure 6.16A) shows the complete bioreactor with each of its parts annotated with an arrow and media being perfused.
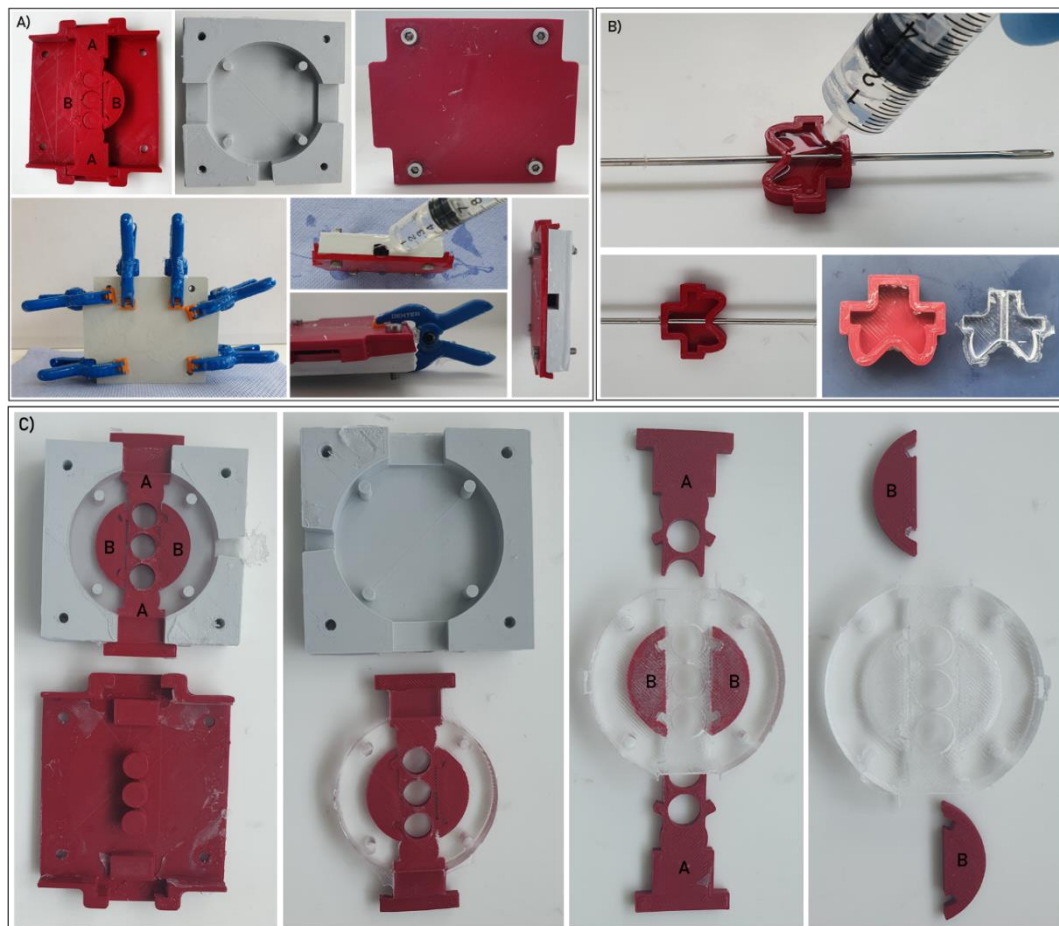
Figure 6.15: PDMS disk and inlet and outlet fittings for version 4 of the bioreactor. A) Assembly of the PDMS disk mould. Base in grey, lid and channel models A and B in red. The mould is closed with screws or clamps. After filling in the mould with liquid PDMS, the aperture is closed with a

PDMS plug and secured with a clamp. B) Assembly of the inlet and outlet fittings composed of a 3D printed part in red and a needle with 1.8 mm. C) Demoulding process of the PDMS disk.

Then, in figure 6.16B), C) and D) are represented the outputs of the simulation for velocity, pressure and shear stress respectively. To represent the results of the simulations are used plane, lines and dots, which are illustrated in figure 6.16F). The red plane passes in the middle of the geometry and between the inlet and outlet. The white line goes from the middle of the geometry from the inlet to the outlet and the black line does the same but tangent to the geometry top (y=0.4cm). The black dots represent the middle point for the inlet, outlet and body (PDMS disk). For each variable output, the graph on top shows in a full line the simulations results obtained along the black line and in the dotted lines the results along the white line. The image below the graph shows in a colour scheme the simulation results for 0.0022 m/s (corresponds to flow of 1.5 mL/min) initial velocity along the red plane. On 6.16E) is present the Reynolds number (on the black dots) calculated using equation 6.3 at the inlet and outlet. For the midpoint of the PDMS disk (referred to as body in the table) equation 6.4 (height 3 mm and length 34 mm). The Re at the inlet and outlet maintain a laminar flow regime but, in the body, the Re values are above 2300 for all the velocities, suggesting a transition to a turbulent regime.

The version 4 of the bioreactor, including the acrylic body, PDMS disk and gel holder is being prepared as a manuscript for publication. The publication will include the fabrication process, simulations and its validation using the co-culture of endothelial and fibroblast in the fibrin gel.
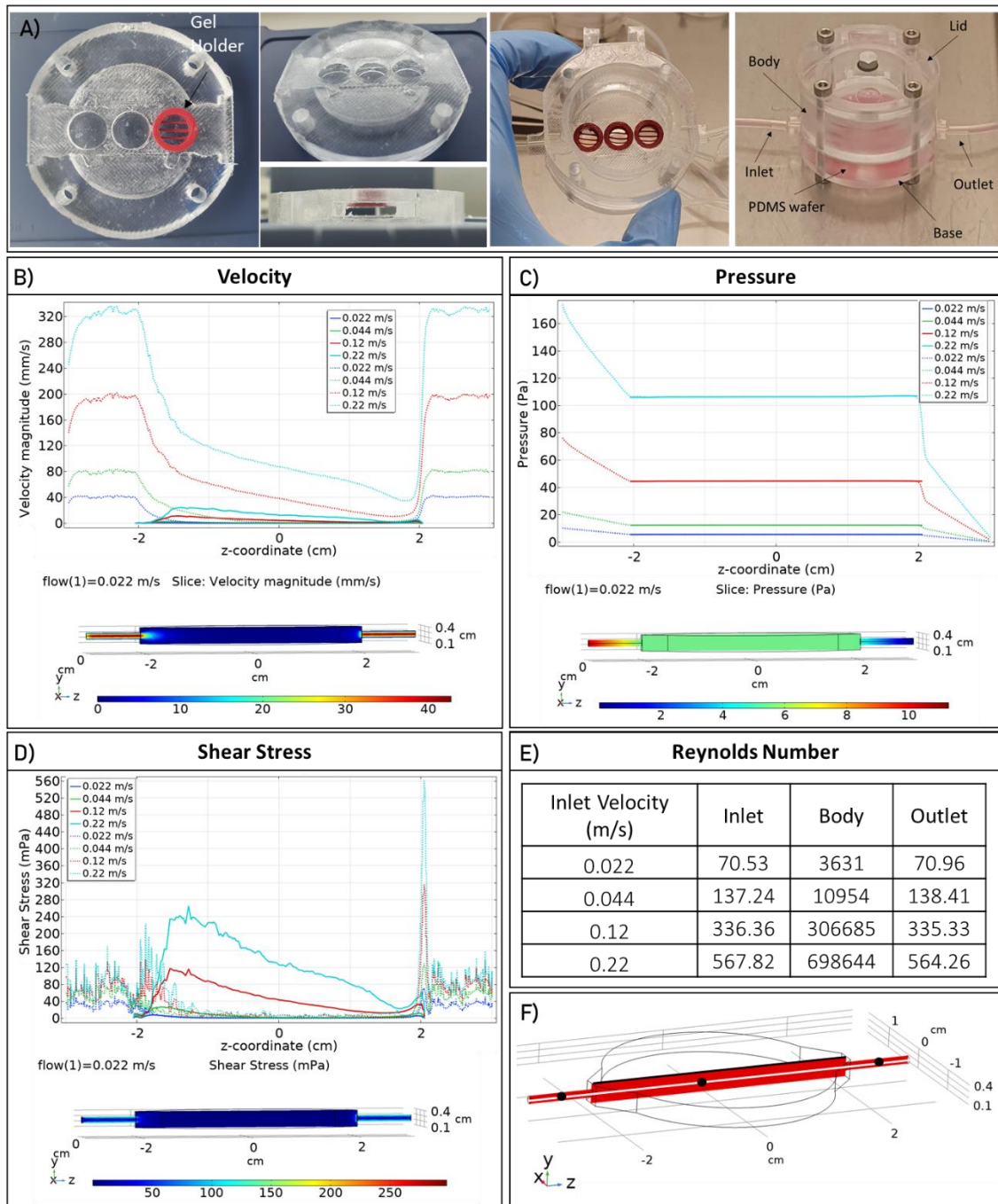
Figure 6.16: Version 4 simulation outcome. A) PDMS disk with gel holder top and side view, bioreactor without lid and with 3 gel holders in place and image on far right shows a complete bioreactor with the arrows indicating its different components. B) Velocity simulation output. Top graph represents de velocity in function of z coordinate at 0.022, 0.044, 0.12 and 0.22 m/s velocity at inlet. The full line represents the velocity along the black line of F) and the dotted line along the white line on F). The image below the plot shows the velocity profile along the red plane in F) at 0.022 m/s initial velocity (1.5 mL/min). C) Pressure simulation output. D) Shear stress simulation output. E) Table with Reynold number calculated at inlet, outlet and body (PDMS disk midpoint), represented by black dots in F), at different initial velocity values. F) Representation of the plane, lines and dots where simulation outputs are shown. Simulations performed with COMSOL Multiphysics®, Laminar flow physics.

6.4 Discussion

The chapter 6 aimed to combine the results obtained during the bioreactor's iterations, illustrated in figure 6.1. These results include technical drawings, flow simulations and images of the fabrication steps. The bioreactor from versions 1 to 4 suffered numerous changes. Versions 1 and 2 focused on experimenting with materials and fabrication methods. The first version was machined manually in acrylic and the second version was CNC machined in acrylic and polycarbonate. Both materials are transparent and biocompatible reason why were chosen, however, the milling process increases the surface roughness, which affected their transparency. This made both materials opaque and not completely transparent. Regarding the fabrication methods, the manual milling allowed to make the geometry designed however the labour time and cost are not ideal for future fabrication method. To address this, the second version was machined in a CNC, but limitations of the technique prevented the body to be machined together with the inlet and outlets, so an additional part had to be fabricated. The inlet/outlet piece was attached to the body with glue which is not ideal as well. Not just because is a high source of leakage with usage but also the fact the glue is not biocompatible. Another feature experimented with in versions 1 and 2 was the sealing method, screws on version 1 and thread on the second version. The screw method as was designed for version 1 consumed a lot of area and make the bioreactor bulkier. The thread method would fix that problem, but the usage showed not to be practical. The fact that both body and lid were made in acrylic or polycarbonate, which are hard plastics make the screw and unscrew task difficult. In addition, the position of the inlet and outlet to be tangent to the surface did not bring advantages, concerning fluid flow, over the position in version 1.

The experimentation done with versions 1 and 2 helped to design the acrylic parts of bioreactor 3. To ensure complete transparency, the bioreactor needed to be laser cut instead of milled. The polycarbonate burns when is laser cut, so acrylic was chosen as the material to build the 3rd version. The fixation between the different parts of the bioreactor would be done by screws which will give the necessary seal. To improve the fixation from version 1, where the lid and body seal in a side flap, in version 2, the screws fasten in the walls of the bioreactor body. This would allow the lid and body to be laser cut and as well make the geometry more compact. The way the laser works is, it receives as input a 2D sketch that cuts in the material sheet, so it cannot make structures such as inlets and outlets that stick out of the geometry or features such as the air inlet seen on the lid of the first version of the bioreactor. In addition, with the optimization of the PDMS disk, the acrylic parts of the bioreactor have the function of sealing the PDMS and

in future allowing air to be added. The PDMS being mould casting allowed more flexibility without changing the entire bioreactor geometry. In this way, despite versions 3 and 4 having different PDMS disks, the acrylic bioreactor structure is the same.

Regarding the PDMS iterations, had two objectives, containing the media to prevent leakages and consequently contaminations, as well as support the model requirements. These requirements are the media contacts only with the vasculature model and the alveolar with the air. The PDMS disk experimented on version 3 was designed to make the media to perfuse through the vasculature biomaterial, however, problems were encountered with media finding alternative ways to perfuse over the fibrin gel. This set up was found in other research articles[173,172,92], but with the main difference being the flow rate. The minimum flow rate tested was 1.5 mL/min (2.2 mm/s) due to pump limitations and in the literature is used passive flow or flows in the range of μm/s. With the limitations presented before it was necessary to design another PDMS disk. In this way, for version 4 the position of the model was lifted to sit above the media channel to allow free media flow underneath. In addiction, to prevent scale up from the data already generated in static vasculature experiments, the PDMS was perforated to accommodate three 8 mm apertures. This feature comes advantageous since one bioreactor can contain 3 repeats. For the 4th version was necessary to build a gel holder on where the model would be built on. The sketch image in figure 6.5 and image in figure 6.16A) show a transwell-like geometry with a base with 3 lines of material, instead of a porous membrane, that is sufficient to give structure to the fibrin gel and at the same time allow media contact. In addiction, the gel holder allows the model to be added and removed for future particle exposures and facilitates the post-processing of the samples.

Regarding the simulations, the only physics available was the laminar flow, but would be interesting to simulate as well with turbulence. The Reynolds number was below 1800 for the inlet and outlet, suggesting laminar flow and good applicability of the physics available. However, the inlet and outlet are circular pipes where the diameter is below the length of the tube, which makes the Reynolds number suitable to be applied. To apply the Reynolds number to non-circular pipes is calculated the hydraulic diameter (4xArea/Perimeter), which for version 1 is 28, for version 2 is 27.7, for version 3 is 4.8 and for version 4 is 5.6. However, the hydraulic diameter is calculated for the midpoint in the body or PDMS disk, but the cross-section changes along the length. This feature is not considered in the Reynolds number.

To surpass this, the COMSOL® calculates the Reynolds number using the characteristic length, determined by mesh size. The data can be seen in appendix 19. The results correspond to the Reynolds profile for the higher initial velocity tested, 15mL/min, where is observed that values are below 15. Nevertheless, the mesh size is a small value that does not represent as well the characteristic length. In this way, a turbulence study to confirm the flow regime would be necessary. Despite that, the five solvers tested all converged to the same values. To confirm that, it was stored the results for velocity, pressure and shear stress at the inlet, body and outlet midpoint for the entire range of initial velocities tested: 1.5, 3.0, 9.0 and 15 mL/min. Independent of the solver selected the value for each condition is the same. In appendix 16 can be seen those values for the velocity at the inlet midpoint at 15 mL/min initial velocity. This validates the simulations using the laminar flow COMSOL® module.

One last consideration is the low shear stress simulated compared to 0.5 a 1 Pa[22] physiological values presented in the introduction. This feature needs to be confirmed with the cells, since the accurate physiological value may not be supported by them and the gel integrity may be compromised. In this way, the next step would be to confirm the cells and gel are capable of supporting 1.5 mL/min and then go higher in the flow range.

Conclusion			
From the chapter	Version 1	▪ Manually machined in acrylic 2 parts (lid and body) ▪ Screws to fixate lid to bioreactor's body	
	Version 2	▪ CNC machined in acrylic or polycarbonate 2 parts (lid and body) ▪ Thread to fixate lid to bioreactor's body ▪ The inlet/outlet tangent to bioreactor's body and part was attached to the body with glue.	
	Version 3	▪ Laser cut in acrylic 3 parts (lid, base and body) ▪ PDMS part to integrate cellular model ▪ 2 sets of screws to fixate lid to bioreactor's body and base to bioreactor's body passing through the PDMS	
	Version 4	▪ Same acrylic parts and screw fixation as in version 3 ▪ PDMS part to integrate cellular model improved ▪ Fabrication of a 3D printed holder to support the cellular model under flow tests	
	Simulations	▪ Reynolds show at inlets and outlets laminar flow regime. ▪ Shear stress tangent to gel holder positions is close to zero, which contrast with 0.5 to 1 Pa felt by the endothelial cells lining the alveolar capillaries.	
	Improvements	▪ Change inside channel from PDMS part used on version 4 to a rectangular shape to increase velocities inside and shear stress. But also facilitates calculations of Reynolds and resistances	
Overall Project	Version 4 used to test the vasculature and the full model underflow		

Chapter 7

Full Model
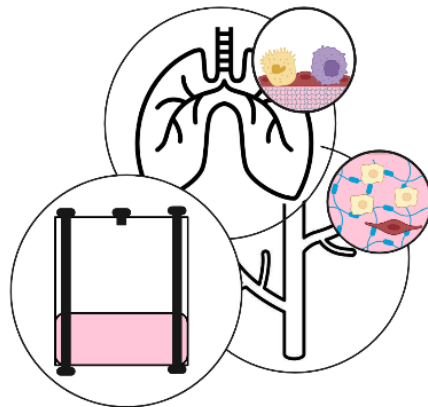
7.1 Introduction

The advanced alveolar region *in vitro* model proposed at the end of the introduction is assembled in this full model chapter. However, bear in mind that is considered a pilot chapter, with the majority of PhD time dedicated to build in parallel and from zero, the three parts of the project. Despite none of the three parts of the project being completely finalised, they were assembled together in this data chapter. This allowed not only to validate the bioreactor, but also to further optimize the individual parts. In addition, demonstrating the feasibility of the full model for future work was also necessary. The assembly of the full model was foreseen to bring out iterations, not only on each individual part but also in the experimental design, which motivated the work present in this chapter.

To create an advanced in vitro model, key features were identified in the literature, which are listed below:

1. Real 3D environment
2. Dimension accuracy
3. Relevant cell population and cell source
4. Vascular Flow
5. Relevant physico-chemical environment

For the alveolar region scenario, this includes a complex 3D structure with an important barrier function. The lung goes through 23 generations of branching before opening into a sac where several alveoli contact with each other to facilitate the gas transfer. Considering not just the geometry, but also the dimensions, an alveolus has a diameter in the order of 250 μm^2 and the barrier can reach a minimum of 0.3 μm^2 when alveolar type I and endothelial cells contact. Adding to the diverse cell population of the barrier, are the fibroblast and alveolar type II for extracellular matrix integrity and alveolar macrophages for immunity. On top, the lungs are a dynamic organ that is in constant movement, so the substrate where the cells attach would need to facilitate that as well. Then, *in vivo,* the source of nutrients is given by a network of capillaries that cover 90% of the alveolar region[9].

To translate all these features into one functional *in vitro* model at moment was not published. However, despite the challenges, some papers have been able to replicate some parts of the alveolar environment.

Regarding incorporating a diverse cell population, the work of Sebastian G. Klein seeded on a Transwell, alveolar type-II cell line (A549), differentiated macrophage-like cells (THP-1) and mast

cells (HMC-1) on the apical and endothelial cells (EA.hy 926) on the basolateral side of the membrane[64]. Another noteworthy work is from Charles J Kirkpatrick group, where collagen coated Transwell was seeded with A549, H441, differentiated THP-1 and endothelial cells (ISO-HAS-1) on the basolateral side of the membrane[237,238]. In addiction to the examples before where a Transwells was used, another way to incorporate a diverse cell population is by using organoids[66,68].

Considering strategies where the geometry was the key aspect, the group of Jordan S. Miller[46] created using stereolithography a vascularized alveolar model using photopolymerizable hydrogels. The acellular model mimicked tidal ventilation and oxygenation. But the cellular model, despite containing an alveolus with 600 μm in diameter and in this way with dimensions similar to *in vivo*, the A549 and fibroblast (IMR-90) co-culture lasted only for 24 hours under submerged conditions. Apart from Jordan S. Miller's work, only other two research articles use fast prototyping techniques, such as 3D bioprinting, to build an alveolus model and both have a similar approach, layering material or cells on top of each other[239,240]. Fast prototyping techniques such as stereolithography and 3D bioprinting have the capacity to seed cells and biomaterials together in a controlled manner and in a pre-designed geometry. This technology is still in its infancy, but has the potential to tackle some current limitations when designing lung *in vitro* models[241].

On the other hand, on more solid ground and with extensive validation is the lung-on-a-chip from Donald E. Ingber from the Wyss Institute[45]. It already has been tested for a range of applications such as: bacteria infection[45], silica nanoparticles exposure[45], pulmonary edema[242], lung inflamation[243], smoke inhalation[244], epithelial barrier function with TEER sensor integration[245], thrombosis[246] and lung cancer[247].

The literature overview presented above shows in brief examples of alveolar models, where the cell diversity was the main focus or the attention was on replicating the 3D physico-chemical environment. The rationale behind this PhD project was to incorporate into one model, some of the cellular and bioengineering approaches presented above. With that thought in mind, the proposed full model joined the alveolar, vascular and bioreactor knowledge build up during the last four data chapters and combine in just one model, fibroblasts, endothelial, A549 and differentiated THP-1, on two biomaterials and underflow. The dynamic air was designed but was not implemented.

7.2 Methods

This chapter contains the experiments performed with the vasculature model underflow, represented in figure 7.1 by stage 1. Then also contains the pilot experiment of the full model assembly under static and underflow, illustrated in stage 2 Then, stage 3 contains a final experiment where was tested the staining of the dTHP-1.
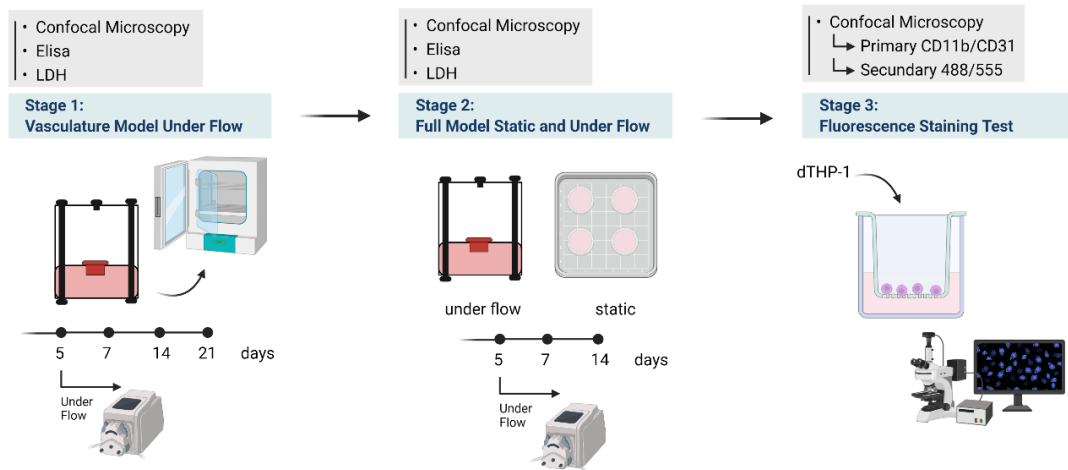
Figure 7.1: Overview of the stages covered in chapter 7. Stage 1 corresponds to the vasculature endothelial and fibroblast co-culture in the fibrin gel underflow. Stage 2 comprises the full model assembly and testing underflow or static. Finally, in stage 3, there is a validation of the fluorescence stain of dTHP-1. Created with BioRender.com

7.2.1 Stage1: Vasculature Model Under Flow

The co-culture of endothelial and fibroblast on fibrin gels underflow, followed the same protocol in section 5.2.4.7 for gel polymerization conditions and cell seeding. However, instead of using a PDMS ring with 8 mm in diameter, was used a part build in TPU in the 3D Printer to hold the fibrin gel. The sketches and images of the part can be seen in figure 7.2. The gel holder was secured on a PDMS ring during fibrin polymerization to ensure complete leakage free culture. The underflow experiments started on the 5th day of culture when the gel holder was removed from the PDMS ring and placed in the bioreactors.
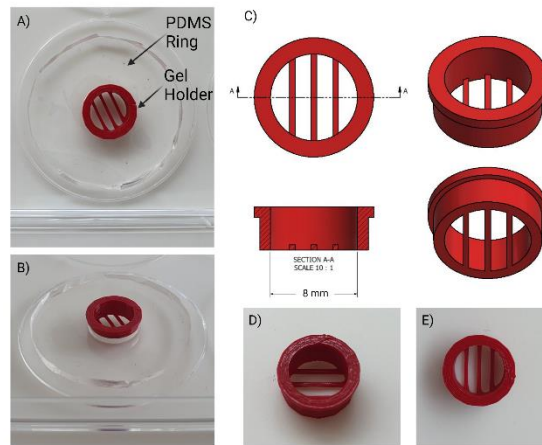
Figure 7.2: Fibrin holder for the full model assembly. Sketch with annotated dimension in mm and images of the part alone and secured by a larger PDMS ring on a 6 well plate lid during static culture. Created with BioRender.com.

The fibrin gel holder was integrated into the bioreactor as shown in figure 6.16. A total of 8 mL of MCDB131 media supplemented to induce angiogenesis plus aprotinin was added to each bioreactor (list of supplements present in table 5.3 from vasculature chapter). The flow rate was 1.5 mL/min, and the gels were always underflow except when to top up media, when pumped was stopped and bioreactors moved to the hood. This happens every two days, between 1-2mL was top up to compensate for evaporation. On days 7, 14 and 21 of culture, one fibrin holder was removed and 750 µL of media was collected for cytokine quantification. The fibrin holder was prepared for imaging as described in section 5.2.4.7.1. and the media analysed for cytokine presence such as IL6, IL8, TGF-β1, TNF-α and the lactate dehydrogenase enzyme (LDH), following protocol from sections 2.5.1, 2.5.4, 2.5.3, 2.5.2 and 2.6 respectively. The LDH value presented is the LDH absorbance of the sample divided by the absorbance value of the media. In this way, the value presented is a ratio between the sample and media, meaning the n-fold increase of the sample regarding the control media.

Each bioreactor contains three slots to place three samples, which at timepoint 7, 14 and 21 one was removed. In this way, each bioreactor has one biological repeat for each timepoint (meaning each biological repeat has only one technical repeat). As a result, until day 7 the 8 mL of media is shared between three biological samples, from day 7 until 14, between 2 samples and between day 14 to 21 to only one sample. In figure 7.3, can be seen the bioreactor is set up together with the pump.
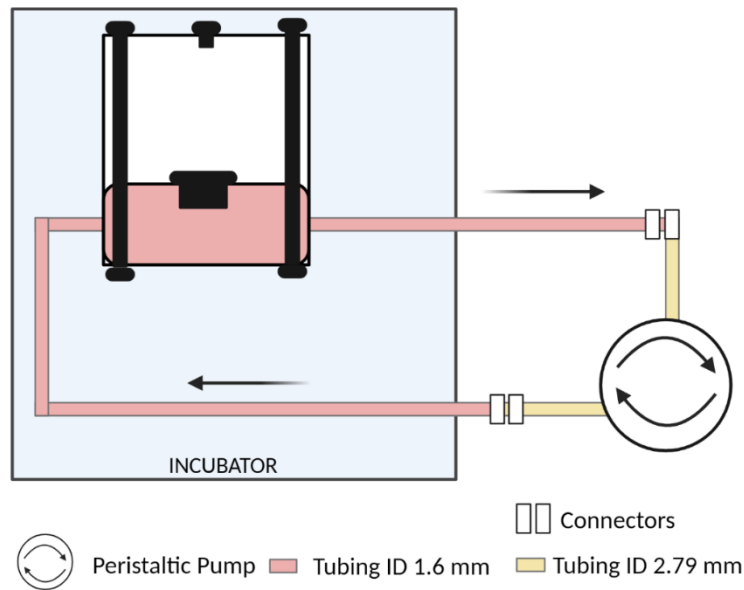
Figure 7.3: Bioreactor set up. The image illustrates the setup of the bioreactor in the incubator connected to the peristaltic pump, arrow indicates flow direction. Created with BioRender.com

7.2.2 Stage 2: Full Model Static and Under Flow

The timeline of the full model assembly is represented in figure 7.4, which includes the preliminary work necessary to derive the dECM. The full model was assembled in 14 days, giving the results obtained in stage 1 from figure 7.1 the vasculature model underflow.

The full model protocol started by assembling the vasculature side of the model first following the protocol on section 7.2.1.

Under Flow: On the 5th day, the vasculature model was transferred to the bioreactor to start the experiment underflow. On the 8th day of culture, the dECM/fibrin is polymerized on top of the vasculature model and the A549s were seeded as described already on protocol 4.2.2.4. While the A549s were under submerged, the TPH-1 were differentiated with PMA on day 9 as described in section 2.3.3.1. The media was changed after 2 days on the 11th and cells were ready to be seeded on the 12th. After two hours, the culture was brought to air liquid interface, which was allowed to recover for 24 hours before adding LPS. The LPS was added by first removing 500 μL (time point zero) and adding fresh 500 μL of media with 4.6 μL of LPS (1.75 mg/mL stock concentration) to make 1000 ng/mL in 8 mL. In addiction, was added 25 μL on top with 1000 ng/mL of LPS. The media was then collected at several time points: 0, 3, 6, 12 and 24 hours, where 500 μL were removed for cytokine determination and the same volume was added. To summarize the conditions for model assembly, table 7.1 contains information about biomaterials polymerization and cell seeding density.

In parallel, was also culture as control only the vasculature model following the protocol in section 7.2.1. In this way, in bioreactor 1 was allocated the vasculature model plus LPS condition, oi bioreactor 2 only the vasculature model, in bioreactor 3 full model plus LPS and in bioreactor 4 the full model. Each bioreactor contains three slots to place three samples, but there is only one time point. In this way, each bioreactor had three biological repeats (meaning each biological had only one technical repeat) for the conditions enumerated above.

Under Static: The static experiment was assembled in parallel to the underflow one, with the difference that on the 5th day the vasculature model was placed on a media holder built in TPU using the 3D printer. The image of the media holder can be seen in figure 4.9. A total volume of 350 µL was added on the bottom and 100 µL on top. For LPS stimulation, a total of 350 µL were removed for timepoint zero and added fresh media with 0.2 µL LPS (1.75 mg/mL stock concentration). In addiction, was added 25 µL on top with 1000 ng/mL of LPS. Every time point, all media was removed and fresh was added.
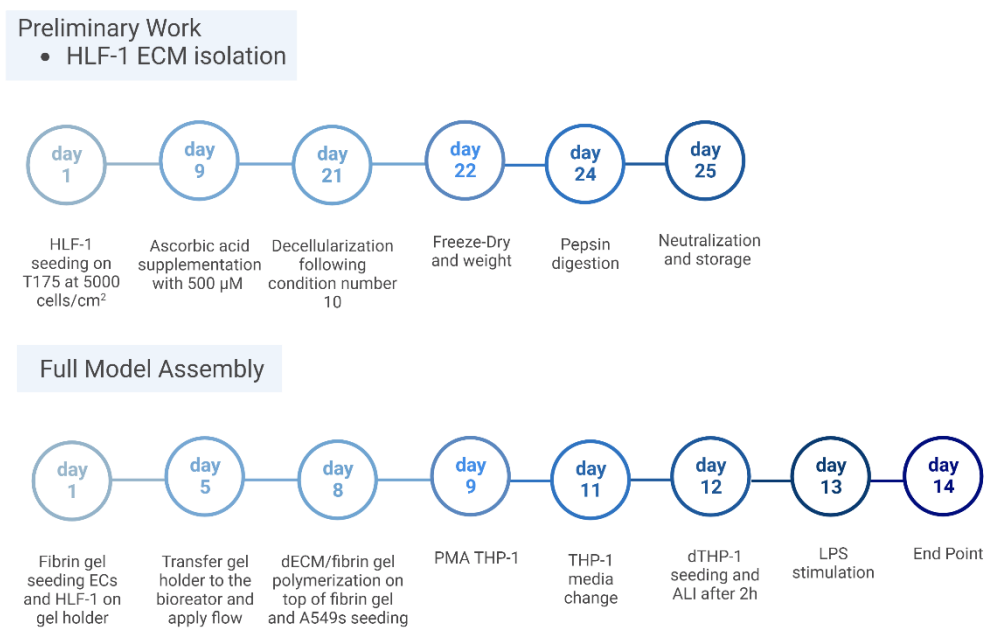
Figure 7.4: Timeline of the full model assembly. The image includes the timeline for the preliminary work for the alveolar biomaterial preparation. Created with BioRender.com

Table 7.1: Summary of the polymerization conditions for the full model. The table contains the cell seeding densities for the full model assembly and biomaterial composition.

	Biomaterial	Cells
Alveolar	dECM/fibrin gel: • 20 mg/mL pepsin digested ECM • 1.25 mg/mL fibrinogen • 5 U/mL Thrombin • Total gel volume: 125 µL • Complete RPMI media	A549: 152 900 cells/ 0.5 cm^2 dTPH-1: 7500 cells/ 0.5 cm^2
Vasculature	Fibrin gel: • 2.5 mg/mL fibrinogen • 5 U/mL Thrombin • Total gel volume: 100 µL • Complete MCDB131 media (No FBS)	HULEC: 25000 cells/ 100 µL gel HLF-1: 250 cells/ 100 µL gel

7.2.2.1 Fluorescence Staining

On day 14, the gel holder from static and underflow experiments were removed from the media holder and bioreactor respectively and added to a 4% PFA solution for 15 minutes. Then, after twice PBS wash the gel holder was placed on a 0.1% Triton solution for 10 minutes in a shaker for the permeabilization step. After repeating the washing step, the gel holder was placed on a 1% BSA blocking solution for 1 hour. Afterwards, both primary antibodies CD31 (#ab9498 from abcam) and CD11b (#ab133357 from abcam) were added in a 1:500 dilution in PBS overnight at 4°C in a shaker. To each gel was added 100 µL with CD31 and CD11b primary antibodies. On the following day, 100 µL of a secondary antibody solution in 1:100 dilution with DAPI (2 µg/mL) and Phalloidin (1:200) diluted in PBS was added to each gel after the washing step. The secondary antibody Goat anti-Mouse Alexa Flour Plus 488 (#A32723 from Invitrogen) was to conjugate with CD31 and the Alexa Flour 555 donkey anti-rabbit (#A31572 from Invitrogen) to CD11b. The secondary antibody solution was incubated at room temperature, protected from light and on a shaker for 1 hour. The gels were washed one last time for three times with PBS with one minute between washes. At this point, the gels were stored at 4°C in PBS or imaged on a Zeiss LSM710. The DAPI was excited at 405 nm, CD31 at 488 nm, CD11b at 543 and Phalloidin at 633 nm.

6.2.2.2 ELISA

The media was analysed for cytokines such as IL6, IL8, TGF-β, TNF-α and for the lactate dehydrogenase enzyme (LDH), following protocol from sections 2.5.1, 2.5.4, 2.5.3, 2.5.2 and 2.6

respectively. The LDH value presented is the LDH absorbance of the sample divided by the absorbance value of the media. In this way, the value presented is a ratio between the sample and media, meaning the n-fold increase of the sample regarding the control media. The collection of media over 24 hours under dynamic makes that at each time point, 5.5% of the media is renewed, which after the four intermediate media samplings 22.2% of the media was added fresh. Regarding the static, in every sampling, all media is renewed.

7.2.3 Stage 3: Fluorescence Staining Test

To confirm the fluorescence crosstalk in stage 2, dTHP-1 were stained with a combination of primary and secondary antibodies present in table 7.2. The cells were handled and differentiated as detailed in section 3.3.2. and seeded on 12 well Transwells at 15000 cells/cm^2. After 24 hours of seeding the cells were processed for staining as followed in section 7.2.2.1. and taking into consideration the combination of primary and secondary antibodies from experiments 1. to 5.

In this way, experiment number 5 replicates entirely the stain from 7.2.2.1 and from 1. to 4. corresponds to combinations of primary and secondary for control. The dTHP-1 as demonstrated in chapter 4 expresses CD11b, and the secondary antibody used was the Donkey anti-rabbit Alexa Flour 555. The CD31 is specific for the endothelial cells and is not expected to be expressed on the macrophages. This primary antibody was used in chapter 5 to stain the endothelial cells. The secondary antibody used for the CD31 was the Goat anti-Mouse Alexa Flour Plus 488.

Table 7.2: Experiment number 1. to 5. primary and secondary antibody appointment.

	Primary	Secondary
1.	Anti-CD11b rabbit monoclonal	Donkey anti-rabbit Alexa Flour 555
2.	Anti-CD11b rabbit monoclonal	Goat anti-Mouse Alexa Flour Plus 488
3.	Anti-CD31 mouse monoclonal	Donkey anti-rabbit Alexa Flour 555
4.	Anti-CD31 mouse monoclonal	Goat anti-Mouse Alexa Flour Plus 488
5.	CD11b CD31	Donkey anti-rabbit Alexa Flour 555 Goat anti-Mouse Alexa Flour Plus 488

7.3 Results

This section includes the results when was combined more than one part of the project (parts illustrated in figure 1.9):

1. Parts 1 and 3 - named vasculature underflow in this chapter
2. Parts 1 and 2 - named full model under static conditions
3. Parts 1, 2 and 3 - named full model under flow conditions

This section follows the same organization as presented in figure 7.1, where stage 1 corresponds to point 1 listed above and points 2. and 3. to stage 2. In addition, there is an extra experiment included in stage 3, where it was tested the fluorescence stain applied to the full model.

7.3.1 Stage 1: Vasculature Model Under Flow

The following data section shows the results from endothelial and fibroblast co-culture with angiogenic media plus aprotinin and underflow. Figure 7.5 shows a representative image of the culture on timepoints 7,14 and 21 and figure 7.6 the cytokine quantification from the media. From the images analysis, is visible the lack of fibroblast proliferation. On day 7 the white arrows point to fibroblast, however, these cells were not found in later time points. The endothelial cells are able to proliferate over 14 days underflow, however on day 21 all the repeats lacked viable cells, but only residues of its presence from DAPI and CD31 stain. In addition, on day 14, the endothelial also show a different morphology as compared to the same day but static, figure 5.28 from the vasculature chapter. The cells do not organize into 3D structures but show a lot of cytoplasm projections.
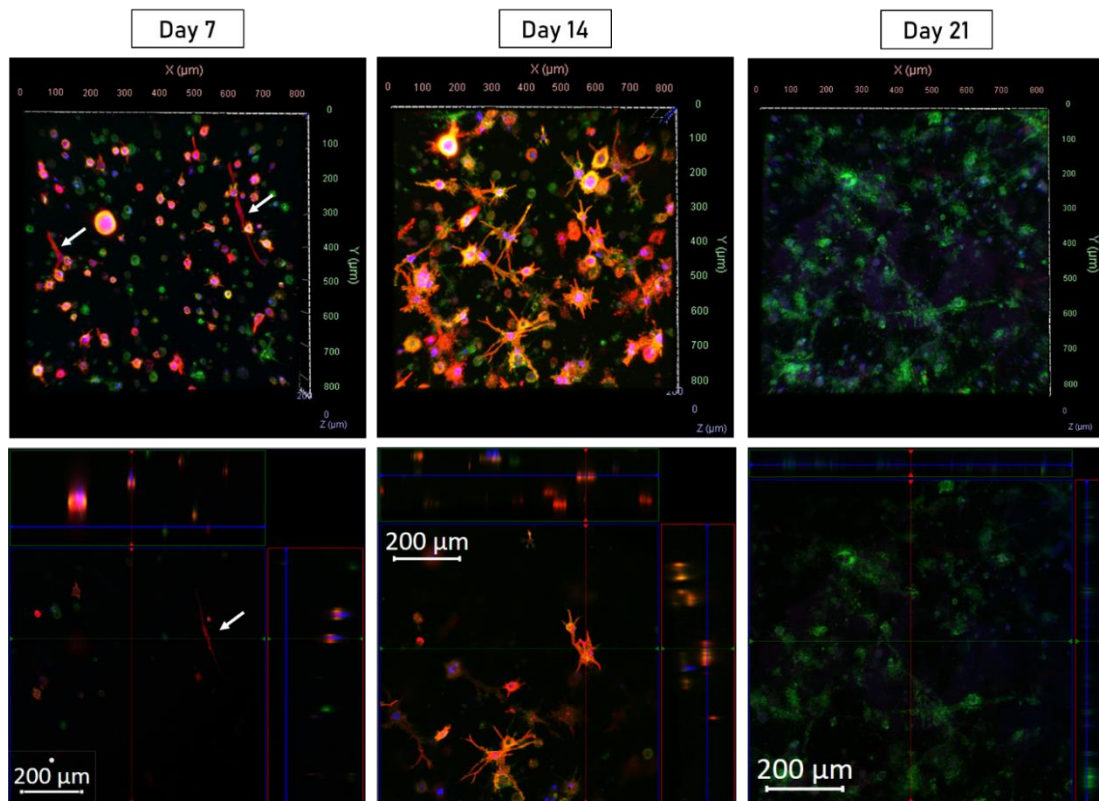
Figure 7.5: Stage 1: vasculature model underflow fluorescence images. Endothelial cells and fibroblast coculture during 21 days under angiogenic media with aprotinin and underflow. The top images represent the top view of the z-stack and the bottom images represent an ortho view. In blue the nucleus is stained with DAPI, in red the F-actin with Phalloidin and in green CD31 staining the endothelial cells. The white arrows indicate fibroblast. The scale bars represent 200 µm (n=3).

Regarding the cytokine quantification in the media, the IL6 and IL8 have a similar trend to static, with maximum secretion detected on day 14. The TGF-β, as well as the LDH ratio, have similar tends, with values slightly increasing from day 7 to 14, but keeping constant from day 14 to 21. Addiction, was also quantified TNF-α from the media but no traces were detected.
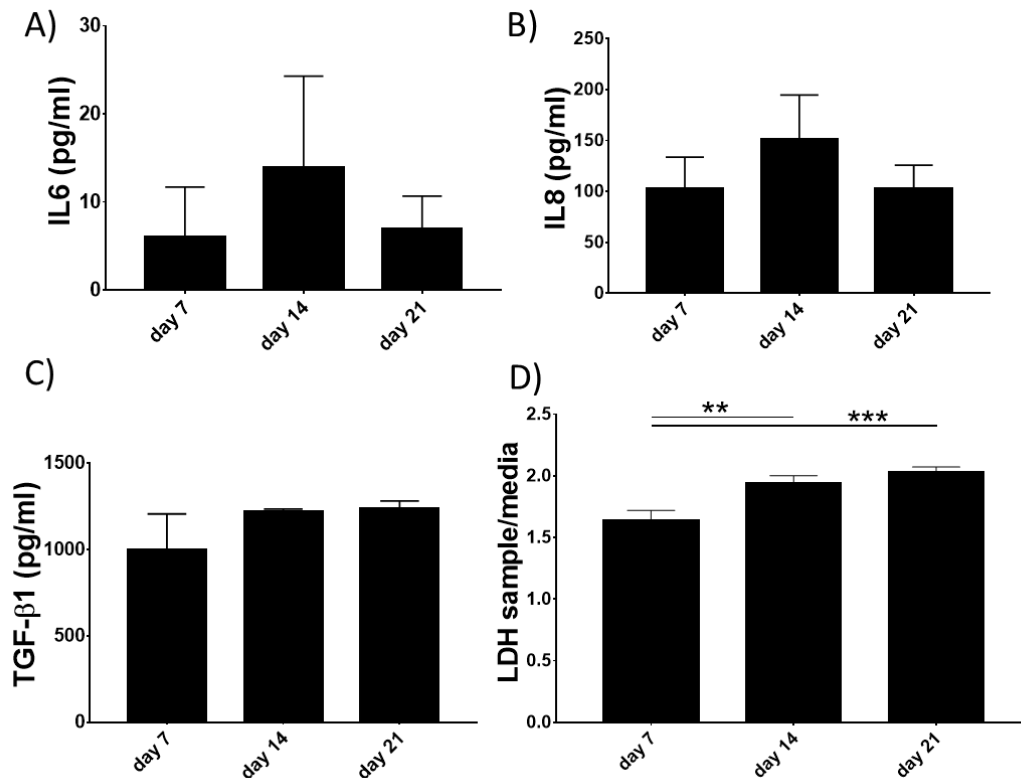
Figure 7.6: Stage 1: vasculature model underflow cytokine quantification. Cytokine quantification of media from endothelial and fibroblasts coculture with angiogenic media plus aprotinin and underflow. A) IL6. B) IL8. C) TGF-β and D) LDH (** p=0.0028 *** p=0.0007). The error bars are SEM (n=3).

7.3.2 Stage 2: Full Model Static and Under Flow

After showing the data from the vasculature underflow, this section focuses on the full model results. Figure 7.7 shows a representative image from the full model on dynamic mode, images A) to C), then on figure D) is represented the full model on static and E) and F) the vasculature only control. From the images analysed, is visible that for all samples, the endothelial and fibroblast are not viable and proliferating. On the other hand, is visible a monolayer of cells on the edge of the vasculature model, which corresponds to the A549. On the full model underflow, is also visible in green and highlighted with white arrows on top of the A549s the dTHP-1 (figure 7.7A) and 7.7B)).

Regarding the cytokine quantification in the media, the results are present in figure 7.8 where IL6, IL8, TFG-β and LDH concentration during 24 hours were determined for the full model underflow and static, as well as for the vasculature control. Note that the experiments underflow, the full model and the vasculature control, were performed in one bioreactor with three samples, where media was sampled over time. This experimental design results in n=3 for

the confocal images but n=1 for the cytokine quantification, which is n=1, the reason for the absence of error bars on these graphs. On the other hand, in the full model under static, the media is not shared and is renewed completely every time that is collected, resulting in n=2 for confocal images and cytokine. In addiction, there is an 80x increase in media volume for experiments in the bioreactors compared to static, so is expected static experiments have a higher concentration of cytokines. As the last consideration, the LPS was added at time point zero, so its effect should be seen later. The differences observed at time point zero are from bioreactors variability. For the experiments underflow the media takes 5.3 minutes to recirculate (volume divided by the flow rate that is 8 mL/1.5 mL/min) so the exposure to LPS is almost immediate after supplementation.

The analysis of IL6 indicates that for the full model underflow, the bioreactor stimulated with LPS did not result in higher IL6 production, however, the cytokine is detected along the 24 hours oscillating from 12 to 8 pg/mL. The bioreactor stimulated with LPS despite having lower values, shows an increase from time point zero with maximal secretion 12 hours after LPS supplementation. The full model under static conditions shows high values of IL6 at time point zero, but drops at later time points. In this case, the LPS did not stimulate IL6 production as well. Regarding the vasculature experiment control, the IL6 is below zero with values lower than the media, or below the detection limit, on conditions stimulated with LPS. In the non LPS conditions, the values oscillate between almost zero and 3 pg/mL, indicating values very close to media values as well. As observed before, LPS did not stimulate IL6 production.

Moving to IL8 analysis, the model underflow shows similar secretion patterns both without and with LPS, with the latter showing higher values. The IL8 increases from time point zero, having a maximum at 12 hours for both conditions and 24 hours as well just for the LPS condition. The full model under static shows high values for time point zero, which drop in later time points. However, the secretion continues to be high. In static, the LPS condition did not lead to higher IL8. The IL8 for the vasculature control was under the detecting limit for both conditions with and without LPS, the reason why there is no plot.
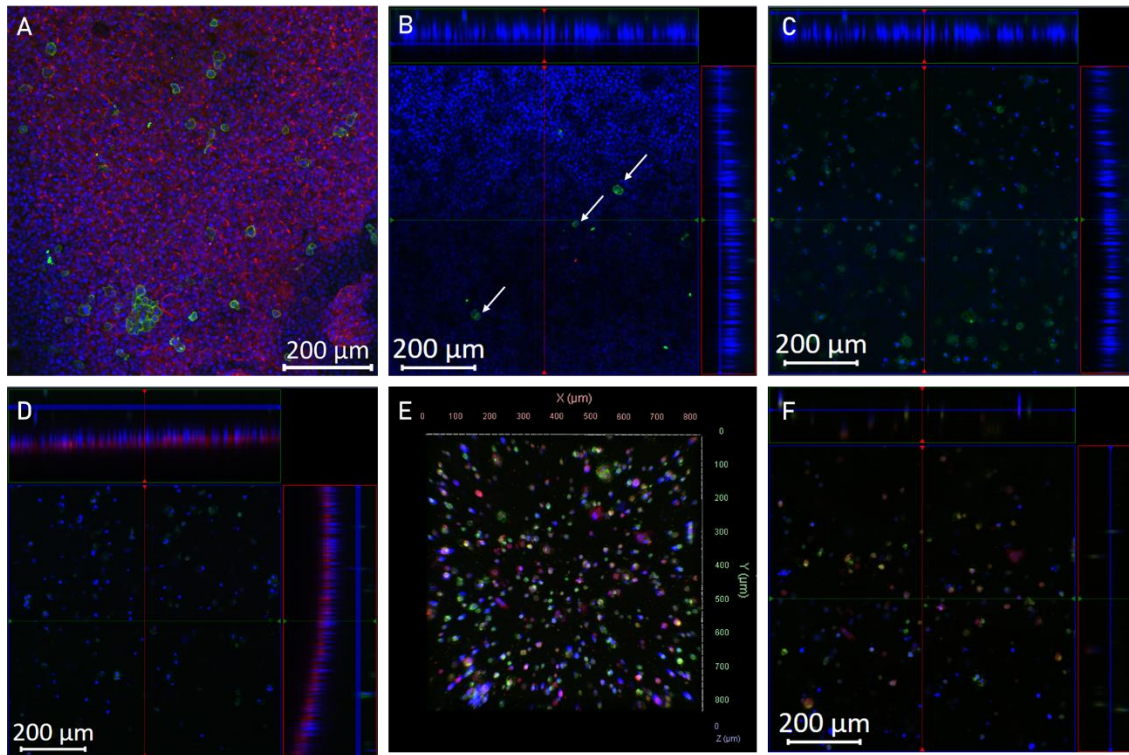
Figure 7.7: Stage 2: full model static and underflow fluorescence images. A) Full model underflow, dTHP-1 in green on top of a monolayer of A549. B) Full model underflow with an ortho view of the alveolar part of the model, dTHP-1 highlighted with the white arrow. C) Full model underflow with an ortho view of the vasculature part of the model. D) Full model under static with an ortho view of the vasculature part of the model. E) and F) Vasculature 3D and ortho view. In blue the nucleus is stained with DAPI, in red the F-actin with Phalloidin and in green CD31 and CD11b staining the endothelial cells and dTHP-1. The scale bars represent 200 µm. (n=3 except for D) that is n=2)
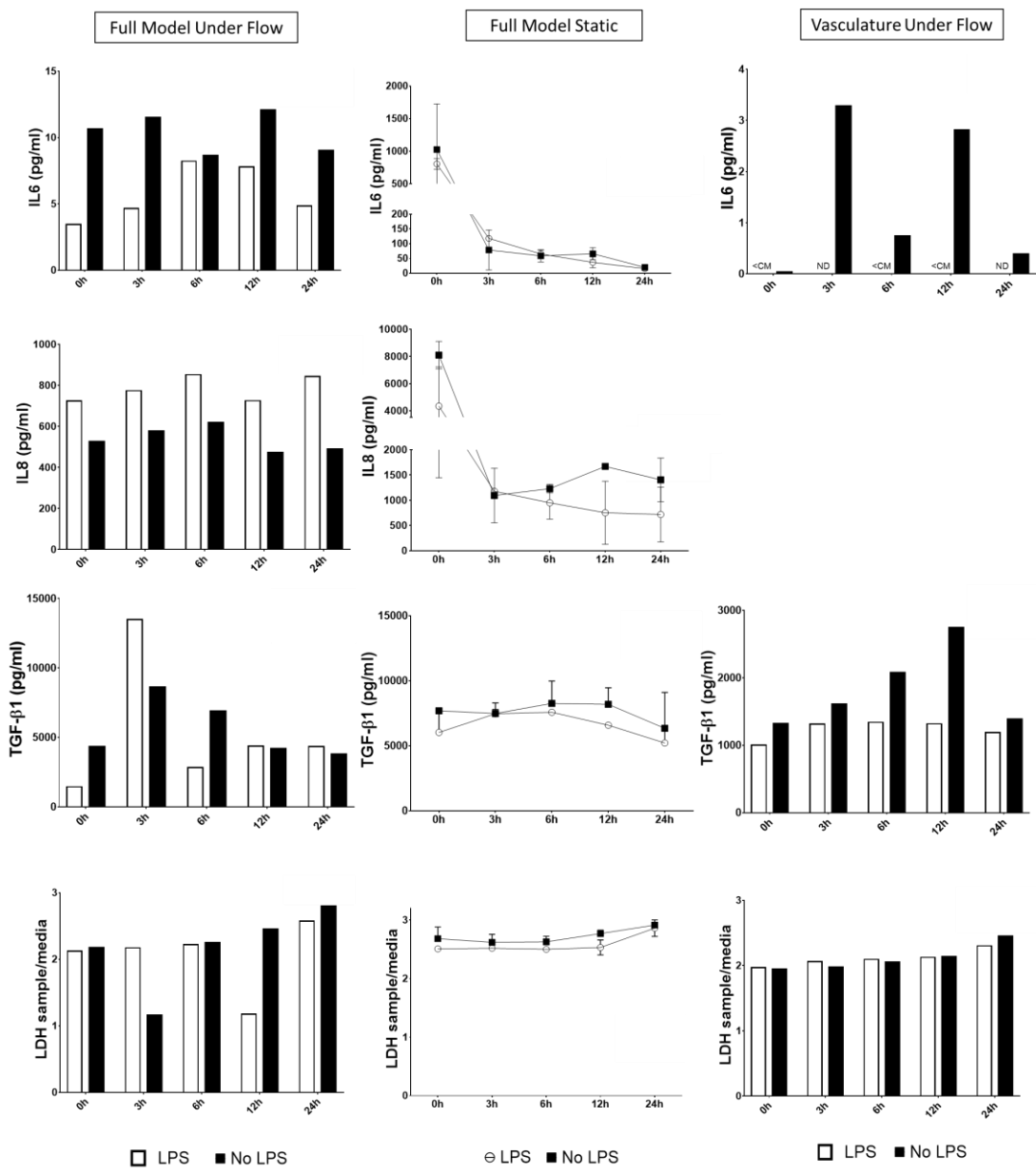
Figure 7.8: Stage 2: full model static and underflow cytokine. The column represents from left to right data from the full model underflow, full model under static and vasculature underflow. The lines contain, IL6, IL8, TGF-β and LDH. For the full model and vasculature underflow, the white bar represents the conditions with LPS and the black without LPS. For the full model under static conditions, the white circle presents the conditions with LPS and the black square without LPS. The error bars are SEM (n=1 for underflow experiments and n=2 for the full model static). Legend: ND represents absorbance values below the limit of detection and the <CM indicates sample concentration below the concentration in the media.

The next cytokine in figure 7.8 is TGF-β, which is detected at high levels during the 24 hours. For the full model underflow, this cytokine has a maximum secretion three hours after LPS supplementation and after that has a downward tendency. The LPS stimulation condition detains the highest values at time point 3 hours. The full model under static also shows a high TGF-β secretion that is maintained constant over time. The LPS supplementation did not lead to higher TGF-β concentrations. The vasculature control also shows high values of this cytokine, the conditions where no LPS was added reached a higher concentration with maximum secretion at 12 hours.

Then, the last metabolite quantified was the LDH, which for the full model underflow, shows one to three times higher than the media over the 24 hours. For the full model but static the LDH oscillates between 2.5 and 3 and 2 to 2.3 for the vasculature only control. The LPS and non LPS conditions have very similar values, except for the full model underflow at time points 3 hours and 12 hours. To conclude figure 7.8 analysis, it was also determined TNF-α concentration from the media, but no traces were detected for all conditions. In addition, as in figure 7.8 the ELISAs were from n=1 underflow or n=2 for static, no statistics were applied.

7.3.3 Stage 3: Fluorescence Staining Test

This section helps to elucidate the antibody crosstalk observed in figure 7.7 between the macrophages and the endothelial cells, where both cells show intensity at 488 and 543 channels. In addition, by increasing the laser intensity of either 488 or 543 nm, both channels were excited. The same was observed in figure 7.9 when dTPH-1 were stained with conditions number 5 replicating the full model stain. The other condition where the dTHP-1 shows a fluorescence signal at both channels is for condition 1. That is CD11b primary with Alexa-555, however, a less intense fluorescence is observed in the 488 nm channel. As expected, conditions 2. to 4. lack fluorescence at 488 and 543, and only Phalloidin and DAPI are present (with DAPI being very faith). The images can be seen in figure 7.9.
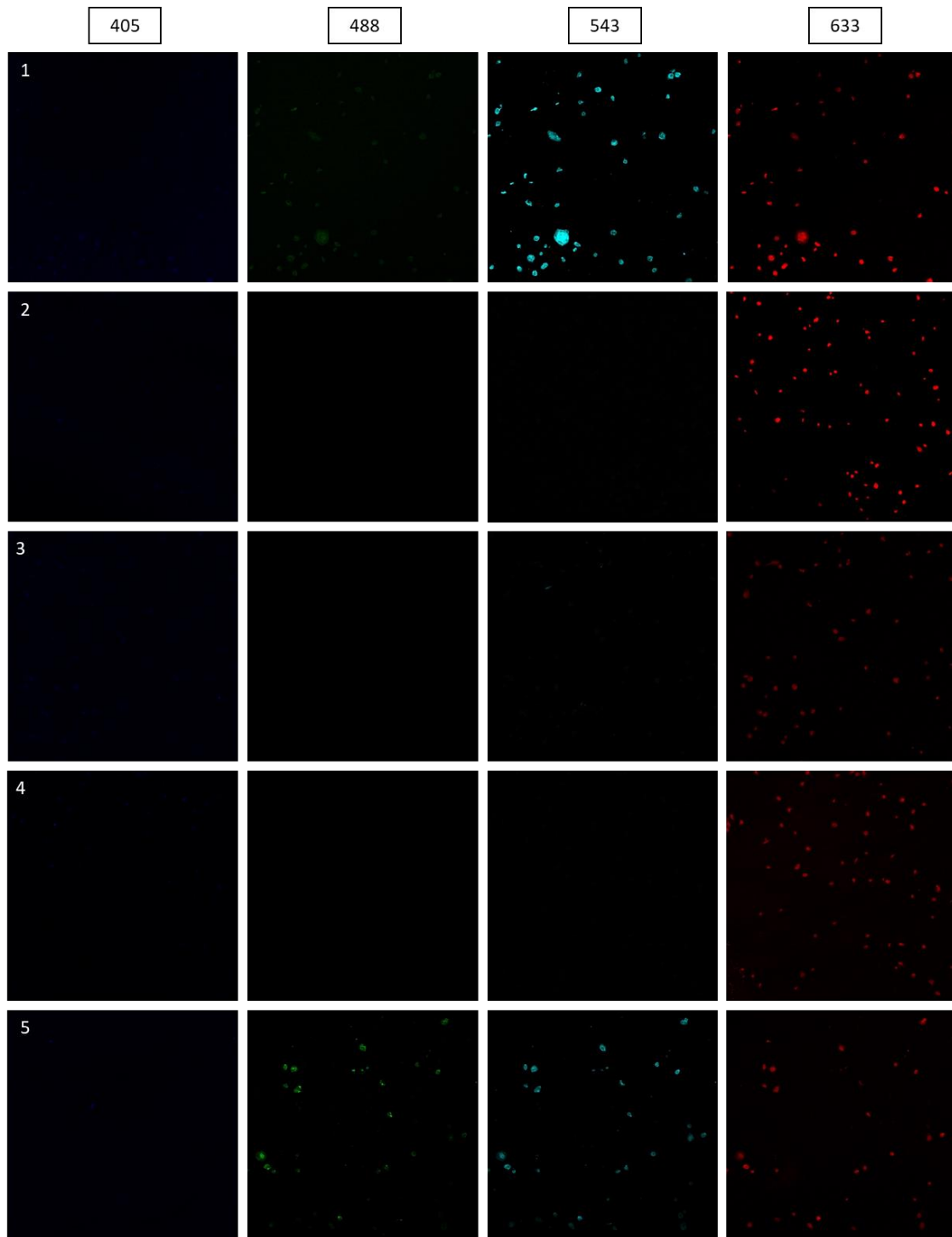
Figure 7.9: Stage 3: fluorescence staining test. dTHP-1 stained with CD11b or CD31 primary antibody and secondary Alexa-488 or Alexa-555. The rows represent conditions number 1. to 5. shown in table 7.2. The columns represent the image from each fluorescence channel. The first column from the left, 405 represents the DAPI stain, which highlights the cell's nucleus. The 488 represents the Alexa-488 channel. The 543 represents the Alexa-555 channel. The 633 represents the Phalloidin stain that highlights the F-actin (n=1).

The chapter 7 aimed to show the data gathered under dynamic conditions using the bioreactor. An overview of the chapter is illustrated in figure 7.1. This data chapter had two main experiments, the first, the vasculature model underflow presented in stage 1 and the second, the full model underflow, in stage 2 of the chapter. The latter had two experimental controls: full model static and vasculature underflow. These experiments helped to validate the bioreactor and determine the next optimization of the cellular model. In addition, there is a third experiment, presented in stage 3, where it was evaluated fluorophore crosstalk and fluorescence channel bleaching. The main conclusions from the chapter are, regarding the vasculature underflow the reduced model viability. If in static from chapter 5 the endothelial cells are viable for 21 days, underflow, the cells only survive for 14 days. In addition, the endothelial cells show a more tip cell morphology and are unable to organize in 3D structures. The full model underflow and static, as well as the vasculature control (experiment from stage 2) show a lack of endothelial cells viability. On the other hand, the full model under flow showed a more confluent A549s monolayer with dTPH-1 on top, which are absent under static conditions. Below can be found a more detailed discussion of stages 1 to 3. The bioreactor's performance is analyzed at the end of the text, in section 7.4.4.

7.4.1 Stage 1: Vasculature Model Under Flow

In this way, starting by evaluating the endothelial and fibroblast cells grown on the bioreactor, some features stand out, such as lack of fibroblast proliferation, morphology switch from the endothelial cells and reduced life span of the model to just 14 days.

If under static conditions the endothelial cells may show a lack of proliferation from the overgrowth of the fibroblasts, underflow, the lack of 3D structure may be from the dynamic environment. Underflow, the cells show on day 14 extensive cytoplasm projections that are associated with tip cell morphology, but then lack stack cells, lumen formation and directionality towards a gradient, which would be necessary to form sprouts.

The tip and stack cells originate from endothelial cells differentiation upon VEGF exposure. Quiescent adjacent cells rely on a delta like-4 transmembrane protein (DLL4) and Notch (DLL4 receptor) signalling balance. When exposed to VEGF, adjacent cells compete for the growth factor. Cells that differentiate into tip cells are able to internalize VEGF and show a high amount of DLL4. Whereas cells that acquired stack cell profile, detain higher Notch and Jagged-1 (transmembrane protein and Notch ligand) that diminishes the activity of Dll4 and VEFG

receptor 3. This downregulates the VEFG receptor making the cells even less susceptible to the VEGF gradient and capable of competing for the tip place[85,248]. Several are the molecules known to promote tip cells, such as semaphorins, netrins and ephrins[248]. Tip cells are also responsible to secrete angiopoietin 2 which is stored in stack cells[81]. In conclusion, the balance between tip and stack cells is done by VEGF and cell-cell contact. So future work should consider higher seeding density of the endothelial cells and also include angiopoietin as a supplement. In addition, a range of flow rates could be experimented with non-angiogenic media, to first understand the impact of the mechanical stimulation alone.

Regarding the fibroblast absence, future work needs to include a higher seeding density of fibroblasts in single culture in the fibrin gel and at different flow rates to understand the effect that the dynamic environment has on cell's viability and proliferation. An alternative, already suggested in the vasculature chapter, is to switch the supporting cells for pericytes. As the last consideration of the results of vasculature underflow, future experiments should include an investigation of what happens to the cells between day 14 to 21, since on static the culture is still showing viable and proliferating cells until day 21.

Regarding the experimental design of the vasculature underflow, under dynamic conditions, the media is 80 times more, which would result in diluting 80 times the cytokines compared with static experiments (present in the vasculature chapter). In addition, from the timepoint sampling, on day 7 there are 3 gels, on day 14, 2 gels and on day 21 only one. This makes the comparison between cytokine secretion underflow and static not straightforward. Comparing figure 5.29 from the vasculature chapter with figure 7.6, IL6 have the same tendency over de 21 days but the concentration is around 10 times more for underflow, indicating more secreting on this cytokine when the vasculature is exposed to dynamic movement. Regarding the IL8, the range of concentrations is the same for both experiments, which also indicates that underflow the cells secrete more IL8.

Another cytokine quantified underflow but not in static was the TGF-β, which plays a role in angiogenesis by stimulating smooth muscle cells (SMC) differentiation and regulating the crosstalk between SMC and endothelial cells[249,250]. The TGF-β is also associated with endothelial cell proliferation and extracellular matrix turnover[251]. The vasculature model underflow shows high levels of this cytokine, however, since it was not quantified on static there is a lack of comparison. Future work should include the measurement of TGF-β in static.

The next metabolite quantified was the lactate dehydrogenase (LDH) which indicates cell membrane integrity. In the vasculature model, the cells presented 1.5 to 2 times more LDH in

the media than in the control. The lack of measurement of this enzyme on static does not allow to conclude if the dynamic movement interferes with cell's viability. However, days 14 and 21 have similar LDH ratios, but from the images, on day 21 the cells are dead, which would be expected to increase the LDH value. Future work should include the measurement of LDH in static and simple 2D cultures to understand LDH baseline levels from the endothelial and fibroblast cells.

.

Conclusion	
From the chapter	▪ Underflow the ECs show tip cell morphology, lack cord formation capacity and are only viable for 14 days ▪ Fibroblasts do not proliferate underflow ▪ Higher IL6 and IL8 secretion underflow
Overall Project	▪ Full model constructed on a 14 days period.

7.4.2 Stage 2: Full Model Static and Under Flow

Moving on to the full model discussion, first some consideration about the experimental design. The model was created for 14 days, which from the vasculature experiment was how long the endothelial cells were viable. If future work increases vasculature model viability, the full model can be easily adjusted, since dTHP-1 were seeded two days before end point and A549 six days before. In addition, work done previously in the group established the A549 and dTHP-1 co-culture in transwell at air liquid interface. The same steps were followed to build the co-culture in the full model, the A549s were cultured for four days under submerged, before seeding PMA differentiated dTHP-1. Then, after two hours both cells were brought to ALI. Regarding the cell seeding density, some adjustments were made compared to the single culture presented in the alveolar chapter. The initial seeding density of the single culture of A549s on dECM/fibrin gel was 2.79×10^5 cells/cm^2, which for seeding on the fibrin gel holder for the bioreactor experiments with 0.5 cm^2 would be seeded 139500 cells, but instead were seeded 10% (152900 cells) more cells that lead to a confluent monolayer of A549s on day 14 of the model.

Regarding the macrophages, 10% of the alveolar area is occupied by those cells[3]. For the full model, on day 12 were seeded 7500 dTHP-1 per fibrin gel. On day 14, were determined 2063.23

± 1275.5 cells per fibrin gel using the confocal images. This data indicates that 72% of the cells die after 2 days under ALI. Together with the cell number, was determined using imageJ, the cell area, which was 212.12 ± 102.56 μm^2. This indicates that only 0.86% of the fibrin gel area is occupied by macrophages. To make the model resemble *in vivo* cell ratios, the dTHP-1 needs to be approximately 10 times more on day 14. If when seeding 7500 dTHP-1 only 2063 cells are present on the second day, the next optimization step of the model should seed 75 000 dTHP-1.

Regarding the media sampling, since there was only one time point, day 14 had per condition three fibrin gel holders. The problem seen on vasculature that every week one less fibrin gel was present, did not occur in the full model experiment. However, despite that, the three models share the same media, which makes n=3 for fluorescence images but n=1 for cytokines. This indicates that future work needs to have one biological repeat per bioreactor and time point.

Moving forward to discuss the results from the full model experiment, one feature that stands out from the images is the lack of vasculature development as observed before. This observation is shared with the vasculature only control, indicating that the polymerization of a second material on top of the fibrin (the dECM/fibrin) did not interfere with the endothelial and fibroblast proliferation and viability. This may be the result of an experimental change that due to time constraints was done. Both cell types were trypsinized twice in 24 hours, which may have compromised their viability. Regarding the A549s the cells show a confluent monolayer after the seeding density adjustment. The presence of a complete A549s coverage is necessary to mimic the complete epithelial coverage *in vivo*. The dTPH-1, despite being in lower numbers as mentioned before, were found on top of the A549. However, due to antibody unexpected crosstalk, the presence of these cells was able to be narrowed down from their position and morphology but not from their specific CD11b staining.

The bioreactor allowed cytokine monitoring over 24 hours, however, the lack of repeats does not allow to make a conclusion from normal and LPS stimulated bioreactors. The high variability seen on time point zero between LPS and non LPS (except for LDH), supports that fact as well. This reinforces what was mentioned before, that future work needs to have one biological repeat (with 3 technical repeats) and time point per bioreactor.

7.4.3 Stage 3: Fluorescence Staining Test

The images from figure 7.9 show what was expected, no fluorescence at 488 and 543 channel from conditions 2. The condition 2 is the combination of CD11b with Alexa-488, which shows secondary antibody species specificity. Conditions 3. and 4. show that dTHP-1 do not express

CD31 surface marker and in this way could not be the cause for signal crosstalk. This indicates that condition 5. shows fluorescence at 488 nm due to fluorescence bleaching.

7.4.4 Bioreactors Performance

The final considerations are relative to the bioreactor's performance, the features that were an advantage and the parts that would need to be improved. Starting with the positive features, those are the transparency, which allowed without disturbing the flow assess media level and bubbles formation. In addition, the bioreactor proved to be easy to assemble at the start of each experiment, or during media change and sampling collection. Where was only necessary to unscrew the lid by hand. All of this, while maintaining the bioreactor's sterility and free of leakage. In addition, the way the fibrin gel holder was fixed, combined with biomaterials integrity over time, allow air liquid interface to be maintained over the two days under constant flow. This is an advantage over Transwells, where media passes the porous and fills in the apical side over time.

Despite the overall bioreactor's performance, some features could be improved. The introduction of a media reservoir was not possible without breaking the continuous flow. This made evaporation a problem, where 1-2 mL needed to be introduced every 2 days. The geometry of the inside channel could be improved to a rectangular shape instead of circular which would reduce pressure drop, increase shear stress and make the fluid circulate at higher velocities. This could help fix the problem of the media reservoir absence. Finally, the PDMS could be produced using other fabrication methods, such as stereography, instead of mould casting, which would decrease the workload and could increase consistency.

Conclusion (From 7.4.2 and 7.4.3)		
From the chapter	Alveolar Model	▪ A549 show confluent monolayer ▪ dTHP-1 found on top of the A549
	Vasculature Model	▪ Vasculature did not develop as observed before
	Bioreactor	▪ Ability to maintain sterility for 14 days ▪ Ability to maintain ALI under constant flow ▪ Easy handling of the gel holder.

Chapter 8

General Discussion

The objective of this final chapter, the general discussion, is to provide an overview of the main problems encountered and define some of the solutions or experiments to have in consideration to drive the model further. Also to compare the *in vitro* model designed with the current literature. Figure 8.1 shows an improved version of figure 1.9 representing the final parts and full model overview. From sections 8.1 to 8.4, can be found a discussion from parts 1 to 3 and the full model, as shown in figure 8.1. At the end of the text, a final image resuming the thesis outcome is presented (figure 8.2) as well as a final table with future work perspectives (table 8.1).
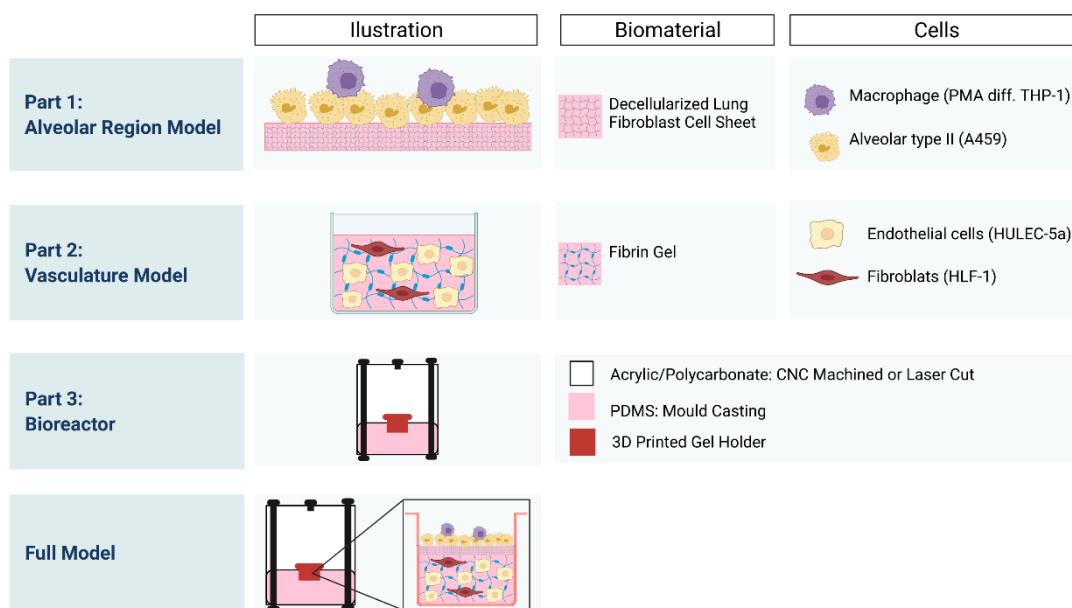
Figure 8.1: Overview of each part of the project and full model.

8.1 Part 1: Alveolar Region Model

Despite the limitations encountered during the biomaterial synthesis to support the alveolar cell model, the strategy to use a cell line (*i.e.* the human lung fibroblasts) to produce the molecules of interest and subsequently derive a biomaterial from collagen crosslink is still relevant. Especially, when compared to using decellularized animal derived lungs as the collagen source for the biomaterial. The primary objective of *in vitro* models is to reduce animal experimentation and consequently animal derived products. Several ECM derived biomaterials are already commercially available, but all of them are derived from animal organs, which rules them out as the alveolar biomaterial[252]. In this way, the project focus on deriving its own cell sheet ECM. The cell derived ECM (CDE) technology has gained increased attention in recent years for being a

pathogen free and less variable source of ECM when compared to both human and animal tissue[117,118]. Although, require long cell culture times, where often the cell sheet detaches from the sides of the flask, have weak mechanical properties and sterilization and storage could be challenging[117,118]. But these limitations are considered to be outweighed by the advantages of having an animal free ECM source[117,118]. The most used strategy when using CDE technology is to grow the cells with the interested secretome in a substrate, which after decellularization is further reseeded with cells[117,118]. This rationale was only found once in the literature for a lung application, when primary human trachea fibroblasts were cultured on sacrificial polyurethane foams for 3 weeks, where afterwards decellularized (0.1% SDS, DNAse and RNAse) and the sacrificial layer removed with a water miscible solvent. The ECM derived scaffold was then reseeded with the same cells[253]. A more frequent application of CDE is in bone grafts, where rat calvaria osteoblasts were grown on hyaluronic acid microparticles under ascorbic acid for 21 days on 24 well plates, after being decellularized (with Triton) followed by implantation on rats calvaria bone[254]. Or bone marrow derived MSC seeded on polyesterurethane (PEU) foams for 24 days, which after decellularization scaffolds were reseeded with the MSC [255]. Regarding wound healing has been documented human primary skin fibroblasts grown on bovine collagen sponges (diameter, 15 mm; thickness, 2.0 mm) for 30 days, which after decellularization (with a glycerol gradient) were implanted in a mouse[256]. For the same application, the cell derived ECM combined adipose derived MSC seeded on electrospun nanofibrous silk[257] or PLGA nanofibrous scaffold[258]. This technology has also been used for vessel formation, using decellularized fibrin gel[259], but also porcine smooth muscle cells grown on PGA mesh[260], or saphenous vein fibroblasts grown on normal flasks for 21 days, decellularized (distilled water overnight at 4°C) and reseeded with smooth muscle cells. The construct was further wrapped around a cylindrical mould with 4.5mm in diameter to produce a tubular structure[261]. To finalize the cell derived ECM examples some papers used a 3D printer to create the substrate where cells are going to be attached, such as PLC/PLGA lab made blend seeded with mesenchymal stromal cells [262] or PCL seeded with fibroblast[263].

In the case of this project the cell derived ECM technology was tested when the dECM scaffold was seeded with the dTHP-1 and hAELVi cells in section 4.3.2. Although not working, that strategy was not the main focus of the thesis. That was to digest the dECM and polymerize it again as is frequently done in organ derived ECM for scaffold[107,108] or bioink formation[114,264]. This is where the novelty of the alveolar biomaterial lays, use cell derived ECM technology to create the ECM. But then, further processed the ECM to crosslink the collagen to create a hydrogel. This contrasts with CDE where the remaining ECM after decellularization is used as substrate.

The advantage of the hydrogel derived ECM is that can be polymerized with the volume/geometry required and not being restricted by the substrate where the cells initially grow. Can also be polymerized at different concentrations. However, the strategy described did not work since the pepsin digested dECM did not crosslink.

.

Next in the section can be found, as already mentioned in chapter 3, the problems encountered during alveolar biomaterial formation and possible solutions. In this chapter, two problems were encountered. The first regards the limitations on the quantification methods chosen for DNA, protein and GAGs that prevented rigorous dECM characterization. In addition, the contradiction between the qualitative and the quantitative characterization of dECM, especially with DNA. The latter, is an important factor for considering the cell sheet decellularized, as established in the literature a maximum of 50 ng dsDNA/mg dry weight[119]. These limitations are likely to be attributed to SDS content, so a monitorization of the surfactant content should be implemented in the decellularization method (using methylene blue assay). As an alternative, Triton treatment alone associated with a DNAse or RNAse to assist in nucleotide fragmentation could pose a solution. From the fluorescence and bright field images (figure 3.1) Triton treatments alone are efficient to remove the DNA, if the number of Triton treatments increases from three times to five may help reduce the DNA without affecting as much the extracellular matrix compared to SDS treatments. Iadditionon, several papers use DNAse or RNAse as the last step in decellularization to promote genetic material fragmentation with significant reductions in DNA[265,266]. This could contribute to reducing DNA content for below 50 ng dsDNA/dry weight to consider the ECM decellularized.

The second problem experienced regards the lack of collagen. This prevented dECM to crosslink upon temperature adjustment to 37 ° or with riboflavin. The human lung fibroblast was cultured under DMEM media with low glucose as recommended by the supplier, with an extra supplementation of 500 µM ascorbic acid to promote collagen synthesis. However, in future is essential to screen for conditions where the lung fibroblasts are more active towards collagen synthesis. With the advantage of knowing the minimum collagen target concentration. The sample with 20% gelatin was able to crosslink with riboflavin. This condition showed approximately 100 times more collagen than 24 hours pepsin digested dECM. So, the future cell culture and decellularization condition should ensure an increase of collagen corresponding to 1400 µg collagen/mg dry weight (100 times the value of collagen content determined for condition 10 in figure 3.14C)). To accelerate the screening process, the HLF-1 cells could be

evaluated after 7 days of culture at the DNA level for genes associated with collagen production. The boost of collagen should include high glutamine, glucose and galactose media and higher ascorbic acid supplementation. Preliminary work done on this area show ten times increase in ascorbic acid supplementation is not cytotoxic and leads to an increase in the order of four times of dry dECM weight (results in appendix 22). In addition, should be considered proline supplementation, as shown in the literature its effect on promoting collagen secretion[157,158] (as already mentioned in the discussion of chapter 3).

The lack of crosslink shifted the strategy initially designed for the alveolar biomaterial. Since the dECM did not polymerize with the change of temperature or by adding a crosslinking reagent, such as the riboflavin. There was a need to find a biomaterial that when polymerized could incorporate the neutralized dECM. The use of fibrin gel in the vasculature model made it compelling to use it in the alveolar. Despite fibrin not being anatomically relevant to the alveolar epithelial cells, in the proposed *in vitro* model, they would be in close contact anyway, since is used fibrin to grow the endothelial cells. In this way, was derived the dECM/fibrin gel for the alveolar biomaterial.

In future the alveolar biomaterial should aim to have the dECM product polymerized without external crosslinkers, to avoid adding more chemicals that can interfere with cell fate. But if not possible, another way to bring value to the dECM product is to combine it with agents that would allow electrospinning or melt electrowriting[267–269]. In this way, the cells would have the advantage of not only to attach into a chemical relevant material, but also to a porous membrane with fibres.

In addition, another feature to have in consideration when in future optimize the dECM product is to be able to bring 3D geometry to the gel. The alveolus is characterized by a curvature that recent work has looked at its effect in deriving cell cycle and the cytoskeleton[270]. The work of Batista, D et al (2020) showed Calu-3 (bronchial cell line), A549 and HPAEC cells (human primary alveolar epithelial cell line) in curved membranes with a diameter in the order of 120 µm. The cells cultured in the curved substrate showed different cross-sectional morphology, proliferation and apoptosis rate, but similar barrier function as when compared to flat growing cells[271]. Applying a pattern on the dECM gel surface of a spherical cavity similar to what was achieved in the work of Nawroth, Janne *et al* (2017)[272] using gelatin as substrate, could be a simple method of introducing real 3D to the alveolar model. The 3D printer used on the project has the possibility to change to a laser head, the same head used for riboflavin crosslink, so the first strategy would be to test if that laser is able to create a pattern on gel surface.

The biomaterials produced in chapter 3, dECM scaffold and dECM/fibrin were tested in chapter 4 to understand their capacity in supporting cell growth and proliferation. The dECM scaffold showed insufficient ability to support the cells so efforts focused on the second biomaterial, the dECM/fibrin gel. This was able to only support dTHP-1 and A459s, leaving the fibroblast, the H441 and hAELVi out of the alveolar model. This reduced the alveolar model to alveolar type II and immune cells representation. In future work, an important point to address is to introduce the hAELVi or H441 cells, to include in the model alveolar type I representation. As already mentioned in section 1.1.1.3 from the general introduction, the alveolar type I contacts directly with the endothelial cells for gas transfer. To mimic this cell-cell interaction and in this way have the most important function of the alveoli represented, is crucial to have type I epithelium cell representation, such as with the hAELVi (or H441).

Noteworthy examples in the literature that combine a heterogeneous cell population when modelling the alveolar region is for example the work of Klein, S *et al* (2013) that seeded on a transwell four cell lines. At this moment, no other work combined such a number of cells: A549, HMC-1 (mast cell line), EA.hy 926 (endothelial cell line on the basolateral side) and PMA differentiated THP-1[64]. However, in the present work, there was a priority on creating a biomaterial that could better support the alveolar model. Two examples where a biomaterial was also formulated to support the model is present on the work of Nishiguchi, A *et al* (2017) that seeded HUVEC, H441 and HPMEC (human pulmonary microvascular endothelial cells) on an electrospinning scaffold[69] . And CCL-210 (lung fibroblasts), A549 and primary alveolar type II on PEG spheres[71]. But the examples above were still under static conditions, contrary to the work of Sundarakrishnan, A. *et al* (2019) that joined primary pulmonary fibroblasts, A549 and HMEC-1 (endothelial cell line) on a silk collagen type I biomaterial and in a custom made bioreactor to introduce media flow[79]. But this model is still under submerged conditions. A feature that was also a priority when seeding the cells on the dECM/fibrin gel. The 3D printed gel holder needed to support air liquid interface, to test the model under such conditions. One final remark is that the presence of endothelial cells in the examples above allows endothelium representation and in this way cell-cell direct interaction with the epithelium cells present in the model. But lack fully developed vasculature (ECs in cord formation), a feature that was not found in any alveolar model and was tried to be included in the present model.

8.2 Part 2: Vasculature Model

The vasculature model was designed to have a co-culture of endothelial and fibroblast cells in fibrin gel. After narrowing down the fibrinogen and thrombin concentration from experiments 1 to 4 (sections 5.3.3.3 to 5.3.3.6), the work moved toward finding the best conditions for culturing both cell types together within this microenvironment.

The strategy of 50+50 µL gel aimed to promote cell migration within the gel and in this way encourage sprouting. However, the cells were not able to migrate as predicted and the fibroblast showed a high catalytic effect against the fibrin gel. The aprotinin supplementation fixed that problem, but further work should find the minimum concentration of this supplement. The angiogenesis needs matrix degradation and aprotinin prevents it, so having a negative impact on the endothelial cells sprouting (as mentioned before in the discussion of chapter 5). This may explain the unexpected high proliferation of the fibroblast and consequently lack of endothelial cells organization when co-culturing both cells under static conditions. The cells were seeded on the 1:100 ratio between fibroblast to endothelial cells, which is 1% fibroblast, much lower than the 26% pericytes that are covering the alveoli capillary[205]. Despite that, was decided to integrate the exact model in the bioreactor to understand first the impact of flow in the cells before doing any iterations in the model.

As addressed in the chapter 7 discussion section, the vasculature model underflow showed cells with morphology similar to tip cells, but lacked stalk cells and cord formation. Several solutions to the problem were already mentioned, such as increasing endothelial cell number and supplementing the culture with angiopoietin. For tip and stack cells differentiation needs to exist VEGF and cell-cell contact. In addiction, there is constant competition for tip cell profile that maintains both profiles of tip and stack cells[248]. Looking into the literature on vasculature models similar to the one deployed in the thesis where endothelial cells were seeded inside fibrin gel, the cell density of 80 000 HUVEC cells/mL[90] was recorded, but also 2.6 million HUVEC cells/mL of gel[92]. In a study where it was used a GAGs-based hydrogel as a scaffold, was used a seeding density of 6 million HUVECs cells/mL[91] and a comparison between fibrin and collagen plus agarose mesh used a range of HUVEC cells from 1.5-3 million cells/mL[273]. The endothelial cell density used in the vasculature model was 250 000 cells/mL, which is lower than the majority of examples shown. The low confluency may be affecting the model outcome, which is easily solved by testing higher seeding densities underflow. But from the examples shown above, is also noticed that all models used HUVECs. In fact, was not find any vasculature model in the literature where HUVECs or primary endothelial cells were not used. The HULEC cell line was selected for its anatomical relevance, but maybe is not capable of angiogenesis. So a different

cell line needs to be considered in future model improvements, one such possibility could be endothelial cell derived from iPSC[274] that have shown similar sprouting as HUVECs when cultured in fibrin and collagen gel[275].

8.3 Part 3: Bioreactor Development and Simulation

The bioreactor designed in this project was tailor made for the *in vitro* model created and with the end application in mind, which is to support the toxicology assessment of inhaled particles. In this way, the comparison with other bioreactors in the literature or already commercially available is not straightforward. However, compared with rotary bioreactors where the cells are cyclic exposed to air or media[218], the bioreactor designed for the project allows constructs to be always at air liquid interface, imitating normal *in vivo* conditions. Regarding the commercially available system from Kirkstall, the designs of both bioreactors are similar. From the commercially available bioreactor, the media flows underneath the Transwell membrane where endothelial cells can be seeded and on the apical side of the membrane cells can be exposed to air or media. Inserts also allow coating or biomaterial polymerization, so a similar alveolar model as the one presented in this thesis could be constructed in the insert as well. The features that set both bioreactors apart are the fact the one presented in this thesis allows three repeats per bioreactor and does not rely on consumables like Transwells. But was designed with dimensions compatible with a 24 well insert, for comparative reasons the PDMS disk fits the 3D printed gels holders or a 24 insert. An advantage shared by both bioreactors is the portability of the cellular model as a consequence of using an insert or a 3D printed part (inspired on an insert as well) as support to build it. This makes it compatible with current exposure systems that were designed to fit Transwells from different sizes, such as the ones from Vitrocell Systems. The fact that the bioreactor was designed to fit a 24 well insert, also allows for future comparison of the developed alveolar *in vitro* model with commercially available models from MatTek (epiAirway™ or EpiAlveolar™) and Epithelix (MucilAir™ and SmallAir™).

Regarding the exposures systems, as mentioned the 3D printed gel holder allows the cellular model to be transported and, in this way, placed in the vitrocell systems, but nebulization of compounds is also possible with the Aeroneb® Labnebulizer (Aerogen®, Galway, Ireland) where the device can attach to the bioreactor. This would require the alteration of the bioreactor lid opening, to be able to fix the device but would give versatility in future to the model. The integration of such a nebulization system is exemplified by the work of Carius, P *et al* (2021)[276] which developed the PerfuPul platform that consists of two chambers separated by a porous membrane and mounted on a glass coverslip.

A fundamental aspect to reproduce the alveolar environment is the constant moving of the alveolar sacs accompanying the inhale and exhale of air. To try to mimic this scenario, plans to include dynamic air were made, but due to time restrictions were never implemented. The introduction of air would impose a displacement on the flexible PDMS. But the assessment of the pressure that the air needed to be pumped in to impose such deformation on the PDMS or the biomaterials used was not addressed. Also, the effect that such pressure can have on the cells.

In future, the positive air pressure, should apply a 5-12% strain (at every 5 seconds)[235] of the substrate where the cells are attached to guarantee physiological stretching conditions. This should also make sure to not have a negative impact on cell viability. However, in case of cells not being able to withstand positive pressure an alternative is to apply negative pressure. Looking at the lungs, the air flows in by the contraction of the diaphragm, which subsequently creates a negative pressure inside the lung and makes air flow in[2]. A couple of organs on a chips devices use a negative vacuum to create a substrate displacement[277,278], and in this way, mimic diaphragm function. On a more macro scale, a similar design was achieved in the [AX]Lung-on-Chip System commercialised by the Alveolix, where a transformed 96 well plate with an ultrathin porous membrane at the bottom deflects by applying negative pressure underneath[279]. To mimic the effect of the diaphragm an extra channel could be added underneath the channel where media flows and vacuum applied. An alternative bioreactor that does not rely on a pneumatic apparatus to impose deformation is advanced by Costa, A *et al* (2020) where a membrane is deformed by electric force[280]. Another example of a bioreactor that integrated a porous and flexible membrane is present in the work of Cei, D *et al* (2020)[281]. This bioreactor, named MALI, contains two chambers separated by a flexible membrane and allows fluid flow to circulate in the basolateral chamber and positive air to be introduced in the apical compartment (making the membrane move). The bioreactor has also integrated an aerosol deposition system to study the effects of aerosol on alveolar cells cultured at ALI and in a biodynamic environment.

MALI bioreactor is the only system at the moment that comprises in a single platform ALI, flow and a stretching substrate together with an integrated exposure system. This is an advantage over using commercially available exposure systems, such as the Vitrocell, Cultrex RFS and PreciseInhale where mechanical stretching is not present.

In conclusion, despite the cellular model presented here still requiring extra work on the biomaterial and at the cellular level, the bioreactor iterations need to follow side by side. Since

there is no point in creating an alveolar cellular model that cannot be mechanically stimulated or tested for toxicology studies.

8.4 Full Model

The full model was considered a pilot chapter, the restricted time to complete the project prevented iterations and repetitions. The model presented in this thesis was designed from zero and most of the laboratory work, approximately 80%, was dedicated to developing the main three parts of the project. The alveolar, vasculature and bioreactor were developed in parallel throughout the course of this PhD. This, in addition to the pandemic of Covid-19 that prevented lab work, delayed consumables, and normal equipment access, significantly impacted the project, particularly the full model assembly. Though, despite the time limit and laboratory constraints incurred due to the pandemic, it was considered essential for the production of the model that focus was given to the assembly of its three component parts, and thus presented within chapter 7. This chapter showed preliminary results on the vasculature (already discussed in section 8.2) and the full model underflow. Regarding the full model, the vasculature side of the model did not behave as previously observed, so comparison with other alveolar models in the literature is not straightforward. For a final overview of each chapter's main results, refer to figure 8.2.
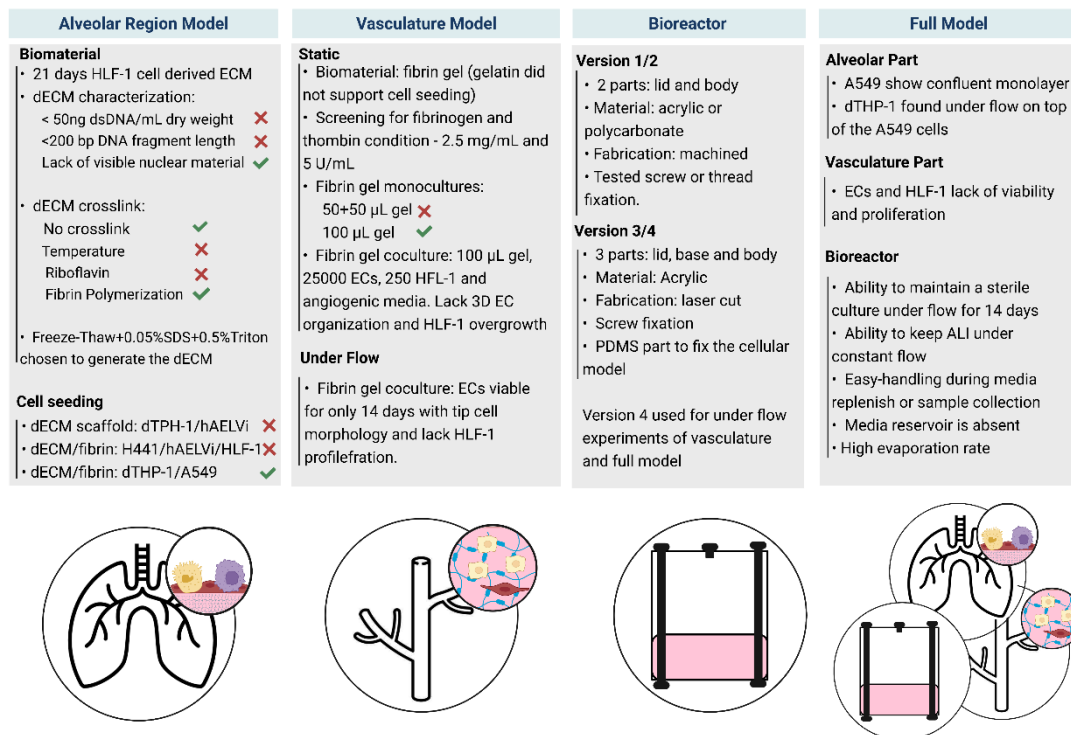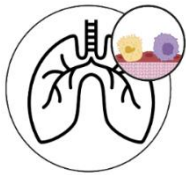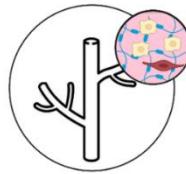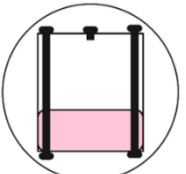

Figure 8.2: Overall of the main results obtained in each part.

Despite not showing a fully functioning model, the thesis includes preliminary data in all three parts of the project and even a pilot chapter where the full model is assembled. The full model aimed to combine four cell lines, in two different biomaterials, underflow and at air liquid interface, and in this way fulfil a bigger view of combining in a single model a bioengineering strategy with a multicellular approach. Models that were considered for combining a multicellular approach were already mentioned in section 8.1. On the other way, models that main objective was to recreate the bioengineering or structural side of the lung can be found on the acellular bioprinted alveolar sac created by Grigoryan, B. *et al* (2019) [46] or in the acellular organ on a chip with 5 generations of branching created by the group of Josue Sznitman [75,76,77]. However, the most validated platform for airways modelling is the lung on a chip developed by Dan Huh and Wyss Institute[45]. Which lays on assumption that mechanical forces govern cell and tissue development,[282] which future strategies to improve this model needs to lay in as well to create a more macroscopic model of the alveolar region. This is without neglecting the importance of a heterogeneous cell population with representation from epithelium, endothelium and immune system. To improve the proposed *in vitro* model and in this way fulfil this bigger view on integrating a heterogeneous cell population under a dynamic environment table 8.1 includes future work perspectives.

Table 8.1: Future work.

Future Work		
Part 1: Alveolar Model 	Biomaterial	▪ Improve collagen biosynthesis from HLF-1 – add higher concentration of ascorbic acid and introduce an extra proline supplement. ▪ Improve decellularization: apply suggestions summarized in the table from section 3.4.2 ▪ Characterize with mass spectrum the HLF-1 secretome ▪ Experiment with electrospinning to create a biomaterial that contains biomolecules but also a fibre organization. ▪ Experiment with laser photopatterning to add curvature to the dECM gel.
	Cells	▪ Section dependent on the material outcome but efforts on having alveolar type I, II and immune cells should be done ▪ Investigate surfactant presence.
Part 2: Vasculature Model 	Cells and Supplements	**Under Flow** ▪ Experiment with angiogenic supplements in reducing aprotinin and adjusting the concentration of the others to guide angiogenesis (Specially PMA). ▪ Consider adding angiopoietin to direct stack cells profile. ▪ Consider increasing ECs seeding density ▪ Consider a different endothelial cell line as iPSC derived ECs ▪ Investigate the reduced life span of the vasculature model underflow. Image days between 14 to 21.
Part 3: Bioreactor 		▪ Improve PDMS disk geometry to reduce pressure drop and increase shear stress ▪ Experiment with other types of fabrication methods such as stereolithography as alternatives to PDMS mould casting ▪ Add media reservoir to facilitate media collection/change ▪ Include the dynamic air setup.
Full Model 		▪ Proteome characterization ▪ Epithelium – endothelium contact characterization ▪ Particle tracking with beads with known dimensions
Future Application		▪ After model validation the aim is to use it for inhaled particles toxicological screening

Chapter 9

Appendices
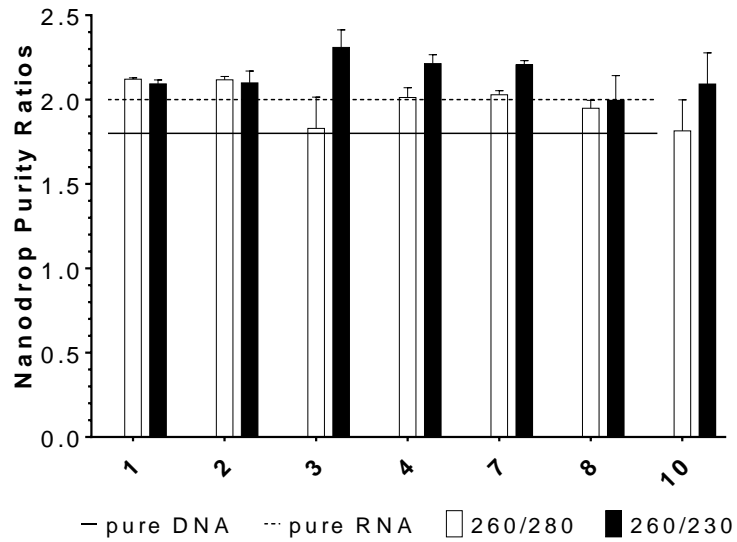
Appendix 1: Nanodrop 260/280 and 260/230 rations for the decellularized conditions. The pure DNA line at 1.8 (-), highlights the value that the 260/280 ratio should have to show pure DNA. The pure RNA line at 2.0 (- -), shows the value that the 260/230 ratio has in presence of pure RNA.
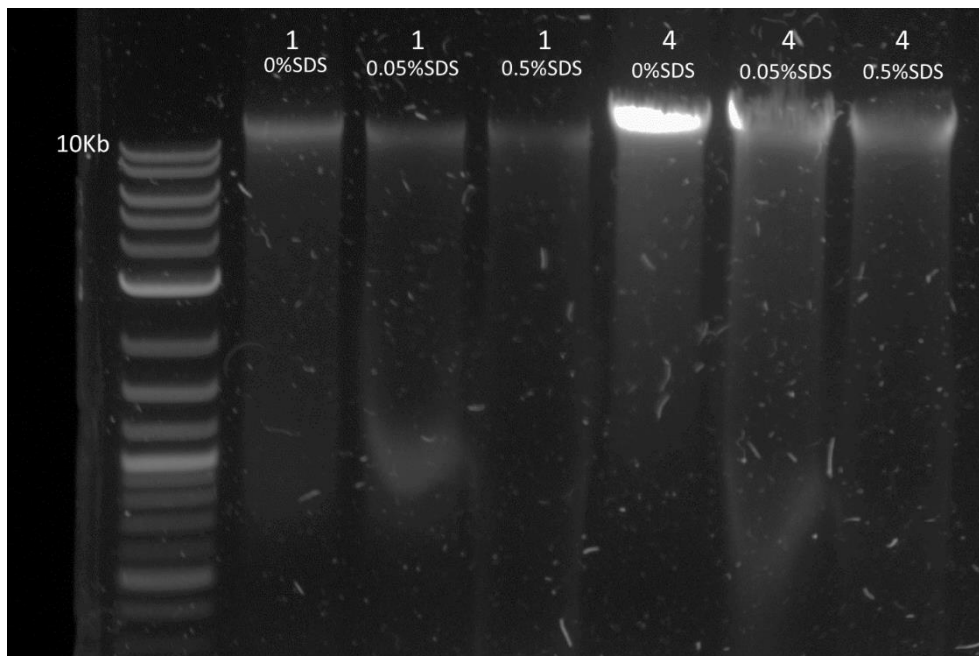
Appendix 2: SDS effect on band intensity on condition 1 and 4 of decellularization. (n=1)

Condition	1	2	3	4	5	6	7	8	9	10
ng/ul	131.1	208.7	42.9	56.4	84.4	90.6	82.8	91.0	70.0	39.8
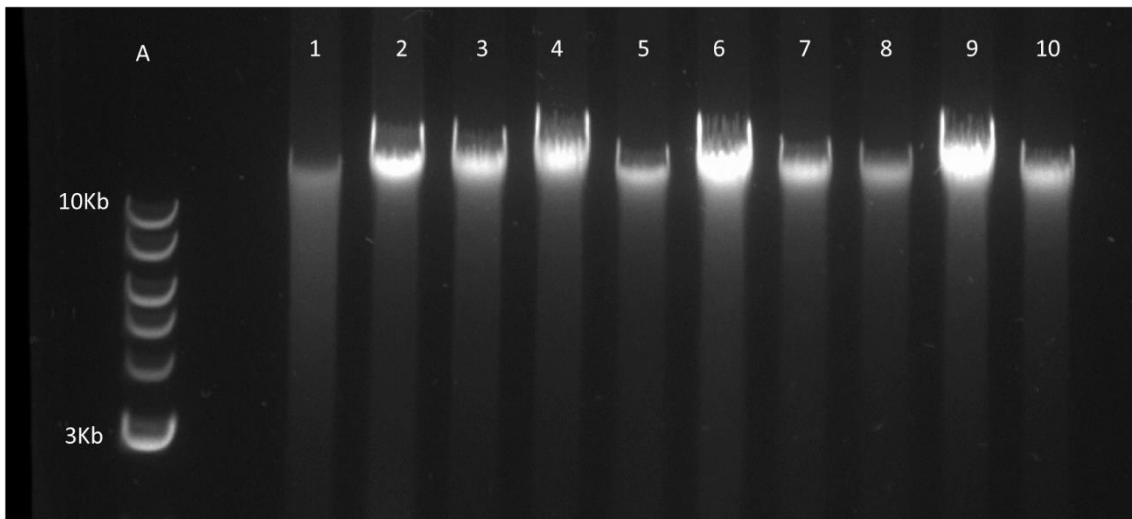
Appendix 3: Top table indicates the concentration of DNA in ng/µl of condition 1-10 of decellularization. Bottom gel shows the band intensity after sybr safe staining of conditions 1-10. (n=3)
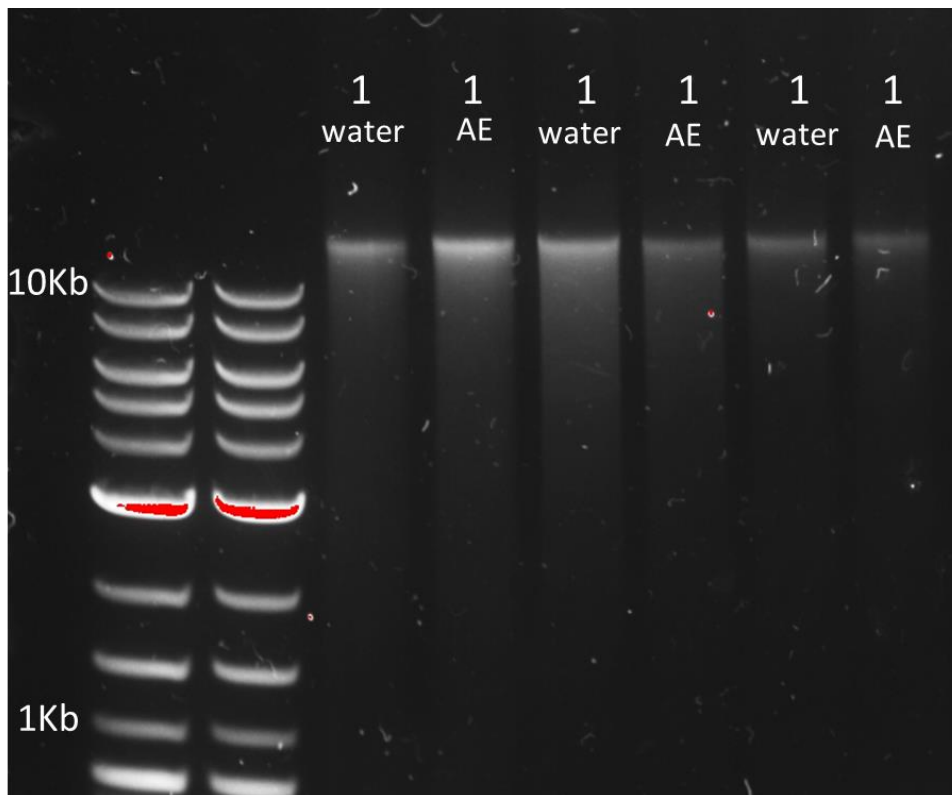
Appendix 4: Effect of water or AE buffer dilution of samples from condition 1 (fresh). (n=3)
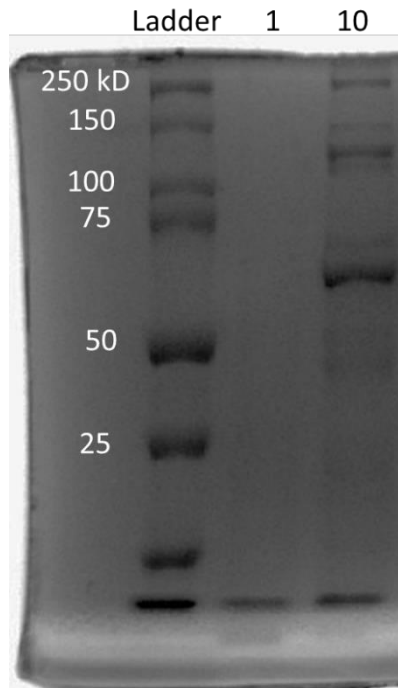
Appendix 5: SDS PAGE gel of pepsin digested condition 1 (Fresh) and 10 (Freeze – Thaw + 0.05%SDS + Triton 0.5% 3x) from decellularization protocols.

100ng dsDNA	Documented		Expected	
SDS	0.01%	1% decrease	0.05% 0.5 %	5% decrease 50% decrease
Triton	0.1%	7% increase	0.05% 0.5 %	3.5% increase 35% increase
Sodium Chloride	200 mM	30% decrease	1M 155.1 mM	150% decrease 23% decrease

Appendix 6: Effect on the signal intensity of the Picogreen assay from compounds that are used in the decellularization or in the papain digestion when used 100 ng of dsDNA. Values from the picogreen manual instructions.

dsDNA (ng)	100	10	1	0.1
Papain	17% decrease	14% decrease	10% increase	11% increase
0.05% SDS	71% decrease	64% decrease	62% decrease	47% decrease
0.5% SDS	100% decrease	101% decrease	102% decrease	114% decrease
0.05% Triton	5% increase	10% increase	10% increase	8% increase
0.5% Triton	4% decrease	11% increase	24% increase	12% increase
0.05 + 0.05	73% decrease	79% decrease	88% decrease	93% decrease
0.05 +0.5	27% decrease	28% decrease	50% decrease	84% decrease

Appendix 7: Influence of SDS and Triton on DNA quantification with TE buffer as the control. The rows correspond to the fluorescence signal for each chemical tested divided by the fluorescence signal of papain. The columns corresponds to 100,10,1 and 0.1 ng of DNA for the different chemical analyses, 0.05% SDS, 0.5% SDS, 0.05% triton, 0.5% triton, 1:1 ration of 0.05% SDS and 0.05% triton and 1:1 ration of 0.05% SDS and 0.5% triton (n=3 to 7).
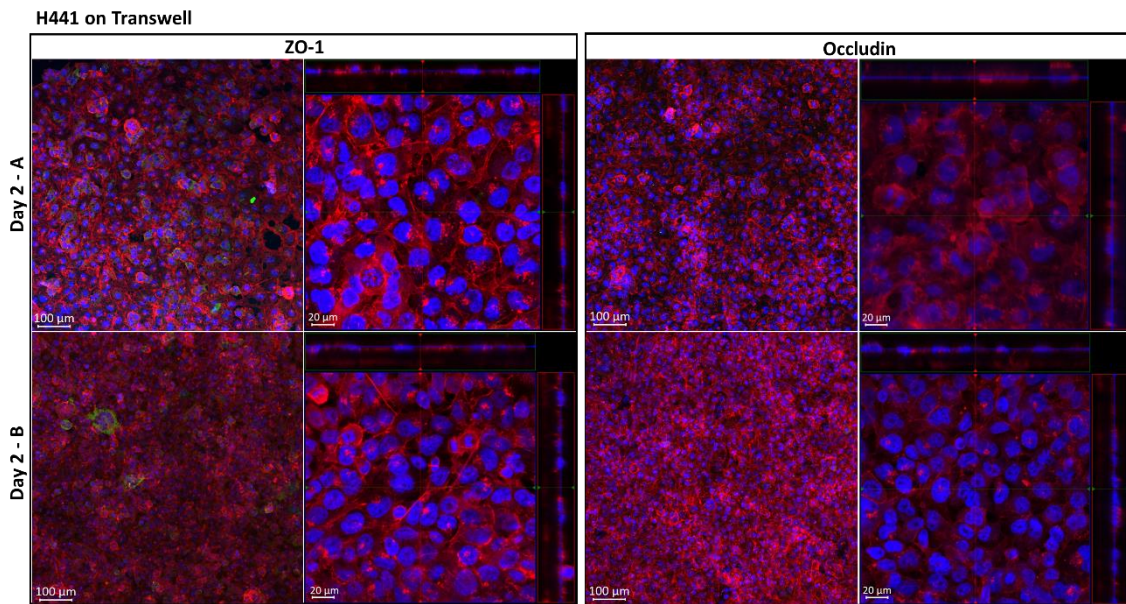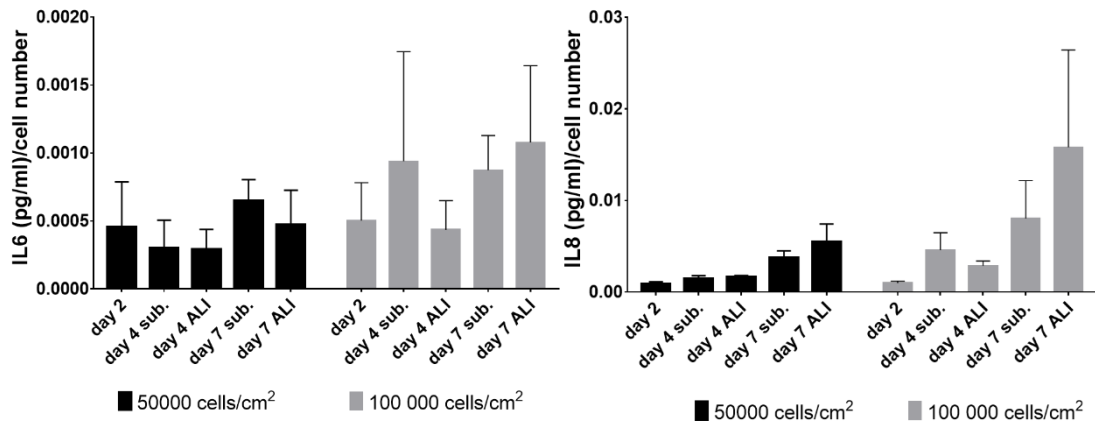
Appendix 8: The graphs of top show the IL6 and IL8 secretion of H441 on day 2 (submerged), day 4 and 7 under submerged or at air-liquid interface (ALI) normalized by the cell number (n=3). The group of images on the bottom show cell morphology on the 2th day of culture of H441 on transwell at 50 000 cells/cm^2 (A) and 100 000 cells/cm^2 (B) with nucleus represented at blue stained with DAPI, F-actin in red stained with Phalloidin and in Z0-1 and occludin surface marker in green. The scale bar represents 100 μm for the image in the left and 20 μm for the image in the right hand side (n=2).
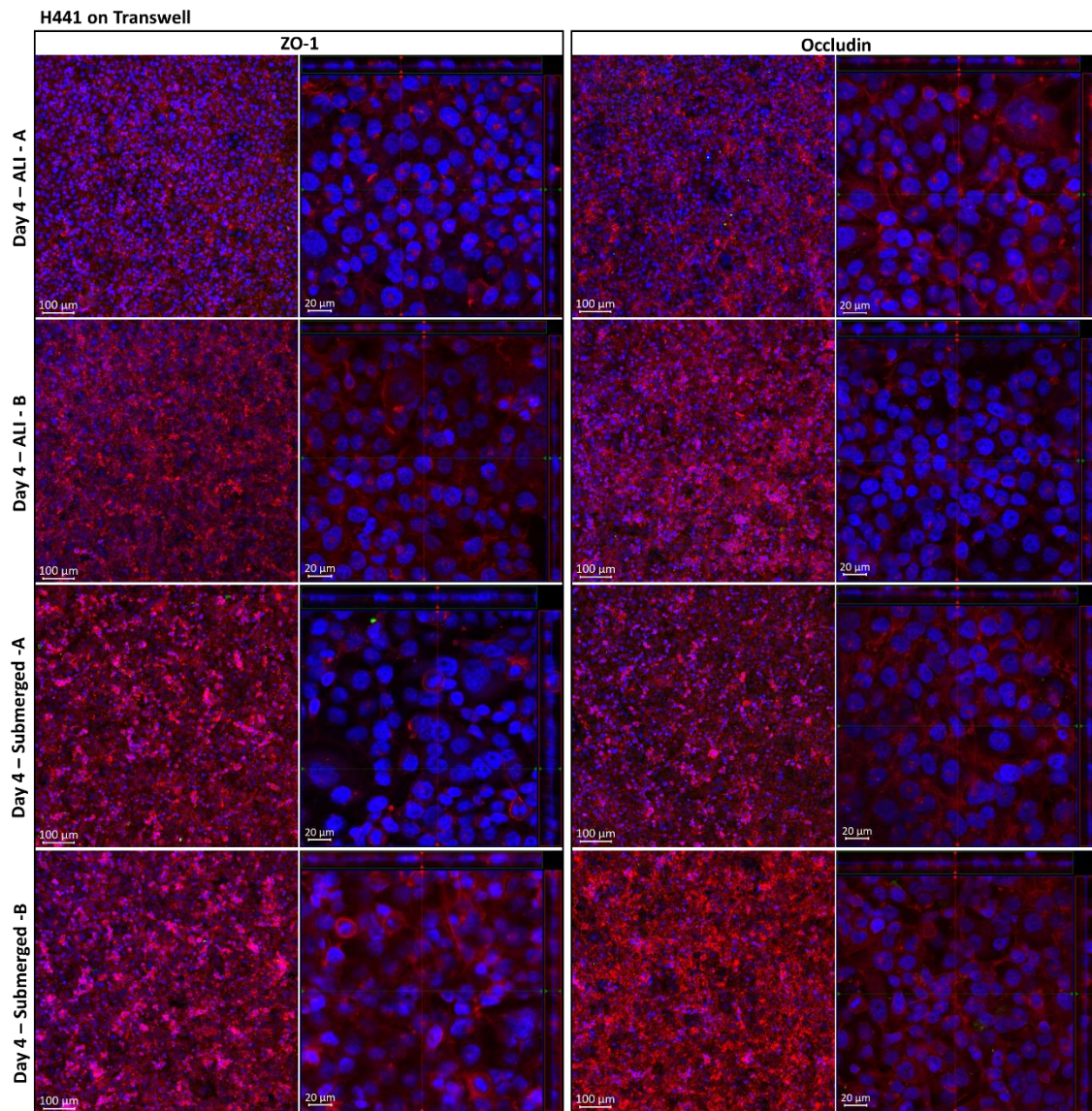
Appendix 9: The images show cell morphology on the 4th day of culture of H441 on transwell at 50 000 cells/cm² (A), 100 000 cells/cm² (B), submerged or at air-liquid interface (ALI). The nucleus represented in blue stained with DAPI, F-actin in red stained with Phalloidin and in Z0-1 and occludin surface marker in green. The scale bar represents 100 µm for the image in the left and 20 µm for the image in the right hand side (n=2).
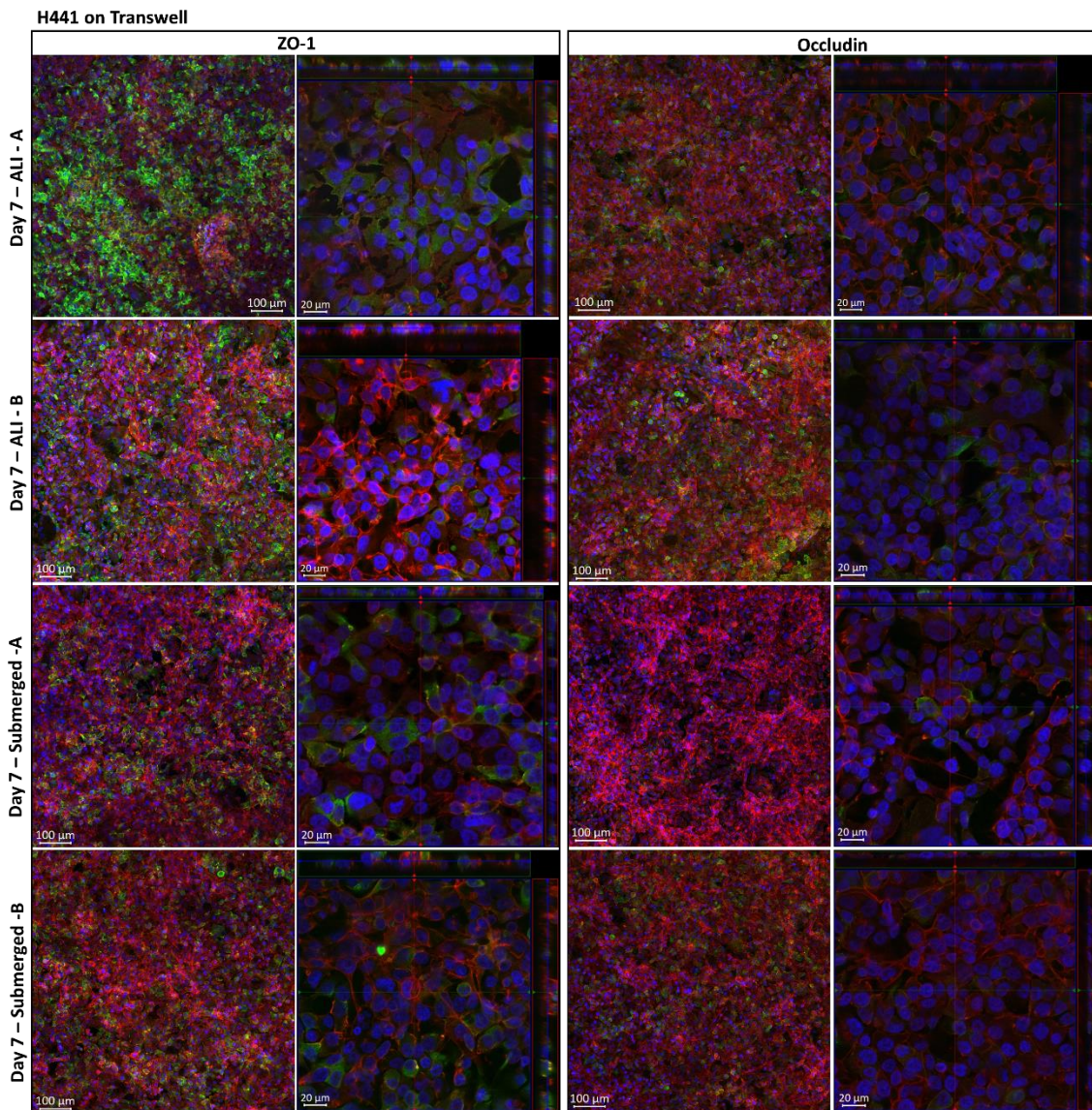
Appendix 10: The images show cell morphology on the 7th day of culture of H441 on transwell at 50 000 cells/cm² (A), 100 000 cells/cm² (B), submerged or at air-liquid interface (ALI). The nucleus represented in blue stained with DAPI, F-actin in red stained with Phalloidin and in Z0-1 and occludin surface marker in green. The scale bar represents 100 µm for the image in the left and 20 µm for the image in the right hand side (n=2).
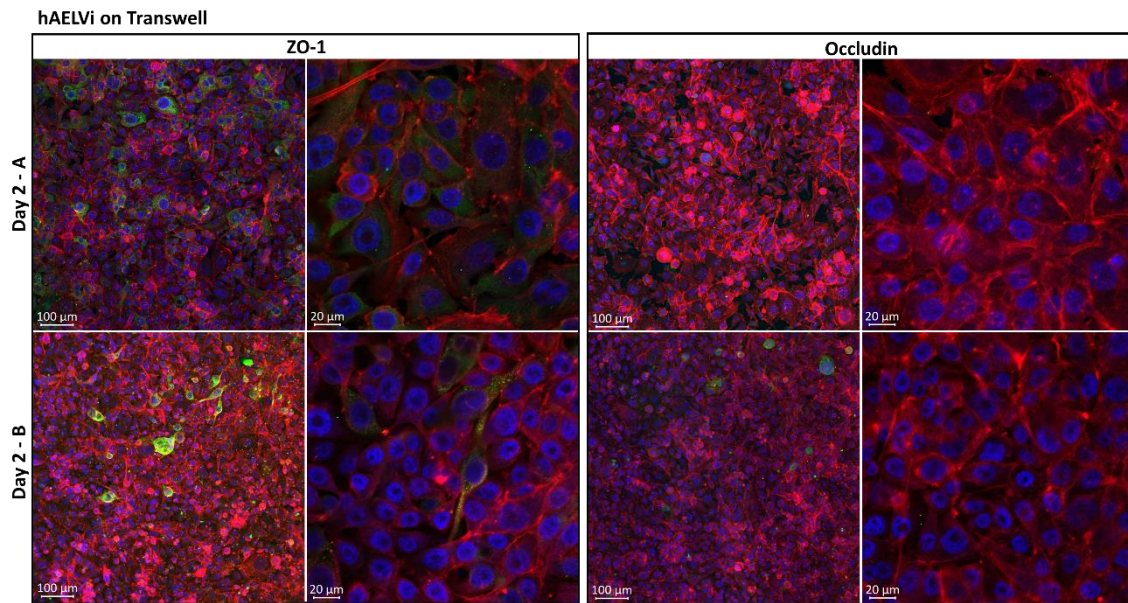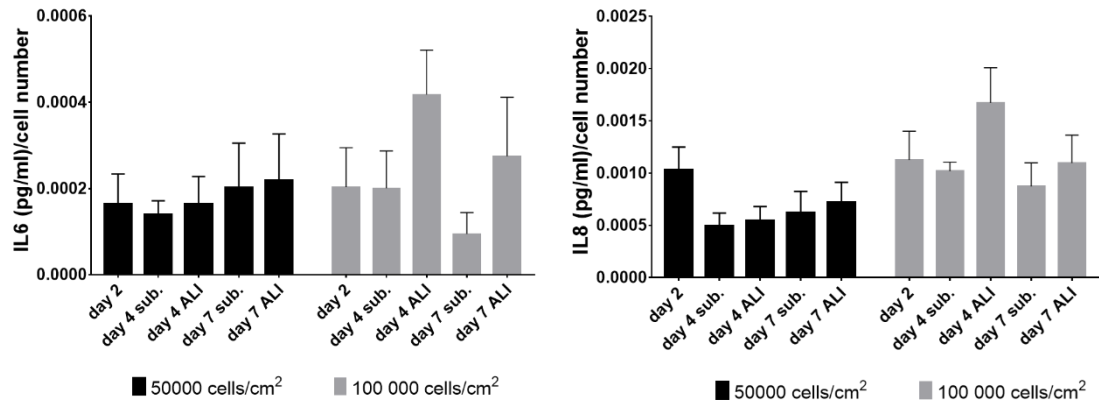
Appendix 11: The graphs of top show the IL6 and IL8 secretion of hAELVI on day 2 (submerged), day 4 and 7 under submerged or at air-liquid interface (ALI) normalized by the cell number (n=3). The group of images on the bottom show cell morphology on the 2th day of culture of hAELVi on transwell at 50 000 cells/cm^2 (A) and 100 000 cells/cm^2 (B) with nucleus represented at blue stained with DAPI, F-actin in red stained with Phalloidin and in Z0-1 and occludin surface marker in green. The scale bar represents 100 μm for the image in the left and 20 μm for the image in the right hand side (n=2).
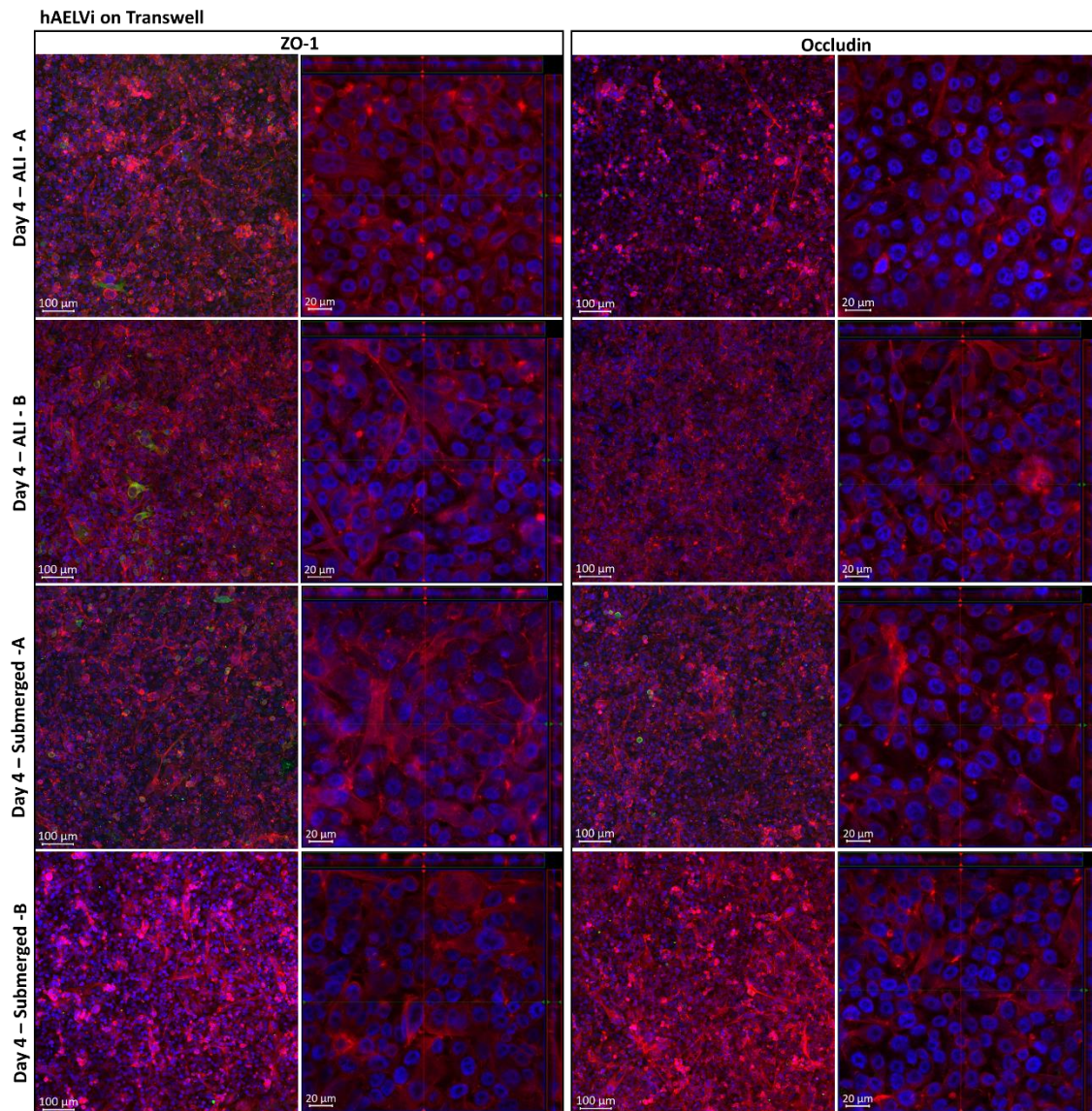
Appendix 12: The images show cell morphology on the 4th day of culture of hAELVi on transwell at 50 000 cells/cm^2 (A), 100 000 cells/cm^2 (B), submerged or at air-liquid interface (ALI). The nucleus represented in blue stained with DAPI, F-actin in red stained with Phalloidin and in Z0-1 and occludin surface marker in green. The scale bar represents 100 µm for the image in the left and 20 µm for the image in the right hand side (n=2).

Appendix 13: The images show cell morphology on the 7th day of culture of hAELVi on transwell at 50 000 cells/cm^2 (A), 100 000 cells/cm^2 (B), submerged or at air-liquid interface (ALI). The nucleus represented in blue stained with DAPI, F-actin in red stained with Phalloidin and in Z0-1 and occludin surface marker in green. The scale bar represents 100 μm for the image in the left and 20 μm for the image in the right hand side (n=2).

Appendix 14: Rheology Theory

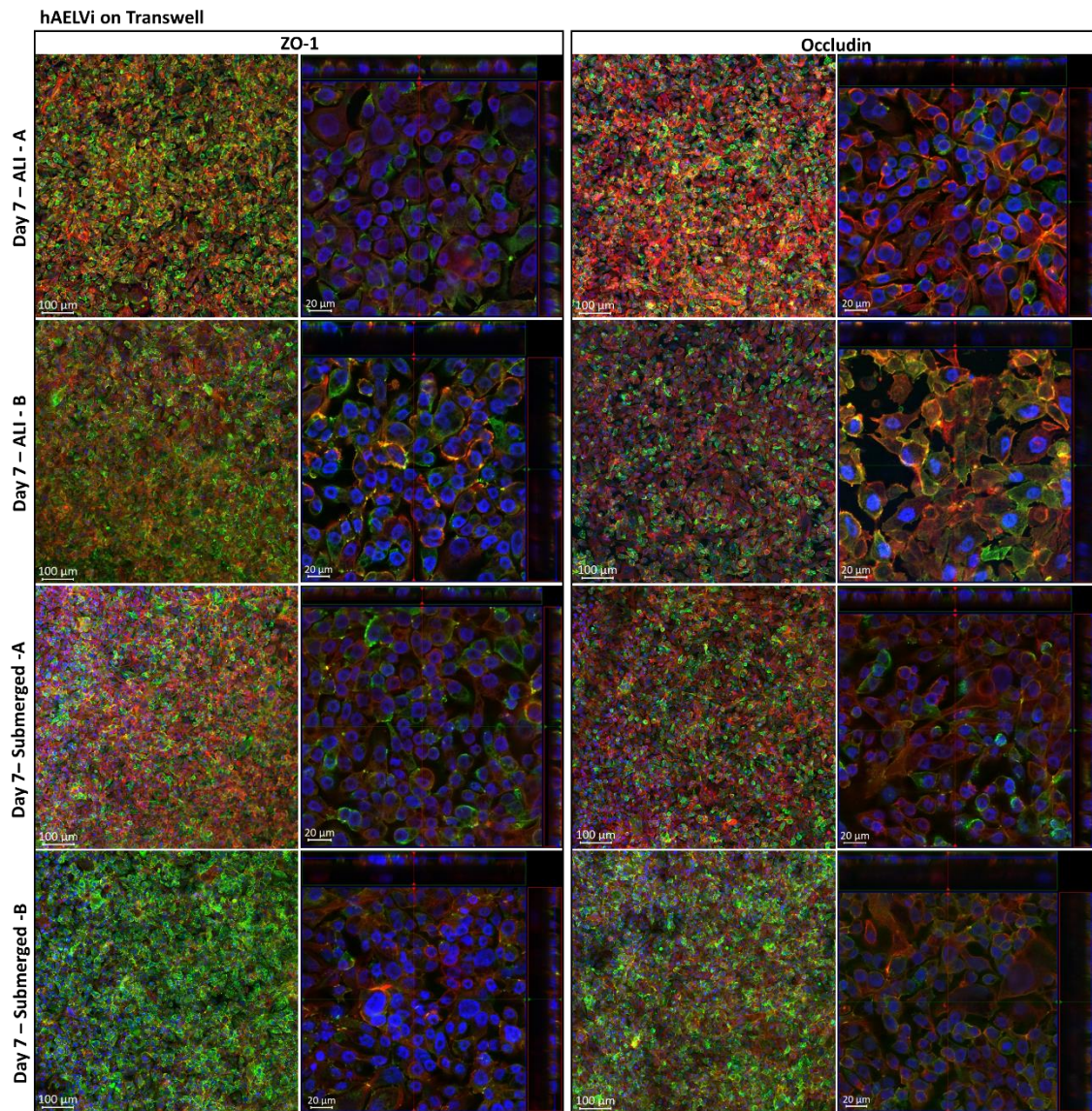Rheology is the science that studies the flow and deformation of materials and can be useful for characterising both fluids and solids. When an external force is applied a fluid or solid behave in distinct ways. The fluid flows and the solid deforms. The liquid behaviour follows the Newton's Law of viscosity. The solid response is modelled by the Hooke's Law of elasticity.

Newton Law of viscosity: When an external stress (or force per unit of area) is applied, the flow persists as long as the stress is applied. When the stress is removed the flow ceases, but the strain (deformation) does not return to zero. The energy applied is dissipated in the flow. The applied force on a surface area, creates a velocity field in the direction of the force and a velocity gradient perpendicular to the surface (where the force is applied). Illustration on appendix 14.1.

.

A)

A

h

y

x

L

At Rest

B)

Δs

F

v

v

dh

dv

v = 0

Under Force F

C)

Shear stress (Pa): $\tau = \dfrac{F}{A}$

Shear rate (s^{-1}): $\gamma = \dfrac{v}{h}$

viscosity (Pa. s): $\eta = \dfrac{\tau}{\dot\gamma}$

D)

Shear thinning

Bingham plastic

Newtonian

shear stress (Pa)

μ

1

Shear thickening

shear rate (s^{-1})
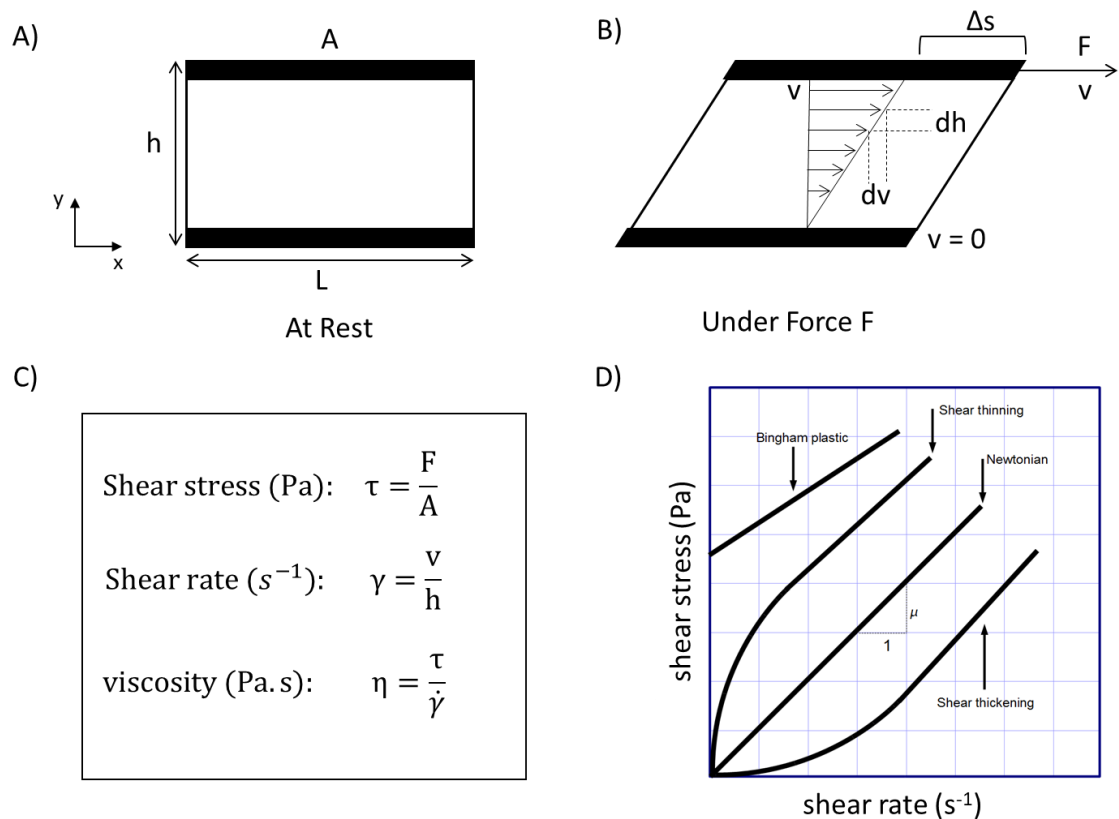
Appendix 14.1: A) and B) Representation of the velocity field at rest and under a force F on moving parallel plates schematic. The height and the length of the geometry is given by h and L respectively. The letter A represent the area where the force F is applied. The force produces a positive velocity gradient $dv_x(y)/dy$ and a deformation Δs. C) The force F applied on the surface area A, creates a pressure determined shear stress (Pa). The changing rate of velocity with the height is determined shear rate (s^{-1}). The internal friction created with the flow is determined viscosity (Pa.s). D) Graphical representation of the shear stress in function of the shear rate. For ideal Newtonian fluids, the stress is proportional to the strain being the slope the viscosity. For newtonian materials the viscosity is independent of the shear rate, constant over time and zero if the stress is removed. For non-newtonian fluids, the material viscosity can increase or

decrease with the shear, named shear thickening or shear thinning respectively. There is also the bingham material, where the shear stress increases lineally with the shear rate above the yield stress.

Hooke's Law: When a force is applied there is an instant deformation of the solid. When the maximum deformation state is reach for the applied forced, there is no further movement. A further change in displacement is only seen if the force change. For the elastic system the strain is proportional to the stress. When the stress is removed the material returns to its original position. The energy applied with the force is stored and used by the material to come back to its initial position. Illustration on appendix 14.2.
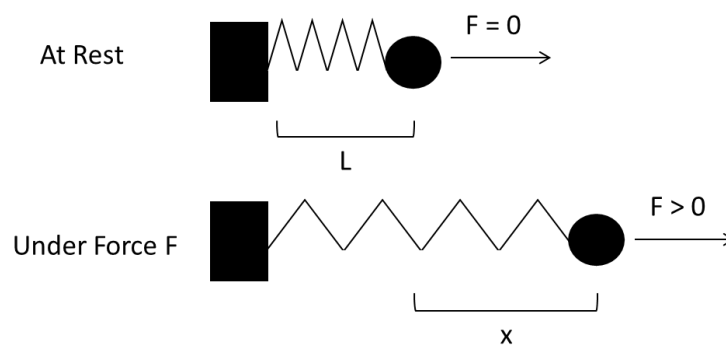
$$\text{Hook's Law: } F = kx$$

Appendix 14.2: Hooke's Law representation with a spring at rest position and under force F. When a force F is applied the spring elongates x with a coefficient k.

The Newtonian and Hookean laws represent two extremes. Newton's law represents the ideal viscous behaviour and Hooke's law the ideal elastic behaviour of the materials. In reality, many materials present a combination of these behaviours, they have an elastic and viscous component, and are termed viscoelastic materials. To evaluate the viscous and elastic component of the materials, the experiment can be performed in the linear viscoelastic region, that is normally observed at low strains and is accessible through the application of small amplitude oscillatory stress. When applying a small amplitude oscillatory stress, the strain response is proportional to the stress amplitude with a phase lag δ. On appendix 14.3 are summarized the visual, vectoral and mathematical treatment of the stress and strain. With the dynamic mechanical analysis, the viscoelasticity is given by two components, the storage and loss modulus. The storage modulus represents the elastic magnitude of the material. The loss modulus represents the viscous component of the material. The storage modulus is determined

by the ratio of the stress in phase with the strain over the strain. By the formula, a higher storage modulus indicates higher stress needs to be applied to provoke the displacement of the material, indicating the presence of a more rigid material. Regarding the loss modulus, this is determined by the ratio of the stress 90° out of phase with strain over the strain. The presence of two material where A has higher viscosity than B, under the same force A will flow slowly than B. For both materials to flow at rate velocity the force applied on A needs to be higher than on B.

A)

$0° < \delta < 90°$

Stress ωt τ_0

90°

Strain ωt $\gamma 0$

B)

G'' G^* δ G'
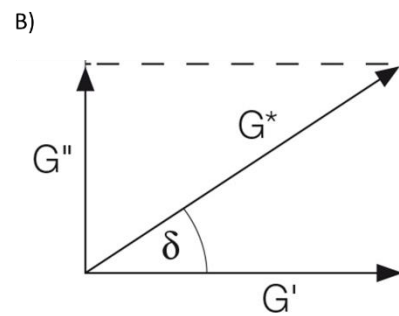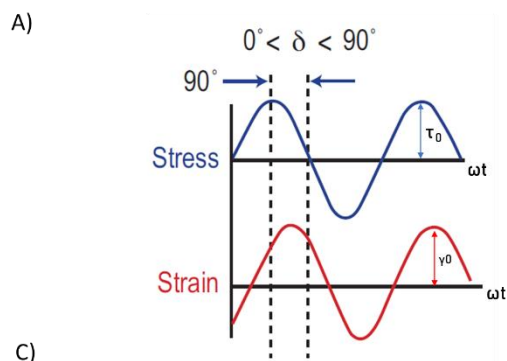
C)

$$G^* = G' + iG''$$

Storage Modulus: $G' = \dfrac{\text{stress in phase with strain}}{\text{strain}}$

Loss Modulus: $G'' = \dfrac{\text{stress } 90° \text{ out of phase with strain}}{\text{strain}}$

D)

$\delta = 0°$ → ideal solid (Hook's Law)

$\delta = 90°$ → ideal liquid (Newton's Law)

$\tan(\delta) = \dfrac{G''}{G'} \Leftrightarrow \delta = \tan^{-1}\left(\dfrac{G''}{G'}\right)$

G' > G'' → more solid behavior

G'' > G' → more liquid behavior

Appendix 14.3: A) Oscillatory stress lagged δ of the strain response. B) Vectoral representation of the complex modulus G*. C) Mathematical representation of the complex modulus G*. The vector can be represented by an imaginary number, the real part is the storage modulus, represented by G'. The imaginary part is the loss modulus, represented by G''. D) Relationship between phase angle and elastic and viscous components.

| Storage Modulus	P Value	Loss Modulus	P Value
5 mg/ml : 5 U/ml vs. 5 mg/ml :1 U/ml	<0,0001	5 mg/ml :5 U/ml vs. 5 mg/ml :1 U/ml	0,0287
5 mg/ml : 5 U/ml vs. 5 mg/ml :0.1 U/ml	<0,0001	5 mg/ml :5 U/ml vs. 5 mg/ml :0.1 U/ml	0,0015
5 mg/ml : 5 U/ml vs. 2.5 mg/ml:0.1 U/ml	0,0035	5 mg/ml :5 U/ml vs. 2.5 mg/ml:5 U/ml	0,0118
5 mg/ml :1 U/ml vs. 5 mg/ml :0.1 U/ml	0,0390	5 mg/ml :5 U/ml vs. 1.25 mg/ml :5 U/ml	0,0097
5 mg/ml :1 U/ml vs. 2.5 mg/ml: 5 U/ml	<0,0001	5 mg/ml :5 U/ml vs. 1.25 mg/ml :1 U/ml	0,0039
5 mg/ml :1 U/ml vs. 2.5 mg/ml:1 U/ml	<0,0001	5 mg/ml :1 U/ml vs. 2.5 mg/ml:5 U/ml	<0,0001
5 mg/ml :1 U/ml vs. 2.5 mg/ml:0.1 U/ml	<0,0001	5 mg/ml :1 U/ml vs. 2.5 mg/ml:1 U/ml	<0,0001
5 mg/ml :1 U/ml vs. 1.25 mg/ml : 5 U/ml	<0,0001	5 mg/ml :1 U/ml vs. 2.5 mg/ml:0.1 U/ml	0,0242
5 mg/ml :1 U/ml vs. 1.25 mg/ml :1 U/ml	<0,0001	5 mg/ml :1 U/ml vs. 1.25 mg/ml :5 U/ml	<0,0001
5 mg/ml :1 U/ml vs. 1.25 mg/ml :0.1 U/ml	<0,0001	5 mg/ml :1 U/ml vs. 1.25 mg/ml :1 U/ml	<0,0001
5 mg/ml :0.1 U/ml vs. 2.5 mg/ml: 5 U/ml	<0,0001	5 mg/ml :1 U/ml vs. 1.25 mg/ml :0.1 U/ml	<0,0001
5 mg/ml :0.1 U/ml vs. 2.5 mg/ml:1 U/ml	<0,0001	5 mg/ml :0.1 U/ml vs. 2.5 mg/ml:5 U/ml	<0,0001
5 mg/ml :0.1 U/ml vs. 2.5 mg/ml:0.1 U/ml	<0,0001	5 mg/ml :0.1 U/ml vs. 2.5 mg/ml:1 U/ml	<0,0001
5 mg/ml :0.1 U/ml vs. 1.25 mg/ml : 5 U/ml	<0,0001	5 mg/ml :0.1 U/ml vs. 2.5 mg/ml:0.1 U/ml	0,0013
5 mg/ml :0.1 U/ml vs. 1.25 mg/ml :1 U/ml	<0,0001	5 mg/ml :0.1 U/ml vs. 1.25 mg/ml :5 U/ml	<0,0001
5 mg/ml :0.1 U/ml vs. 1.25 mg/ml :0.1 U/ml	<0,0001	5 mg/ml :0.1 U/ml vs. 1.25 mg/ml :1 U/ml	<0,0001
2.5 mg/ml: 5 U/ml vs. 2.5 mg/ml:1 U/ml	0,0047	5 mg/ml :0.1 U/ml vs. 1.25 mg/ml :0.1 U/ml	<0,0001
2.5 mg/ml: 5 U/ml vs. 2.5 mg/ml:0.1 U/ml	<0,0001	2.5 mg/ml:5 U/ml vs. 2.5 mg/ml:0.1 U/ml	0,0139
2.5 mg/ml:1 U/ml vs. 2.5 mg/ml:0.1 U/ml	0,0187	2.5 mg/ml:0.1 U/ml vs. 1.25 mg/ml :5 U/ml	0,0114
2.5 mg/ml:1 U/ml vs. 1.25 mg/ml : 5 U/ml	0,0020	2.5 mg/ml:0.1 U/ml vs. 1.25 mg/ml :1 U/ml	0,0047
2.5 mg/ml:1 U/ml vs. 1.25 mg/ml :1 U/ml	0,0005		
2.5 mg/ml:0.1 U/ml vs. 1.25 mg/ml : 5 U/ml	<0,0001		
2.5 mg/ml:0.1 U/ml vs. 1.25 mg/ml :1 U/ml	<0,0001		
2.5 mg/ml:0.1 U/ml vs. 1.25 mg/ml :0.1 U/ml	<0,0001		

Appendix 15: List of p values from loss and storage modulus plot from figure 5.12.

		PARDISO	MUMPS	SPOOLES	GMRES_SAAMG	GMRES_ GM
Version 1 (0,0.725, -2)		81.945	81.945	81.945	81.945	81.945
Version 2 (1.5, 1.68, 1.7)		81.945	81.945	81.945	81.945	81.945
Version 3	Geom. A (-2.03, -0.5, 2)	301.76	301.76	301.76	301.77	301.76
	Geom. B (-0.39, 0.88, -0.4)	316.34	316.34	316.34	316.34	316.34
	Geom. C (-2.47, -0.14, -4)	309.38	309.38	309.38	309.38	309.40
Version 4 (0, 0.25, -2.5)		327.1	327.1	327.1	327.1	327.1

 Appendix 16: Solver comparison for version 1 to 4 of the bioreactor. The result corresponds to the velocity (mm/s) at inlet midpoint (coordinate in cm in brackets) and at 15 mL/min inlet flow rate.
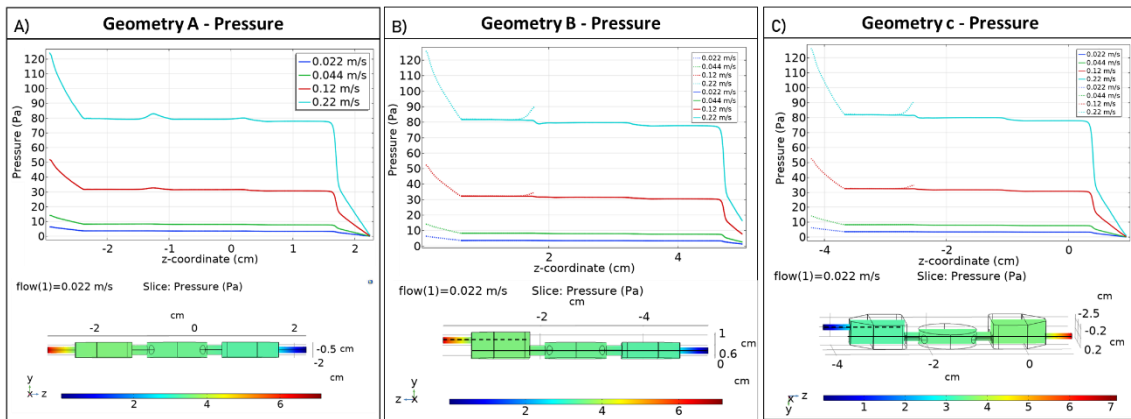
Appendix 17: A) Pressure simulation output for geometry A. Top graph represents the pressure in function of the z coordinate from inlet to outlet with initial velocity of 0.022, 0.044, 0.12 and 0.22 m/s at the inlet. Middle image shows the pressure magnitude at zy plane that passes from inlet to outlet in colour scheme at 0.022 m/s (1.5 mL/min). B) Pressure simulation output for geometry B. The dotted line represents the pressure in function of the z coordinate at the inlet level and the full line at the outlet level. The lines can be found represented in black in the middle image. C) Pressure simulation output for geometry C.
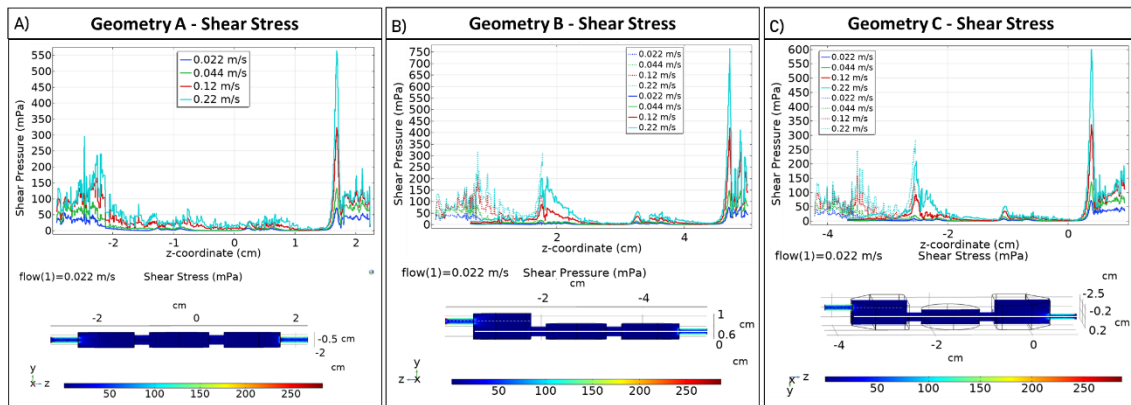
Appendix 18: A) Shear stress simulation output for geometry A. Top graph represents the shear stress in function of the z coordinate from inlet to outlet with initial velocity of 0.022, 0.044, 0.12 and 0.22 m/s at the inlet. Middle image shows the shear stress magnitude at zy plane that passes from inlet to outlet in colour scheme at 0.022 m/s (1.5 mL/min). B) Shear stress simulation output for geometry B. The dotted line represents the shear stress in function of the z coordinate at the inlet level and the full line at the outlet level. The lines can be found represented in white in the middle image. C) Shear stress simulation output for geometry C.

297
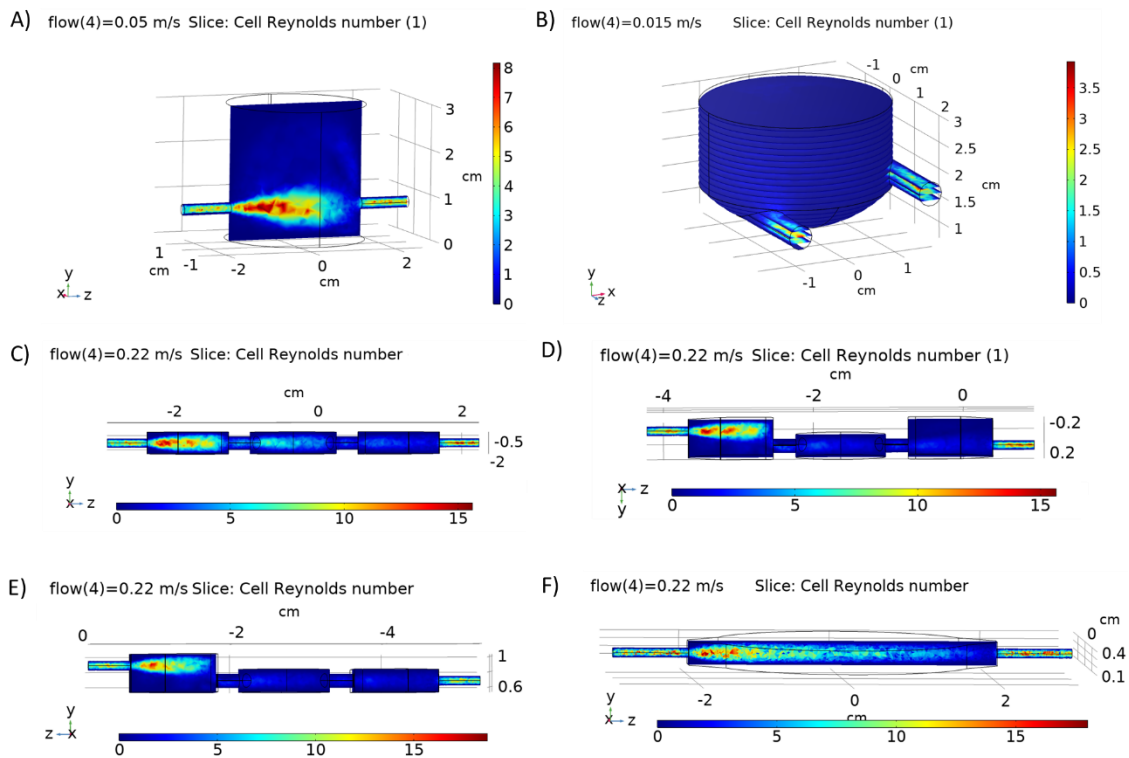
Appendix 19: Reynolds number profile at 15 mL/min inlet initial velocity. A) Version 1. B) Version 2. C) Version 3 layout 1. D) Version 3 layout 2. E) Version 3 layout 3. F) Version 4.
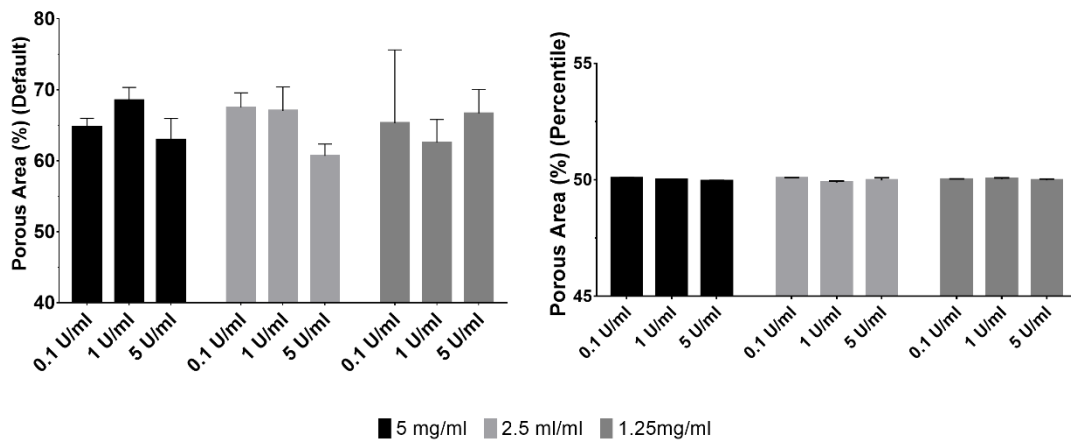
Appendix 20: Percentage of area corresponded to porous in the fibrin gel depending on fibrinogen and thrombin concentration. (n=3 except for 1.25mg/ml + 5 mg/ml and 1.25mg/ml + 0.1 mg/ml which is n=2, however the number of images analysed range from 36 to 18). One the left corresponds to the data analysed with the Default algorithm and on the right with the Percentile. The error bars represent SEM.
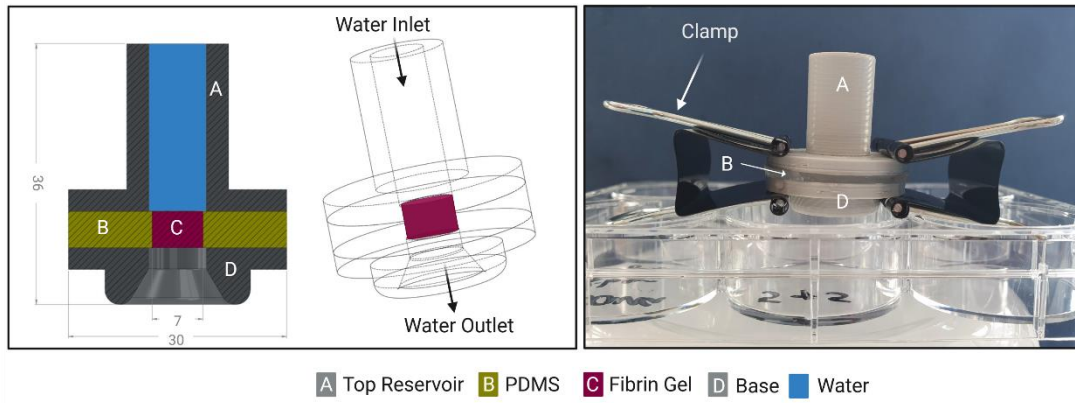
Appendix 21: Permeability apparatus. The fibrin gel identified as C in the image polymerized on a PDMS ring, identified with the letter B. Then, with a use of two claps a top reservoir and a base were fixed on the PDMS ring. The top reservoir was filled with water that was collated to a well of a 6 well plate. The water level was kept constant to maintain constant pressure. Created with BioRender.com

Ascorbic acid (µM)	Experiment 1	Experiment 2	Experiment 3	Mean
500	5.8 mg (average of 10 pellets)	4 mg (average of 10 pellets)	5.2 mg (average of 8 pellets)	5
5000	19 mg (1 pellet)	22.5 mg (average of 2 pellets)	24 mg (1 pellet)	21.8

Appendix 22: Average weight in milligrams (mg) of dECM pellet under 500 or 5000 µM of ascorbic acid supplementation. The 10 times increase of ascorbic acid lead to a 4.36 increase in dECM dry weight.

Chapter 10

References

1. Morrisey, E. E. & Hogan, B. L. M. Review Preparing for the First Breath : Genetic and Cellular Mechanisms in Lung Development. *DEVCEL* **18**, 8–23 (2009).

2. Hsia, C. C. W., Hyde, D. M. & Weibel, E. R. Lung Structure and the Intrinsic Challenges of Gas Exchange. **6**, (2016).

3. Fishman, J. A. *et al. Fishman's Pulmonary Diseases and Disorders*. (2015). doi:00000446-200612000-00016 [pii]

4. William F. Ganong. *Review of Medical Physiology*. *Lange*

5. https://smart.servier.com/.

6. Oberdörster, G., Oberdörster, E. & Oberdörster, J. Nanotoxicology: An emerging discipline evolving from studies of ultrafine particles. *Environ. Health Perspect.* **113**, 823–839 (2005).

7. Reynolds, S. D. & Malkinson, A. M. Clara cell: Progenitor for the bronchiolar epithelium. *Int. J. Biochem. Cell Biol.* **42**, 1–4 (2010).

8. Haefeli-Bleuer, B. & Weibel, E. R. Morphometry of the human pulmonary acinus. *Anat. Rec.* **220**, 401–414 (1988).

9. LPETER GEHR & BACHOFEN, M. and E. R. W. THE NORMAL HUMAN LUNG:ULTRASTRUCTURE AND MORPHOMETRIC ESTIMATION OF DIFFUSION CAPACITY. **4**, 211–230 (1978).

10. Ochs, M. *et al.* The Number of Alveoli in the Human Lung. *Am. J. Respir. Crit. Care Med.* **169**, 120–124 (2004).

11. Weibel, E. R. On the tricks alveolar epithelial cells play to make a good lung. *Am. J. Respir. Crit. Care Med.* **191**, 504–513 (2015).

12. Weibel, E. R. Lung morphometry: the link between structure and function. *Cell Tissue Res.* **367**, 413–426 (2017).

13. Herzog, E. L., Brody, A. R., Colby, T. V., Mason, R. & Williams, M. C. Knowns and unknowns of the alveolus. *Proc. Am. Thorac. Soc.* **5**, 778–782 (2008).

14. Rock, J. R. & Hogan, B. L. M. Epithelial Progenitor Cells in Lung Development, Maintenance, Repair, and Disease. *Annu. Rev. Cell Dev. Biol.* **27**, 493–512 (2011).

15. Williams, M. C. Alveolar Type I Cells: Molecular Phenotype and Development. *Annu. Rev. Physiol.* **65**, 669–695 (2003).

16. Fehrenbach, H. Alveolar epithelial type II cell : Defender of the alveolus revisited Alveolar epithelial type II cell : defender of the alveolus revisited. (2001). doi:10.1186/rr36

17. Ruaro, B. *et al.* The history and mystery of alveolar epithelial type ii cells: Focus on their physiologic and pathologic role in lung. *Int. J. Mol. Sci.* **22**, 1–16 (2021).

18. Béla Suki, Dimitrije Stamenovic, and R. H. Lung Parenchymal Mechanics. *NIH Public Access* **1**, 1317–1351 (2011).

19. G J Laurent. Lung collagen: more than scaffolding. *Thorax* **21**, 418–428 (1986).

20. Blickensdorf, M., Timme, S. & Figge, M. T. Hybrid Agent-Based Modeling of Aspergillus fumigatus Infection to Quantitatively Investigate the Role of Pores of Kohn in Human Alveoli. *Front. Microbiol.* **11**, 1–13 (2020).

21. Namati, E., Thiesse, J., De Ryk, J. & McLennan, G. Alveolar dynamics during respiration: Are the pores of Kohn a pathway to recruitment? *Am. J. Respir. Cell Mol. Biol.* **38**, 572–578 (2008).

22. Rounds, S. & Voelkel, N. *The pulmonary endothelium*. *New York* (2009 John Wiley & Sons Ltd.

Wiley-Blackwell, 2009).

23. Stanfield, C. L. *Principles of Physiology*. *Pearson Education* (2013). doi:10.1177/0734282905285244

24. Bachofen, H., Schurch, S., Urbinelli, M. & Weibel, E. R. Relations among alveolar surface tension, surface area, volume, and recoil pressure. *J. Appl. Physiol.* **62**, 1878–1887 (1987).

25. Clements, J. A. LUNG SURFACTANT : A Personal Perspective. *Annu. Rev. Physiol.* (1997).

26. Han, S. & Mallampalli, R. K. The Role of Surfactant in Lung Disease and Host Defense against Pulmonary Infectios. *ATS Journals* (2015). doi:10.1513/AnnalsATS.201411-507FR

27. Perez-Gil, J. & Weaver, T. E. Pulmonary Surfactant Pathophysiology: Current Models and Open Questions. *Physiology* **25**, 132–141 (2010).

28. Miller, A. J. & Spence, J. R. In Vitro Models to Study Human Lung Development, Disease and Homeostasis. *Physiology* **32**, 246–260 (2017).

29. Clift, M. J. D., Jenkins, G. J. S. & Doak, S. H. An Alternative Perspective towards Reducing the Risk of Engineered Nanomaterials to Human Health. *Small* **16**, 1–6 (2020).

30. Hoymann, H. G. Invasive and noninvasive lung function measurements in rodents. *J. Pharmacol. Toxicol. Methods* **55**, 16–26 (2007).

31. Bender Kim, C. F. *et al.* Identification of bronchioalveolar stem cells in normal lung and lung cancer. *Cell* **121**, 823–835 (2005).

32. Snoeck, H.-W. Modeling human lung development and disease using pluripotent stem cells. *Development* **142**, 13–16 (2015).

33. Haley, P. J. Species differences in the structure and function of the immune system. *Toxicology* **188**, 49–71 (2003).

34. Mercer, R. R. & Crapo, J. D. Three-dimensional reconstruction of the rat acinus. *J. Appl. Physiol.* **63**, 785–94 (1987).

35. Richard A. Parent. *Comparative Biology of the Normal Lung*. *Comparative Biology of the Normal Lung* (2016). doi:10.1016/c2012-0-01154-4

36. Hay, M., Thomas, D. W., Craighead, J. L., Economides, C. & Rosenthal, J. Clinical development success rates for investigational drugs. *Nat. Biotechnol.* **32**, 40–51 (2014).

37. Avorn, J. The $2.6 Billion Pill — Methodologic and Policy Considerations. *N. Engl. J. Med.* (2015). doi:10.1056/NEJMp1002530

38. Goh, J. Y., Weaver, R. J., Dixon, L., Platt, N. J. & Roberts, R. A. Development and use of in vitro alternatives to animal testing by the pharmaceutical industry 1980-2013. *Toxicol. Res. (Camb).* **4**, 1297–1307 (2015).

39. https://ec.europa.eu/growth/sectors/cosmetics/animal-testing_pt on 11/10/2017.

40. Taniguchi, D. *et al.* Scaffold-free trachea regeneration by tissue engineering with bio-3D printing. *Interact. Cardiovasc. Thorac. Surg.* **26**, 745–752 (2018).

41. de Jong, P. M. *et al.* Ciliogenesis in human bronchial epithelial cells cultured at the air-liquid interface. *Am. J. Respir. Cell Mol. Biol.* **10**, 271–277 (1994).

42. Dobbs, L. G., Pian, M. S., Maglio, M., Dumars, S. & Allen, L. Maintenance of the differentiated type II cell phenotype by culture with an apical air surface. *Am. J. Physiol. Cell. Mol. Physiol.* **273**, L347–L354 (1997).

43. Skardal, A. *et al.* Multi-tissue interactions in an integrated three-tissue organ-on-a-chip platform. *Sci. Rep.* **7**, 8837 (2017).

44. Novak, R. *et al.* Robotic fluidic coupling and interrogation of multiple vascularized organ chips. *Nat. Biomed. Eng.* **4**, 407–420 (2020).

45. Dongeun Huh, Benjamin D. Matthews, Akiko Mammoto, Martín Montoya-Zavala, Hong Yuan Hsin, D. E. I. Reconstituting Organ-Level Lung Functions on a Chip. *Science (80-.).* **328**, 1662–1669 (2010).

46. Grigoryan, B. *et al.* Multivascular networks and functional intravascular topologies within biocompatible hydrogels. *Science-* **464**, 458–464 (2019).

47. Horvath, L. *et al.* Engineering an in vitro air-blood barrier by 3D bioprinting. *Sci. Rep.* **5**, (2015).

48. WHITCUTTJ, M., ADLER, K. & WU, R. A BIPHASIC CHAMBER SYSTEM FOR MAINTAINING P O L A R I T Y OF. *Vitr. Cell. Dev. Biol.* **24**, (1988).

49. Ghaedi, M., Niklason, L. E. & Williams, J. C. Development of Lung Epithelium from Induced Pluripotent Stem Cells. *Curr. Transplant. Reports* **2**, 81–89 (2015).

50. Miller, A. J. *et al.* Generation of lung organoids from human pluripotent stem cells in vitro. *Nat. Protoc.* **14**, 518–540 (2019).

51. Lancaster, M. A. & Knoblich, J. A. Organogenesis in a dish: Modeling development and disease using organoid technologies. *Science (80-.).* **345**, 1247125–1247125 (2014).

52. Rossi, G., Manfrin, A. & Lutolf, M. P. Progress and potential in organoid research. *Nat. Rev. Genet.* doi:10.1038/s41576-018-0051-9

53. Fatehullah, A., Tan, S. H. & Barker, N. Organoids as an in vitro model of human development and disease. *Nat. Cell Biol.* **18**, 246–254 (2016).

54. Barkauskas, C. E. *et al.* Lung organoids: current uses and future promise. *Development* **144**, 986–997 (2017).

55. Gilpin, S. E. & Wagner, D. E. Acellular human lung scaffolds to model lung disease and tissue regeneration. 1–10 (2018). doi:10.1183/16000617.0021-2018

56. Tibbitt, M. W. & Anseth, K. S. Hydrogels as Extracellular Matrix Mimics for 3D Cell Culture. **103**, 655–663 (2009).

57. Qin, D., Xia, Y. & Whitesides, G. M. Soft lithography for micro- and nanoscale patterning. *Nat. Protoc.* **5**, 491–502 (2010).

58. Bhatia, S. N. & Ingber, D. E. Microfluidic organs-on-chips. *Nat. Biotechnol.* **32**, 760–772 (2014).

59. Tenenbaum-katan, J., Artzy-schnirman, A., Fishler, R., Korin, N. & Sznitman, J. Biomimetics of the pulmonary environment in vitro : A microfluidics perspective. *Biomicrofluidics* **042209**, (2018).

60. Murphy, S. V & Atala, A. 3D bioprinting of tissues and organs. *Nat. Biotechnol.* **32**, 773–785 (2014).

61. Mandrycky, C., Wang, Z., Kim, K. & Kim, D. H. 3D bioprinting for engineering complex tissues. *Biotechnol. Adv.* **34**, 422–434 (2016).

62. Galliger, Z., Vogt, C. D. & Panoskaltsis-Mortari, A. 3D bioprinting for lungs and hollow organs. *Transl. Res.* **211**, 19–34 (2019).

63. Zhao, J. *et al.* Bioreactors for tissue engineering: An update. *Biochem. Eng. J.* **109**, 268–281 (2016).

64. Klein, S. G., Serchi, T., Hoffmann, L., Blömeke, B. & Gutleb, A. C. An improved 3D tetraculture system mimicking the cellular organisation at the alveolar barrier to study the potential toxic effects of particles on the lung. *Part. Fibre Toxicol.* **10**, (2013).

65. Berg, J. *et al.* Optimization of cell-laden bioinks for 3D bioprinting and efficient infection with

influenza A virus. *Sci. Rep.* **8**, 1–13 (2018).

66.   Chen, Y. *et al.* Long-Term Engraftment Promotes Differentiation of Alveolar Epithelial Cells from Human Embryonic Stem Cell Derived Lung Organoids. *Stem Cells Dev.* **27**, 1339–1349 (2018).

67.   Barkauskas, C. E. *et al.* Type 2 alveolar cells are stem cells in adult lung Find the latest version : Type 2 alveolar cells are stem cells in adult lung. *J. Clin. Invest.* **123**, 3025–3036 (2013).

68.   Yamamoto, Y. *et al.* Long-term expansion of alveolar stem cells derived from human iPS cells in organoids. *Nat. Methods* **14**, 1097–1106 (2017).

69.   Nishiguchi, A., Singh, S., Wessling, M. & Kirkpatrick, C. J. Basement Membrane Mimics of Biofunctionalized Nano fi bers for a Bipolar-Cultured Human Primary Alveolar-Capillary Barrier Model. (2017). doi:10.1021/acs.biomac.6b01509

70.   Link, P. A., Pouliot, R. A., Mikhaiel, N. S., Young, B. M. & Heise, R. L. Tunable Hydrogels from Pulmonary Extracellular Matrix for 3D Cell Culture. 1–9 (2017). doi:10.3791/55094

71.   Lewis, K. J. R. *et al.* Epithelial-mesenchymal crosstalk influences cellular behavior in a 3D alveolus-fibroblast model system. *Biomaterials* **155**, 124–134 (2018).

72.   Kedaria, D. & Vasita, R. Bi-functional oxidized dextran – based hydrogel inducing microtumors : An in vitro three-dimensional lung tumor model for drug toxicity assays. (2017). doi:10.1177/2041731417718391

73.   Stucki, A. O. *et al.* A lung-on-a-chip array with an integrated bio-inspired respiration mechanism. *Lab Chip* 1302–1310 (2015). doi:10.1039/c4lc01252f

74.   Felder, M., Stucki, A. O., Stucki, J. D., Geiser, T. & Guenat, O. T. The potential of microfluidic lung epithelial wounding: towards in vivo-like alveolar microinjuries. *Integr. Biol.* (2014). doi:10.1039/C4IB00149D

75.   Fishler, R. & Sznitman, J. A microfluidic model of biomimetically breathing pulmonary acinar airways. *J. Vis. Exp.* **2016**, 1–9 (2016).

76.   Fishler, R., Mulligan, M. K. & Sznitman, J. Acinus-on-a-chip: A microfluidic platform for pulmonary acinar flows. *J. Biomech.* **46**, 2817–2823 (2013).

77.   Fishler, R., Hofemeier, P., Etzion, Y., Dubowski, Y. & Sznitman, J. Particle dynamics and deposition in true-scale pulmonary acinar models. *Sci. Rep.* **5**, 1–11 (2015).

78.   Ghaedi, M. *et al.* Alveolar epithelial differentiation of human induced pluripotent stem cells in a rotating bioreactor. *Biomaterials* **35**, 699–710 (2014).

79.   Sundarakrishnan, A. *et al.* Bioengineered in Vitro Tissue Model of Fibroblast Activation for Modeling Pulmonary Fibrosis. *ACS Biomater. Sci. Eng.* **5**, 2417–2429 (2019).

80.   Nichols, J. E. *et al.* Giving new life to old lungs: methods to produce and assess whole human paediatric bioengineered lungs. *J. Tissue Eng. Regen. Med.* **11**, 2136–2152 (2017).

81.   Kolte, D., McClung, J. A. & Aronow, W. S. *Vasculogenesis and Angiogenesis. Translational Research in Coronary Artery Disease: Pathophysiology to Treatment* (Elsevier Inc., 2015). doi:10.1016/B978-0-12-802385-3.00006-1

82.   Russell, C. & Peters, C. Endothelial Cells, Angiogenesis and Vasculogenesis. *Stemcell Technol.* 1–4 (2013).

83.   Drake, C. J. Embryonic and adult vasculogenesis. *Birth Defects Res. Part C - Embryo Today Rev.* **69**, 73–82 (2003).

84.   Gerhard M. Artmann, Stephen Minger, J. H. *Stem Cell Engineering: Principles and Applications*. (Springer, 2011).

85.   Carmeliet, P. & Jain, R. K. Molecular mechanisms and clinical applications of angiogenesis. *Nature*

473, 298–307 (2011).

86. Yun, E. J., Lorizio, W., Seedorf, G., Abman, S. H. & Vu, T. H. VEGF and endothelium-derived retinoic acid regulate lung vascular and alveolar development. *Am. J. Physiol. - Lung Cell. Mol. Physiol.* **310**, L287–L298 (2016).

87. Kim, D., Eom, S., Park, S. M., Hong, H. & Kim, D. S. A collagen gel-coated, aligned nanofiber membrane for enhanced endothelial barrier function. *Sci. Rep.* **9**, 1–11 (2019).

88. Ehsan, S. M., Welch-Reardon, K. M., Waterman, M. L., Hughes, C. C. W. & George, S. C. A three-dimensional in vitro model of tumor cell intravasation. *Integr. Biol. (United Kingdom)* **6**, 603–610 (2014).

89. Griffith, C. K. *et al.* Diffusion Limits of an *in Vitro* Thick Prevascularized Tissue. *Tissue Eng.* **11**, 257–266 (2005).

90. Ghajar, C. M., Blevins, K. S., Hughes, C. C. W., George, S. C. & Putnam, A. J. Mesenchymal Stem Cells Enhance Angiogenesis in Mechanically Viable Prevascularized Tissues via Early Matrix Metalloproteinase Upregulation. *Tissue Eng.* **12**, 2875–2888 (2006).

91. Chwalek, K., Tsurkan, M. V., Freudenberg, U. & Werner, C. Glycosaminoglycan-based hydrogels to modulate heterocellular communication in in vitro angiogenesis models. *Sci. Rep.* **4**, 4–11 (2014).

92. Moya, M. L., Hsu, Y.-H., Lee, A. P., Hughes, C. C. W. & George, S. C. *In Vitro* Perfused Human Capillary Networks. *Tissue Eng. Part C Methods* **19**, 730–737 (2013).

93. Zheng, Y. *et al.* In vitro microvessels for the study of angiogenesis and thrombosis. *Proc. Natl. Acad. Sci. U. S. A.* **109**, 9342–9347 (2012).

94. Kolesky, D. B., Homan, K. A., Skylar-scott, M. A. & Lewis, J. A. Three-dimensional bioprinting of thick vascularized tissues. *PNAS* **113**, 3179–3184 (2016).

95. Lipps, C. *et al.* Expansion of functional personalized cells with specific transgene combinations. *Nat. Commun.* **9**, (2018).

96. Kuehn, A. *et al.* Human alveolar epithelial cells expressing tight junctions to model the air-blood barrier. *ALTEX* **33**, 251–260 (2016).

97. https://www.inscreenex.de/products/human-immortalized-cell-lines/alveolar-epithelial-cells-hu.html.

98. Tennanth, J. EVALUATION_OF_THE_TRYPAN_BLUE_TECHNIQUE_FOR.1.pdf.

99. Huang, K. T., Chen, Y. H. & Walker, A. M. Inaccuracies in MTS assays: Major distorting effects of medium, serum albumin, and fatty acids. *Biotechniques* **37**, 406–412 (2004).

100. Adan, A., Alizada, G., Kiraz, Y., Baran, Y. & Nalbant, A. Flow cytometry: basic principles and applications. *Crit. Rev. Biotechnol.* **37**, 163–176 (2017).

101. Husain, Z., Rojas, J., Maghari, A. & Lambert, W. C. Why immunofluorescence? *Skinmed* **9**, 52–54 (2011).

102. Vanderlinde, R. E. Measurement of Total Lactate Dehydrogenase Activity. *Ann. Clin. Lab. Sci.* **15**, (1985).

103. Busch, M., Bredeck, G., Kämpfer, A. A. M. & Schins, R. P. F. Investigations of acute effects of polystyrene and polyvinyl chloride micro- and nanoplastics in an advanced in vitro triple culture model of the healthy and inflamed intestine. *Environ. Res.* **193**, (2021).

104. Upadhyay, S. & Palmberg, L. Air-liquid interface: Relevant in vitro models for investigating air pollutant-induced pulmonary toxicity. *Toxicol. Sci.* **164**, 21–30 (2018).

105. Xing, Q. *et al.* Decellularization of Fibroblast Cell Sheets for Natural Extracellular Matrix Scaffold Preparation. *Tissue Eng. Part C Methods* **21**, (2015).

106. De Hilster, R. H. J. *et al.* Human lung extracellular matrix hydrogels resemble the stiffness and viscoelasticity of native lung tissue. *Am. J. Physiol. - Lung Cell. Mol. Physiol.* **318**, L698–L704 (2020).

107. Freytes, D. O., Martin, J., Velankar, S. S., Lee, A. S. & Badylak, S. F. Preparation and rheological characterization of a gel form of the porcine urinary bladder matrix. *Biomaterials* **29**, 1630–1637 (2008).

108. Fernández-Pérez, J. & Ahearne, M. The impact of decellularization methods on extracellular matrix derived hydrogels. *Sci. Rep.* **9**, 1–12 (2019).

109. Jang, J. *et al.* Tailoring mechanical properties of decellularized extracellular matrix bioink by vitamin B2-induced photo-crosslinking. *Acta Biomater.* **33**, 88–95 (2016).

110. Nishiguchi, A. & Taguchi, T. A pH-driven genipin gelator to engineer decellularized extracellular matrix-based tissue adhesives. *Acta Biomater.* **131**, 211–221 (2021).

111. Chen, W. *et al.* 3D printing electrospinning fiber-reinforced decellularized extracellular matrix for cartilage regeneration. *Chem. Eng. J.* **382**, 122986 (2020).

112. Fernández-Pérez, J., Kador, K. E., Lynch, A. P. & Ahearne, M. Characterization of extracellular matrix modified poly(ε-caprolactone) electrospun scaffolds with differing fiber orientations for corneal stroma regeneration. *Mater. Sci. Eng. C* **108**, 0–8 (2020).

113. Ahn, G. *et al.* Precise stacking of decellularized extracellular matrix based 3D cell-laden constructs by a 3D cell printing system equipped with heating modules. *Sci. Rep.* **7**, 1–11 (2017).

114. Pati, F. *et al.* Printing three-dimensional tissue analogues with decellularized extracellular matrix bioink. *Nat. Commun.* **5**, 1–11 (2014).

115. He, M., Callanan, A., Lagaras, K., Steele, J. A. M. & Stevens, M. M. Optimization of SDS exposure on preservation of ECM characteristics in whole organ decellularization of rat kidneys. *J. Biomed. Mater. Res. - Part B Appl. Biomater.* **105**, 1352–1360 (2017).

116. Tsuchiya, T. *et al.* Ventilation-Based Decellularization System of the Lung. *Biores. Open Access* **5**, 118–126 (2016).

117. Fitzpatrick, L. E. & McDevitt, T. C. Cell-derived matrices for tissue engineering and regenerative medicine applications. *Biomater. Sci.* **3**, 12–24 (2015).

118. Xing, Q. *et al.* Natural Extracellular Matrix for Cellular and Tissue Biomanufacturing. *ACS Biomater. Sci. Eng.* **3**, 1462–1476 (2017).

119. Crapo, P. M., Gilbert, T. W. & Badylak, S. F. An overview of tissue and whole organ decellularization processes. *Biomaterials* **32**, 3233–3243 (2011).

120. Choi, M., Sultana, T., Park, M. & Lee, B. T. Fibroblast cell derived extracellular matrix containing electrospun scaffold as a hybrid biomaterial to promote in vitro endothelial cell expansion and functionalization. *Mater. Sci. Eng. C* **120**, 111659 (2021).

121. Hong, Y., Koh, I., Park, K. & Kim, P. On-Chip Fabrication of a Cell-Derived Extracellular Matrix Sheet. *ACS Biomater. Sci. Eng.* **3**, 3546–3552 (2017).

122. Rubi-Sans, G. *et al.* Engineering Cell-Derived Matrices: From 3D Models to Advanced Personalized Therapies. *Adv. Funct. Mater.* **30**, 1–19 (2020).

123. Gilbert, T. W., Sellaro, T. L. & Badylak, S. F. Decellularization of tissues and organs. *Biomaterials* **27**, 3675–3683 (2006).

124. He, M. & Callanan, A. Comparison of methods for whole-organ decellularization in tissue engineering of bioartificial organs. *Tissue Eng. - Part B Rev.* **19**, 194–208 (2013).

125. Keane, T. J., Swinehart, I. T. & Badylak, S. F. Methods of tissue decellularization used for

preparation of biologic scaffolds and in vivo relevance. *Methods* **84**, 25–34 (2015).

126. Sigma-Aldrich, I. of P. https://www.sigmaaldrich.com/life-science/metabolomics/enzyme-explorer/analytical-enzymes/papain.html.

127. Whiteman, P. The quantitative measurement of Alcian Blue-glycosaminoglycan complexes. *Biochem. J.* **131**, 343–350 (1973).

128. Mathapati, S. *et al.* Qualitative and quantitative detection of sodium deoxycholic acid in decellularized tissue. *Indian J. Thorac. Cardiovasc. Surg.* **26**, 129–131 (2010).

129. Zvarova, B. *et al.* Residual Detergent Detection Method for Nondestructive Cytocompatibility Evaluation of Decellularized Whole Lung Scaffolds. *Tissue Eng. - Part C Methods* **22**, 418–428 (2016).

130. Choudhury, D., Han, W. T., Wang, T. & Naing, M. W. Organ-Derived Decellularized Extracellular Matrix: A Game Changer for Bioink Manufacturing? *Trends Biotechnol.* **xx**, (2018).

131. Zaborniak, I. & Chmielarz, P. Riboflavin-mediated radical polymerization – Outlook for eco-friendly synthesis of functional materials. *Eur. Polym. J.* **142**, 110152 (2021).

132. Santhiago, M. R. & Randleman, J. B. The biology of corneal cross-linking derived from ultraviolet light and riboflavin. *Exp. Eye Res.* **202**, 108355 (2021).

133. Schneider, K. H. *et al.* Riboflavin-mediated photooxidation to improve the characteristics of decellularized human arterial small diameter vascular grafts. *Acta Biomater.* **116**, 246–258 (2020).

134. Tirella, A., Liberto, T. & Ahluwalia, A. Riboflavin and collagen: New crosslinking methods to tailor the stiffness of hydrogels. *Mater. Lett.* **74**, 58–61 (2012).

135. Taghizadeh, M. *et al.* Photosensitizer-induced cross-linking: A novel approach for improvement of physicochemical and structural properties of gelatin edible films. *Food Res. Int.* **112**, 90–97 (2018).

136. Gallagher, S. R. & Desjardins, P. R. Quantitation of DNA and RNA with absorption and fluorescence spectroscopy. *Curr. Protoc. Protein Sci.* 1–21 (2008). doi:10.1002/0471140864.psa04ks52

137. Sullivan, D. C. *et al.* Decellularization methods of porcine kidneys for whole organ engineering using a high-throughput system. *Biomaterials* **33**, 7756–7764 (2012).

138. Wang, Y. *et al.* Method for perfusion decellularization of porcine whole liver and kidney for use as a scaffold for clinical-scale bioengineering engrafts. *Xenotransplantation* **22**, 48–61 (2015).

139. Asrin Emami, Tahereh Talaei-Khozani, Zahra Vojdani, N. Z. fard. Comparative assessment of the efficiency of various decellularization agents for bone tissue engineering. *J. Biomed. Mater. Res. Part B* (2020).

140. Simsa, R. *et al.* Systematic in vitro comparison of decellularization protocols for blood vessels. *PLoS One* **13**, 1–19 (2018).

141. Syed, O., Walters, N. J., Day, R. M., Kim, H. W. & Knowles, J. C. Evaluation of decellularization protocols for production of tubular small intestine submucosa scaffolds for use in oesophageal tissue engineering. *Acta Biomater.* **10**, 5043–5054 (2014).

142. Maghsoudlou, P., Totonelli, G., Loukogeorgakis, S. P., Eaton, S. & De Coppi, P. A decellularization methodology for the production of a natural acellular intestinal matrix. *J. Vis. Exp.* 1–6 (2013). doi:10.3791/50658

143. Poornejad, N. *et al.* The impact of decellularization agents on renal tissue extracellular matrix. *J. Biomater. Appl.* **31**, 521–533 (2016).

144. Dew, L., English, W. R., Chong, C. K. & MacNeil, S. Investigating Neovascularization in Rat

Decellularized Intestine: An in Vitro Platform for Studying Angiogenesis. *Tissue Eng. - Part A* **22**, 1317–1326 (2016).

145. Seo, Y., Jung, Y. & Kim, S. H. Decellularized heart ECM hydrogel using supercritical carbon dioxide for improved angiogenesis. *Acta Biomater.* **67**, 270–281 (2018).

146. Jung, K. H., Choi, Y. C., Chun, J. Y., Min, S. G. & Hong, G. P. Effects of concentration and reaction time of Trypsin, Pepsin, and Chymotrypsin on the hydrolysis efficiency of porcine placenta. *Korean J. Food Sci. Anim. Resour.* **34**, 151–157 (2014).

147. Nalinanon, S., Benjakul, S., Kishimura, H. & Osako, K. Type I collagen from the skin of ornate threadfin bream (Nemipterus hexodon): Characteristics and effect of pepsin hydrolysis. *Food Chem.* **125**, 500–507 (2011).

148. Gratzer, P. F. & Robert D. Harrison, and T. W. Matrix Alteration and Not Residual Sodium Dodecyl Sulfate Cytotoxicity Affects the Cellular Repopulation of a Decellularized Matrix. *Tissue Eng.* **12**, (2006).

149. Brown, B. N. *et al.* Surface characterization of extracellular matrix scaffolds. *Biomaterials* **31**, 428–437 (2010).

150. Voytik-Harbin, S. L., Brightman, A. O., Waisner, B. Z., Robinson, J. P. & Lamar, C. H. Small intestinal submucosa: A tissue-derived extracellular matrix that promotes tissue-specific growth and differentiation of cells in vitro. *Tissue Eng.* **4**, 157–174 (1998).

151. Zanetti-Polzi, L., Aschi, M., Daidone, I. & Amadei, A. Theoretical modeling of the absorption spectrum of aqueous riboflavin. *Chem. Phys. Lett.* **669**, 19–28 (2017).

152. Yao, Q. *et al.* Recent development and biomedical applications of decellularized extracellular matrix biomaterials. *Mater. Sci. Eng. C* **104**, 109942 (2019).

153. Baiguera, S. *et al.* Dynamic decellularization and cross-linking of rat tracheal matrix. *Biomaterials* **35**, 6344–6350 (2014).

154. Gao, S. *et al.* Comparison of glutaraldehyde and carbodiimides to crosslink tissue engineering scaffolds fabricated by decellularized porcine menisci. *Mater. Sci. Eng. C* **71**, 891–900 (2017).

155. Gelse, K., Pöschl, E. & Aigner, T. Collagens - Structure, function, and biosynthesis. *Adv. Drug Deliv. Rev.* **55**, 1531–1546 (2003).

156. Karna, E., Szoka, L., Huynh, T. Y. L. & Palka, J. A. Proline-dependent regulation of collagen metabolism. *Cell. Mol. Life Sci.* **77**, 1911–1918 (2020).

157. Georges Bellon *, Brahim Chaqour, Yanusz Wegrowski, Jean-Claude Monboisse, J.-P. B. & Laboratory. Glutamine increases collagen gene transcription in cultured human fibroblasts. *Biochim. Biophys. Acta 1268* **1268**, 159–167 (1995).

158. Hamanaka, R. B. *et al.* Glutamine metabolism is required for collagen protein synthesis in lung fibroblasts. *Am. J. Respir. Cell Mol. Biol.* **61**, 597–606 (2019).

159. Szoka, L., Karna, E., Hlebowicz-Sarat, K., Karaszewski, J. & Palka, J. A. Exogenous proline stimulates type I collagen and HIF-1α expression and the process is attenuated by glutamine in human skin fibroblasts. *Mol. Cell. Biochem.* **435**, 197–206 (2017).

160. Ryszer, T. Understanding the Mysterious M2 Macrophage through Activation Markers and Effector Mechanisms. *Hindawi Publ. Corp.* (2015). doi:10.32388/n35phw

161. Inoue, H., Nagata, N., Kurokawa, H. & Yamanaka, S. iPS cells: a game changer for future medicine. *EMBO J.* **33**, 409–417 (2014).

162. Klein, S. G., Hennen, J., Serchi, T., Blömeke, B. & Gutleb, A. C. Potential of coculture in vitro models to study inflammatory and sensitizing effects of particles on the lung. *Toxicol. Vitr.* **25**, 1516–1534 (2011).

163. Nichols, J. E. *et al.* Modeling the lung: Design and development of tissue engineered macro- and micro-physiologic lung models for research use. (2014). doi:10.1177/1535370214536679

164. Artzy-Schnirman, A. *et al.* Capturing the Onset of Bacterial Pulmonary Infection in Acini-On-Chips. *Adv. Biosyst.* **3**, 1–9 (2019).

165. Barosova, H. *et al.* Inter-laboratory variability of A549 epithelial cells grown under submerged and air-liquid interface conditions. *Toxicol. Vitr.* **75**, 105178 (2021).

166. Tibor, B., Marco, H. & Andre, B. Successful re-endothelialization of a perfusable biological vascularized matrix (BioVaM) for the generation of 3D artificial cardiac tissue. (2014). doi:10.1007/s00395-014-0441-x

167. Gaetani, R., Aude, S., Demaddalena, L. L. & Strassle, H. Evaluation of Different Decellularization Protocols on the Generation of Pancreas-Derived Hydrogels. *Tissue Eng. Part C* **24**, 697–709 (2018).

168. Place, T. L., Domann, F. E. & Case, A. J. Limitations of oxygen delivery to cells in culture: An underappreciated problem in basic and translational research. *Free Radic. Biol. Med.* **113**, 311–322 (2017).

169. Neufeld, G. & Kessler, O. Pro-angiogenic cytokines and their role in tumor angiogenesis. *Cancer Metastasis Rev.* **25**, 373–385 (2006).

170. Bouïs, D., Kusumanto, Y., Meijer, C., Mulder, N. H. & Hospers, G. A. P. A review on pro- and anti-angiogenic factors as targets of clinical intervention. *Pharmacol. Res.* **53**, 89–103 (2006).

171. Morin, K. T. & Tranquillo, R. T. In vitro models of angiogenesis and vasculogenesis in fibrin gel. *Exp. Cell Res.* **319**, 2409–2417 (2013).

172. Hsu, Y. H., Moya, M. L., Hughes, C. C. W., George, S. C. & Lee, A. P. A microfluidic platform for generating large-scale nearly identical human microphysiological vascularized tissue arrays. *Lab Chip* **13**, 2990–2998 (2013).

173. van Duinen, V. *et al.* Perfused 3D angiogenic sprouting in a high-throughput in vitro platform. *Angiogenesis* **22**, 157–165 (2019).

174. Vinci, M., Box, C. & Eccles, S. A. Three-dimensional (3D) tumor spheroid invasion assay. *J. Vis. Exp.* **2015**, 1–9 (2015).

175. Parigoris, E. *et al.* Cancer Cell Invasion of Mammary Organoids with Basal-In Phenotype. *Adv. Healthc. Mater.* **10**, 1–10 (2021).

176. Kam, Y., Guess, C., Estrada, L., Weidow, B. & Quaranta, V. A novel circular invasion assay mimics in vivo invasive behavior of cancer cell lines and distinguishes single-cell motility in vitro. *BMC Cancer* **8**, 1–12 (2008).

177. Parry, D. A. D. & Squire, J. M. *Fibrous Proteins: Structures and Mechanisms*. *Subcellular Biochemistry* **82**, (2017).

178. Ryan, E. A., Mockros, L. F., Weisel, J. W. & Lorand, L. Structural origins of fibrin clot rheology. *Biophys. J.* **77**, 2813–2826 (1999).

179. Hwang, C. M. *et al.* Fabrication of three-dimensional porous cell-laden hydrogel for tissue engineering. *Biofabrication* **2**, (2010).

180. Lipowiecki, M. *et al.* Permeability of rapid prototyped artificial bone scaffold structures. *J. Biomed. Mater. Res. - Part A* **102**, 4127–4135 (2014).

181. Levy, J. H., Welsby, I. & Goodnough, L. T. Fibrinogen as a therapeutic target for bleeding: A review of critical levels and replacement therapy. *Transfusion* **54**, 1389–1405 (2014).

182. Mann, K. G., Brummel, K. & Butenas, S. What is all that thrombin for? *J. Thromb. Haemost.* **1**,

1504–1514 (2003).

183. Yadav, L., Puri, N., Rastogi, V., Satpute, P. & Sharma, V. Tumour angiogenesis and angiogenic inhibitors: A review. *J. Clin. Diagnostic Res.* **9**, XE01–XE05 (2015).

184. Carmeliet, P. & Jain, R. K. Angiogenesis in cancer and other diseases. *Nature* **407**, 249–257 (2000).

185. Volz, A. C., Huber, B., Schwandt, A. M. & Kluger, P. J. EGF and hydrocortisone as critical factors for the co-culture of adipogenic differentiated ASCs and endothelial cells. *Differentiation* **95**, 21–30 (2017).

186. Ulrich-Merzenich, G., Zeitler, H., Panek, D., Bokemeyer, D. & Vetter, H. Vitamin C promotes human endothelial cell growth via the ERK-signaling pathway. *Eur. J. Nutr.* **46**, 87–94 (2007).

187. Telang, S., Clem, A. L., Eaton, J. W. & Chesney, J. Depletion of ascorbic acid restricts angiogenesis and retards tumor growth in a mouse model. *Neoplasia* **9**, 47–56 (2007).

188. Davis, G. E. *et al.* Control of vascular tube morphogenesis and maturation in 3D extracellular matrices by endothelial cells and pericytes. *Methods Mol. Biol.* **1066**, 17–28 (2013).

189. Xu, H. *et al.* Protein kinase C α promotes angiogenic activity of human endothelial cells via induction of vascular endothelial growth factor. *Cardiovasc. Res.* **78**, 349–355 (2008).

190. Taylor, C. J., Motamed, K. & Lilly, B. Protein kinase C and downstream signaling pathways in a three-dimensional model of phorbol ester-induced angiogenesis. *Angiogenesis* **9**, 39–51 (2006).

191. Wu, T. C. *et al.* Phorbol ester-induced angiogenesis of endothelial progenitor cells: The role of NADPH oxidase-mediated, redox-related matrix metalloproteinase pathways. *PLoS One* **14**, 1–18 (2019).

192. Woolard, J., Bevan, H. S., Harper, S. J. & Bates, D. O. Molecular diversity of VEGF-A as a regulator of Its biological activity. *Microcirculation* **16**, 572–592 (2009).

193. Gaengel, K., Genové, G., Armulik, A. & Betsholtz, C. Endothelial-mural cell signaling in vascular development and angiogenesis. *Arterioscler. Thromb. Vasc. Biol.* **29**, 630–638 (2009).

194. Argraves, K. M. Sphingosine-1-phosphate signaling in vasculogenesis and angiogenesis. *World J. Biol. Chem.* **1**, 291 (2010).

195. Aoki, M., Aoki, H., Ramanathan, R., Hait, N. C. & Takabe, K. Sphingosine-1-Phosphate Signaling in Immune Cells and Inflammation: Roles and Therapeutic Potential. *Mediators Inflamm.* **2016**, (2016).

196. Fritz, H. & Wunderer, G. Biochemistry and applications of aprotinin, the kallikrein inhibitor from bovine organs. *Arzneimittel-Forschung/Drug Res.* **33**, 479–494 (1983).

197. Ye, Q. *et al.* Fibrin gel as a three dimensional matrix in cardiovascular tissue engineering. *Eur. J. Cardio-thoracic Surg.* **17**, 587–591 (2000).

198. Jockenhoevel, S. *et al.* Fibrin gel - advantages of a new scaffold in cardiovascular tissue engineering. *Eur. J. Cardio-thoracic Surg.* **19**, 424–430 (2001).

199. Mühleder, S. *et al.* The role of fibrinolysis inhibition in engineered vascular networks derived from endothelial cells and adipose-derived stem cells. *Stem Cell Res. Ther.* **9**, 1–13 (2018).

200. Collen, A., Koolwijk, P., Kroon, M. & Van Hinsbergh, V. W. M. Influence of fibrin structure on the formation and maintenance of capillary-like tubules by human microvascular endothelial cells. *Angiogenesis* **2**, 153–166 (1998).

201. Kaiser, N. J., Kant, R. J., Minor, A. J. & Coulombe, K. L. K. Optimizing Blended Collagen-Fibrin Hydrogels for Cardiac Tissue Engineering with Human iPSC-derived Cardiomyocytes. *ACS Biomater. Sci. Eng.* **5**, 887–899 (2019).

202. Takehara, H., Sakaguchi, K., Sekine, H., Okano, T. & Shimizu, T. Microfluidic vascular-bed devices

for vascularized 3D tissue engineering: tissue engineering on a chip. *Biomed. Microdevices* **22**, 1–7 (2020).

203. Thomson, K. S., Dupras, S. K., Murry, C. E., Scatena, M. & Regnier, M. Proangiogenic microtemplated fibrin scaffolds containing aprotinin promote improved wound healing responses. *Angiogenesis* **17**, 195–205 (2014).

204. Kato, K. *et al.* Pulmonary pericytes regulate lung morphogenesis. *Nat. Commun.* **9**, 1–14 (2018).

205. Sims, D. E. The Pericyte - A review. *Tissue&Cell&Cell* **18**, (1986).

206. Chiaverina, G. *et al.* Dynamic Interplay between Pericytes and Endothelial Cells during Sprouting Angiogenesis. *Cells* **8**, 1–13 (2019).

207. Bai, J. *et al.* Angiogenic responses in a 3D micro-engineered environment of primary endothelial cells and pericytes. *Angiogenesis* **24**, 111–127 (2021).

208. Mahfouzi, S. H., Amoabediny, G. & Safiabadi Tali, S. H. Advances in bioreactors for lung bioengineering: From scalable cell culture to tissue growth monitoring. *Biotechnol. Bioeng.* **118**, 2142–2167 (2021).

209. Selden, C. & Fuller, B. Role of bioreactor technology in tissue engineering for clinical use and therapeutic target design. *Bioengineering* **5**, 1–10 (2018).

210. Ren, X. *et al.* Engineering pulmonary vasculature in decellularized rat and human lungs. *Nat. Biotechnol.* **33**, 1097–1102 (2015).

211. Gorman, D. E., Wu, T., Gilpin, S. E. & Ott, H. C. A fully automated high-throughput bioreactor system for lung regeneration. *Tissue Eng. - Part C Methods* **24**, 671–678 (2018).

212. Raredon, M. S. B. *et al.* Biomimetic Culture Reactor for Whole-Lung Engineering. *Biores. Open Access* **5**, 72–83 (2016).

213. Ackermann, M. *et al.* Bioreactor-based mass production of human iPSC-derived macrophages enables immunotherapies against bacterial airway infections. *Nat. Commun.* **9**, 1–13 (2018).

214. Badenes, S. M. *et al.* Defined essential 8' medium and vitronectin efficiently support scalable xeno-free expansion of human induced pluripotent stem cells in stirred microcarrier culture systems. *PLoS One* **11**, 1–19 (2016).

215. Rodrigues, A. L. *et al.* Dissolvable Microcarriers Allow Scalable Expansion And Harvesting Of Human Induced Pluripotent Stem Cells Under Xeno-Free Conditions. *Biotechnol. J.* **14**, 1–12 (2019).

216. Spratt, J. R. *et al.* Prolonged extracorporeal preservation and evaluation of human lungs with portable normothermic ex vivo perfusion. *Clin. Transplant.* **34**, 1–9 (2020).

217. Warnecke, G. *et al.* Normothermic perfusion of donor lungs for preservation and assessment with the Organ Care System Lung before bilateral transplantation: A pilot study of 12 patients. *The Lancet* **380**, 1851–1858 (2012).

218. Raredon, M. S. B., Ghaedi, M., Calle, E. A. & Niklason, L. E. A Rotating Bioreactor for Scalable Culture and Differentiation of Respiratory Epithelium. *Cell Med.* **7**, 109–121 (2015).

219. Ghaedi, M. *et al.* Alveolar epithelial differentiation of human induced pluripotent stem cells in a rotating bioreactor. *Biomaterials* **35**, 699–710 (2014).

220. Siti-Ismail, N., Samadikuchaksaraei, A., Bishop, A. E., Polak, J. M. & Mantalaris, A. Development of a novel three-dimensional, automatable and integrated bioprocess for the differentiation of embryonic stem cells into pulmonary alveolar cells in a rotating vessel bioreactor system. *Tissue Eng. - Part C Methods* **18**, 263–272 (2012).

221. Sciences, B., Division, E. & Scientific, C. Development of a Three-Dimensional Bioengineering

Technology to Generate Lung Tissue for Personalized Disease Modeling. 969–976 (2014).

222. Jeans, A. R. *et al.* Pharmacodynamics of voriconazole in a dynamic in vitro model of invasive pulmonary aspergillosis: Implications for in vitro susceptibility breakpoints. *J. Infect. Dis.* **206**, 442–452 (2012).

223. Box, H. *et al.* Pharmacodynamics of isavuconazole in a dynamic In Vitro model of invasive pulmonary aspergillosis. *Antimicrob. Agents Chemother.* **60**, 278–287 (2016).

224. Blume, C. *et al.* Temporal monitoring of differentiated human airway epithelial cells using microfluidics. *PLoS One* **10**, 1–13 (2015).

225. Chandorkar, P. *et al.* Fast-track development of an in vitro 3D lung/immune cell model to study Aspergillus infections. *Sci. Rep.* **7**, 1–13 (2017).

226. Martin, K. C. *et al.* Symmetry-breaking in branching epithelia: cells on micro-patterns under flow challenge the hypothesis of positive feedback by a secreted autocrine inhibitor of motility. *J. Anat.* **230**, 766–774 (2017).

227. Ucciferri, N. *et al.* In vitro toxicological screening of nanoparticles on primary human endothelial cells and the role of flow in modulating cell response. *Nanotoxicology* **8**, 697–708 (2014).

228. Sbrana, T. *et al.* Dual flow bioreactor with ultrathin microporous TEER sensing membrane for evaluation of nanoparticle toxicity. *Sensors Actuators, B Chem.* **223**, 440–446 (2016).

229. Tomei, A. A., Choe, M. M. & Swartz, M. A. Effects of dynamic compression on lentiviral transduction in an in vitro airway wall model. *Am. J. Physiol. - Lung Cell. Mol. Physiol.* **294**, 79–86 (2008).

230. Dassow, C. *et al.* Biaxial distension of precision-cut lung slices. *J. Appl. Physiol.* **108**, 713–721 (2010).

231. Arold, S. P., Wong, J. Y. & Suki, B. Design of a new stretching apparatus and the effects of cyclic strain and substratum on mouse lung epithelial-12 cells. *Ann. Biomed. Eng.* **35**, 1156–1164 (2007).

232. Desai, L. P., Chapman, K. E. & Waters, C. M. Mechanical stretch decreases migration of alveolar epithelial cells through mechanisms involving Rac1 and Tiam1. *Am. J. Physiol. - Lung Cell. Mol. Physiol.* **295**, 958–965 (2008).

233. Heise, R. L., Stober, V., Cheluvaraju, C., Hollingsworth, J. W. & Garantziotis, S. Mechanical stretch induces epithelial-mesenchymal transition in alveolar epithelia via hyaluronan activation of innate immunity. *J. Biol. Chem.* **286**, 17435–17444 (2011).

234. Huang, Z., Wang, Y., Nayak, P. S., Dammann, C. E. & Sanchez-Esteban, J. Stretch-induced fetal type II cell differentiation is mediated via ErbB1-ErbB4 interactions. *J. Biol. Chem.* **287**, 18091–18102 (2012).

235. Nossa, R., Costa, J., Cacopardo, L. & Ahluwalia, A. Breathing in vitro: Designs and applications of engineered lung models. *J. Tissue Eng.* **12**, (2021).

236. Darbyshire, A. G. & Mullin, T. Transition to turbulence in constant-mass-flux pipe flow. *J. Fluid Mech.* **289**, 83–114 (1995).

237. Jennifer Y. Kasper*, Maria I. Hermanns, R. E. U. and C. J. K. A responsive human triple-culture model of the air blood barrier incorporation of.pdf. *J. Tissue Eng. Regen. Med.* 1285–1297 (2015).

238. Dohle, E. *et al.* Human Co- and Triple-Culture Model of the Alveolar-Capillary Barrier on a Basement Membrane Mimic. *Tissue Eng. - Part C Methods* **24**, 495–503 (2018).

239. Horvath, L. *et al.* Engineering an in vitro air-blood barrier by 3D bioprinting. *Sci. Rep.* **5**, (2015).

240. Dayoon Kang, Ju An Park, Woojo Kim, Seongju Kim, Hwa-Rim Lee,* Woo-Jong Kim, Joo-Yeon Yoo,

and S. J. All-Inkjet-Printed 3D Alveolar Barrier Model with Physiologically Relevant.pdf. *Av. Sci.* (2021).

241. Barreiro Carpio, M. *et al.* 3D Bioprinting Strategies, Challenges, and Opportunities to Model the Lung Tissue Microenvironment and Its Function. *Front. Bioeng. Biotechnol.* **9**, 1–24 (2021).

242. Huh, D. *et al.* A Human Disease Model of Drug Toxicity-Induced Pulmonary Edema in a Lung-on-a-Chip Microdevice. *Sci. Transl. Med.* **4**, 159ra147-159ra147 (2012).

243. Benam, K. H. *et al.* Small airway-on-a-chip enables analysis of human lung inflammation and drug responses in vitro. *Nat. Methods* **13**, 151–157 (2016).

244. Benam, K. H. *et al.* Matched-Comparative Modeling of Normal and Diseased Human Airway Responses Using a Microengineered Breathing Lung Chip. *Cell Syst.* **3**, 456-466.e4 (2016).

245. Henry, O. Y. F. *et al.* Organs-on-chips with integrated electrodes for trans-epithelial electrical resistance (TEER) measurements of human epithelial barrier function. *Lab Chip* **17**, 2264–2271 (2017).

246. Jain, A. *et al.* Primary Human Lung Alveolus-on-a-chip Model of Intravascular Thrombosis for Assessment of Therapeutics. *Clin. Pharmacol. Ther.* **103**, 332–340 (2018).

247. Hassell, B. A. *et al.* Human Organ Chip Models Recapitulate Orthotopic Lung Cancer Growth, Therapeutic Responses, and Tumor Dormancy In Vitro. *Cell Rep.* **21**, 508–516 (2017).

248. Eilken, H. M. & Adams, R. H. Dynamics of endothelial cell behavior in sprouting angiogenesis. *Curr. Opin. Cell Biol.* **22**, 617–625 (2010).

249. Goumans, M. J., Liu, Z. & Ten Dijke, P. TGF-β signaling in vascular biology and dysfunction. *Cell Res.* **19**, 116–127 (2009).

250. Goumans, M. J., Lebrin, F. & Valdimarsdottir, G. Controlling the angiogenic switch: A balance between two distinct TGF-β receptor signaling pathways. *Trends Cardiovasc. Med.* **13**, 301–307 (2003).

251. Iruela-Arispe, M. L. & Sage, E. H. Endothelial cells exhibiting angiogenesis in vitro proliferate in response to TGF-β1. *J. Cell. Biochem.* **52**, 414–430 (1993).

252. Badylak, S. F., Freytes, D. O. & Gilbert, T. W. Extracellular matrix as a biological scaffold material: Structure and function. *Acta Biomater.* **23**, S17–S26 (2015).

253. Wolchok, J. C. & Tresco, P. A. The isolation of cell derived extracellular matrix constructs using sacrificial open-cell foams. *Biomaterials* **31**, 9595–9603 (2010).

254. Tour, G., Wendel, M. & Tcacencu, I. Cell-derived matrix enhances osteogenic properties of hydroxyapatite. *Tissue Eng. - Part A* **17**, 127–137 (2011).

255. Sadr, N. *et al.* Enhancing the biological performance of synthetic polymeric materials by decoration with engineered, decellularized extracellular matrix. *Biomaterials* **33**, 5085–5093 (2012).

256. Seo, Y. K., Song, K. Y., Kim, Y. J. & Park, J. K. Wound healing effect of acellular artificial dermis containing extracellular matrix secreted by human skin fibroblasts. *Artif. Organs* **31**, 509–520 (2007).

257. Navone, S. E. *et al.* Decellularized silk fibroin scaffold primed with adipose mesenchymal stromal cells improves wound healing in diabetic mice. *Stem Cell Res. Ther.* **5**, 1–15 (2014).

258. Tang, K. C. *et al.* Human adipose-derived stem cell secreted extracellular matrix incorporated into electrospun poly(lactic-co-glycolic acid) nanofibrous dressing for enhancing wound healing. *Polymers (Basel).* **11**, 1–13 (2019).

259. Syedain, Z. H., Meier, L. A., Lahti, M. T., Johnson, S. L. & Tranquillo, R. T. Implantation of

completely biological engineered grafts following decellularization into the sheep femoral artery. *Tissue Eng. - Part A* **20**, 1726–1734 (2014).

260. Quint, C. *et al.* Decellularized tissue-engineered blood vessel as an arterial conduit. *Proc. Natl. Acad. Sci. U. S. A.* **108**, 9214–9219 (2011).

261. Bourget, J. M. *et al.* Human fibroblast-derived ECM as a scaffold for vascular tissue engineering. *Biomaterials* **33**, 9205–9213 (2012).

262. Pati, F. *et al.* Ornamenting 3D printed scaffolds with cell-laid extracellular matrix for bone tissue regeneration. *Biomaterials* **37**, 230–241 (2015).

263. Lee, H., Yang, S., Kim, M. & Kim, G. H. A scaffold with a bio-mimetically designed micro/ nano-fibrous structure using decellularized extracellular matrix. *RSC Adv.* **6**, 29697–29706 (2016).

264. Dabaghi, M. *et al.* A robust protocol for decellularized human lung bioink generation amenable to 2d and 3d lung cell culture. *Cells* **10**, 1–23 (2021).

265. Price, A. P., England, K. A., Matson, A. M., Blazar, B. R. & Panoskaltsis-Mortari, A. Development of a decellularized lung bioreactor system for bioengineering the lung: The matrix reloaded. *Tissue Eng. - Part A* **16**, 2581–2591 (2010).

266. Cortiella, J. *et al.* Influence of acellular natural lung matrix on murine embryonic stem cell differentiation and tissue formation. *Tissue Eng. - Part A* **16**, 2565–2580 (2010).

267. Gao, S. *et al.* Fabrication and characterization of electrospun nanofibers composed of decellularized meniscus extracellular matrix and polycaprolactone for meniscus tissue engineering. *J. Mater. Chem. B* **5**, 2273–2285 (2017).

268. Chen, W. *et al.* 3D printing electrospinning fiber-reinforced decellularized extracellular matrix for cartilage regeneration. *Chem. Eng. J.* **382**, 122986 (2020).

269. Grant, R., Hallett, J., Forbes, S., Hay, D. & Callanan, A. Blended electrospinning with human liver extracellular matrix for engineering new hepatic microenvironments. *Sci. Rep.* **9**, 1–12 (2019).

270. Baptista, D., Teixeira, L., van Blitterswijk, C., Giselbrecht, S. & Truckenmüller, R. Overlooked? Underestimated? Effects of Substrate Curvature on Cell Behavior. *Trends Biotechnol.* **37**, 838–854 (2019).

271. Baptista, D. *et al.* 3D alveolar in vitro model based on epithelialized biomimetically curved culture membranes. *Biomaterials* **266**, (2021).

272. Nawroth, J. C. *et al.* Automated fabrication of photopatterned gelatin hydrogels for organ-on-chips applications. *Biofabrication* **10**, (2018).

273. Kniebs, C. *et al.* Influence of Different Cell Types and Sources on Pre-Vascularisation in Fibrin and Agarose–Collagen Gels. *Organogenesis* **16**, 14–26 (2020).

274. Patsch, C. *et al.* Generation of vascular endothelial and smooth muscle cells from human pluripotent stem cells. *Nat. Cell Biol.* **17**, 994–1003 (2015).

275. Fitzsimmons, R. E. B., Ireland, R. G., Zhong, A., Soos, A. & Simmons, C. A. Assessment of fibrin-collagen co-gels for generating microvessels ex vivo using endothelial cell-lined microfluidics and multipotent stromal cell (MSC)-induced capillary morphogenesis. *Biomed. Mater.* **16**, (2021).

276. Carius, P. *et al.* PerfuPul—A Versatile Perfusable Platform to Assess Permeability and Barrier Function of Air Exposed Pulmonary Epithelia. *Front. Bioeng. Biotechnol.* **9**, 1–16 (2021).

277. Felder, M. *et al.* Impaired wound healing of alveolar lung epithelial cells in a breathing lung-on-a-chip. *Front. Bioeng. Biotechnol.* **7**, 1–5 (2019).

278. Dongeun Huh, Benjamin D. Matthews, A. M. M. M.-Z. & Hong Yuan Hsin, D. E. I. Reconstituting Organ-Level Lung. *Science (80-.).* **328**, 1662–1669 (2010).

279.   Thompson, C. L., Fu, S., Knight, M. M. & Thorpe, S. D. Mechanical Stimulation: A Crucial Element of Organ-on-Chip Models. *Front. Bioeng. Biotechnol.* **8**, 1–18 (2020).

280.   Costa, J. *et al.* Bioreactor With Electrically Deformable Curved Membranes for Mechanical Stimulation of Cell Cultures. *Front. Bioeng. Biotechnol.* **8**, 1–9 (2020).

281.   Cei, D. *et al.* Development of a dynamic in vitro stretch model of the alveolar interface with aerosol delivery. *Biotechnol. Bioeng.* **118**, 690–702 (2021).

282.   Ingber, D. E. Developmentally inspired human 'organs on chips'. *Dev.* **145**, 10–13 (2018).